Università degli Studi di Padova

Administrative unit: **University of Padova**

Department: **Land, Environment, Agriculture and Forestry (LEAF)**

PhD Program: **Land, Environment, Resources and Health (LERH)**

Batch:XXXI

Assessing different survey and gridding techniques for Digital Elevation Models generation and the related influence on stony debris flows modelling. A case study from Cancia basin (Venetian Dolomites, North-Eastern Italian Alps)

PhD Program Coordinator: Prof. Davide Matteo Pettenella

Supervisor: Carlo Gregoretti

Co-Supervisor: Alberto Guarnieri

PhD candidate: Mauro Boreggio

Università degli Studi di Padova

Sede Amministrativa: **Università degli Studi di Padova**

Dipartimento; **Territorio e Sistemi Agro-Forestali (TESAF)**

CORSO DI DOTTORATO DI RICERCA: **Land, Environment, Resources, Health (LERH)**

Ciclo: XXXI

Valutando diverse tecniche di rilievo e di interpolazione per la generazione di Modelli Digitali del Terreno, e la loro influenza sulla modellazione di propagazione di colate detritiche granulari. Il caso studio del bacino di Rovina di Cancia (Dolomiti Venete, Alpi Italiane Nord-Orientali)

Coordinatore: Prof. Davide Matteo Pettenella

Supervisore: Prof. Carlo Gregoretti

Co-Supervisore: Dr. Alberto Guarnieri

Dottorando: Mauro Boreggio

Abstract

In the Dolomites area (North-Eastern Italian Alps), debris flows can be regarded as one of the most hazardous geomorphological processes. In the last few years, these natural phenomena amplified their occurrence rate due to the rise of extreme rainfall events, and the increasing availability of debris material yielded by the retreat of the glaciers and the permafrost areas to higher elevations. In order to cope with debris flow hazard, it is common to couple structural and non-structural measurements, such as the zoning of risk prone areas by means of routing models. Since the motion of gravity-driven flows is extremely sensitive to surface morphology, topographic data in the form of Digital Elevation Models (DEMs) represent the most important input in debris flow routing models. As a matter of fact, a DEM can be regarded as a mathematical representation of the bare earth in digital form, and it is commonly used to represent the surface morphology in three dimensions. The "quality" of DEMs depends on the accuracy, density, and spatial distribution of the topographic data (i.e., on the employed survey technique); on the characteristics of the surveyed surface; and on the applied gridding methodology. Therefore, the choice of both the survey technique and the gridding methodology might represent a critical concern for the reliability of routing modeling outcomes. In order to advance in the knowledge regarding the influence of geomatic techniques on the numerical modeling of stony debris flows routing, in the present research we initially assessed the performances of common digital terrain modelling algorithms (i.e., linear triangulation, natural neighbor, nearest neighbor, inverse distance to a power, ANUDEM, completely regularize spline function, thin-plate spline function, thin-plate spline plus tension function, multi-quadratic function, inverse multi-quadratic function, point ordinary kriging, and block ordinary kriging) and survey techniques (i.e., full-waveform Light Detection And Ranging, LiDAR; and Global Navigation Satellite System, GNSS) in characterizing the complex topography of a debris flow channel located in the Venetian Dolomites. After that, their inherent influence on the results of a Geographic Information System (GIS)-based cell model for simulating stony debris flows routing is investigated through a combination of statistical and visual techniques, by considering both high- and low-magnitude flow conditions. On one hand, the research points out that the linear triangulation, the natural neighbor algorithm, and the thin-plate spline plus tension and completely regularized spline basis functions could represent the best choice for applications relying on the proper representation of the surface shape (e.g., hydraulic and hydrological modeling). In fact, these gridding algorithms proved to ensure the best trade-off between interpolation accuracy and shape reliability. However, the research also shows that the choice of the gridding methodology actually does not represent a determining factor in debris flows routing modeling. On the other hand, the analysis carried out on the capability of the two tested survey techniques in characterizing the topography of the studied debris flow channel, highlights a high degree of interoperability, since both of them could be used to generate bias-free and accurate high-resolution DEMs of morphologically complex areas. However, the pairwise comparison of the GNSS- and LiDAR-derived DEMs reveals that, although the two investigated survey techniques provide a comparable (i.e., not statistically different) topographic characterization of the channel bathymetry, meaningful vertical discrepancies could be detected in correspondence of morphologically complex channel features (e.g., channel banks and longitudinal/transversal slope discontinuities). Furthermore, the detected discrepancies proved to be able to affect the cell routing model behavior, thus leading to the conclusion that the choice of the survey technique could represent a critical concern for the reliability of routing modeling outcomes.

Riassunto

In area Dolomitica (Alpi Italiane Nord-Orientali), le colate detritiche rappresentano uno dei processi geomorfologici più pericolosi. Negli ultimi anni, questi fenomeni naturali hanno amplificato la loro frequenza di accadimento a causa dell'aumento di eventi pluviometrici estremi, ed alla crescente disponibilità di materiale detritico prodotto dal ritiro dei ghiacciai e delle aree a permafrost a quote più elevate. Per fronteggiare il rischio da colata detrtica è comune accoppiare misure stutturali e non strutturali, come ad esempio la mappatura delle aree a rischio mediante l'impiego di modelli matematico-numerici di propagazione. Poiché il moto di flussi gravitativi è estremamente sensibile alla morfologia della superficie, ne consegue che i dati topografici sotto forma di Modelli Digitali del Terreno rappresentano il dato di input principale nei modelli di propagazione di colata detritica. Infatti, un Modello Digitale del Terreno può essere considerato come una rappresentazione matematica della superficie in forma digitale, ed è comunemente usato per rappresentare la morfologia terrestre in tre dimensioni. La "qualità" dei Modelli Digitali del Terreno dipende dall'accuratezza, dalla densità e dalla distribuzione spaziale del dato topografico (ovvero, dalla tecnica di rilievo impiegata); dalle caratteristiche della superficie campionata; e dal metodo di interpolazione utilizzato. Pertanto, la scelta della tecnica di rilievo e della metodologia di interpolazione potrebbe rappresentare un fattore critico per l'affidabilità dei risultati dei modelli di propagazione. Con l'obiettivo di progredire nella conoscenza relativa all'influenza delle tecniche geomatiche sulla modellazione numerica di colate detritiche, nella presente ricerca abbiamo inizialmente valutato le prestazioni di differenti algoritmi di modellistica digitale del terreno (ossia, linear triangulation, natural neighbor, nearest neighbor, inverse distance to a power, ANUDEM, completely regularize spline function, thin-plate spline function, thin-plate spline plus tension function, multi-quadratic function, inverse multi-quadratic function, point ordinary kriging, and block ordinary kriging) e tecniche di rilievo (ossia, full-waveform Light Detection And Ranging, LiDAR; and Global Navigation Satellite System, GNSS) nel rappresentare la complessa topografia di un canale da colata detritica ubicato nelle Dolomiti Venete. Successivamente, la loro influenza intrinseca sui risultati di un modello a celle su base GIS idoneo a simulare la propagazione di flussi detritici in regime granulo-inerziale è stata esplorata mediante una combinazione di tecniche statistiche e visive, considerando condizioni di flusso sia di alta che di bassa magnitudo. Da un lato, la ricerca sottolinea che gli algoritmi di interpolazione linear triangulation, natural neighbor, thin-plate spline plus tension e completely regularized spline potrebbero rappresentare la scelta migliore per applicazioni che si basano sulla corretta rappresentazione della morfologia superficiale (ad esempio, modellistica idraulica ed idrologica). Infatti, questi algoritmi hanno dimostrato di garantire il miglior compromesso tra accuratezza verticale ed affidabilità delle forme. Tuttavia, la ricerca mostra anche che la scelta della metodologia di interpolazione in realtà non rappresenta un fattore determinante ai fini dei risultati della modellistica di propagazione di colate detritiche. Dall'altro lato, l'analisi condotta sulle potenzialità delle due tecniche di rilievo testate nel rappresentare la topografia del canale da colata detritica studiato, evidenzia un elevato grado di interoperabilità poiché entrambe potrebbero essere utilizzate per generare non distorti ed accurati Modelli Digitali del Terreno densi di aree morfologicamente complesse. Tuttavia, il confronto diretto dei Modelli Digitali del Terreno generati rivela che, nonostante le due tecniche di rilievo forniscano una caratterizzazione della batimetria del canale comparabile (ossia, non statististicamente differente), discrepanze altimetriche significative potrebbero essere riscontrate in corrispondenza di aree del canale morfologicamente complesse (ad esempio, sponde e punti di discontinuità topografica). Inoltre, le discrepanze riscontrate si sono dimostrate in grado di influenzare il comportamento del modello di propagazione a celle, portando così alla conclusione che la scelta della tecnica di rilievo potrebbe rappresentare un fattore critico per l'affidabilità dei risultati dei modelli da colata detritica.

Contents

1 Introduction 1

2 Evaluating the differences of gridding techniques for Digital Elevation Models generation and their influence on the modeling of stony debris flows routing: A case study from Rovina di Cancia basin (North-eastern Italian Alps) 3

Summary 3

2.1 Introduction 4

2.2 Material and Methods 5

2.2.1 Background on the tested interpolation algorithms 5

2.2.2 Study area and data acquisition 7

2.2.2.1 Study site 7

2.2.2.2 Data acquisition 8

2.2.2.2.1 Full-waveform aerial laser scanner survey 8

2.2.2.2.2 Real-time kinematic GPS survey 8

2.2.3 GIS-based routing cell model 9

2.2.4 LiDAR data pre-processing and vertical accuracy analysis 11

2.2.5 DEMs generation and interpolation algorithms comparison 12

2.2.5.1 DEMs interpolation 12

2.2.5.2 Comparison of interpolation methods 13

2.2.6 Evaluation of the effects of gridding techniques on debris flow routing model results 14

2.3 Results & Discussion 15

2.3.1 LiDAR data vertical accuracy assessment 15

2.3.2 Exploratory Spatial Data Analysis results 17

2.3.3 Comparison of interpolation methods 18

2.3.4 Effects of gridding techniques on debris flow routing modeling 25

2.4 Conclusions 30

Supplementary material 31

3 Investigating the performance of ground- and airborne-based survey techniques in a morphologically complex area, and the related influence on stony debris flows routing modeling 39

Summary 39

3.1 Introduction 40

3.2 Materials and Methods 41

3.2.1 Field site 41

3.2.2 Aerial-based elevation data 42

3.2.3 Ground-based elevation data 43

3.2.4 Data interpolation 44

3.2.5 DEMs vertical accuracy analysis 44
3.2.6 DEMs vertical uncertainty investigation 45
3.2.7 Survey techniques comparison 46
3.2.8 Evaluation of the survey techniques effects on debris flows routing modeling 47
3.3 Results and discussion 48
3.3.1 DEMs vertical accuracy analysis 48
3.3.2 DEMs vertical uncertainty investigation 50
3.3.3 Survey techniques comparison 52
3.3.4 Evaluation of the survey techniques effects on debris flows routing modeling 53
3.4 Conclusions 56
Supplementary material 57
4 GIS-based cell model for simulating debris flow runout on a fan 61
Summary 61
4.1 Introduction 62
4.2 The model 64
4.2.1 Overview 64
4.2.2 Continuity equation 65
4.2.3 Hydraulic links between cells: discharge exchange relationships 65
4.2.4 Erosion and deposition 66
4.3 Numerical scheme, initial and boundary conditions 67
4.4 Rio Lazer basin and debris flow that occurred on November 4th, 1966 69
4.5 Simulation of debris flow that occurred on November 4th, 1966 70
4.5.1 Simulation of debris flow triggering and solid–liquid hydrograph 70
4.5.2 Simulation of debris flow spreading along the fan using the cell model 73
4.6 Sensitivity analysis of parameters and discussion 75
4.7 Conclusions 78
5 The Debris Flow Occurred at Ru Secco Creek, Venetian Dolomites, on 4 August 2015: Analysis of the Phenomenon, Its Characteristics and Reproduction by Models 81
Summary 81
5.1 Introduction 82
5.2 Materials and Methods 83
5.2.1 The Study Site and the Rock Fall Occurred on 14 November 2014 83
5.2.2 Topographical Data 85
5.2.3 The Precipitation 87
5.2.4 The Models 87
5.2.4.1 Hydrological Modeling 87

5.2.4.2 The GIS-Based Cell Model 88
5.3 The debris flow event: Geomorphological Analysis 90
5.4 The phenomenon reproduction by models 92
5.4.1 Hydrological Simulations 93
5.4.2 The solid-liquid hydrographs 95
5.4.3 Routing Simulations 95
5.5 Discussion of results 97
5.6 Conclusions 101
Supplementary material 102
6 Conclusion 107
Bibliography 109

List of Figures

Figure 2.1: Aerial view of the Rovina di Cancia study site. A) Debris flow triggering area (~1 670 m a.s.l.), B) Natural rock step located at the end of the debris flow triggering area (~1 500 m a.s.l.), C) Man-built flat deposition area (~1 340 m a.s.l.), D) Final flat circular deposition basin (~1 000 m a.s.l.). Dotted white line: LiDAR data coverage and hydraulic model domain; dotted black line: RTK-GPS data coverage. 7

Figure 2.2: A) Histogram of the errors. Superimposed, the normal distribution with mean and standard deviation estimated from all data. B) Normal Q-Q plot of the errors. C) Histogram of the errors without outliers. Superimposed, the normal distribution with mean and standard deviation estimated from the thresholded errors dataset. D) Normal Q-Q plot of the errors without outliers. ΔZ denote the vertical error. 16

Figure 2.3: Histogram with superimposed the normal distribution (A), normal Q-Q plot (B), and box-plot (C) of the LiDAR ground point dataset. 17

Figure 2.4: Quantiles map of the variable elevation (the red arrow indicates the trend direction, which corresponds to the channel gradient) (A), scatterplot elevation values versus east coordinate (rho Pearson = 0.48; rho Spearman = 0.47) (B), and scatterplot elevation values versus north coordinate (rho Pearson = 0.82; rho Spearman = 0.84) (C)..... 18

Figure 2.5: Choropleth symbol map of the thin-plate spline function absolute errors at the spatial resolution of 1.00 m. Note that the greatest absolute errors mainly occur at the top of the banks and in the rough upper part of the channel. Within the channel the spatial pattern of errors appears to be "random". 22

Figure 2.6: Local Moran's I index map of the thin-plate spline function absolute errors at the spatial resolution of 1.00 m. Note the local clusters of high and low errors values, mainly located along the upper part of the channel where the topographic roughness is higher due to the presence of boulders and bank failures. Moreover, local outliers concentrate near the rock step at an altitude of about 1 500 m a.s.l.. 22

Figure 2.7: NMAD values variation as a function of the sample density (A, spatial resolution equal to 1.00 m, and B, spatial resolution equal to 0.50 m). Median values variation as a function of the sample density (C, spatial resolution equal to 1.00 m, and D, spatial resolution equal to 0.50 m). 24

Figure 2.8: Overview of the interpolation artefacts: A) spiky features in the upper part of the debris flow channel due to function under- and over-shooting at slope discontinuities, B) noisy relief with discontinuos spatial pattern of slopes, C) striping effect oriented according to the direction of variogram modeling, D) undulating surface, E) over-smoothed surface (red: ANUDEM contour lines, black: natural neighbour contour lines), F) striping effect oriented according to the sample direction. 25

Figure 2.9: Scatterplot of the pixel-wise standard deviations of the twelve 1-meter resolution DEMs heights and the pixel-wise standard deviation of the corresponding twelve simulated erosion/deposition depths: (A) full dataset-derived DEMs and 300-year return period (rho Pearson = 0.126, rho Spearman = 0.205), (B) full dataset-derived DEMs and 50-year return period (rho Pearson = 0.129, rho Spearman = 0.208), (C) 50% thinning-derived DEMs and 300-year return period (rho Pearson = 0.167, rho Spearman = 0.252), and (D) 50% thinning-derived DEMs and 50-year return period (rho Pearson = 0.172, rho Spearman = 0.256). The continuous red line corresponds to the linear regression line, whereas the dotted blue lines correspond to the marginal mean of the two correlated variables. 26

Figure 2.10: 5x5 moving windows Pearson's correlation coefficient between the pixel-wise standard deviations of the twelve 50% thinning-derived 1-meter resolution DEMs heights and the pixel-wise standard deviation of the corresponding twelve 50-year return period simulated erosion/deposition depths. 26

Figure 2.11: Comparison of simulated debris flow solid-liquid hydrographs. 27

Figure 2.12: Comparison of pre- (continuous lines) and post-event (dotted lines) DEMs cross-section profiles. 28

Figure 3.1: Aerial view of the Rovina di Cancia basin. (A) Debris flow triggering area (~1670 m a.s.l.), (B) natural rock step located at the end of the debris flow triggering area (~1500 m a.s.l.), (C) man-built flat deposition area (~1340 m a.s.l.), (D) final flat circular deposition basin (~1000 m a.s.l.). The dotted white line delineates the study reach. 42

Figure 3.2: Histogram of the LiDAR-derived DEM vertical errors with superimposed the normal distributions having mean and standard deviation values computed though one of the three employed approaches. Note the different degree of fitting at the mean and at the tails of the errors distribution. ΔZ denotes the vertical error. 49

Figure 3.3: Scatterplots of (A) points density, (B) Euclidean distance to the nearest sampled topographic breakline, and (C) LiDAR-derived DEM slope values against the observed LiDAR-derived DEM absolute errors. The dotted blue lines correspond to the marginal mean of the two correlated variables. 50

Figure 3.4: Q-Q plots of observed and modeled elevation uncertainty in the case of GNSS-derived DEM: (A) FIS 1, (B) FIS 2, and (C) FIS 3. The dashed black line depicts the 1:1 relationship, whereas the blue and red continuous lines correspond to a FIS error of ± 0.10 and ± 0.20 m, respectively. 51

Figure 3.5: Q-Q plots of observed and modeled elevation uncertainty in the case of LiDAR-derived DEM: (A) FIS 1, (B) FIS 2, and (C) FIS 3. The dashed black line depicts the 1:1 relationship, whereas the blue and red continuous lines correspond to a FIS error of ± 0.10 and ± 0.20 m, respectively. 51

Figure 3.6: FIS 3-based DEMs elevation uncertainty estimates. (A) Box-plots and corresponding raster grids, in the case of (B) GNSS- and (C) LiDAR-derived DEMs. 52

Figure 3.7: (A) Unthresholded DoD map, and (B) corresponding thresholded one (95% probabilistic confidence interval) calculated by using the propagated FIS-based DEMs elevation uncertainty estimates. 53

Figure 3.8: Elevation discrepancy distribution of the (A) unthresholded and (B) thresholded at a 95% confidence interval DoD maps. Note that the gray bars correspond to the non-significant elevation discrepancies. 53

Figure 3.9: Comparison of the simulated 300-years return period debris flow solid-liquid discharges (continuous lines) and corresponding volumetric sediment concentrations (dotted lines), in the case of GNSS- and LiDAR-derived DEMs (blue and red lines, respectively). Insert: thresholded (95% probabilistic confidence interval) DoD map. 54

Figure 3.10: Comparison of the terrain profiles before (continuous lines) and after the modeled 300-years return period event scenario (dotted lines), in the case of GNSS- and LiDAR-derived DEMs (blue and red lines, respectively). Insert: thresholded (95% probabilistic confidence interval) DoD map. 55

Figure 3.11: Comparison of the terrain profiles before (continuous lines) and after the modeled 300-years return period event scenario (dotted lines), in the case of GNSS- and LiDAR-derived DEMs (blue and red lines, respectively). The inserts correspond to the simulated erosion/deposition depths, in the case of (A) GNSS- and (B) LiDAR-derived DEMs. Dotted black line denotes the rock step. 55

Figure 4.1: The eight possible flow directions (left) and outflow from central cell (right). 64

Figure 4.2: Hydraulic links between two neighboring cells. 66

Figure 4.3: Aerial photo of Rio Lazer flooded area with superimpose d the DEM contours of triggering basin (continuous line) and inundated areas (dotted line). 69

Figure 4.4: Photo taken just after the event occurred the 4th of November 1966. 70

Figure 4.5: Map of deposition area divided in 4 zones corresponding to 4 classes of deposition depths. The houses in green are those that were present when the event occurred, and the red and blue lines correspond to the DEM contour and the Rio Lazer torrent, respectively. 71

Figure 4.6: Land use (left) and CN (right) maps of the triggering basin. (For interpretation of the references to color in this figure legend, the reader is referred to the web version of this article.) 72

Figure 4.7: Hydrographs of runoff (QW) and runoff contributing to debris flow (shaded part, QR). 72

Figure 4.8: Solid–liquid input hydrograph. 73

Figure 4.9: Maps of deposition depths simulated by present model (simulation n. 1, left), observed (middle) and simulated by the automata model (simulation n. 12, top and right) and by the TRENT2D model (simulation n. 20, bottom and right). 74

Figure 4.10: Maps of deposition depths correctly simulated (blue), no-correctly simulated (red), simulated but no observed (gray) and observed but no simulated (green) for the simulations 1 (left), 12 (top and right) and 20 (bottom and right) with that of the observed deposition depths (middle). There also erosion depths simulated but not observed (azure) or corresponding to observed deposition depths (brown) 75

Figure 5.1: Aerial view of whole area with the contributing hydrological basins and the basins of Rovina di Cancia and Rudan. 83

Figure 5.2: Frontal view of the upper basins that contributed to the phenomenon. The blue arrows show the runoff routing, the red arrows the debris flow starting locations and its routing, and the black arrows the path of the debris flow on the right slope, that did not contribute significatively to solid-liquid wave routing along Ru Secco (flight of 5 August 2015). 84

Figure 5.3: Pre-event images: view of the large debris deposits covering the Ru Salvela and Ru Secco creeks during their removal (flight of 1 July 2015) (a) and the culverting of the Ru Secco in correspondence with the ski resort area (b). . 85

Figure 5.4: View of the collapsed cliff on the northwestern side of the Mount Antelao (flight of 1 July 2015) and the deposits of debris material from the base of the collapsed cliff to just upstream the confluence with Ru Secco creek. Top right insert shows the debris material covering the Vallon d'Antermoia rocky surface at the base of the collapsed cliff (flight of 1 July 2015). Bottom right insert shows the Ru Salvela creek covered by debris material till the confluence with Ru Secco creek that was obstructed (picture taken on November 2014). 85

Figure 5.5: Schematic view of the cover of the topographical data. 86

Figure 5.6: Hyetograph of the rainfall depths from the rain gauge and the corrected radar estimates. 87

Figure 5.7: The eight possible flow directions (a) and the two possible flow conditions of the routing model (b); partial redrawing of the Figures 1 and 2 of Gregoretti et al. (2016b). 89

Figure 5.8: View of the area subjected to deposition or erosion and land use. The upper image (a) is the general view of the areas routed by debris flows and subjected to deposition or erosion. The top right insert is the post-event view of the area depicted in Fig. 5.3b while the other three inserts show the downstream view of debris flow route incising the debris material covering the Ru Salvela creek (bottom middle), the observed and simulated cross-section of the channel excavated by debris flow above the culvert (bottom left) and a particular of a bank erosion after the upper culvert (top left). The position of the cross-sections that are shown in the supplemental materials is also indicated. The lower image (b) is the landuse of terrain for the routing simulation. 91

Figure 5.9: Deposition and erosion depths map for the two groups of reaches. Upper image (a) is the map of estimated deposition and erosion for the reaches I-III, while the image below (b) is that simulated. Images (c,d) are the corresponding of (a,b) for the reaches IV-V respectively. The position of the six sections (B, D, E, F, H, and I) is also shown. 93

Figure 5.10: Modeled runoff hydrographs for the five basins corresponding to the measures (a) and corrected radar estimates (b) of rainfall depth. 98

Figure 5.11: Simulated hydrographs of solid-liquid (a) and solid discharge (b), Q and QS respectively, corresponding to the traces of the six sections of Fig. 5.9. 99

Figure 5.12: The deposition and erosion depths (Left) and flow depths (Right) maps at different times [(a) t = 12.3 min, (b) t = 15.0 min, (c) 18.3 min, (d) t = 30.7 min, (e) t = 34.7 min, (f) t = 70.0 min] from the beginning of the simulation of the area close to the culvert and parking. 100

List of Tables

Table 2.1: Computed standard and robust accuracy measures. 15

Table 2.2: Global accuracy measures for each tested interpolation algorithm and chosen spatial resolution (* the values refer to the errors distribution after the outliers removal). 20

Table 2.3: Supplementary DEM quality indices and global Moran'I index values for each tested interpolation algorithm and chosen spatial resolution (* the values refer to the errors distribution after the outliers removal). 21

Table 2.4: 50% thinning-derived 1-meter resolution DEMs model run results (50-year return period). 29

Table 3.1: Parametrizations of the three developed FISs for the GNSS-derived DEM (italics denotes the changes between the developed FISs). 46

Table 3.2: Parametrizations of the three developed FISs for the LiDAR-derived DEM (italics denotes the changes between the developed FISs). 47

Table 3.3: Computed standard and robust DEMs accuracy measures. 49

Table 4.1: Values of CN and slope velocity for each soil type of the triggering basin 73

Table 4.2: Results of simulation 1 for each class of the deposition depth intervals. 76

Table 4.3: Simulation results with present model: percentages of the simulated deposition areas respect to that measured and values of evaluation factors/parameters. In bold the value of the parameter that is varied respect to run 1 77

Table 4.4: Simulation results with the models of Deangeli (2008) and Armanini et al. (2009): percentages of the simulated deposition areas respect to that measured and values of evaluation factors/parameters. 78

Table 5.1: Parameters adopted in the hydrological model. Symbols are defined as follows: CN, Curve Number for computing the excess rainfall; U, runoff velocity; fc infiltration rate.). 94

Table 5.2: Morphometric characteristics of the basins: AB, basin area; AT, threshold area for channel network; zO, basin outlet altitude; zM, mean basin altitude; zMAX , maximum basin altitude; SLMEAN, mean slope; SLMAX, maximum slope; b0, outlet width. 94

Table 5.3: Values of the parameters used in the routing simulations for the different terrains. 98

List of Abbreviations

Chapter 2

ALS	Airborne Laser Scanner
DFRM	Debris Flow Routing Model
DEM(s)	Digital Elevation Model(s)
ESDA	Exploratory Spatial Data Analysis
GIS	Geographical Information System
GPS	Global Positioning System
IDP	Inverse Distance to a Power function
LiDAR	Light Detection and Ranging
MAE	Mean Absolute Error
NMAD	Normalized Median of Absolute Deviations
RBFs	Radial Basis Functions
RMSE	Root Mean Square Error
RTK-GPS	Real Time Kinematic – GPS
TIN(s)	Triangulated Irregular Network(s)

Chapter 3

ALS	Aerial Laser Scanning
DEM(s)	Digital Elevation Model(s)
DoD	DEM of Difference
FIS(s)	Fuzzy Inference System(s)
GCD	Geomorphic Change Detection
GIS	Geographic Information System
(rtk)GNSS	(Real-Time Kinematic) Global Navigation Satellite System
TS	Total Station
InSAR	Interferometric Synthetic Aperture Radar
LiDAR	Light Detection and Ranging
minLoD	minimum Level of Detection
NMAD	Normalized Median of Absolute Deviations
RMSE	Root Mean Square Error
TIN(s)	Triangulated Irregular Network(s)
TLS	Terrestrial Laser Scanning

Chapter 4

A	cell area
AC	part of AD with correctly simulated deposition depths
A	wave celerity
A	cell area
AC	part of AD with correctly simulated deposition depths
ACC	part of class observed area with correctly simulated deposition depths
AD	area with observed deposition depths
pADD	class measured area
AS∩D	overlapping area between AD and AS
AS∩T	area with simulated deposition depths
b	dynamic constant
c	sediment volumetric concentration of the mixture
cD	limit inferior sediment volumetric concentration for deposition
c*	solid volumetric concentration of dry bed
C	conductance coefficient
CN	curve number
d	sediment deposition/erosion depth
dg	grain size of mixture
dM	mean sediment diameter of bed in the triggering area
F	fitting parameter
g	acceleration due to gravity
h	flow depth in a cell
hERR	minimum flow depth for erosion
hROUT	minimum flow depth for routing
ib	rate of change of bed elevation
K	Egashira empirical coefficient
Qi,k	flow exchanged by the cell i, with the neighboring k
Q	solid–liquid discharge
QR	runoff discharge contributing to solid–liquid input Hydrograph ***DEM***
QW	runoff discharge
U	mean velocity along a possible flow direction
ULIM	limit superior velocity for deposition (ULIM-D) or erosion (ULIM-E)
VCX	volume corresponding to the correctly simulated deposition depth in area X
VDE	deposited or entrained volume
VR	runoff volume contributing to the solid–liquid input
VD	measured sediment deposited volume
VDE	deposited or entrained volume
VR	runoff volume contributing to the solid–liquid input hydrograph
VROUT	solid–liquid routing volume
VS	solid routing volume
VX	simulated sediment deposited volume in area X
X	overlay of observed and simulated deposition areas
Y	deposition area simulated but no observed
Yd	relative submergence
Z	deposition area observed but no simulated
α	angle controlling deposition and entrainment
Δt	time step
Δx	grid size
θ	angle respect to the horizontal of the line joining the centers of two neighboring cells of DEM
θLIM	limit superior angle for deposition (θLIM-D) or erosion (θLIM-E)
Θ	angle respect to the horizontal of the line joining the centers of flow surface of two neighboring cells
Ω, ΩM	evaluation factors
φ	static friction angle
φD	dynamic friction angle
ρ	water density
ρS	sediment density
AMC	Antecedent Moisture Content
CFL	Courant–Friedrichs–Levi
CN	Curve Number
Digital Elevation Model	
FLO-2D	well-known commercial model for debris routing;
GIS	Geographical Information System
LiDAR	Light Detection and Ranging
SCS	Soil Conservation Service
SPH	Smooth Particle Hydrodynamics
TRENT2D	Transport in Rapidly Evolutive Natural Torrent

Chapter 5

A	cell area
AT	threshold area for channel network
AB	basin area
b0	outlet width
b1	morphological exponent
S	potential maximum retention
SLMEAN	mean slope
SLMAX	maximum slope
tIa	time at which Ia occurs
U	mean velocity along a possible flow direction

c	sediment volumetric concentration of the mixture
cD	limit inferior sediment volumetric concentration for deposition
c*	solid volumetric concentration of dry bed
cF	solid volumetric concentration of the debris flow front
CN	curve number
d	sediment diameter
D	deposition rate
E	erosion rate
fc	infiltration rate
g	acceleration due to gravity
h	flow depth in a cell
I	Rainfall intensity
Ia	Initial abstraction
K	Egashira empirical coefficient
P	Cumulative rainfallk
Pe	Excess rainfall
PeSCS	excess rainfall computed through the SCS-CN
Q0	runoff peak discharge
Q	solid–liquid discharge
Qp	Peak solid-liquid discharge
QS	solid discharge
VLIM	limit superior velocity for deposition (VLIM-D) or erosion (VLIM-E)
VMAX	Maximum velocity
z	Bed level
zO	Basin outlet altitude
zM	Basin mean altitude
zMAX	Basin maximum altitude
α	Angle controlling deposition and entrainment
Δt	time step
Δx	grid size
θ	angle respect to the horizontal of the line joining the centers of two neighboring cells of DEM
θLIM	limit superior angle for deposition (θLIM-D) or erosion (θLIM-E)
Θ	angle respect to the horizontal of the line joining the centers of flow surface of two neighboring cells of DEM
MC	Antecedent Moisture Content
CFL	Courant–Friedrichs–Levi
DEM	Digital Elevation Model
GIS	Geographical Information System
LiDAR	Light Detection and Ranging
SCS	Soil Conservation Service

1 Introduction

Recalling the definition proposed by Costa (1984), debris flows can be described as gravity-induced rapid mass movements intermediate between landslides and floods, with mechanical characteristics different from either of these processes, and with inherent properties that vary according to the water and clay content, sediment size and sorting.

Among the geomorphic processes occurring in steep mountain basins, debris flows can be regarded as one of the most hazardous phenomena due to their magnitude, routing velocity, and high occurrence rate in a wide spectrum of morphological settings (Hürlimann et al., 2006; Blasone et al., 2014). In particular, in the Dolomites area (North-eastern Italian Alps) debris flows mainly initiate by mobilization of the channel-bed material due to surface runoff (Berti et al., 1999, Berti & Simoni, 2005; Gregoretti & Dalla Fontana, 2008; Theule et al., 2012; Tiranti & Deangeli 2015). Furthermore, in the last few years the phenomena showed in this area an increase in the occurrence rate possibly by the rise of extreme rainfall events (Easterling et al., 2000; Floris et al., 2010), and the larger availability of debris material yielded by the retreat of the glaciers and the permafrost areas to higher elevations (Degetto et al., 2015).

In order to cope with debris flow hazard, a common practice is the mapping of the areas historically or potentially threatened (Ghilardi et al., 2001), by adopting an empirical- (e.g., Scheidl and Rickenmann, 2010; Berti and Simoni, 2014) or a model-based (e.g., Rickenmann et al., 2006; Armanini et al., 2009; Gregoretti et al., 2016) approach. In the latter case, since the topography is the major control over fluxes of water and sediments (Moore et al., 1991; Hancock, 2006; Saksena & Merwade, 2015), the proper representation of the channel and fan morphology through DEMs[1] is a precondition for the reliability of routing modeling outcomes.

DEMs are always generated starting from a given topographic dataset (e.g., points and lines) by means of deterministic or stochastic interpolation algorithms, in a basic step often referred to as gridding (Hengl & Reuter, 2009). The topographic data acquisition method is usually driven by the specific application and its requirements in terms of accuracy and sampled data density (Höhle and Potuckova, 2011). In the past, the analytical aerial photogrammetry along with the classic ground-based surveys were the main measurement techniques for gathering topographic information on areas featuring different extension. In the last two decades, the sensor modernization has promoted the development of new and highly automated remote-sensing techniques, such as the Airborne and Terrestrial Laser Scanning (ALS or LiDAR, and TLS, respectively), the long- and close-range digital photogrammetry, and the Interferometric Synthetic Aperture Radar (InSAR; e.g., Lillesand et al., 2004; Höhle & Potuckova, 2011; Milan et al., 2011; Molina et al., 2014; Adams et al., 2016; Hsieh et al., 2016). All these new techniques provide high-resolution topographic data (i.e., meter and sub-meter data resolution), that are acquired within a short time and with a high accuracy level. Nevertheless, classic ground-based surveys by means of GNSS or Total Station (TS) have not been completely set aside, since they ensure a proper trade-off between accuracy and cost for those scenarios involving small areas without the need for a massive topographic data acquisition (Casas et al., 2006; Gomarasca, 2009).

Considered the wide range of ground-, airborne-, and satellite-based survey techniques currently available and their inherent limitations that result in trade-offs between cost, accuracy, resolution, spatial coverage, and sampling frequency, the choice of the proper survey method for a given application is not a trivial issue. For this reason, recent research efforts have been undertaken in order to investigate the main benefits and limitations of the available measurement techniques under different conditions and environments (e.g., Gallay et al., 2013; Molina et al., 2014; Bangen et al., 2014; Tarolli, 2014; Passalacqua et al., 2015). However, to date little work has been done in order to evaluate the performance of ground- and airborne-based survey techniques in morphologically complex areas, such as those where debris flows occur. Furthermore, notwithstanding a number of authors proved the potential impact of the topographic data source on floods modeling outcomes (e.g., Wilson and Atkinson, 2005; Casas et al., 2006; Cook and Merwade, 2009; Alho et al., 2009; Ali et al., 2015; Bakula et al., 2016; Reil et al., 2017; Bhuyian and Kalyanapu, 2018),

[1] The terms Digital Elevation Model(s), Digital Terrain Model(s), and Digital Surface Model(s) are often used when dealing with the digital representation of the earth surface and of the object on it. Although their definitions can vary in the literature, for the purpose of the present research the terms Digital Elevation Model(s) and Digital Terrain Model(s) are referred to a mathematical representation of the bare earth in digital form, and are considered synonyms.

no attempt to evaluate the influence of different survey techniques on the debris flow routing models behaviour has been yet carried out.

It is also worth noting that despite the recent developments in the field of remote-sensing allow to reach high sampling density (e.g., up to one point per square centimetre in non-vegetated areas for TLS- and dense image matching-derived points clouds, Heritage & Large, 2009; Fonstad et al., 2013), artefacts (e.g., cut-offs, over-smoothing, and over-shooting) and uncertainties in DEMs may be formed during the gridding step, whichever interpolation technique is used (Carrara et al., 1997; Smith et al., 2005; Heritage et al., 2009; Milan et al., 2011). However, the magnitude and the spatial pattern of these uncertainties can greatly vary with different interpolation methods, since each technique considerably differs both in its sensitivity to the spatial distribution of the sampled data and their associated errors (Hengl & Reuter, 2009; Garnero & Godone, 2011), and in its ability to fit the real morphology (Smith et al., 2005). Consequently, the choice of the gridding methodology and of its related parameters are very significant decisions in determining the realistic digital representation of the surface morphology, especially in uneven terrain (e.g., Desmet, 1997; Blöschl & Grayson, 2000; Chaplot et al., 2006; Weng, 2006; Heritage et al., 2009, McDonnell & Lloyd, 2015).

Although a number of previous researches have analyzed the performance of many interpolation algorithms using different datasets related to several physical variables (e.g. hydrological, pedological, and topographical) and environments, the existing literature tends to be somewhat contradictory about the most reliable one. Furthermore, despite the general awareness on the potential impact of DEMs interpolation uncertainties on the numerical modeling, little work has been done to understand how these uncertainties affect debris flow routing models results.

In order to fill the outlined literature gaps, the open science questions addressed by the research are: (1) how do the gridding and survey techniques commonly used for DEMs generation perform in morphologically complex areas? and (2) what is their inherent impact on stony debris flows routing modeling outcomes?. Therefore, the main objective of the research is to improve the knowledge concerning the influence of geomatic techniques[2] on the numerical modeling of stony debris flows routing, by focusing on the Rovina di Cancia basin (western slope of Mount Antelao, Venetian Dolomites). In order to achieve this goal, we first analyze the performance of several digital terrain modeling algorithms (i.e., linear triangulation, natural neighbor, nearest neighbor, inverse distance to a power, ANUDEM, completely regularize spline function, thin-plate spline function, thin-plate spline plus tension function, multi-quadratic function, inverse multi-quadratic function, point ordinary kriging, and block ordinary kriging) in representing the complex topography of the study site, and then we assess their inherent influence on the results of a GIS-based cell routing model previously calibrated and validated against two real debris flow events (Chapter 2). After that, in Chapter 3 we investigate and compare the performance of a ground-based (i.e., GNSS) and an airborne-based (i.e., full-waveform LiDAR) survey technique in characterizing the topography of the selected debris flow channel. Furthermore, we assess the influence of the different topographic characterization of the channel morphology on debris flow routing modeling results, by considering both high- and low-magnitude flow conditions. The employed GIS-based cell routing model is introduced in Chapter 4, whereas its latest refinements along with the back- and sensitivity-analysis of the debris flow event occurred on the Ru Secco creek (Northern slope of Mount Antelao, Venetian Dolomites) the 4th of August 2015 are presented in Chapter 5. An overall conclusion summarizing the main findings of the research and its related biases completes the thesis (Chapter 6).

[2] According to the Oxford dictionary definitions, geomatic can be defined as “the mathematics of the earth: the science of the collection, interpretation, and processing of data, especially instrumental data related to the earth surface”.

2 Evaluating the differences of gridding techniques for Digital Elevation Models generation and their influence on the modeling of stony debris flows routing: A case study from Rovina di Cancia basin (North-eastern Italian Alps)

This chapter represents an edited version of ***Boreggio M.[3], Bernard M., Gregoretti C. (2018). Evaluating the Differences of Gridding Techniques for Digital Elevation Models Generation and Their Influence on the Modeling of Stony Debris Flows Routing: A Case Study From Rovina di Cancia Basin (North-Eastern Italian Alps).*** *Front. Earth Sci. 6:89. doi: 10.3389/feart.2018.00089.*

Summary

Debris flows are among the most hazardous phenomena in mountain areas. To cope with debris flow hazard, it is common to delineate the risk-prone areas through routing models. The most important input to debris flow routing models are the topographic data, in the form of Digital Elevation Models (DEMs). The quality of the DEMs depends on the accuracy, density, and spatial distribution of the sampled points; on the characteristics of the surface; and on the gridding method used to obtain them. Therefore, the choice of the DEMs interpolation method affects the realistic representation of the channel and fan morphology, and thus reasonably the debris flow routing modeling outcomes. In this paper, we initially investigate the performance of common interpolation methods (i.e. linear triangulation, natural neighbour, nearest neighbour, inverse distance to a power, ANUDEM, Radial Basis Functions, and ordinary kriging) in building DEMs with the complex topography of a debris flow channel located in the Venetian Dolomites (North-eastern Italian Alps), by using small footprint full-waveform Light Detection And Ranging (LiDAR) data. The investigation is carried out through a combination among statistical analysis of vertical accuracy, algorithm robustness, and spatial clustering of vertical errors, and multi-criteria shape reliability assessment. After that, we examine the influence of the tested interpolation algorithms on the performance of a Geographic Information System (GIS)-based cell model for simulating stony debris flows. In detail we investigate both the correlation between the DEMs heights uncertainty resulting from the gridding procedure and that on the corresponding simulated erosion/deposition depths, both the effect of interpolation algorithms on simulated areas, erosion and deposition volumes, solid-liquid discharges, and channel morphology after the event. The comparison among the tested interpolation methods highlights that the ANUDEM and ordinary kriging algorithms are inadequate in building DEMs with complex topography. Conversely, the linear triangulation, the natural neighbour algorithm, and the thin-plate spline plus tension and completely regularized spline functions ensure the best trade-off among accuracy and shape reliability. Anyway, the evaluation of the effects of gridding techniques on debris flow routing modeling reveals that the choice of the interpolation algorithm does not significantly affect the model outcomes.

[3] The author carried out the analysis on topographic data, the interpolation of DEMs, the comparison among the different gridding routines, the numerical simulations, and the analysis on the obtained results.

2.1 Introduction

Taking up the definition proposed by Iverson (2005), "debris flows can be defined as turbulent flowing mixtures of sediment and liquid in nearly equal proportions". Debris flows are found in a wide variety of mountainous environments worldwide (Berti et al., 1999), and in particular, in the Dolomites area (North-eastern Italian Alps) they mainly initiate by mobilization of the channel-bed material due to surface runoff (Berti et al., 1999, Berti & Simoni, 2005; Gregoretti & Dalla Fontana, 2008; Theule et al., 2012; Tiranti & Deangeli 2015). Debris flows seem to have increased in occurrence in the last few years, possibly by the rise of extreme rainfall events (Easterling et al., 2000; Floris et al., 2010), and the availability of debris material provided by retreat of the glaciers and the permafrost areas to higher elevations (Degetto et al., 2015) owing to the global climatic change. To reduce debris flow hazard, it is common to couple structural and non-structural measurements, such as the zoning of risk prone areas and the development of emergency plans (Ghilardi et al., 2001).

Hazard mapping consists in identifying the areas that are threatened either historically or potentially by debris flows. The methods used to simulate potential hazard scenarios are both empirical-based (e.g. Scheidl & Rickenmann, 2010; Berti & Simoni, 2014) and model-based (e.g. Rickenmann et al., 2006; Medina et al., 2008; Deangeli, 2008; Armanini et al., 2009; Hussin et al., 2012; Gregoretti et al., 2018). Since topography is the major control over fluxes of water and sediments (Moore et al., 1991; Hancock, 2006; Saksena & Merwade, 2015), topographic data in the form of Digital Elevation Models (DEMs) represent the most important input in debris flows routing models (e.g. Rickenmann et al., 2006; Sodnik et al., 2012).

A DEM can be defined as a mathematical representation of the bare earth in digital form (Erdogan, 2009; Vosselman & Maas, 2010), and it is commonly used to represent the surface morphology in three dimensions (Heritage et al., 2009). Two very well-known formats for the storage of DEMs data are the raster and the grid structure, also known as pixel- and lattice-model respectively (e.g. Wilson & Gallant, 2000; Wise, 2000; Wise, 2007; Smith et al., 2005; Pfeifer, 2005; Hengl & Reuter, 2009; Cilloccu et al., 2009; Vosselman & Maas, 2010; Höhle & Potuckova, 2011). Within the raster structure, each value represents the orthometric height of the whole area covered by the raster element (i.e. the square cell). Conversely, a grid structure represents the orthometric height information onto a regular two-dimensional array of points, which by convection are taken to lie in the centre of square pixels, and it is clearly the appropriate data format for DEMs because the elevation estimates relate to points and not to areas.

The grid heights are typically determined starting from sampled topographic data by means of deterministic or stochastic interpolation algorithms, in a basic step often referred to as gridding (Hengl & Reuter, 2009). Despite recent developments in the field of remote sensing allow to reach high sampling density (up to one point per square centimetre in non-vegetated areas for terrestrial laser scanner- and structure from motion-derived points clouds, Heritage & Large, 2009; Fonstad et al., 2013), artefacts (e.g. cut-offs, over-smoothing, and over-shooting) and uncertainties in DEMs may be formed during the gridding step whichever interpolation technique is used (Carrara et al., 1997; Smith et al., 2005; Heritage et al., 2009; Milan et al., 2011). However, the magnitude and spatial pattern of these uncertainties can greatly vary with different interpolation methods, since each technique considerably differs both in its sensitivity to the spatial distribution of the sampled data and their associated errors (Hengl & Reuter, 2009; Garnero & Godone, 2011), and in its ability to fit the real morphology (Smith et al., 2005). Consequently, the choice of the gridding methodology and its related parameters are very significant decisions in determining the realistic digital representation of the surface morphology (especially in uneven terrain, like the areas where debris flows occur), and thus for the reliability of routing modeling outcomes (Desmet, 1997; Blöschl & Grayson, 2000; Chaplot et al., 2006; Weng, 2006; Heritage et al., 2009, McDonnell & Lloyd, 2015).

Although many studies have compared the performance of many interpolation algorithms using different datasets related to several physical variables (e.g. hydrological, pedological, and topographical) and environments, the existing literature tends to be somewhat contradictory about the most reliable one. Furthermore, despite the general awareness about the potential impact of DEMs interpolation uncertainties on the numerical modeling, little work has been done to understand how these uncertainties affect the debris flow routing models results. In order to fill this gap, in this study we first compare the performance of several commonly used digital terrain modelling algorithms in representing the complex topography of a debris flow channel located in the Venetian Dolomites, by using small footprint full-waveform LiDAR data. As one of the major remote sensing techniques which developed exponentially during the last decade in landslides

investigation and hydraulic modeling is the LiDAR technology (e.g. French, 2003; Cavalli & Marchi, 2008; Scheidl et al., 2008; Sodnik et al., 2012; Jaboyedoff et al., 2012; Bossi et al., 2014; Tarolli, 2014), we assumed that nowadays this kind of data represents the most frequently used topographic information to create accurate high-resolution DEMs of mountain catchments. In detail, the investigation is performed through a combination among statistical analysis of vertical accuracy, algorithm robustness, and spatial clustering of vertical errors, and multi-criteria shape reliability assessment. Finally, we assess the influence of the tested interpolation algorithms on the results of a GIS-based debris flow cell routing model by investigating both the correlation between the DEMs heights uncertainty resulting from the interpolation procedure and that on the corresponding simulated erosion/deposition depths, both their effect on simulated areas, erosion and deposition volumes, solid-liquid discharges, and channel morphology after the event.

Therefore, this research may be useful to digital elevation data users involved in hazard modeling and prediction in morphologically complex areas, who are increasingly looking for a global, freely available, high-accuracy digital representation of the earth surface. It represents an up to date question, as demonstrated by the recent launch of the research topic in Frontiers in Earth Science "A global high-resolution digital elevation model: a paradigm shift in high impact research and applications".

The paper is organized as it follows. After the description of the main works of previous authors on the topic of discrete spatial data interpolation shown in the supplementary material, the section Materials and Methods is outlined in six subsections. Here, after a short review of the theory underpinning the examined interpolation algorithms (Subsection 2.2.1), the selected study site and the used topographic dataset are described (Subsection 2.2.2), along with the employed debris flow routing model (Subsection 2.2.3). After that, the methodologies followed during the pre-processing of the topographic data, the study of the interpolation algorithms, and the evaluation of their influence on the routing modeling outcomes are explained in Subsections 2.2.4, 2.2.5, and 2.2.6, respectively. The sections Results and Discussion and Conclusions complete the paper.

2.2 Material and Methods

2.2.1 Background on the tested interpolation algorithms

Several interpolation and approximation methods were developed to predict the values of spatial phenomena in unsampled locations. In this study, twelve different algorithms commonly used for digital terrain modeling were applied using the software package ArcGIS™ (rel. 10.3): (i) linear triangulation, (ii) natural neighbour, (iii) nearest neighbour, (iv) inverse distance to a power, (v) ANUDEM, Radial Basis Functions, among which (vi) completely regularized spline function, (vii) thin-plate spline function, (viii) thin-plate spline plus tension function, (ix) multi-quadratic function, (x) inverse multi-quadratic function, (xi) point ordinary kriging, and (xii) block ordinary kriging. All the selected interpolators are already widely described in literature, so in the following we briefly summarize their main features in a narrative way. For in-depth theoretical and mathematical reviews of the techniques often used for gridding elevation data in connection with GIS, the readers are referred to the works of Mitas & Mitasova (1999), Blöschl & Grayson (2000), Johnston et al. (2001), El-Sheimi et al. (2005), Hengl & Reuter (2009), and McDonnell & Lloyd (2015).

Of the tested interpolation algorithms, the linear triangulation, the natural neighbour, and the nearest neighbour methods employ triangulated irregular networks (TINs), which consist in a sheet of continuous and connected triangular facets (defined according to the Delaunay's criterion) with vertices at the sampled points. On the other hand, the inverse distance to a power, the ANUDEM, the Radial Basis Functions, and the kriging algorithms directly apply on the set of scattered points values.

The linear triangulation is the simplest method for fitting a surface exploiting the Delaunay tessellation of the three-dimensional space. It represents a special case of piecewise polynomials interpolation, where each triangle containing a grid cell centre is regarded as a local area, and a first-order planar surface is fitted on each of them. Once the bivariate local linear function (i.e. the first-order planar surface) is defined in this way, the value of the grid cell centre can be estimated. It works effectively with a moderate amount of evenly distributed data points, and it allows an easy incorporation of topographic discontinuities and structural features. However, the interpolated values always lie within

the range of the sampled values, and the resulting DEM may not be smooth due to the discontinuities created at the edges of each triangle.

The natural neighbour function uses a weighted average of the grid cell centre nearest neighbour values, with weights dependent on proportions of the overlapping between the grid cell centre Thiessen polygon and the Thiessen polygons of its surrounding sampled points. The resulting surface resembles a rubber-sheet passing through the input points, and it does not contain any peaks, pits, ridges or valleys that are not represented by the sampled data. It works equally well with regularly and irregularly distributed sampled data, anyhow the interpolated values always lie within the range of the sampled values.

The nearest neighbour method assigns to the grid cell centre the value of the sampled data point that is closest in space, often resulting in a polygon shaped surface. Since it often provides unrealistic results, the nearest neighbour algorithm is rarely used with topographic datasets. However, it could be useful to interpolate spatial fields with low (or nearly absent) spatial dependence since sample data are considered reference values only for the surrounding area and no gradation across area boundaries is assumed.

The inverse distance to a power function (IDP) is one of the most widely used methods for digital surface modeling. It relies on a distance-weighted average of the data points occurring within a neighbourhood surrounding the grid cell centre, with weights inversely proportional to a power of the Euclidean distance between the interpolated and the sampled data point. The greater the power exponent, the smaller effect the points far from the grid node have during the interpolation procedure. It usually results in an interpolated pattern that is smooth everywhere except at the sampled points, where local extrema are produced (bull's-eyes effect). The technique is particularly suitable for narrow datasets, where other fitting algorithms may be affected by errors. However, it does not work effectively with unevenly distributed data points, or in the presence of clustering and outliers. Furthermore, the interpolated values always lie within the range of the sampled values.

The ANUDEM algorithm is the only tested method based on a morphological approach specifically intended for digital terrain modeling. The approach couples the minimization of the sum of a specified terrain smoothness functional and a weighted sum of squares of the residuals from the elevation data, with an automatic drainage enforcement algorithm, which ensures a connected drainage structure and a sensible representation of ridges and streams in the fitted surface. It uses a multi-resolution, iterative, finite difference computational structure based on a regular two-dimensional grid. For scattered points dataset it is essentially a bivariate, discretised, smoothing thin-plate spline plus tension function, in which the smoothness functional has been empirically determined to allow the interpolated DEM to follow abrupt changes in the land surface (such as streams and ridges). Moreover, it is a hybrid technique that allows to incorporate soft information (such as layers representing pits, streams, lake boundaries, ridges, cliffs, and coastline) assisting the interpolation procedure, and it can predict values which are outside the range of the input data.

The Radial Basis Functions (RBFs) are a class of spline functions for interpolation (and approximation) frequently used for digital terrain modeling. They are based on the assumptions that the fitted surface should pass through (or close to) the data points and, at the same time, should be as smooth as possible. These conditions can be formulated within the variational principles, as the minimization of the sum of the deviations from the measured points and the smoothness seminorm of the spline function. The solution of this minimising condition can be expressed as sum of two components: a trend function described by means of a low order polynomial, and a linear combination of basis functions which depend only to the Euclidean distance between the interpolated and the sampled data point. There are several different basis functions (e.g. thin-plate spline, thin-plate spline plus tension, completely regularized spline, multi-quadratic spline, and the inverse multi-quadratic spline) depending on the choice of the smoothness seminorm, and each of these yields a different gridded surface with its own properties. Overall, the RBFs produce good results for gently varying landscapes, whereas they are inappropriate for irregular topographies where large changes in elevation within short horizontal distances can lead the functions to under- and over-shoot, even generating values outside the range of the sample data.

Kriging is a generic term used to denote a number of closely related stochastic least-squares algorithms based on the regionalized variables theory, asserting that the fitted surface is one of the infinite possible realisations of a random process. It uses distance-weighted averages on punctual or block support, with weights depending on the spatial correlation of the random variable usually modelled by a function known as variogram. Kriging can be defined as the best linear unbiased estimator of a spatial variable as it provides estimates that are unbiased and with minimum variance.

Linearity implies that the estimated value at any unknown point is a linear combination of its surrounding measurements, whose weights are calculated by solving a system of linear equations, which contains the semi-variances defined from a fitted variogram function. The kriging algorithm models the variation of any spatial variable as the sum of three major components: a structural component or trend, a random but spatially correlated component, and a spatially uncorrelated Gaussian noise term. Depending on the assumptions underpinning the model, it is possible to recognize three principal kriging algorithms: the simple kriging which assumes a constant and known mean over the area of interest, the ordinary kriging which assumes a constant but unknown mean over the area of interest, and the universal kriging which assumes that an unknown mean changes smoothly over the area of interest. Ordinary kriging algorithm is the most popular one, and it serves well in many situations since its assumptions are easily satisfied. It is also robust regarding to both moderate departures from these assumptions, and a non-optimal choice of the theoretical variogram model. Overall, kriging is not really appropriate for interpolating elevation data mainly because: it causes a loss of sample variance under-estimating large sampled values and over-estimating small ones, it ignores the hydrological connectivity of the terrain, and it is extremely sensitive to hot-spots causing many artefacts. In practice, kriging and RBFs can give very similar results. The main advantage of kriging is that it provides direct estimates of the prediction quality in terms of estimation variance, so giving valuable information about the reliability of the interpolated values over the area of interest. Moreover, the measurement errors can be more directly introduced in the interpolation model by means of the so-called nugget variance. However, it is less robust than RBFs, and the estimates reliability heavily depends on the proper selection of the theoretical variogram model and its fitting.

2.2.2 Study area and data acquisition

2.2.2.1 Study site

The study focused upon a 2 km length reach of the Rovina di Cancia debris flow channel (western slope of Mount Antelao, Venetian Dolomites, North-eastern Italian Alps, Fig. 2.1). The channel originates in the scree at the base of Salvella fork (2 450 m a.s.l.), and the debris flows usually initiate at about 1 670 m a.s.l. (Fig. 2.1A). The channel ends within a flat circular deposition basin bounded downstream by a gabion wall (1 000 m a.s.l., Fig. 2.1D). At an altitude of 1 340 m a.s.l., just downstream a man-built flat deposition area (Fig. 2.1C), the channel joins on the left with the Bus de Diau creek which basically provides a liquid input to the debris flows routing along the Cancia channel.

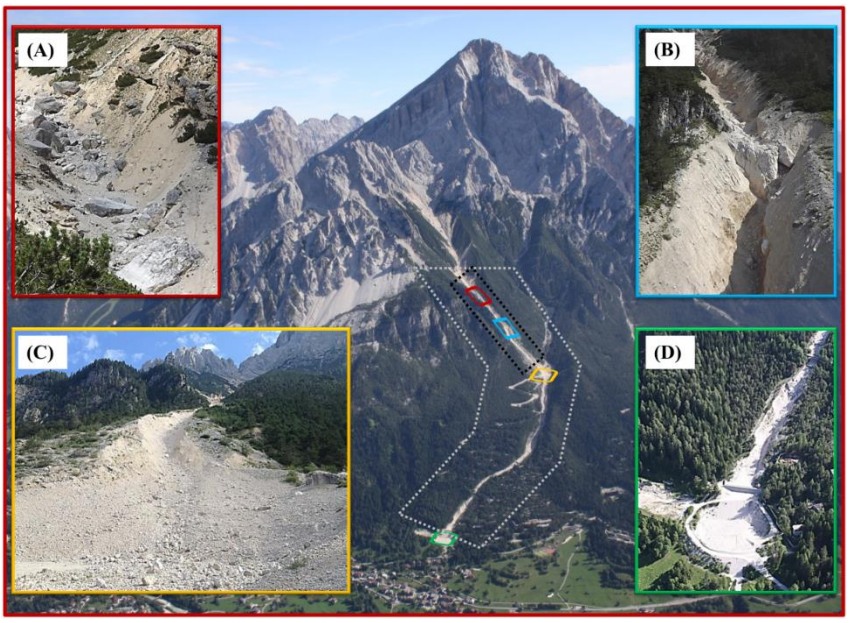

Fig. 2.1: Aerial view of the Rovina di Cancia study site. A) Debris flow triggering area (~1 670 m a.s.l.), B) Natural rock step located at the end of the debris flow triggering area (~1 500 m a.s.l.), C) Man-built flat deposition area (~1 340 m a.s.l.), D) Final flat circular deposition basin (~1 000 m a.s.l.). Dotted white line: LiDAR data coverage and hydraulic model domain; dotted black line: RTK-GPS data coverage.

From a geomorphological point of view, the debris flow catchment can be divided into three main sectors. In the upper part, massive rock cliffs prevail. They are composed of Upper Triassic to Lower Jurassic dolomites and limestones, underlined by the Raibl Formation, in a typical dolomitic stratigraphy configuration. The medium part is characterized by screes of poorly sorted and highly permeable debris, with boulders that can reach diameters of about 3-4 metres, while the downstream part is covered by old debris flow deposits, including postglacial sediment material.

The Cancia area is prone to stony debris flows owing to the plenty availability of loose and coarse sediments, and the impulsive hydrological regime of the basin. In particular, the smaller grain sized material is provided by both the failure and the erosion of the banks, whereas gravel, pebbles and cobbles are provided by the upper part of the basin characterized by rocky material. The pluviometric regime of the area is characterized by short duration and high intensity rainfall events, usually occurring during the summer season (July and August).

Different stony debris flow events have been recorded in the past decades probably due to recent changes in the rainfall pattern. The most significant ones are those occurred on 2 July 1994, on 7 August 1996, and on 18 July 2009 (Simoni et al., 2018). The first flooded the inhabited fan with about 30 000 m³ of debris. The second mobilized about 45 000 - 60 000 m³ of debris damaging some houses and cars but without losses of human life, while the latter mobilized about 40 000 m³ of debris and, after the filling of the retaining basin, it flooded some houses causing two casualties. The most recent debris flow events are those occurred on 23 July 2015 (about 30 000 m³ of mobilized debris) and on 04 August 2015 (about 25 000 m³ of mobilized debris).

2.2.2.2 Data acquisition

2.2.2.2.1 Full-waveform aerial laser scanner survey

The study site of Rovina di Cancia was surveyed by Helica s.r.l. on 21 October 2015 using a I-HBEP helicopter (Eurocopter AS 350 B3) equipped with a long-range, small footprint, full-waveform RIEGL LMS-Q780™ sensor. A comprehensive overview about the Airborne Laser Scanner technology (ALS) can be found e.g. in Vosselman & Maas (2010), while the state-of-the-art on full-waveform topographic LiDAR systems as well as on the related data processing techniques can be found e.g. in Mallet & Bretar (2009) and Wagner et al. (2006). The employed instrument works according to the time-of-flight distance measurement principle, and makes use of a powerful laser source, multiple-time-around processing, echo digitalization, and waveform analysis. This combination allows the operation at varying flying altitudes, and it is therefore ideally suited for aerial survey of wide areas and complex terrains. The ALS system was completed by five Global Positioning System (GPS) ground stations located within a maximum distance of 50 km from the surveyed area, which served as reference stations for the off-line differential GPS calculation. Furthermore, a Phaseone iXA 180 medium-format frame digital camera was accommodated on the scanner assembly ground plate to allow the simultaneous acquisition of range and image data. The technical features of the employed laser-scan system as well as the employed flight parameters are reported in Table 2.1S and Table 2.2S of the supplementary material, respectively.

After the aerial survey, the LIDAR data provider classified the raw points cloud into ground and non-ground echoes by the software package Terrascan™, setting parameters refined by the company itself over the years. For the study area of Rovina di Cancia (Fig. 2.1), the mean LiDAR points density (i.e. ground and non-ground points density) was 20.79 points m-2. After the filtering step, the mean LiDAR ground points density resulted in 3.33 points m-2, corresponding to a mean ground points distance of 0.28 m.

2.2.2.2.2 Real-time kinematic GPS survey

In order to assess the vertical accuracy of both LiDAR data and interpolated DEMs, over 3 000 independent Real Time Kinematic GPS (RTK-GPS) measurements were acquired along the upper part of the channel on October-November 2015 (Fig. 2.1 and Fig. 2.1SA of the supplementary material). This positioning technique ensures high-precision topographic measurements that can be considered control values for laser scanner- and photogrammetric-derived points clouds (Cilloccu et al., 2009; Caroti & Piemonte 2010). As a matter of fact, the nominal positioning accuracy for dual-frequency GPS systems operating in kinematic mode with baseline less than 20 km ranges between 0.02 and 0.05 m. Since the control values should be at least three times more accurate than data being evaluated (e.g. Höhle & Höhle, 2009;

Höhle & Potuckova, 2011), it means that RTK-GPS measurements can be used to assess the accuracy of points clouds with accuracy up to 0.06 m.

In order to describe accurately the channel morphology, a cross-sections morphological-guided spatial sampling scheme was adopted (e.g. Aguilar et al., 2005; Heritage et al., 2009). In detail, the ground measurements were acquired in coded cross-sections keeping orthogonal to the flow direction, and taking care to acquire relevant topographic features (such as talweg position, toe and top bank, Fig. 2.1SB of the supplementary material). Both the ground points sampling distance and the cross-sections inter-distance were defined during the field survey according to the local terrain roughness. The mean points sampling distance was 0.65 m (with a maximum of 2.73 m, and a minimum of 0.06 m), whereas the mean cross-section inter-distance was 3.25 m (with a maximum of 9.80 m, and a minimum of 0.89 m). The mean points density for the surveyed area was 1.38 points m^{-2}.

The real-time three dimensional rover position was obtained by connecting via radio waves to a master station located at a maximum distance less than 1 km in order to minimize measurement errors (Fig. 2.1SA of the supplementary material). The positioning was based on phase solutions employing both L1 and L2 signal frequencies. To achieve the maximum accuracy, during the ground survey only fixed solutions were acquired. In addition, the three dimensional position of each surveyed ground point was calculated as average of the measurements carried out on five epochs. This measurements redundancy allowed minimizing the influence of the technology inherent error sources (e.g. atmosphere delay, multipath, and clocks synchronization). The reported RTK-GPS data planimetric precision was 0.005 m ± 0.001 m (with a maximum of 0.03 m), while the reported vertical precision was 0.008 ± 0.002 m (with a maximum of 0.05 m). The average planimetric dilution of precision value was 2.55 ± 0.45 (with a maximum of 3.50). The average number of GPS satellites viewed during the survey (GPS and GLONASS constellations) was 10 (with a maximum of 14).

The geographic coordinates of the GPS-RTK measurements were projected in the coordinate system WGS84-UTM32 (i.e. the LiDAR data geodetic-cartographic datum, see Subsection 2.2.4), whereas the orthometric heights were computed based on the local geoid model ITALGEO2005[4].

2.2.3 GIS-based routing cell model

The employed GIS-based debris flow cell routing model (DFRM) is able to simulate the routing and the deposition of solid-liquid mixtures with a grain-collision dominated rheology (Gregoretti et al., 2018), also known as stony debris flows (Takahashi, 2007). It represents the fully bi-phase version of the one proposed by Gregoretti et al. (2016a), and allows a better simulation of the entrainment process.

The model discretizes the flow domain by using the square cells of a DEM. Each cell is hydraulically linked with its eight surrounding ones (Fig. 2.2SA of the supplementary material), and the flow always occurs according to positive free surface drops (Fig. 2.2SB and Fig. 2.2SC of the supplementary material). The governing equations of the mathematical model are those of mass and momentum conservation of both the overall sediment-water mixture and the solid phase, along with the Exner's equation in union with a modified version of the one dimensional empirical law of Egashira & Ashida (1987) for the rate of change of bed elevation.

In differential form, the continuity equations at the cell scale are:

$$\mathrm{A}\frac{\mathrm{d(h+z)}}{\mathrm{dt}} + \sum_{\mathrm{k=1}}^{8} \mathrm{Q_k} = 0 \tag{2.1}$$

$$A\frac{d(ch+c_{*}z)}{dt} + \sum_{k=1}^{8} cQ_k = 0 \tag{2.2}$$

where A is the area of the square cell, h is the flow depth, z is the bottom elevation, t is the time, c is the sediment volumetric concentration of the mixture, c_* is the dry sediment concentration (also known as maximum packaging

[4] Nominal conversion accuracy equal to ± 0.035 m at 1σ.

concentration), and Q_k is the discharge exchanged by the reference cell with its surrounding ones, assumed to be positive if outflowing and negative otherwise.

In the model, the water-sediment mixture is supposed to be a continuous mean composed by granular material immersed in an interstitial fluid with equal velocities for the two phases. According to the kinematic wave approximation, in the case of gravity-driven flow (Fig. 2.2SB of the supplementary material) the momentum equation is that of uniform flow in a Chezy-like form. Conversely, in the case of flow along negative slopes (Fig. 2.2SC of the supplementary material) the momentum equation is that of broad-crested weir. This latter equation is used to cope with flow routing in areas having local topographic depressions, and in the presence of obstacles like hydraulic structures and houses. The corresponding discharges are:

$$Q_{i,k} = C\Delta x h w_k \sqrt{g h sin\theta_k} \qquad w_k = \frac{sin\theta_k}{\sum_{k=1}^{n} sin\theta_k} \tag{2.3}$$

$$Q_{i,k} = C_q \Delta x s_k \sqrt{2g}(h - z_k)^{1.5} \quad s_k = \frac{h - z_k}{\sum_{k=1}^{m}(h - z_k)} \tag{2.4}$$

where C is the conductance coefficient (Tsubaki, 1972) representative of the grain-inertial rheology (Takahashi, 1978; Takahashi, 2007), Δx is the cell size, w_k and s_k are weighting functions introduced to allow multi-flow directions, g is the gravity acceleration, h is the flow depth, z is the bottom elevation, and ϑ_k is the angle formed with the horizontal by the line joining the centre of the reference cell with its surrounding ones.

The Exner's equation is:

$$\frac{d_z}{d_t} = -i_b \tag{2.5}$$

$$i_b = KU_{MAX}(sin\alpha_{MAX} - sin\vartheta_{LIM}) \tag{2.6}$$

being i_b the rate of change of bed elevation as proposed in Gregoretti et al. (2016a), K is an empirical constant ranging between 0 and 1, U_{MAX} is the velocity corresponding to the steepest of the eight possible flow directions K_{MAX}, $\alpha_{MAX} = \vartheta_{KMAX}$ in the case of gravity-driven flow, otherwise $\alpha_{MAX} = (\vartheta_K + \theta_k)_{MAX}$ being θ_k the angle that the horizontal forms with the line joining the centre of the reference cell and that along which the flow is directed, ϑ_{LIM} and U_{LIM} are limit values for ϑ and U respectively. The parameters ϑ_{LIM} and U_{LIM} assume different values for erosion ($U_{LIM\text{-}E}$ and $\vartheta_{LIM\text{-}E}$) and deposition ($U_{LIM\text{-}D}$ and $\vartheta_{LIM\text{-}D}$), and they should be determined by field measurements or numerical back analysis. The erosion velocity i_b is positive if $U_{MAX} > U_{LIM\text{-}E}$ and $\alpha_{MAX} > \vartheta_{LIM\text{-}E}$, whereas it is negative if $U_{MAX} < U_{LIM\text{-}D}$ and $\alpha_{MAX} < \vartheta_{LIM\text{-}D}$. Erosion and deposition are computed only along the steepest downslope flow direction given the one-dimensional nature of the Egashira & Ashida's law. Moreover, considering all the possible flow directions could lead to unrealistically large deposition rate along directions transverse to the steepest downslope flow direction, and a cell could be subjected to both erosion and deposition in the same time interval. Erosion is also computed only for increasing flow depths ($dh/dt > 0$), according to the instrumental field observations of Berger et al. (2011). Other two constrains are imposed to erosion and deposition processes: entrainment of sediment by the overflowing mixture is possible only if c is smaller than the physic limiting upper value of $0.9c_*$ (Takahashi, 2007); similarly, deposition occurs only if c is larger than a limiting lower sediment concentration for debris flow (c_D) assumed equal to 0.05.

From a numerical point of view, the governing equations are solved through a finite difference technique with explicit scheme subject to the Courant-Friedrichs-Lewy stability condition. The initial conditions are represented by the inflow solid-liquid hydrograph computed at the inlet section by means of a coupled hydrological and triggering model (e.g. Gregoretti et al. 2016b; Gregoretti et al. 2018). The computation procedure starts defining for each cell the possible solid-liquid discharges towards its eight surrounding ones according to equations (2.3) and (2.4). Then, the rate of change of bed elevation corresponding to the steepest downslope flow direction is computed by equation (2.6). At the end of each

computational time step, the cell free surface and bed elevation are simultaneously updated based on the computed outflow/inflow and deposited/entrained volumes.

2.2.4 LiDAR data pre-processing and vertical accuracy analysis

Raw and filtered LiDAR datasets were delivered in ASCII files consisting of X, Y, Z (ellipsoidal heights related to the reference ellipsoid WGS84) and intensity data, arranged in 1 km x 1 km tiles based on the projected coordinate system WGS84-UTM32. Although at national and regional level the geodetic-cartographic datum Roma40-Gauss Boaga represents the formally accepted coordinate system, no datum transformation was performed in order to avoid accuracy loss in the delivered topographic datasets. Conversely, the ellipsoidal heights were converted in orthometric heights based on the local geoid model ITALGEO2005 in order to allow the direct comparison with the GPS validation measurements (see Subsection 2.2.2.2.2). No additional attributes (e.g. GPS time for every laser shot, scan angle, edge of flight line information, echo amplitude, echo width) were included within the delivered datasets.

Before analysing the vertical accuracy of aerial laser data, the filtered LiDAR dataset was converted in LAS format and then critically examined to check for classification errors (i.e. commission and omission errors). It represents a key step since the LiDAR-derived DEMs quality strongly depends on the correct classification of the raw points cloud into terrain and off-terrain echoes (e.g. Vosselman & Maas, 2010). The visual inspection of the LiDAR data via LASview™ highlighted many data voids in morphologically complex areas, due to misclassified LiDAR points as non-ground when they truly represented ground features such as big boulders within the channel (Fig. 2.3S of the supplementary material). As this kind of classification errors could heavily affect the routing model outcomes, the delivered raw points cloud was re-classified into ground and non-ground points within the software package LAStools™. For the study area of Rovina di Cancia, the re-classification procedure yielded a mean LiDAR ground points density equal to 4.34 points m^{-2} (i.e. 30% more than the density of the delivered LiDAR ground points dataset), with an observed mean ground points distance corresponding to 0.25 m.

Since a number of error sources can affect the accuracy of LiDAR points clouds determining systematic errors and many outliers (e.g. accuracy in the aircraft absolute positioning and attitude data, accuracy of system calibration as determination of boresight angles and offsets between instruments, internal scanner errors, automated processing of the points cloud), an extensive vertical accuracy assessment was carried out on the re-classified LiDAR ground points dataset using the independent RTK-GPS measurements. An automated routine based on a proximal point algorithm (e.g. Reutebuch et al., 2003; Webster & Dias 2006; Pourali et al., 2014) was then coded in order to directly compare the LiDAR and the validation data. This approach is suitable to accurate heights comparison, since errors introduced through gridding are eliminated (Hodgson and Bresnahan, 2004; Höhle & Potuckova, 2011; Pourali et al., 2014). The validation technique involves a user specified horizontal search radius around the GPS control point for comparison with the LiDAR ground points. In order to limit the influence of the channel slope on the computed residuals, a horizontal search radius equal to 0.50 m was used. It has also allowed an average number of LiDAR ground points within the search radii equal to four, thus ensuring a sufficient sample size for reliable accuracy measures. All LiDAR ground points within that search area are selected, and then their orthometric heights are compared to that of the GPS validation point. The computed elevation differences were considered as vertical “errors”, and they were statistically analysed within the R open-source software package (R Development Core Team, 2008).

The derivation of accuracy measures has to consider that outliers may exist and that the distribution of the errors might not be normal. For this reason, the framework outlined in Höhle & Potuckova (2011), based on the standard (e.g. mean error, standard deviation, and their confidence intervals) and robust accuracy measures (e.g. median, Normalized Median of Absolute Deviations (NMAD), sample quantiles of absolute errors, and their confidence intervals) reported in Table 2.4S of the supplementary material, was followed. The readers are referred to the works of Höhle & Höhle (2009) and Höhle & Potuckova (2011) for a complete dissertation of the method.

It is worth pointing out that we compared two points datasets having different measurement support size, location, and spatial distribution, which pose inherent uncertainties on the accuracy assessment results.

2.2.5 DEMs generation and interpolation algorithms comparison

2.2.5.1 DEMs interpolation

Prior to DEMs interpolation, a thoroughly Exploratory Spatial Data Analysis (ESDA) was performed on the re-classified LiDAR ground points dataset. This analysis was carried out at the purpose of gaining insight into the studied spatial variable. A number of features of the topographic dataset were investigated by the ESDA tools of the Geostatistical Analyst™ module (ArcGIS™, rel. 10.3), among which: spatial and marginal distribution via Voronoi's polygon map, points pattern analysis, and standard statistic plots and indices; second-order or intrinsic stationarity by trend analysis; and spatial dependency through variography.

Among the tested interpolation methods, the TIN-based routines (i.e. linear triangulation, natural neighbour, and nearest neighbour) does not require a dataset specific parametrization. Conversely, the remaining deterministic (i.e. inverse distance to a power, ANUDEM, and Radial Basis Functions) and geostatistical (i.e. point ordinary kriging, and block ordinary kriging) methods were parametrized as it follows.

The most important parameters of IDP and RBFs algorithms were optimized via cross-validation by minimising the mean square prediction error. In fact, in its common form of "leave one out", it represents the most frequently used technique as exploratory mean to find the best dataset specific algorithm parametrization (Erdogan, 2009). These algorithms were also parametrized to use a number of neighbours ranging from 7 to 25, according to Oliver & Webster (2014). Furthermore, the presence of a linear global trend following the gradient of the channel (see Subsection 2.3.2 and Fig. 2.4A) led to the use of a one sector elliptical search neighbourhood oriented according to the direction of the greatest spatial continuity (i.e. the direction perpendicular to the trend) was used during the interpolation procedure. The ellipse major semi-axis was set equal to the range of the directional empirical variogram computed along the direction of the greatest spatial continuity. Conversely, the ellipse minor semi-axis, corresponding to the direction of the least spatial continuity (i.e. the trend direction), was defined by cross-validation. It allowed to favour during the interpolation procedure the points with the greatest spatial correlation. The ANUDEM algorithm was tested using only the re-classified LiDAR ground points as input data. The algorithm roughness penalty was defined as a mixture of minimum curvature and minimum potential, and the drainage enforcement option was enabled. Moreover, the standard vertical error and the first elevation tolerance were set equal to the computed random vertical error of the re-classified LiDAR points dataset (see Subsection 2.3.1 and Tab. 2.1). The geostatistical interpolation was performed through the ordinary kriging algorithm, employing a Gaussian theoretical variogram model fitted on the directional empirical one computed perpendicularly to the trend. In fact, as suggest by Chilès (1984) and Oliver & Webster (2014), a statistically sound procedure to kridge points dataset with a dominant linear global trend consists in applying the ordinary kriging algorithm using a theoretical variogram model fitted on the directional empirical one computed along the direction of the greatest spatial continuity. This theoretical variogram can be considered as the variogram of the residuals (i.e. the theoretical variogram of the spatially correlated component of the studied variable). The nugget parameter of the theoretical Gaussian variogram was set equal to the square of the computed random vertical error of the re-classified LiDAR points dataset, so predicting filtered (or, "error-free") values. Furthermore, the points dataset was kridged using both a punctual and a block support, with a block dimension corresponding to 0.50 and 1.00 m (i.e. the DEMs spatial resolution, see below). For the upscaling procedure, the number of averaged punctual predictions within each block was defined according to the LiDAR footprint, which represents the input data support dimension. All the employed interpolation techniques parametrizations are summarized in Table 2.3S of the supplementary material.

The spatial resolution of DEMs was set according to the rules outlined by Hengl (2006). In detail, the author proposed empirical and analytical criteria to select the optimal grid resolution for points dataset interpolation, including those based on GPS horizontal error, map scale, size and shape of the smallest objects being mapped, points pattern geometry, and spatial correlation. Many of the described methods refer to the Whittaker-Nyquist-Kotelnikov-Shannon sampling theorem (e.g. El-Sheimi et al., 2005), which states that an original continuous signal can be reconstructed from the sampled data without any loss of information only if the sampling frequency is twice than the original one (Nyquist frequency). Thus, a raster grid cell size that retains the highest information content of the original points dataset is equal to half the average spacing between the closest points pairs. The re-classified ground LiDAR points were randomly distributed with an average mutual distance equal to 0.25 m. However, the 5% quantile of the nearest neighbour distances distribution was 0.10 m, while the 95% quantile was 0.57 m (Tab. 2.5S of the supplementary material). Therefore, a

spatial resolution of 0.05-0.30 m is deemed to be appropriate for the employed LiDAR dataset. Nevertheless, the processing power of the available hardware along with the data management efficiency of GIS software limit the ability to generate digital surfaces at these very fine spatial resolutions. Thus, for each combination of interpolator and related parameters, DEMs were generated with a spatial resolution equal to 0.50 and 1.00 m (corresponding to 2.17 and 4.34 ground LiDAR points per cell, respectively). Notably, a spatial resolution of 0.50 m matches the source data information content according to the root mean square slope criterion developed by Hutchinson (1996).

2.2.5.2 Comparison of interpolation methods

Once the DEMs were generated, the overall performance of each tested interpolation algorithm was assessed by computing the vertical bias and accuracy of the corresponding gridded digital surface through the independent GPS points dataset. In detail, the accuracy measures were statistically derived from the differences between the GPS height value and the elevation value of the grid cell centre containing the GPS point itself. In order to choose between standard or robust accuracy measures (see Subsection 2.2.4 and Tab. 2.4S of the supplementary material), the sample error distributions were firstly check for outliers and normality. The outlier threshold was set equal to three times the Root Mean Square Error (RMSE) according to the rules outlined by Höhle & Höhle (2009), whereas the sample error distributions normality was tested both graphically by means of the normal Q-Q plot, both statistically through the D'Agostino K^2 omnibus test due. This test was chosen for its reliability with large samples having kurtosis slightly higher than the normal distribution (Gallay et al., 2013). Therefore, the median of the vertical errors was chosen as robust estimator of the DEMs vertical bias, whereas, for the vertical accuracy of DEMs, the NMAD along with the 68.3% and 95% quantiles of the absolute errors distribution were chosen as robust estimators. The Mean Absolute Error (MAE), the minimum and maximum vertical error and the corresponding range, the weighted determination coefficient (Krause et al., 2005) along with the slope and the intercept parameters of the linear regression between measured and interpolated values, and the total drainage sink area (i.e. number and extension of raster cells whose neighbours are all of higher elevation) were also used as supplementary aspatial DEM quality indices. This latter index was used here as interpolation errors indicator, since the higher the number of interpolation artefacts in the gridded DEM, the larger the total drainage sink area will be (Wise 2000; Wise, 2007; Setiawan et al., 2013).

It is worth pointing out that all these descriptive statistics are aspatial summary accuracy indices. However, a number of authors suggested that the vertical error of DEMs is not spatially uniform, but it can assume some form of spatial pattern (e.g. Li, 1993; Wood & Fisher, 1993; Wood, 1996; Yang & Hodler, 2000; Weng, 2006; Erdogan, 2009). Since DEMs with identical global accuracy values may have a different spatial pattern of errors (with digital surfaces having evenly distributed error values more reliable than those with high error clustering), to evaluate the performance of an interpolation method it is also important to investigate the spatial distribution of vertical errors and their clustering extension. For deterministic gridding methods, the best way to examine the spatial distribution of vertical errors is by means of accuracy maps obtained after comparing the interpolated DEM with a second more accurate surface. These maps have the advantage of clearly indicate where serious and perhaps anomalous errors occur. Unfortunately, as in this study, the availability of a more accurate control surface for comparison is rare. Thus, the spatial distribution of vertical errors was graphically investigated through choropleth symbol maps, in which the size and the colour of each independent validation point is established according to the error magnitude. Conversely, the error clustering extent was statistically assessed by means of both global and local indicators of spatial autocorrelation (i.e. the Global Moran's I index and the Anselin Local Moran's I index, respectively). The Global Moran's I index measures the overall spatial autocorrelation based on both features location and features value simultaneously, so evaluating whether the pattern expressed is clustered (index value approaching to 1), dispersed (index value approaching to -1), or random (index value approaching to 0). It indicates clustering of high or low error values, without showing where the clusters are. To overcome this drawback, the Anselin Local Moran's I index was also used. As the name suggests, it represents the local form of the Global Moran's I index, and it is used to graphically detect local pockets of dependence.

Since a critical concern in assessing the reliability of a gridding method is represented by its sensitivity with respect to changes in certain parameters (e.g. search neighbourhood) or conditions (e.g. sample density), we further evaluated the stability (or robustness) of each tested interpolation algorithm focusing on the sample size. In detail, we investigated the change in the performance of each tested gridding method considering a decreasing number of LiDAR ground points. So,

thinned datasets were obtained by randomly splitting the re-classified LiDAR ground points at densities corresponding to the 95%, 75%, and 50% (which correspond to 4.13, 3.29, and 2.64 points m^{-2}, respectively). These thinned sample datasets were therefore interpolated at the spatial resolutions of 0.50 and 1.00 m, keeping unchanged for each gridding technique the optimized model parameters (Tab. 2.3S of the supplementary material). After that, on each thinning-derived DEM, a comprehensive accuracy assessment was carried out following the approach above outlined, and the results obtained at the vary sample densities were finally compared. Note that a total 96 DEMs were generated for this investigation.

As recognized by vary authors the success of a digital terrain modeling algorithm mainly depends on the purposes (e.g. Hengl & Reuter, 2009; Schwendel et al., 2012). Unlike DEMs for ortho-photos production where the absolute accuracy of elevation values is the most important feature, DEMs for hydrological and hydraulic modeling must represent the catchment and channel shape realistically and close to the sampled topographic data thus ensuring that slopes and flow paths are correctly represented. For this reason, the shape reliability of each generated DEM was investigated through a combination among visualization techniques and residual analysis. The shape reliability is here defined as the degree of maintenance of the channel shape (as described by the sampled topographic data) in the interpolated DEM. In a pre-selection phase, for each generated DEM derivatives like slope, aspect, and curvature, along with shaded relief and surface roughness maps, were visually examined in order to identify interpolation artefacts. For the gridded surfaces that ensured a satisfactory representation of the channel topography, a multi-criteria morphological based comparison was then undertaken. The established morphological criteria include the plano-altimetric representation of longitudinal and transversal linear features (e.g. channel margins, hydraulic structures, and steps), and the representation of channel bottom forms (e.g. sediment sheets, boulders, and rugged reaches). They were defined considering the morphological features of the channel that need to be correctly represented in the interpolated DEM in order to guarantee a reliable numerical modeling of debris flow routing. Noteworthy, this approach relies on qualitative analysis depending on the expert judgment of a user, and this is its main limit. To overcome this drawback, the ability of each tested gridding method to fulfill the topographic sampled data (i.e. the ability to faithfully represent the surveyed topography) was quantitatively assessed through a residual analysis.

2.2.6 Evaluation of the effects of gridding techniques on debris flow routing model results

The hydraulic simulation of the Rovina di Cancia debris flow was carried out by using the cell routing model proposed by Gregoretti et al. (2018a) and described in Subsection 2.2.3.

Since the effects of the digital elevation uncertainty resulting from the gridding procedure on debris flows routing modeling could be masked by an inaccurate model parametrization, the input parameters of the cell model were previously calibrated against two real debris flow events (occurred at Rovina di Cancia on 18 July 2009 and on Ru Secco the 4th of August 2015, respectively). In detail, the calibration procedure was undertaken by comparing the simulation results with both the observed erosion/deposition depth maps and the witnessed routing times. Both the back-analysis provided the same optimal model parametrization, thus guaranteeing a certain high degree of predictivity (for further details see Gregoretti et al., 2018a,b).

For all the model runs, both the calibrated values of the input parameters (i.e. C, K, $U_{LIM\text{-}D}$, $U_{LIM\text{-}E}$, $\vartheta_{LIM\text{-}D}$, and $\vartheta_{LIM\text{-}E}$) and the initial conditions (i.e. the upstream solid-liquid hydrograph) were kept unchanged, varying only the initial topographic surface generated according to the twelve tested interpolation algorithms. Therefore, this approach allowed the investigation of the influence of the algorithms itself on the modelling outcomes.

Two event scenarios, corresponding respectively to 50- and 300-year return period, were defined by means of a coupled hydrological and triggering model (e.g. Gregoretti et al. 2016b; Gregoretti et al. 2018), starting from the rainfall depth-duration frequencies curves. It enabled to investigate the influence of gridding methods on debris flow routing model results for events of different magnitude, characteristics of two usual design return periods.

For the sake of simplicity, in the different model runs we employed only the full dataset- and the 50% thinning-derived 1-meter resolution DEMs as input topographic data, carrying out a total of 48 simulations (i.e. twelve DEMs, two points densities, and two event scenarios).

To evaluate the influence of gridding methods on debris flow routing modelling, we initially explored the relationship between the uncertainties on digital elevation and on the model results. In detail, for each combination of points density and event scenario we correlated the pixel-wise standard deviation of the twelve DEMs heights (i.e. the standard deviation at the cell scale in the twelve input topographic data of the routing model) and the pixel-wise standard deviation of the corresponding twelve simulated erosion/deposition depths (i.e. the standard deviation at the cell scale of the corresponding twelve routing model outputs). This allowed elucidating if the cells with high uncertainty in the simulated erosion/deposition depths were spatially linked to those with high topographic uncertainty. It must be noted that the correlation was investigated both globally (i.e. at the channel extent), and locally by means of moving windows. The moving windows size was set equal to 3x3 and 5x5 m, according to the spatial continuity of the correlated variables. The bivariate moving windows correlation analysis was carried out through the R package developed by Evans & Ram (2018). After that, for each combination of data density and event scenario, we compared the model run results in terms of simulated areas, erosion and deposition volumes, solid-liquid discharges, and channel morphology after the event.

2.3 Results & Discussion

2.3.1 LiDAR data vertical accuracy assessment

The results of the vertical accuracy assessment carried out on the re-classified LiDAR points cloud are summarized in Table 2.1. It turns out that the outliers have a great influence on the mean and standard deviation of vertical errors values. Respectively, they drop from 0.032 to 0.026 m and from 0.304 to 0.260 m after the outliers removal. The histogram and the normal Q-Q plot shown respectively in Figure 2.2A and Figure 2.2B highlight that the vertical errors distribution is non-normal. In particular, the histogram shows that the kurtosis of the vertical errors distribution is positive (i.e. the distribution has a more acute peak around the mean and fatter tails than the normal one). Furthermore, the normal Q-Q plot deviates from the straight line at the extremes, which clearly indicates the presence of outliers in the vertical errors sample. After removing the outliers, the values of the mean and standard deviation of vertical errors decrease (Tab. 2.1). However, they are somewhat greater than the corresponding robust ones (i.e. greater than the values of the median and NMAD of the vertical errors, see Subsection 2.2.4 and Tab. 2.4S of the supplementary material), and the histogram and normal Q-Q plot shown respectively in Figure 2.2C and Figure 2.2D highlig ht that the thresholded vertical errors distribution does not follow the normal one.

Accuracy measures	**Value (m)**	**Confidence interval**
Mean	0.0323	[0.028, 0.038]
Standard deviation	0.304	[0.301, 0.308]
Root Mean Square Error (RMSE)	0.306	[-]
Threshold for outliers removal (3*RMSE)	0.928	[-]
N. outliers (% of the error sample)	251 (1.98%)	[-]
Mean (after outliers removal)	0.026	[0.022, 0.031]
Standard deviation (after outliers removal)	0.260	[0.257, 0.263]
Median	0.020	[-0.020, 0.050]
Normalized Median of Absolute Deviations (NMAD)	0.237	[0.208, 0.267]
68.3% sample quantile of absolute errors distribution	0.250	[0.220, 0.280]
95% sample quantile of absolute errors distribution	0.630	[0.500, 0.780]

Tab. 2.1: Computed standard and robust accuracy measures.

The median of the vertical errors is 0.020 m, and it represents the systematic vertical shift between the re-classified LiDAR points cloud and the GPS validation data. This altimetric bias has been eliminated by means of a 2.5D calibration procedure (i.e. a rigid translation in the Z dimension of the re-classified LiDAR points cloud). After the calibration procedure, the vertical accuracy of the re-classified LiDAR points cloud depends only on its random vertical error

component, and it can be evaluated by means of the standard deviation of vertical errors. In this case, the robust estimator of the standard deviation is equal to 0.237 m, and it corresponds approximately to the 68.3% quantile of the absolute vertical errors distribution.

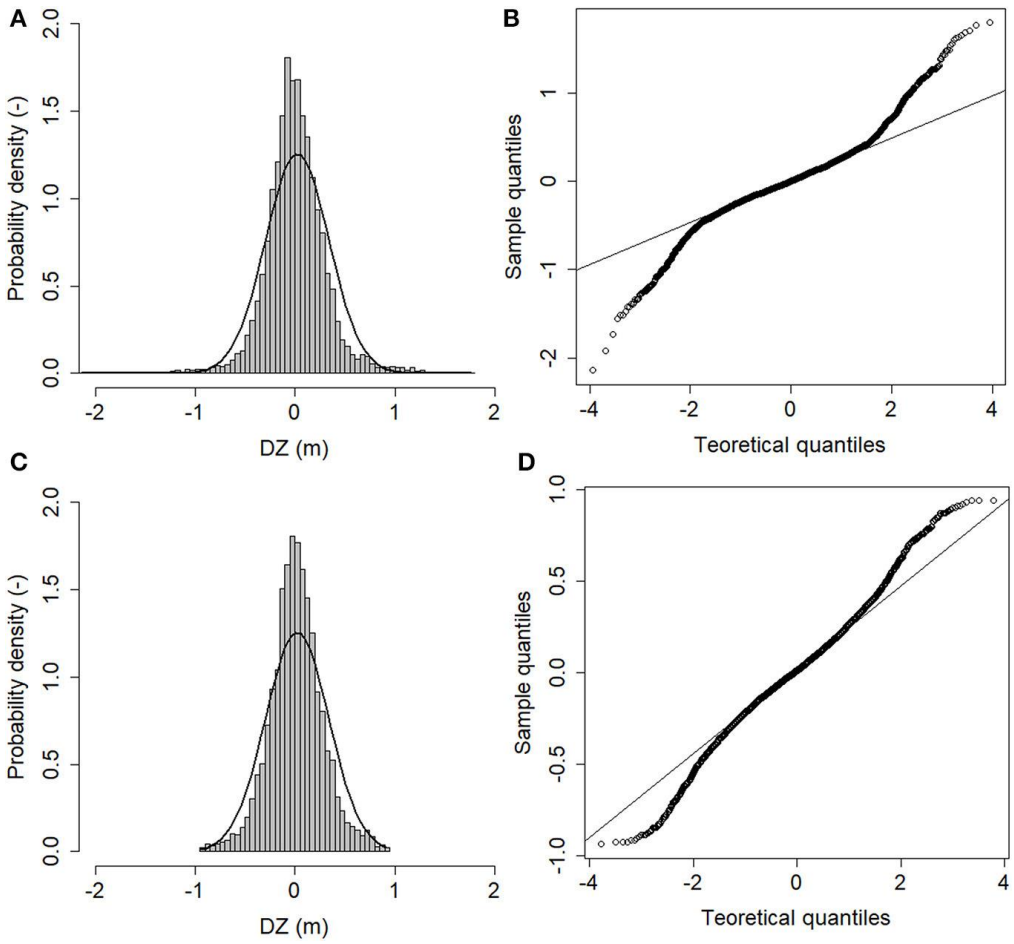

Fig. 2.2: A) Histogram of the errors. Superimposed, the normal distribution with mean and standard deviation estimated from all data. B) Normal Q-Q plot of the errors. C) Histogram of the errors without outliers. Superimposed, the normal distribution with mean and standard deviation estimated from the thresholded errors dataset. D) Normal Q-Q plot of the errors without outliers. ΔZ denote the vertical error.

The median of the vertical errors is 0.020 m, and it represents the systematic vertical shift between the re-classified LiDAR points cloud and the GPS validation data. This altimetric bias has been eliminated by means of a 2.5D calibration procedure (i.e. a rigid translation in the Z dimension of the re-classified LiDAR points cloud). After the calibration procedure, the vertical accuracy of the re-classified LiDAR points cloud depends only on its random vertical error component, and it can be evaluated by means of the standard deviation of vertical errors. In this case, the robust estimator of the standard deviation is equal to 0.237 m, and it corresponds approximately to the 68.3% quantile of the absolute vertical errors distribution.

Figure 2.4S of the supplementary material depicts the difference between the employed accuracy measures. It has been obtained superimposing to the vertical errors sample distribution the normal ones calculated by using the mean and standard deviation of the vertical errors sample, the mean and standard deviation of the vertical errors sample without outliers, and the median and NMAD of the vertical errors sample, respectively. On one hand, the graph shows that the standard accuracy measures are not able to match the vertical errors sample distribution. Furthermore, even the application of an outliers threshold does not eliminate each of them from the vertical errors sample, and so the standard accuracy measures remain inaccurate. On the other hand, since the robust accuracy measures are able to apply a smoother transition between accepting and rejecting an observation from the vertical errors sample, they fit the vertical errors sample distribution best, both at the mean and at the tails. This finding validates the suggestions proposed by Höhle & Höhle

(2009), who recommend the use of robust accuracy measures (i.e. median, NMAD, and sample quantiles of the absolute errors dstribution) when the histogram (or the normal Q-Q plot) of the errors sample distribution reveals non-normality, since they are not influenced by outliers or distribution skewness.

2.3.2 Exploratory Spatial Data Analysis results

The results of the spatial distribution analysis carried out on the re-classified LiDAR points dataset are summarized in Table 2.5S of the supplementary material. The mean Voronoi's influence area of the LiDAR ground points is equal to 0.237 m^2, with an interquartile range corresponding to 0.174 m^2. It means that the spread of the influence area values is small, and so the sampling network can be considered homogeneous. Moreover, the average mutual distance between closest LiDAR points pairs is equal to 0.29 m ± 0.13 m, while the maximum is 3.48 m. The 5% quantile of the mutual distances distribution corresponds to 0.10 m, while the 95% quantile is equal to 0.57 m. The former statistic can be regarded as a robust measure of the minimum distance between closest ground points pairs, whereas the latter as a robust measure of their maximum distance.

As shown in Figure 2.3A, the marginal distribution of the re-classified LiDAR dataset is roughly unimodal, approximatively symmetric (skewness coefficient equal to 0.30) and approximatively mesokurtic (kurtosis equal to 2.40). However, the normal Q-Q plot deviates from the straight line at the extremes (Fig. 2.3B), indicating that the elevation values distribution is non-normal. Moreover, the box-plot shown in Figure 2.3C does not reveal the presence of outliers within the dataset, as also confirmed by a coefficient of variation lesser than one.

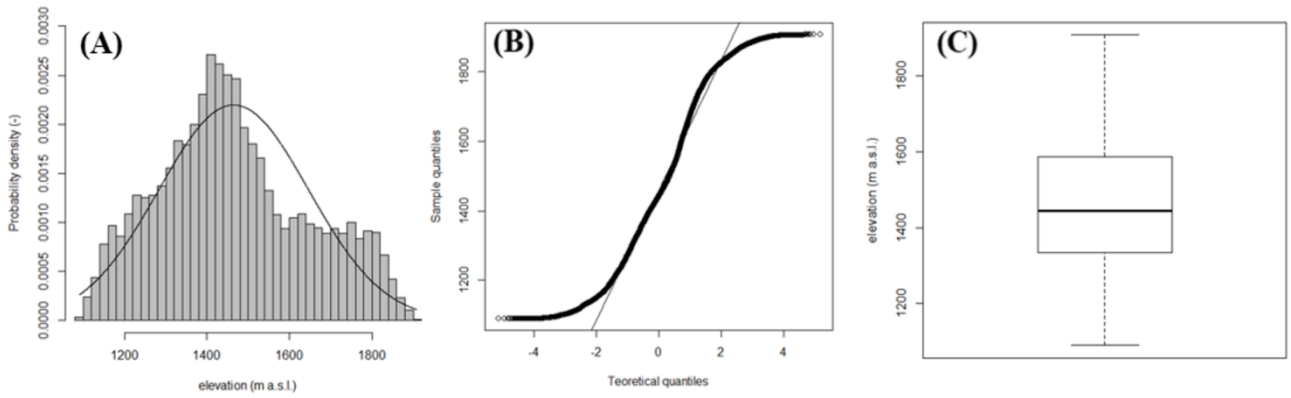

Fig. 2.3: Histogram with superimposed the normal distribution (A), normal Q-Q plot (B), and box-plot (C) of the LiDAR ground point dataset.

The quantiles map of the elevation values (Fig. 2.4A) clearly shows a trend in the NE-SW direction. It means that the variable to be interpolated is not stationary within the domain since its mean changes smoothly in the space. To find the trend degree, the correlation between the elevation values and the east-north spatial coordinates has been analysed through the scatter-plots shown respectively in Figure 2.4B and Figure 2.4C. The Pearson's correlation coefficient, which provides a measure of the linear relationship between two variables, is equal to 0.48 along the east direction and 0.82 along the north direction. It is often useful to supplement the linear correlation coefficient with the Spearman's rank correlation coefficient, which represents another measure of the relationship strength (Isaaks & Srivastava, 1989). Unlike the Pearson's coefficient, the Spearman's rank coefficient is not strongly influenced by extreme pairs, and large differences between the two correlation coefficients may be due to the presence of few erratic pairs or to a non-linear relationship between the two variables. Along the east direction, the Spearman's rank coefficient is equal to 0.47, whereas along the north direction it corresponds to 0.84. Since both along the east and north direction the differences between the Pearson's and Spearman's correlation coefficient values are small, it can be stated that the variable to be interpolated exhibits a linear global trend.

The directional empirical variogram of the elevation values computed perpendicularly to the channel gradient (i.e. along the direction of the greatest spatial continuity) is shown in Figure 2.5SA of the supplementary material with

overlying the fitted Gaussian theoretical model. The theoretical variogram levels off at a range of about 180 m reaching a plateau of 450 m^2, and it shows a parabolic structure near the origin (Fig. 2.5SB of the supplementary material) followed by an inflection point. The nugget to sill ratio along the considered variogram modelling direction is close to zero, thus indicating the presence of a strong spatial structure.

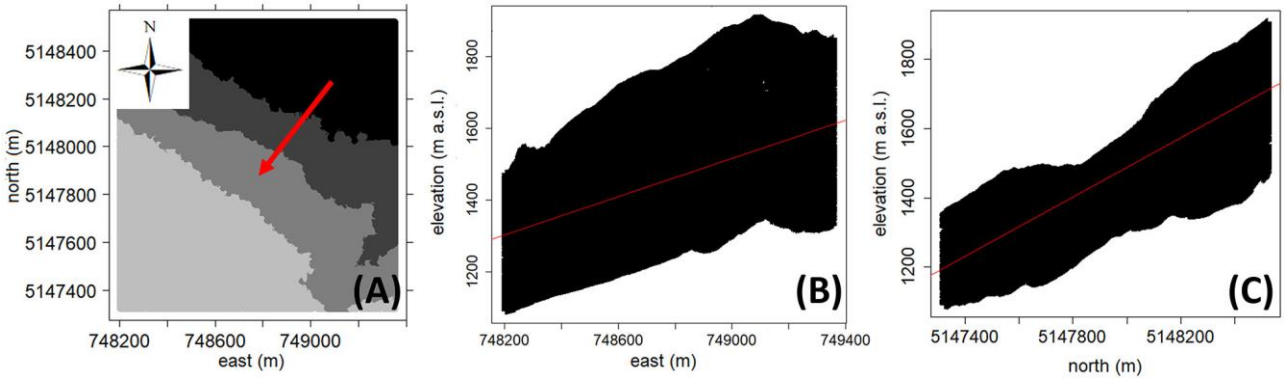

Fig. 2.4: Quantiles map of the variable elevation (the red arrow indicates the trend direction, which corresponds to the channel gradient) (A), scatterplot elevation values versus east coordinate (rho Pearson = 0.48; rho Spearman = 0.47) (B), and scatterplot elevation values versus north coordinate (rho Pearson = 0.82; rho Spearman = 0.84) (C).

2.3.3 Comparison of interpolation methods

The computed global accuracy measures for each interpolated DEM are summarized in Table 2.2. For both the chosen spatial resolutions, all the tested interpolation algorithms provide a comparable number of outliers (~1% of the vertical errors sample), which affect the standard accuracy measures. Moreover, all the vertical error sample distributions are non-normal (the only exception is the ANUDEM algorithm that yields a K^2 omnibus test p-value equal to 0.10 at the spatial resolution of 1.00 m). Overall, the median of the vertical errors is centimetric (smaller than ± 0.040 m), meaning that the interpolation vertical bias can be regarded as negligible. However, a closer look of the computed error medians reveals that only the ordinary kriging algorithm provides positive values (0.018 and 0.034 m at the spatial resolutions of 1.00 and 0.50 m respectively). Moreover, the ANUDEM and nearest neighbour algorithms yield the lowest median values at both the chosen spatial resolutions (respectively, -0.007 and -0.016 m at the spatial resolution of 1.00 m, and -0.016 and -0.006 m at the spatial resolution of 0.50 m), whereas the highest values are provided by the thin-plate spline plus tension (-0.031 m at the spatial resolution of 1.00 m) and ordinary kriging (0.034 m at the spatial resolution of 0.50 m) algorithms. NMAD values range from 0.288 to 0.429 m, and from 0.201 to 0.337 m at the spatial resolutions of 1.00 and 0.50 m respectively. At both the grid cell sizes, the thin-plate spline and multi-quadratic basis functions yield the lowest values (respectively, 0.288 and 0.288 m at the spatial resolution of 1.00 m, and 0.201 and 0.203 m at the spatial resolution of 0.50 m), whereas the ANUDEM and ordinary kriging algorithms show the lowest performance (i.e. the highest NMAD values, equal to 0.429 and 0.390 m at the spatial resolution of 1.00 m, and 0.347 and 0.337 m at the spatial resolution of 0.50 m, respectively). It must be noted that for all the tested gridding methods, the higher the spatial resolution of the interpolated DEM (i.e. the smaller the raster grid cell size), the smaller the corresponding NMAD value (i.e. the better the interpolation). This finding is in general agreement with that observed for example by Bater et al. (2009), who noticed an improvement on the interpolation algorithms performance as the spatial resolution of the generated DEMs increased from 1.50 to 0.50 m. However, the percentages of NMAD variation (i.e. how much an interpolator increases its prediction accuracy as the spatial resolution increases) change according to the considered gridding algorithm. In detail, the thin-plate spline and multi-quadratic basis functions exhibit the greatest percentages of NMAD variation (corresponding to 29.90 and 29.38%, respectively), where the ordinary kriging algorithm along with the inverse multi-quadratic basis function show the smallest ones (corresponding to 13.69 and 15.72%, respectively). It means that although all the tested interpolation algorithms improve their performance as the chosen raster grid cell size decreases, for some of them the choice of an optimal spatial resolution is a more critical concern. The 95% sample quantiles of the absolute vertical errors distributions range from 0.770 to 0.945 m, and from 0.738 to 0.945 m at the spatial resolutions of 1.00 and 0.50 m respectively. This statistic can be regarded as a robust measure of the maximum (unsigned) interpolation vertical error.

For both the chosen spatial resolutions, the thin-plate spline and multi-quadratic basis functions yield the lowest quantiles values (respectively, 0.770 and 0.778 m at the spatial resolution of 1.00 m, and 0.745 and 0.738 m at the spatial resolution of 0.50 m), along with the linear triangulation (0.777 m) and the natural neighbour algorithm (0.777 m) only at the spatial resolution of 1.00 m. Conversely, the ANUDEM and ordinary kriging algorithms perform worst (i.e. yield the highest sample quantile values, equal to 0.922 and 0.945 m at the spatial resolution of 1.00 m, and 0.802 and 0.945 m at the spatial resolution of 0.50m, respectively), along with the inverse multi-quadratic basis function (0.825 m) only at the spatial resolution of 0.50 m. It is worth pointing out that overall no significant differences in the computed accuracy measures are found among point and block ordinary kriging.

The supplementary DEMs quality measures along with the Global Moran's I index values are reported in Table 2.3. The MAE values range from 0.243 to 0.338 m, and from 0.184 to 0.329 m at the spatial resolutions of 1.00 and 0.50 m respectively. At both the grid cell sizes, the thin-plate spline and multi-quadratic basis functions yield the lowest MAE values (respectively, 0.243 and 0.248 m at the spatial resolution of 1.00 m, and 0.184 and 0.187 m at the spatial resolution of 0.50 m), whereas the ANUDEM and ordinary kriging algorithms show the lowest performance (i.e. the highest MAE values, corresponding to 0.338 and 0.329 m at the spatial resolution of 1.00 m, and 0.266 and 0.329 m at the spatial resolution of 0.50 m, respectively). The vertical error range is between 2.212 and 2.812 m, and between 1.327 and 2.597 m at the spatial resolutions of 1.00 and 0.50 m respectively. The lowest error ranges are provided by the thin-plate spline (2.212 and 1.907 m, at the spatial resolutions of 1.00 and 0.50 m respectively). Conversely, the ANUDEM and ordinary kriging algorithms return the highest range values at the spatial resolution of 1.00 m (respectively, 2.711 and 2.812 m), whereas the ordinary block kriging performs worst at the resolution of 0.50 m (2.597 m). Respect to the linear regression parameters, the intercept values are all negative at both the chosen spatial resolutions, with the worst results provided by the ANUDEM and ordinary kriging algorithms (approximatively -2.00 m). On the other hand, both the slopes and the weighted regression coefficients does not reveal noteworthy differences among the tested gridding methods, with all values equal to one. The analysis of the total drainage sink area points out a correspondence between the spatial resolution increment and the number of pits, irrespective to the gridding algorithm. The only exception is the ANUDEM algorithm, which also provides (as expected) the lowest number of sinks at both the chosen spatial resolutions (respectively, 3 and 2). Conversely, the multi-quadratic basis function performs worst (i.e. it yields the highest number of sinks) at both the grid cell sizes (respectively, 30 and 273). It must be noted that the increase in the total drainage sink area is not only related to the cell size halving, but also to an increment in the number of pits. In other words, the higher the spatial resolution, the higher the number of interpolation artefacts. This finding is clearly in contrast with the previous one. However, it should be noted that the vertical accuracy assessment on the interpolated DEMs has been carried out by comparing two points datasets (i.e. the RTK-GPS points and grid cells centres containing the GPS points themselves) that do not spatially overlap. Therefore, the better accuracy (i.e. the smaller NMAD values) of the finer gridded surfaces might be only due to the lower distances between the grid cell centre and the GPS validation point.

The analysis of the absolute errors spatial pattern by means of the visual inspection of choropleth symbol maps (Fig. 2.5) reveals that for all the tested interpolation algorithms the greatest (unsigned) vertical errors occur at breaks of slope (e.g. at the top of the banks) and in morphologically complex areas (e.g. in the upper part of the channel due to the presence of big boulders, and at the rock step located about 200 m downstream the initiation area (~1 500 m a.s.l.), Fig. 2.1B), regardless of both the points density of the dataset used during the interpolation procedure and the chosen raster grid cell size. Moreover, within the channel there are subtle differences among the different tested interpolation algorithms, and the spatial pattern of vertical errors visually appears to be random. However, a closer look of these maps highlights some local pockets of spatial dependence common to all the tested routine, as also confirmed by the Anselin local Moran's I index maps (Fig. 2.6).

The Global Moran's I index values range from 0.242 to 0.501, and from 0.329 to 0.583 at the spatial resolutions of 1.00 and 0.50 m respectively. It means that all the tested interpolation algorithms yield a considerable degree of error clustering, with the highest values provided by the ANUDEM and ordinary kriging algorithms (respectively, 0.466 and 0.501 at the spatial resolution of 1.00 m, and 0.531 and 0.583 at the spatial resolution of 0.50m). Noteworthy, for all the tested gridding methods, the higher the spatial resolution, the higher the degree of error clustering, with the highest percentages variation yielded by the thin-plate spline and multi-quadratic basis functions (35.44 and 40.86%, respectively).

	DEM resolution (m)	n. outliers (-)	median (m)	NMAD (m)	68.3% quantile (m)	95.0% quantile (m)	D'agostino K^2 test (p-value)*
Linear triangulation	1.00	27	-0.021	0.291	0.306	0.777	0.000
Natural neighbour	1.00	27	-0.021	0.291	0.306	0.777	0.000
IDP	1.00	27	-0.023	0.294	0.314	0.793	0.000
Nearest neighbour	1.00	23	-0.016	0.289	0.316	0.839	0.000
ANUDEM	1.00	20	-0.007	0.429	0.427	0.922	0.103
Completely regularized spline	1.00	26	-0.029	0.307	0.310	0.782	0.000
Thin-plate spline	1.00	30	-0.020	0.288	0.298	0.770	0.000
Thin-plate spline plus tension	1.00	26	-0.031	0.310	0.310	0.782	0.000
Multi-quadratic spline	1.00	26	-0.021	0.288	0.300	0.778	0.000
Inverse multi-quadratic spline	1.00	22	-0.026	0.339	0.351	0.840	0.000
Point ordinary kriging	1.00	21	0.018	0.390	0.406	0.945	0.000
Block ordinary kriging	1.00	21	0.018	0.390	0.406	0.945	0.000
Linear triangulation	0.50	35	-0.022	0.212	0.225	0.765	0.000
Natural neighbour	0.50	35	-0.022	0.212	0.225	0.765	0.000
IDP	0.50	37	-0.018	0.216	0.239	0.775	0.000
Nearest neighbour	0.50	26	-0.006	0.228	0.238	0.779	0.000
ANUDEM	0.50	24	-0.016	0.347	0.331	0.802	0.000
Completely regularized spline	0.50	32	-0.021	0.239	0.247	0.772	0.000
Thin-plate spline	0.50	41	-0.018	0.201	0.217	0.745	0.000
Thin-plate spline plus tension	0.50	31	-0.020	0.242	0.250	0.769	0.000
Multi-quadratic spline	0.50	40	-0.017	0.203	0.217	0.738	0.000
Inverse multi-quadratic spline	0.50	26	-0.023	0.286	0.302	0.825	0.000
Point ordinary kriging	0.50	21	0.034	0.337	0.406	0.945	0.000
Block ordinary kriging	0.50	21	0.034	0.337	0.354	0.898	0.000

Tab. 2.2: Global accuracy measures for each tested interpolation algorithm and chosen spatial resolution (the values refer to the errors distribution after the outliers removal).*

	DEM resolution (m)	MAE (m)*	error range (m)*	slope (-)*	intercept (-)*	wR^2 (-)*	n. pits (-)	Moran's I index (-)
Linear triangulation	1.00	0.252	2.237	1.000	-0.928	1.000	11	0.339
Natural neighbour	1.00	0.252	2.237	1.000	-0.928	1.000	11	0.339
IDP	1.00	0.256	2.351	1.000	-0.859	1.000	14	0.316
Nearest neighbour	1.00	0.261	2.461	1.000	-0.655	1.000	22	0.242
ANUDEM	1.00	0.338	2.711	1.000	-1.695	1.000	3	0.466
Completely regularized spline	1.00	0.262	2.346	1.000	-1.050	1.000	12	0.372
Thin-plate spline	1.00	0.243	2.212	1.000	-0.823	1.000	19	0.316
Thin-plate spline plus tension	1.00	0.263	2.343	1.000	-1.063	1.000	12	0.374
Multi-quadratic spline	1.00	0.248	2.369	1.000	-0.896	1.000	30	0.301
Inverse multi-quadratic spline	1.00	0.289	2.454	1.000	-1.211	1.000	6	0.378
Point ordinary kriging	1.00	0.329	2.812	1.000	-1.801	1.000	17	0.501
Block ordinary kriging	1.00	0.329	2.812	1.000	-1.802	1.000	17	0.501
Linear triangulation	0.50	0.198	2.037	1.000	-1.028	1.000	104	0.445
Natural neighbour	0.50	0.198	2.037	1.000	-1.028	1.000	104	0.445
IDP	0.50	0.204	2.048	1.000	-0.974	1.000	102	0.414
Nearest neighbour	0.50	0.214	2.295	1.000	-0.813	1.000	190	0.329
ANUDEM	0.50	0.266	2.246	1.000	-1.641	1.000	2	0.531
Completely regularized spline	0.50	0.214	1.988	1.000	-1.195	1.000	32	0.489
Thin-plate spline	0.50	0.184	1.907	1.000	-0.888	1.000	177	0.428
Thin-plate spline plus tension	0.50	0.216	2.01	1.000	-1.204	1.000	29	0.490
Multi-quadratic spline	0.50	0.187	1.955	1.000	-0.901	1.000	273	0.424
Inverse multi-quadratic spline	0.50	0.251	2.222	1.000	-1.311	1.000	21	0.472
Point ordinary kriging	0.50	0.329	1.327	1.000	-1.801	1.000	64	0.583
Block ordinary kriging	0.50	0.298	2.597	1.000	-1.962	1.000	64	0.583

Tab. 2.3: Supplementary DEM quality indices and global Moran'I index values for each tested interpolation algorithm and chosen spatial resolution (the values refer to the errors distribution after the outliers removal).*

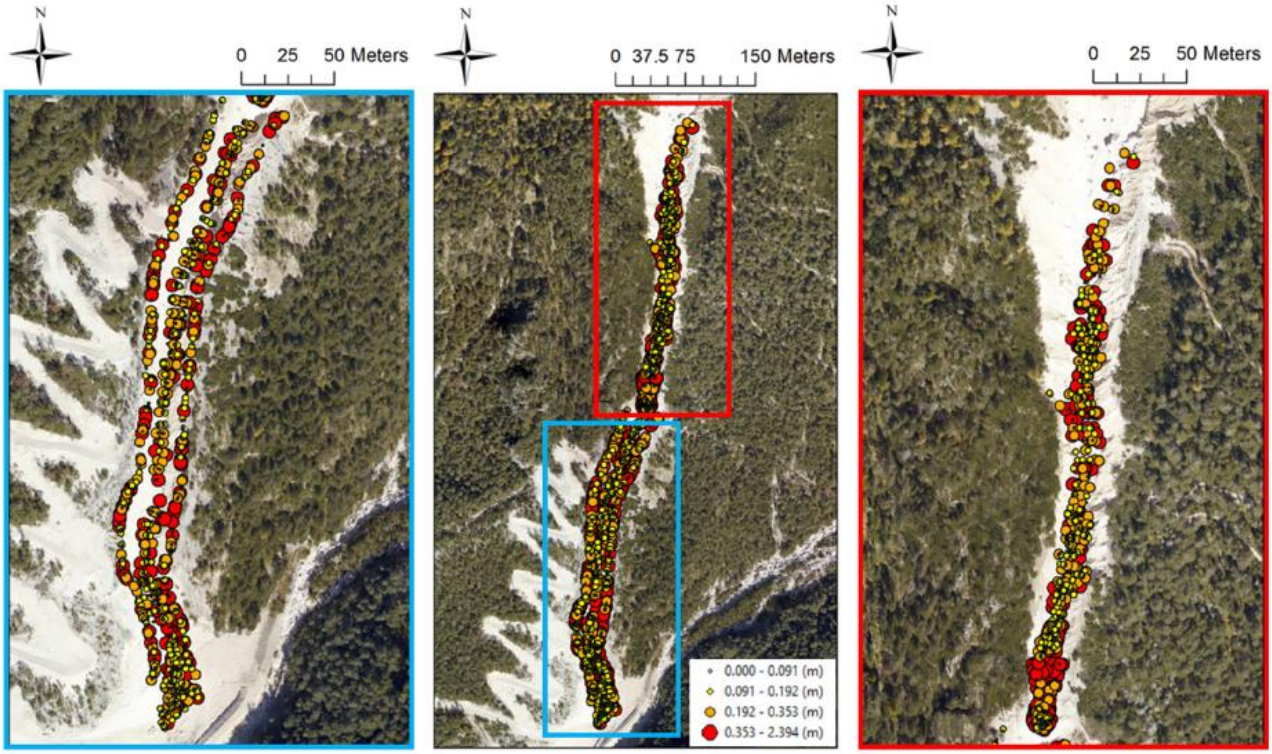

Fig. 2.5: Choropleth symbol map of the thin-plate spline function absolute errors at the spatial resolution of 1.00 m. Note that the greatest absolute errors mainly occur at the top of the banks and in the rough upper part of the channel. Within the channel the spatial pattern of errors appears to be "random".

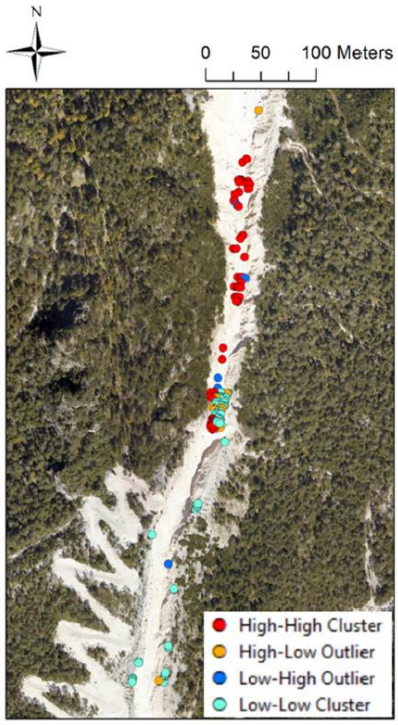

Fig. 2.6: Local Moran's I index map of the thin-plate spline function absolute errors at the spatial resolution of 1.00 m. Note the local clusters of high and low errors values, mainly located along the upper part of the channel where the topographic roughness is higher due to the presence of boulders and bank failures. Moreover, local outliers concentrate near the rock step at an altitude of about 1 500 m a.s.l..

The results of the interpolation algorithms robustness analysis in terms of NMAD and median of the vertical errors values variation on the basis of the sample density are summarized in Figure 2.7. The graphs of Figure 2.7A and Figure 2.7B can be divided in two distinct regions. The first region (continuous border line) includes the interpolation algorithms which are stable (or robust) in relation to the sample density (i.e. the NMAD value does not change as the number of points used in the interpolation procedure decreases). Conversely, the second one (dotted border line) includes the routines whose prediction accuracy changes according to the sample density (the only exception is the ANUDEM algorithm, which provides consistent NMAD values). Moreover, in the two delineated regions, the spread of the NMAD values for each sample density differs. As a matter of fact, in the first region the spread of the values is smaller than that of the values in the second one, meaning that the interpolators within the first region yield similar accuracy values at each sample density. For both the chosen spatial resolutions, the thin-plate spline and multi-quadratic basis functions yield the more consistent NMAD values, which are also the lowest for each sample density. They are followed by the TIN-based interpolation algorithms, and the inverse distance to a power method. Conversely, at both the grid cell sizes, the ordinary kriging algorithm and the inverse multi-quadratic radial basis function are the least robust interpolation algorithms, along with the completely regularized spline function (only at the spatial resolution of 0.50 m). Furthermore, the graphs of Figure 2.7C and Figure 2.7D highlight that all the tested gridding methods yield consistent vertical biases (i.e. the median of the vertical errors does not change with the sample density). The only exception is the ordinary kriging algorithm, which also provides positive median values (up to 0.10 m at a sample density equal to 50%). It is worth pointing out that at the lowest sample densities (i.e. 75 and 50%) the kriging algorithm performs worst in terms of both systematic and random vertical error. This evidence is clearly in contrast with what reported in McDonnell & Lloyd (2015), who stated that for irregular spatial fields as the sample density decreases the kriging algorithm outperforms deterministic interpolation methods.

The visual inspection carried out on the DEMs derivatives highlights that all the generated gridded surfaces contain noticeable interpolation artefacts (e.g. triangular facets, spiky features, striping effect, undulating, noisy or over-smoothed relief, and discontinuos spatial pattern of slope and curvature), regardless of both the points density of the dataset used during the interpolation procedure and the chosen raster grid cell size (Fig. 2.8). However, for the linear triangulation, natural neighbour, ANUDEM, completely regularized spline, thin-plate spline plus tension, and ordinary kriging algorithms, they do not prevent an overall satisfactory visual representation of the channel morphology. Conversely, the interpolators inverse distance to a power, nearest neighbour, and inverse multi-quadratic function yield overly noisy DEMs. Furthermore, despite their excellent overall statistical performance, also the thin-plate spline and multi-quadratic radial basis functions do not ensure a realistic representation of the study site topography due to function under- and over-shooting causing relevant spiky features in correspondence of slope discontinuities, both internally and externally to the channel area (Fig. 2.8A). This finding endorses the importance of integrating statistical and qualitative techniques when an interpolation algorithm performance analysis is undertaken, as suggested by a number of earlier studies (e.g. Wood & Fisher, 1993; Wood, 1996; Declercq, 1996; Desmet, 1997; Yang & Hodler 2000; Chaplot et al., 2006; Podobnikar, 2009; Setiawan et al., 2013). The multi-criteria morphological based comparison points out that the completely regularized spline and the thin-plate spline plus tension functions ensure the most realistic plano-altimetric representation of both longitudinal and transversal linear features, both channel bottom forms. Conversely, the ANUDEM and ordinary kriging methods prove the lowest shape reliability mainly due to surface over-smoothing, with slope discontinuities and channel bottom forms not well defined in the corresponding DEMs. Moreover, a meaningful striping effect perpendicular to the trend direction (i.e. along the considered variogram modeling direction) affecting the kriging-derived DEMs suggests that the methodology here followed to kridge the LiDAR points dataset does not represent a suitable procedure to interpolate DEMs for hydrological and hydraulic modeling (Fig. 2.8C). The linear triangulation and the natural neighbour algorithm perform in an intermediate position, with an overall realistic representation of channel features although the contours in some cases appear irregular or with spurious shapes. The results of the residual analysis carried out on the full dataset-derived 0.50 meters-resolution DEMs are shown (as an example) in Figure 2.6S of the supplementary material. It turns out that the ANUDEM algorithm has the lowest ability to fulfill the topographic sampled data, followed by the ordinary kriging algorithm. On the other hand, no significant differences in the ability of honouring the sampled topographic data are detected among the remaining tested gridding methods.

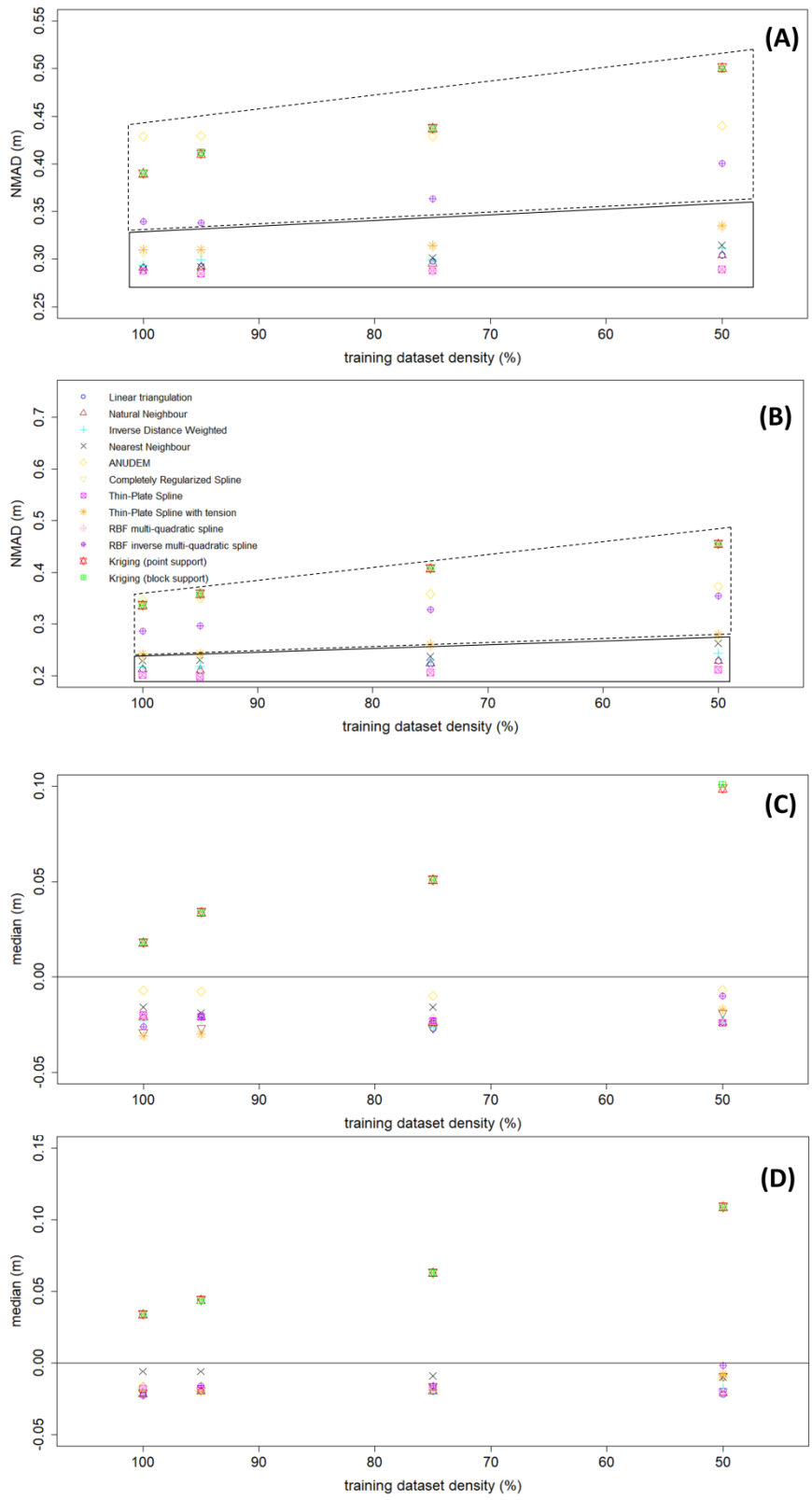

Fig. 2.7: NMAD values variation as a function of the sample density (A, spatial resolution equal to 1.00 m, and B, spatial resolution equal to 0.50 m). Median values variation as a function of the sample density (C, spatial resolution equal to 1.00 m, and D, spatial resolution equal to 0.50 m).

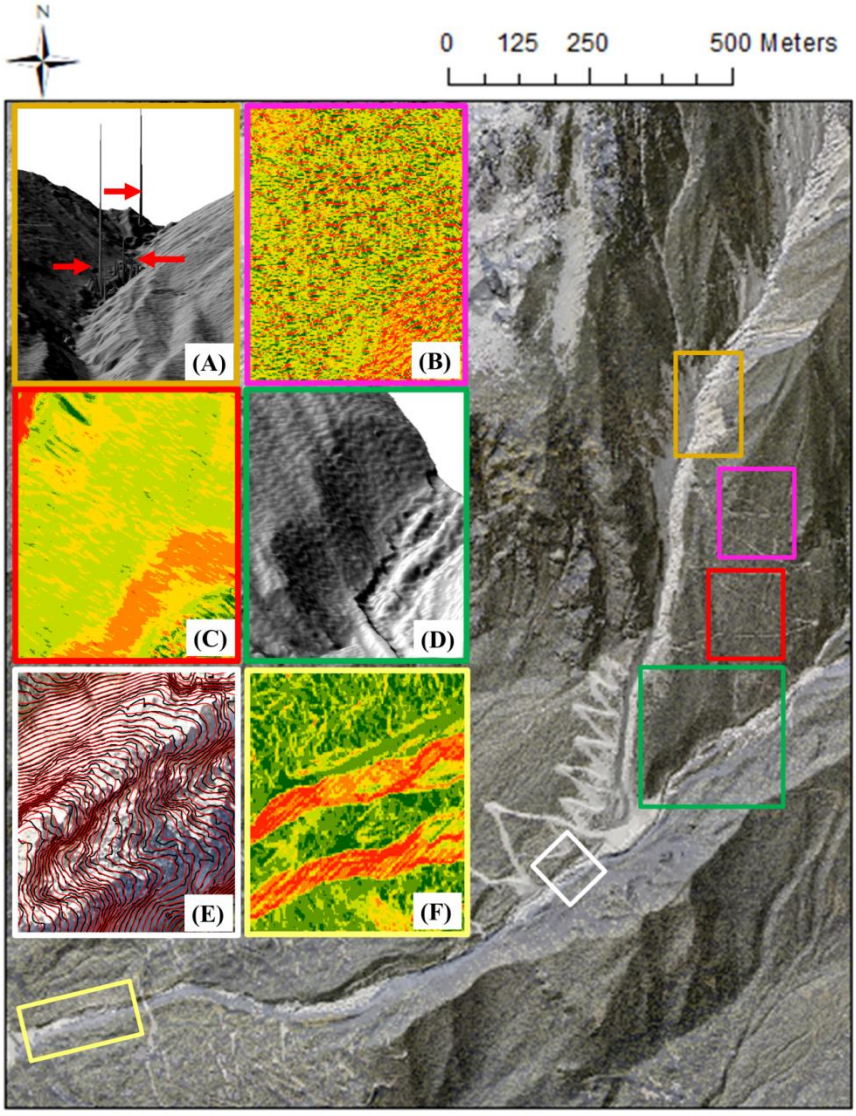

Fig. 2.8: Overview of the interpolation artefacts: A) spiky features in the upper part of the debris flow channel due to function under- and over-shooting at slope discontinuities, B) noisy relief with discontinuos spatial pattern of slopes, C) striping effect oriented according to the direction of variogram modeling, D) undulating surface, E) over-smoothed surface (red: ANUDEM contour lines, black: natural neighbour contour lines), F) striping effect oriented according to the sample direction.

2.3.4 Effects of gridding techniques on debris flow routing modeling

For the two modelled event scenarios (i.e. 50 and 300 years return periods), the results of the global (i.e. at the channel extent) correlation analysis between the pixel-wise standard deviation of the twelve full dataset-derived 1-meter resolution DEMs heights, and the pixel-wise standard deviation of the corresponding twelve simulated erosion/deposition depths are summarized in Figure 2.9A and Figure 2.9B, respectively. For both the event scenarios, the Pearson's and the Spearman's rank correlation coefficient approach similar low values, respectively equal to 0.13 and 0.21 (i.e. about 15-20% of the perfect positive correlation between the two analysed variables). Only a slight improvement in the correlation strength is noted using the 50% thinning-derived 1-meter resolution DEMs in the model runs (Fig. 2.9C and Fig. 2.9D). Furthermore, also the moving windows correlation analysis does not emphasize a strong spatial link between cells with high uncertainty in the simulated erosion/deposition depths and those with high uncertainty in the input topographic data (Fig. 2.10), regardless of both the magnitude of the modelled event scenario and the points density of the dataset used during the interpolation procedure.

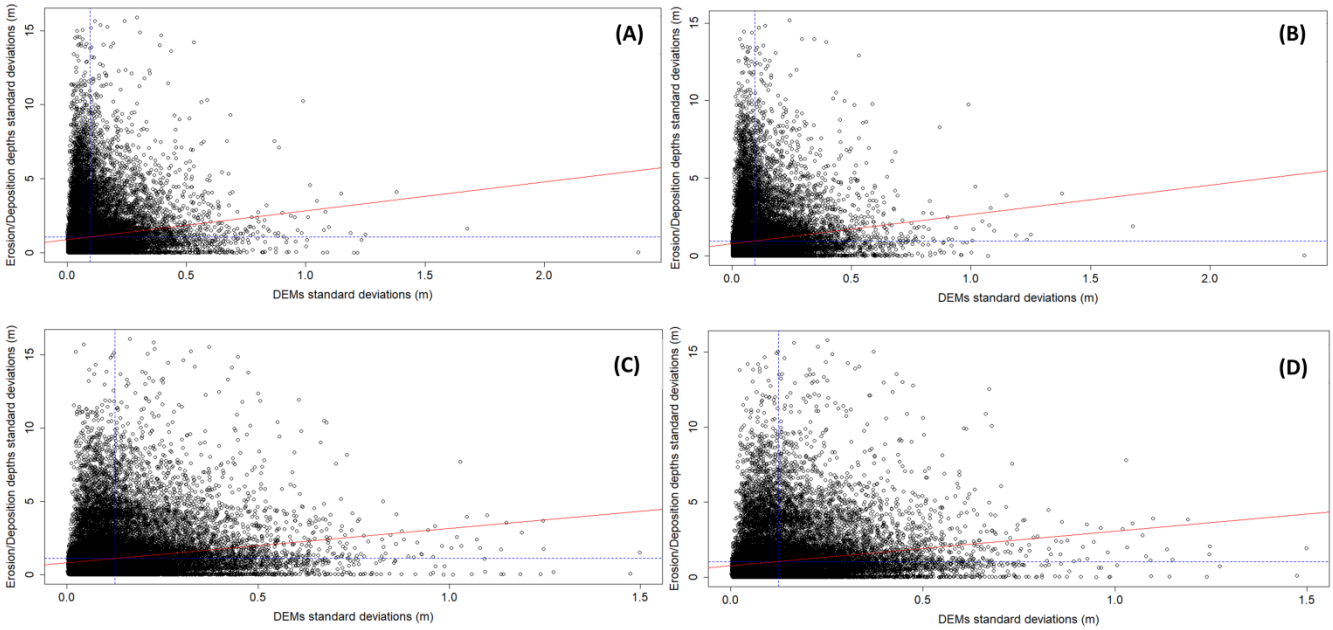

Fig. 2.9: *Scatterplot of the pixel-wise standard deviations of the twelve 1-meter resolution DEMs heights and the pixel-wise standard deviation of the corresponding twelve simulated erosion/deposition depths: (A) full dataset-derived DEMs and 300-year return period (rho Pearson = 0.126, rho Spearman = 0.205), (B) full dataset-derived DEMs and 50-year return period (rho Pearson = 0.129, rho Spearman = 0.208), (C) 50% thinning-derived DEMs and 300-year return period (rho Pearson = 0.167, rho Spearman = 0.252), and (D) 50% thinning-derived DEMs and 50-year return period (rho Pearson = 0.172, rho Spearman = 0.256). The continuous red line corresponds to the linear regression line, whereas the dotted blue lines correspond to the marginal mean of the two correlated variables.*

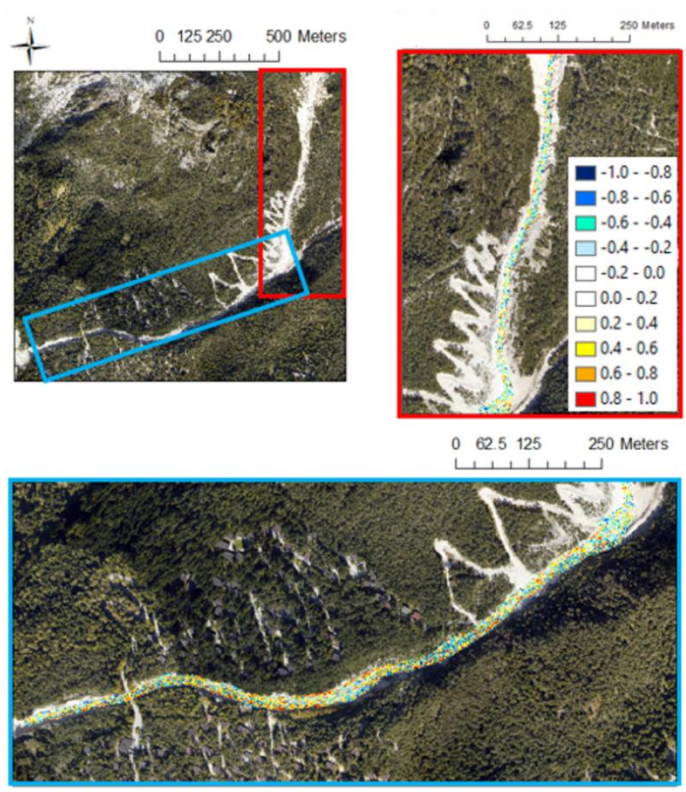

Fig. 2.10: 5x5 moving windows Pearson's correlation coefficient between the pixel-wise standard deviations of the twelve 50% thinning-derived 1-meter resolution DEMs heights and the pixel-wise standard deviation of the corresponding twelve 50-year return period simulated erosion/deposition depths.

For the 50% thinning-derived 1-meter resolution DEMs, we report (as an example) the 50-year return period run results, in terms of simulated erosion/deposition areas and volumes (Tab. 2.4), solid-liquid discharges (Fig. 2.11), and channel morphology after the event (Fig. 2.12). Overall, the results do not highlight a noteworthy change depending on the used topographic surface, regardless of both the magnitude of the scenario and the points density of the dataset used during the interpolation procedure. In detail, in Table 2.4 the spread of the simulated flooded area values is smaller than 2 000 m^2 (i.e. smaller than 10% of the mean of all the simulated flooded area values), whereas for the simulated erosion and deposition areas it corresponds to 854 m^2 (i.e. 7% of the mean of all the simulated erosion area values) and 1 191 m^2 (i.e. 6% of the mean of all the simulated deposition area values), respectively. Similarly, the spread of the simulated erosion and deposition volume values is equal to 6 166 m^3 (i.e. 14% of the mean of all the simulated erosion volume values) and 3 217 m^3 (i.e. 13% of the mean of all the simulated deposition volume values), respectively. Clearly, these differences can be regarded as negligible when the cell model is used at forecasting purposes, or to identify the areas mainly subjected to large erosion and deposition phenomena. The solid-liquid hydrographs shown in Figure 2.11 relate to two cross-sections located in the upper part of the channel, just downstream the triggering area of the Rovina di Cancia debris flow. All the hydrographs show a comparable well-defined triangular shape with similar values of peak discharge, time to peak, and duration. It means that the dynamic of the simulated flow is not strongly influenced by the topographic uncertainty due to the different tested interpolation algorithms. This finding is also confirmed by the cross-section profiles of the pre- (continuous line) and post-event (dotted lines) DEMs shown in Figure 2.12. The reported cross-section profiles are representative of a channel reach mainly subject to erosion processes (Fig. 2.12A), deposition processes (Fig. 2.12B), and mixed erosion and deposition processes (Fig. 2.12C). For all the cross-sections, the DEMs profiles do not highlight meaningful differences in the channel morphology after the event. Even more important, the observed small differences in the erosion and deposition profiles do not appear to be linked to the profiles variability of the input DEMs.

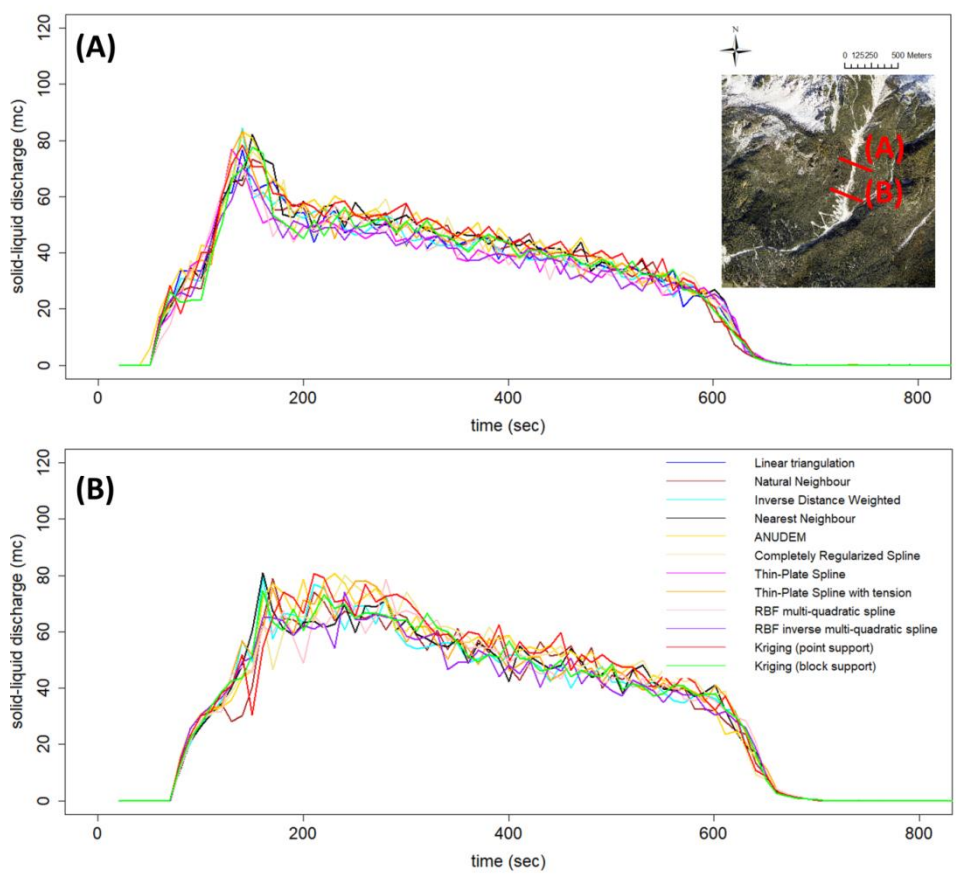

Fig. 2.11: Comparison of the simulated debris flow solid-liquid hydrographs (A, upstream section, and B, downstream section).

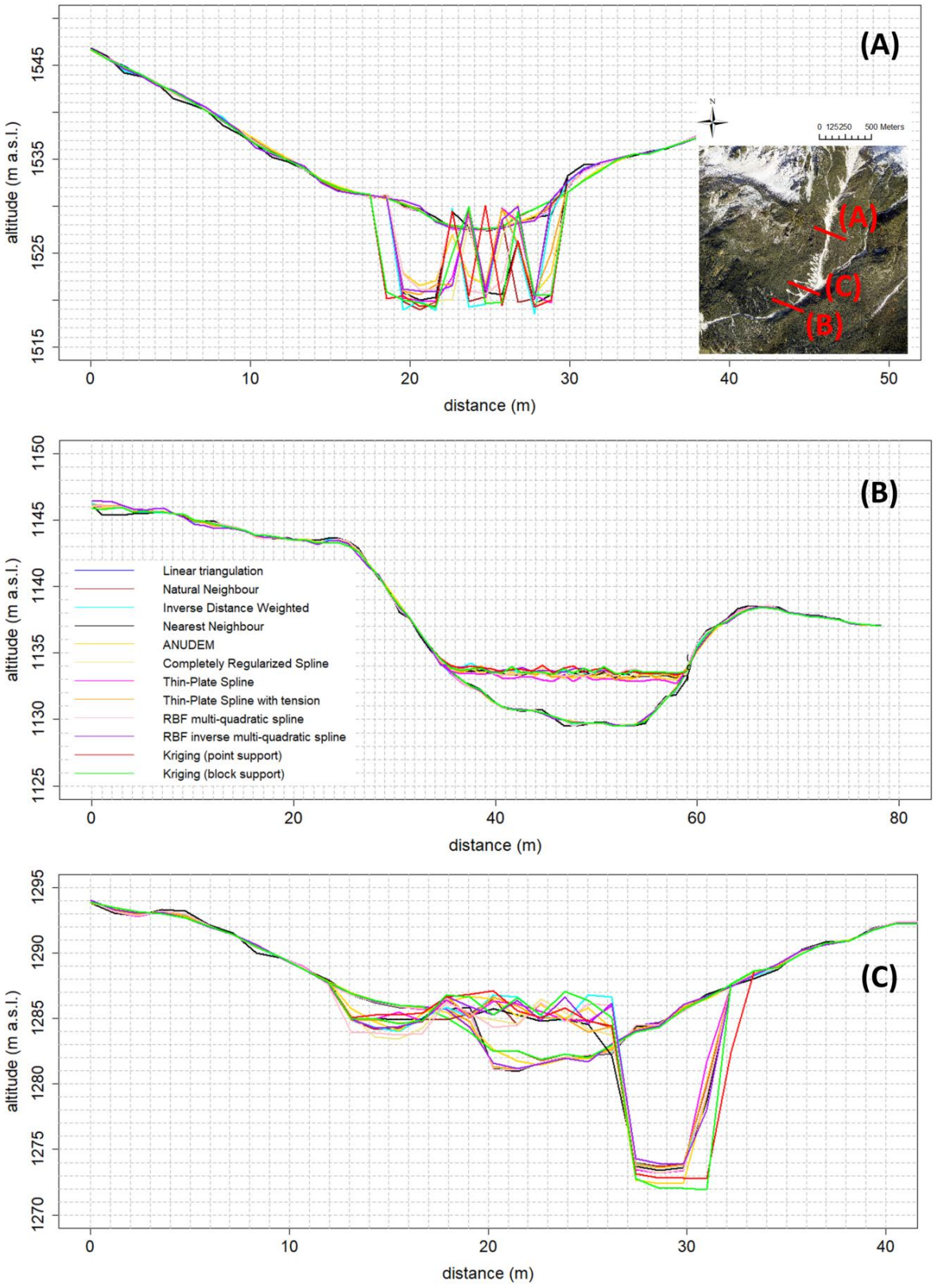

Fig. 2.12: Comparison of the pre- (continuous lines) and post-event (dotted lines) DEMs cross-section profiles (erosional (A), depositional (B), and mixed erosional-depositional reach (C) of the Rovina di Cancia debris flow channel).

	Flooded area (m^2)	Erosion area (m^2)	Deposition area (m^2)	Erosion volume (m^3)	Deposition volume (m^3)
Linear triangulation	30 525.00	11 850.00	18 675.00	-42 041.18	24 300.35
Natural neighbor	30 574.00	11 862.00	18 712.00	-41 672.18	24 265.99
IDP	31 050.00	11 911.00	19 139.00	-44 062.71	25 315.81
Nearest neighbor	30 515.00	11 748.00	18 767.00	-42 104.00	24 376.84
ANUDEM	30 233.00	11 990.00	18 243.00	-42 796.95	22 933.06
Completely regularized spline	30 788.00	11 956.00	18 832.00	-44 627.68	24 732.76
Thin-plate spline	29 885.00	11 519.00	18 366.00	-40 776.85	23 228.63
Thin-plate spline plus tension	30 313.00	11 769.00	18 544.00	-41 283.94	23 278.35
Multi-quadratic spline	30 544.00	11 905.00	18 639.00	-42 873.98	24 501.13
Inverse multi-quadratic spline	31 338.00	12 292.00	19 046.00	-45 422.73	25 621.91
Point ordinary kriging	31 807.00	12 373.00	19 434.00	-46 715.08	26 150.98
Block ordinary kriging	31 630.00	12 315.00	19 315.00	-46 943.16	26 002.85

Tab. 2.4: 50% thinning-derived 1-meter resolution DEMs model run results (50-year return period).

2.4 Conclusions

In this study we compared the performance of twelve gridding algorithms (i.e. linear triangulation, natural neighbour, nearest neighbour, inverse distance to a power, ANUDEM, completely regularize spline function, thin-plate spline function, thin-plate spline plus tension function, multi-quadratic function, inverse multi-quadratic function, point ordinary kriging, and block ordinary kriging) in building DEMs with the complex topography of a debris flow channel located in the Venetian Dolomites. After that, we paid special attention in assessing the relationship existing between the digital elevation uncertainty due to the use of the different tested interpolation methods and the uncertainty on the results of a GIS-based cell model for simulating stony debris flows routing.

The investigation carried out on the performance of the tested interpolation algorithms highlighted that the ordinary kriging, applied according to the followed methodology (i.e. employing a theoretical variogram model fitted on the directional empirical one computed perpendicularly to the linear trend), is inadequate in reproducing the complex topography of the debris flow channel. In fact, it has demonstrated an overall unsatisfactory statistical performance, a low robustness, and a poor shape reliability. Also the ANUDEM algorithm has exhibited an overall unsatisfactory performance (from both the quantitative and qualitative point of view), despite it represents the only tested interpolation method specifically intended for digital terrain modeling. Conversely, the thin-plate spline function proved to be the most accurate and stable interpolation algorithm, along with the multi-quadratic radial basis function. However, they have demonstrated a low ability in faithfully representing the shape of the channel, mainly due to function under- and over-shooting causing relevant spiky features in correspondence of slope discontinuities. This lead to the conclusion that when the absolute accuracy of DEM elevation values is the most important feature, these algorithms could represent the best choice also in natural landscapes featuring a high morphological complexity. On the other hand, when also the realistic representation of surface shape is important, the linear triangulation, the natural neighbour algorithm, and the thin-plate spline plus tension and completely regularized spline basis functions could represent a better choice, since they ensure a proper trade-off among accuracy and shape reliability.

The evaluation of the effects of gridding techniques on debris flow routing modeling revealed that the correlation between the uncertainty in the cell elevations due to the different tested interpolation methods and the uncertainty in the corresponding simulated erosion/deposition depths was weak, regardless of both the magnitude of the modelled event scenario and the points density of the dataset used during the interpolation procedure. Also the results of the different model runs in terms of simulated areas, erosion and deposition volumes, solid-liquid discharges, and channel morphology after the event did not highlight a significant change in the model behaviour depending on the used topographic surface. This leads to the conclusion that the choice of the interpolation algorithm does not represent a determining factor for debris flows routing modeling.

The extrapolation of this conclusion must be done with care at least for two reasons. In fact, the investigation was performed on a channelized-debris flow, whose flow depths are larger than the DEMs height uncertainty resulting from the interpolation procedure. So, future researches have to be carried out in order to test the influence of the gridding algorithms on non-channelized debris flows, since in this case small interpolation errors might have a greater impact on the dynamic of the simulated flow, and thus on the resulting erosional/depositional pattern. Furthermore, also the use of different rheological models and/or sediments erosion and deposition process schematizations might lead to different conclusions. Therefore, in order to confirm the finding of this paper more work has to be done also by testing different debris flow routing models.

Supplementary material

In recent years, the topic of spatial data interpolation has attracted a lot the scientific research within the GIS community (Weng, 2006; Chaplot et al., 2006, Hengl & Reuter, 2009). As a matter of fact, a number of previous authors have investigated several gridding routines, by following different methodologies and obtaining varying results. In the following, a brief review of the main contributions related to this research issue is outlined.

Focusing on top soil erodibility k-values and mean annual hours of sunshine data, Declercq (1996) compared the performance of the piecewise polynomials, quadratic and cubic splines, Delaunay triangulation with linear interpolation, nearest neighbor algorithm, inverse distance to a power method, and block kriging without drift. His original datasets consisted of 878 soil borings k-values acquired in an area of 30 by 90 km in northern Belgium, and 532 values of mean annual hours of sunshine collected by meteorological stations throughout the European Union, respectively. In order to validate the predictive accuracy of the tested gridding algorithms, Declercq (1996) employed the split-sample technique by omitting during the interpolation procedure 110 and 152 sampled k-values and sunshine data, respectively. Therefore, since interpolation methods with a similar statistical accuracy can generate quite different spatial patterns, the author evaluated the so-called “spatial pattern fidelity”, which he defined as the ability of an interpolated model to preserve the regional and local spatial patterns of the sampled values. Finally, he assessed the suitability of the selected gridding methods by considering the amount of processing time needed. The research highlighted that the piecewise polynomials, the splines, and the linear triangulation are not recommendable, since highly inaccurate values and erratic models could be produced in poorly informed regions or with abruptly changing values. On the other hand, the linear distance weighting does not accurately predict the local spatial patterns, since it gives too little weight to the immediate surroundings of a grid cell center. Conversely, the squared distance weighting and the kriging algorithm perform well in terms of both accuracy and spatial patterns prediction.

By analyzing the effects of the interpolation errors on DEMs analysis, Desmet (1997) evaluated the performance of a suite of gridding methods for a small arable field located in the Belgian Loess Belt. The studied interpolation routines include the piecewise polynomials, a simplified thin-plate spline function, the linear triangulation, the inverse distance to a power method, and the block kriging without drift. His original dataset consisted of 1,044 irregularly spaced ground points collected by means of an automatic theodolite, within a study area of 3.5 ha (mean point density equal to 300 points ha-1). In order to evaluate the accuracy of the tested algorithms, during the interpolation procedure Desmet (1997) omitted respectively 50,100, and 200 points from the original dataset, and computed the root mean square error, the mean absolute error, and the standard deviation of error as precision measures. Therefore, by considering that the smoothness of the selected land surface had to be correctly represented in the interpolated DEMs, the author performed a shape reliability analysis both by examining the spatial pattern of the generated maps, both by cross-sections profiling. The author concluded that, at least for smooth surfaces, the distance-weighted methods (i.e., the kriging and the inverse distance to a power algorithms) are not able to reproduce the actual surface morphology. On the other hand, the thin-plate spline interpolation performs best in terms of both precision and shape reliability, even if the extrapolation of this conclusion must be done with care due to the extremely smooth topography of the selected study area.

In an attempt to provide more useful insights into the performance of different interpolation methods, Yang & Hodler (2000) compared five surface modelling algorithms by using a set of integrative criteria. They include the absolute and relative statistical accuracy, the visual pleasantness and faithfulness of the generated surfaces, the sensitivity respect to changes in sample size and searching condition, and the computational intensity. The compared methods include the Delaunay triangulation with linear interpolation, the minimum curvature function, the inverse distance to a power method, the multi-quadratic radial basis function, and the point kriging without drift. Their original datasets consisted of respectively 201 and 504 elevation points, irregularly sampled from a 1:24 000 USGS topographical map (Stone Mountain area, Georgia, United States). They concluded that the multi-quadratic radial basis function proved to be statistically the best, with also a visual performance similar to that of the minimum curvature function and the point kriging without drift. However, they pointed out that being the multi-quadratic radial basis function highly sensitive respect to changes in the sample size, it should be used with caution.

Focusing on a geologically uniform 50-hectare gully area in the Arnhem Land (Australia), Hancock (2006) examined the differences in the catchment geomorphology and hydrology as a result of the kriging and linear triangulation interpolation of a photogrammetrically-derived point cloud. In order to assess the influence of the selected gridding methodology on the catchment properties, the author used both qualitative (i.e., visual inspection of pseudo-3D projection of DEMs, and cross-sections profiling) both quantitative (i.e., area-slope relationship, hypsometric curve, cumulative area distribution, width function, Strahler network convergence, and optimal channel network energy) measures. Furthermore, given the potential impact of the interpolation errors on numerical models output, Hancock (2006) employed the generated gridded surfaces in a long-term landscape evolution model. In detail, he analyzed the geomorphological and hydrological differences in the two input DEMs after a 50,000 years modelled period. The author concluded that both the kriging and the linear triangulation algorithm can be used with confidence for gridding elevation data, provided that the irregularly spaced point values are of good quality.

By investigating the performance of varying gridding algorithms on three natural landscapes and at nested spatial scales (i.e., catchment, hillslope, and micro-plot), Chaplot el al. (2006) evaluated the performance of the inverse distance to a power method, the point kriging without drift, the point kriging with a full second-order polynomial drift, the multi-quadratic radial basis function, and the completely regularized spline. In order to evaluate the effects of the sampling density on interpolation accuracy, they decimated the original datasets according to different equivalent sampling distances. Therefore, for each generated dataset, the authors assessed the prediction accuracy via split-sample method, by using the mean error as a measure of bias and the root mean square error as a global accuracy measure. In addition, t-tests for dependent samples were performed to evaluate the significance of the differences between the estimated and observed heights at randomly chosen validation points. Chaplot el al. (2006) conclude that, irrespective of the surface area, landscape morphology and sampling density, few differences exist between the tested interpolation techniques, provided that the sampling density is high. In contrast, at lower sampling densities the performance of the tested techniques tends to be vary, with the kriging algorithm which overall exhibits the greatest range of applicability.

By evaluating the error associated with LiDAR-derived DEMs interpolation, Bater et al. (2009) examined seven surface modelling routines by using small footprint LiDAR data collected on Clayoquot Sound (Vancouver Island, British Columbia, Canada). The selected gridding methods include the Delaunay triangulation with linear, quintic and natural neighbor interpolation, the regularized spline and the thin-plate spline with tension methods, the ANUDEM algorithm, and the inverse distance to a power method. Their original dataset consisted of 4,500,000 LiDAR ground points, within a study area of 4 by 7 km (mean ground point density equal to 0.15 points m-2). Bater et al. (2009) produced a total of 48 DEMs, by using spatial resolutions of 0.5, 1.0, and 1.5 m according to the Whittaker-Shannon sampling theorem. Therefore, following a split-sample approach similar to that of Decqlerq (1996), the authors validated the predictive ability of the tested algorithms by using the mean error as a measure of bias and both the root mean square error and the mean absolute error as a measure of global accuracy. The research concluded that overall the natural neighbor interpolation must be favored for its ease of use, simple parametrization, generally smooth and visually appealing surfaces, consistent accuracy, and conservative predictions. On the other hand, the ANUDEM, the triangulation with quintic interpolation, and the thin-plate spline with tension algorithms might provide good alternatives.

By investigating the magnitude and spatial pattern of DEMs vertical error, Erdogan (2009) compared four commonly used interpolation algorithms focusing on a rocky hill area near the Afyon Kocatepe University (Turkey). The selected interpolation routines include the multi-quadratic radial basis function, the inverse distance to a power method, the thin-plate spline algorithm, and the point kriging without drift. His original dataset consisted of 24,000 ground locations sampled at regular 2, 4, 10, and 20 m intervals, within a 120,000 m² study area. In order to compare the accuracy of the tested gridding algorithms, Erdogan (2009) computed the mean error, the maximum and minimum error, and the root mean square error indices through the “leave one-out” cross-validation technique. Therefore, he examined the robustness of the selected interpolation routines via split-sample method (by decimating the raw datasets at densities corresponding to 95, 75, and 50%), and performed a jack-knifing by means of an independent set of 173 irregularly spaced surveyed validation points. Finally, since the spatial distribution of DEMs error usually shows some form of spatial clustering, Erdogan (2009) investigated the extent of error clustering through the use of choropleth symbol maps,

prediction error surfaces, and both global (i.e., Moran's I and Getis Ord Gi* indexes) and local (i.e., LISA and Getis Ord Gi* indexes) autocorrelation measures. The author concluded that the inverse distance to a power method cannot provide a realistic digital representation of hilly areas, mainly due to its inability in modelling the steep surfaces common in such a morphology. On the other hand, the thin-plate spline algorithm is the most appropriate, stable and effective along with the multi-quadratic radial basis function.

By assessing the influence of the survey strategy and gridding methodology on DEMs quality, Heritage et al. (2009) compared five different interpolation routines focusing upon a gravel point bar on the River Nent (North Pennine uplands, Cumbria, UK). The selected gridding algorithms include the inverse distance to a power method, the point kriging without drift (by using both the default variogram option available in Surfer™, both a model fitted on the experimental variogram of the surveyed data), the minimum curvature function, and the Delaunay triangulation with linear interpolation. The gridding methods were tested by using topographic data acquired through an EDM theodolite, according to seven different sampling strategies (i.e., cross sections, bar outline only, bar and chute outline, bar and chute outline with spot heights, and aerial LiDAR equivalent derived from degraded terrestrial laser scans). In order to assess the accuracy of the generated DEMs, Heritage et al. (2009) acquired a second more accurate control surface through a terrestrial laser scanner, which allowed them to statistically analyze the DEMs vertical error and its spatial variation by means of digital elevation models of elevation difference. They concluded that the triangulation with linear interpolation using bar and chute outline with spot heights or aerial LiDAR data represent the best overall combinations in fluvial environments.

Focusing on four hydraulically different mountain streams located in the southern part of New Zealand's North Island, Schwendel et al. (2012) examined 0.10 meters-resolution DEMs created by using seven interpolation algorithms. The selected gridding routines include the Delaunay triangulation with linear and natural neighbour interpolation, the point kriging without drift, the point kriging with linear drift, the multi-quadratic radial basis function, the modified Shepard's method, and the inverse distance to a power method. The selected gridding methods were applied by using topographic data acquired through a differential GPS system (operating in RTK mode), according to a terrain sensitive sampling strategy. Their original datasets consisted of average point densities between 0.6 and 11.7 points m-2, within study areas between 132 and 2,438 m^2. During a pre-selection phase, Schwendel et al. (2012) qualitatively examined DEMs-derived shaded relief models and contour maps in order to exclude from further analysis the interpolation methods that did not reach a minimum level of realistic surface representation. Therefore, the authors tested the reduced number of interpolation methods by undertaking a morphological criteria-based comparison. Furthermore, they performed a residual analysis by using the mean error, the error standard deviation, and the mean absolute error as DEMs quality measures. They concluded that, when it is crucial that surfaces are represented as realistic as possible (e.g., for morphological budgeting purposes), the triangulation with linear interpolation is the most suitable and consistent gridding method in a range of streambed environments.

Focusing on two different tillage plots (namely, bench terraces and furrows) both located in the Wonosobo District (Central Java Province, Indonesia), Setiawan et al. (2013) compared the Delaunay triangulation with linear and natural neighbour interpolation, the nearest neighbour algorithm, the minimum curvature function, the inverse distance to a power method, the multi-quadratic radial basis function, and the point kriging without drift. Following a split-sample approach similar to that of Decqlerq (1996), Setiawan et al. (2013) assessed the accuracy of the tested algorithms using the mean error as a measure of bias and the error standard deviation as a global accuracy measure. Furthermore, the authors incorporated in the quantitative assessment both the weighted coefficient of determination and the intercept value of the linear regression between measured and interpolated values, both the total area of sink drainage as an indicator of spatial error. Finally, they visually examined the shape similarity of the interpolated DEMs by means of 3D views of shaded relief models and cross-sections profiling. They concluded that any interpolation method that is overdoing the smoothing process (e.g., the ordinary kriging algorithm or the multi-quadratic radial basis function) cannot provide optimum results in the case of discontinuous surfaces. Conversely, the linear triangulation and the natural neighbor interpolation show better performance, despite their simpler mathematical conceptualization.

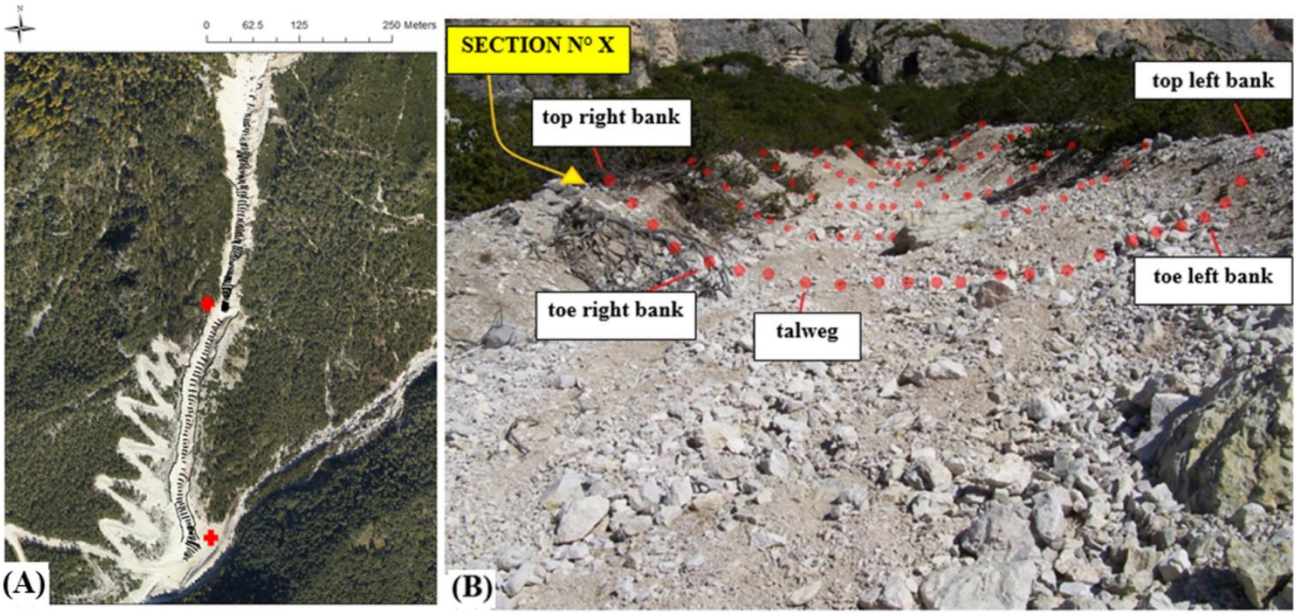

Fig. 2.1S: A) Overview of the GPS validation points collected along the upper part of the Rovina di Cancia channel (red marks on the base stations). B) Schematic representation of the adopted cross-sections, morphological-guided spatial sampling scheme.

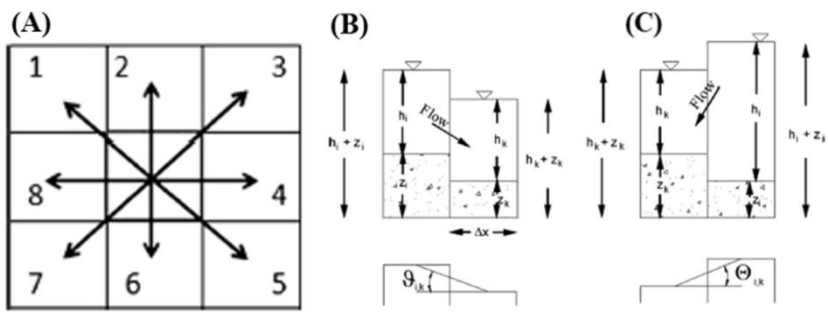

Fig. 2.2S: The eight possible flow directions (A), and the adopted hydraulic links between two neighbouring cells in the case of positive (B) and negative (C) slopes (Gregoretti et al., 2018).

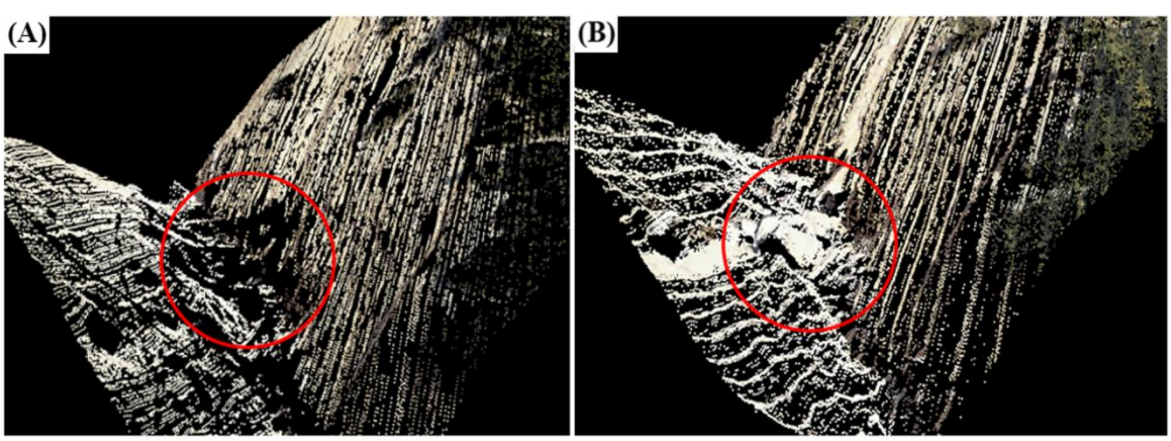

Fig. 2.3S: Example of classification error (omission error) along the triggering area of the Rovina di Cancia channel. A) 3D view of the delivered ground LiDAR points. B) 3D view of the delivered non-ground LiDAR points. Red mark on big boulders located within the channel.

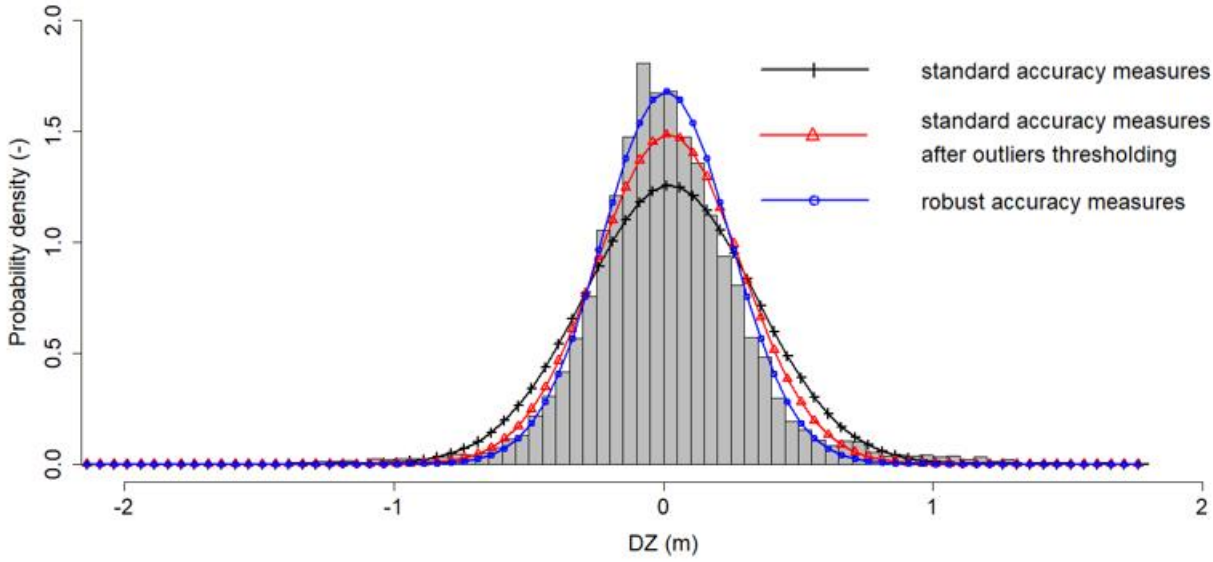

Fig. 2.4S: Histogram of the errors sample. Superimposed are the normal distribution curves with mean and standard deviation computed through one of the three employed approaches. Note the different degree of fitting of the curves near the mean and at the tails. ΔZ denotes the vertical error.

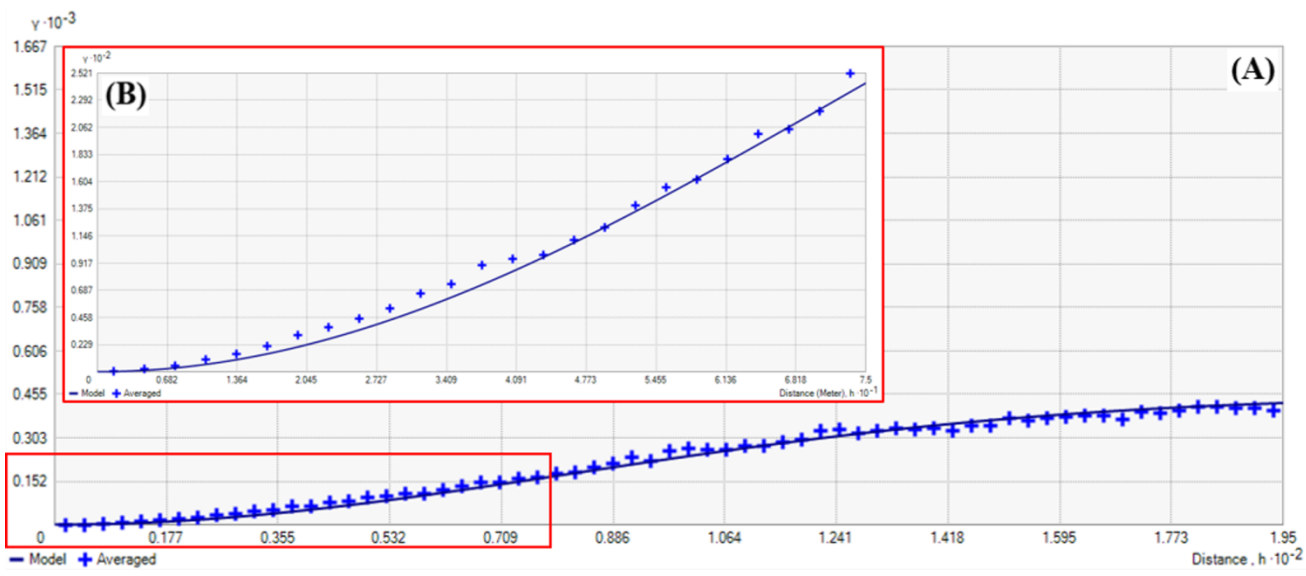

Fig. 2.5S: A) Empirical variogram computed perpendicularly to the channel gradient with overlying the fitted Gaussian theoretical model. B) Detail of the computed empirical and theoretical function near the origin.

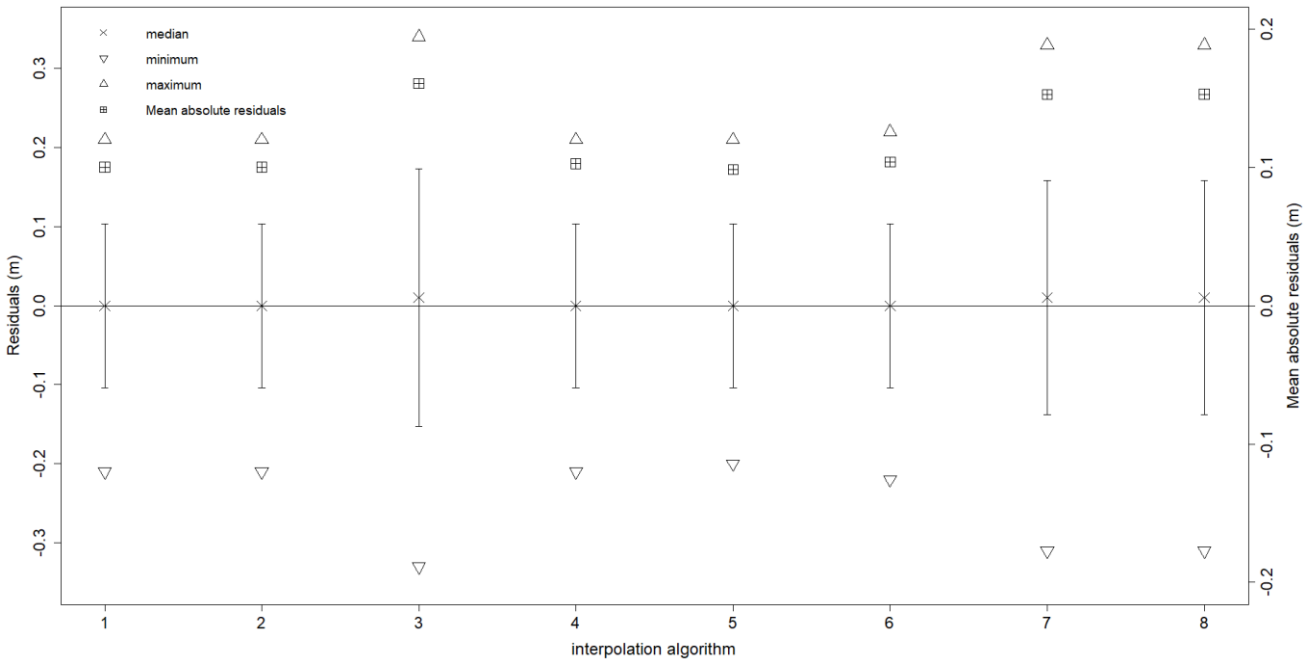

Fig. 2.6S: Residual analysis results (1: Linear triangulation, 2: natural neighbour, 3: ANUDEM, 4: Completely regularized spline, 5: Thin-plate spline plus tension, 6: Kriging (point support), 7: Kriging (block support)).

Parameter	**Value**
Maximum Measurement Range	2100-3200 m @ laser power level = 50% and PRR = 400 KHz (at natural target reflectivity ≥ 20%)
Minimum Range	50 m
Maximum Operating Flight Altitude Above Ground Level	2600 m @ laser power level = 50% and PRR = 400 KHz (at natural target reflectivity ≥ 60%; max scan angle = 60°; additional roll angle ± 5°)
Range Accuracy	20 mm @ 250 m range (1σ)
Range Precision	20 mm @ 250 m range (1σ)
Laser Pulse Repetition Rate (PRR)	up to 400 KHz
Effective Measurement Rate	up to 266 KHz @ 60° scan angle
Laser Wavelength	near infrared
Laser Beam Divergence	≤ 0.25 mrad (corresponding to an increase of 0.25 m of beam diameter per 1000 m distance)
Number Of Targets Per Pulse	digitized waveform processing (limited only by the maximum data rate allowed for the RIEGL data recorded)
Scanning Mechanism	rotating polygon mirror
Scan Pattern	parallel scan lines
Scan Angle Range	± 30° = 60° total
Scan Speed	14 - 200 lines/sec @ laser power level ≥ 50%
Angular Step Width Δϑ	Δϑ ≥ 0.012° @ laser power level ≥ 50%
Intensity Measurement	16 bit intensity information for each echo signal

Tab. 2.1S: Technical specifications of RIEGL LMS-Q780™ sensor.

Parameter	Value
Operating Flight Altitude Above Ground Level	800 m
Helicopter Cruise Velocity	50 kts (corresponding to ~ 25 m/s)
Side Overlap Flight Strips	50%
Forward Overlap Aerial Imagery	65%
Number Of Flight Strips	14 (13 flight strips + 1 cross flight strip)
Survey Time	2h:40':00''

Tab. 2.2S: Main flight parameters of the aerial survey carried out over the study area on November 2015.

Accuracy measure	Notational expression	Confidence interval
Mean Error	$\hat{\mu} = \frac{1}{n}\sum_{i=1}^{n} \Delta h_i$	$\hat{\mu} - t_{\alpha/2}\frac{\hat{\sigma}}{\sqrt{n}} < \hat{\mu} < \hat{\mu} + t_{\alpha/2}\frac{\hat{\sigma}}{\sqrt{n}}$
Standard Deviation of Error	$\hat{\sigma} = \sqrt{\frac{1}{n-1}\sum_{i=1}^{n}(\Delta h_i - \hat{\mu})^2}$	$\sqrt{\frac{(n-1)\cdot\hat{\sigma}^2}{\chi^2_{\alpha/2}}} < \hat{\sigma} < \sqrt{\frac{(n-1)\cdot\hat{\sigma}^2}{\chi^2_{1-\alpha/2}}}$
Median (50% sample quantile of error distribution)	$\hat{Q}_{\Delta h_i}(0.50) = m_{\Delta h_i}$	Bootstrap-based Confidence Interval
Normalized Median of Absolute Deviations	$\widehat{NMAD} = 1.4826 \cdot median(\lvert\Delta h_i - m_{\Delta h_i}\rvert)$	Bootstrap-based Confidence Interval
68.3% sample quantile of absolute errors distribution	$\hat{Q}_{\lvert\Delta h_i\rvert}(0.683)$	Bootstrap-based Confidence Interval
95.0% sample quantile of absolute errors distribution	$\hat{Q}_{\lvert\Delta h_i\rvert}(0.95)$	Bootstrap-based Confidence Interval

Tab. 2.3S: Employed standard and robust accuracy measures (Δh denotes the individual vertical "errors" i = 1, ..., n; n is the sample size; $m_{\Delta h_i}$ represents the median of the errors; $t_{\alpha/2}$ is the upper critical value for the t distribution with n-1 degrees of freedom; $\chi^2_{\alpha/2}$ and $\chi^2_{1-\alpha/2}$ are the critical values for the chi-square distribution with n-1 degrees of freedom).

Interpolation algorithm	Parametrization
Linear triangulation	n/a
Natural Neighbour	n/a
Inverse Distance to a Power	Power exponent = 2.99, neighbourhood type = ellipse (one sector), maximum neighbours = 25, minimum neighbours = 7, angle = 125.0°, major semi-axis = 180.0.0 m, minor semi-axes = 175.0 m
Nearest Neighbour	n/a
ANUDEM	Drainage enforcement = enabled, first roughness penalty = 0.5, second roughness penalty = 0.0, discretisation standard error factor = 1.0, vertical standard error = 0.237 m, first elevation tolerance = 0.237 m, second elevation tolerance = 200.0, maximum number of iterations = 20
Completely regularize spline	Kernel parameter = 930.17, neighbourhood type = ellipse (one sector), maximum neighbours = 25, minimum neighbours = 7, angle = 125°, major semi-axis = 180.0 m, minor semi-axes = 175.0 m
Thin-plate spline	Kernel parameter = $1 \cdot e^{20}$, neighbourhood type = ellipse (one sector), maximum neighbours = 25, minimum neighbours = 7, angle = 125.0°, major semi-axis = 180.0 m, minor semi-axes = 175.0 m
Thin-plate spline plus tension	Kernel parameter = 1339.74, neighbourhood type = ellipse (one sector), maximum neighbours = 25, minimum neighbours = 7, angle = 125.0°, major semi-axis = 180.0 m, minor semi-axes = 175.0 m
Multi-quadratic spline	Kernel parameter = 0.26, neighbourhood type = ellipse (one sector), maximum neighbours = 25, minimum neighbours = 7, angle = 125.0°, major semi-axis = 180.0 m, minor semi-axes = 175.0 m
Inverse multi-quadratic spline	Kernel parameter = $1.17 \cdot e^{-38}$, neighbourhood type = ellipse (one sector), maximum neighbours = 25, minimum neighbours = 7, angle = 125.0°, major semi-axis = 180.0 m, minor semi-axes = 175.0 m
Point ordinary kriging	Nugget parameter = 0.056 m, range = 180.0 m, sill = 450 m^2, neighbourhood type = ellipse (one sector), maximum neighbours = 25, minimum neighbours = 7, angle = 125.0°, major semi-axis = 180.0 m, minor semi-axes = 30.0 m.
Block ordinary kriging	Nugget parameter = 0.056 m, range = 180.0 m, sill = 450 m^2, neighbourhood type = ellipse (one sector), maximum neighbours = 25, minimum neighbours = 7, angle = 125.0°, major semi-axis = 180.0 m, minor semi-axes = 30.0 m, number of averaged point predictions = 32 and 8 (block dimension equal to 1.00 and 0.50 m, respectively)

Tab. 2.4S: Employed interpolation routines and related parametrization.

Voronoi's influence areas	Value (m^2)	Mutual distances	Value (m)
Minimum	0.001	Minimum	0.010
25% sample quantile	0.087	5% sample quantile	0.104
Median	0.150	Median	0.270
Mean	0.238	Mean	0.290
75% sample quantile	0.261	95% sample quantile	0.566
Maximum	30.360	Maximum	3.481

Tab. 2.5S: Voronoi's influence areas and mutual distances values.

3 Investigating the performance of ground- and airborne-based survey techniques in a morphologically complex area, and the related influence on stony debris flows routing modeling

This chapter represents an edited version of ***Boreggio M.[5], Bernard M., Gregoretti C. (2018). Investigating the performance of ground- and airborne-based survey techniques in a morphologically complex area, and the related influence on stony debris flows routing modeling*** *(currently in preparation).*

Summary

Among the geomorphic processes occurring in steep mountain basins, debris flows can be regarded as one of the most hazardous phenomena. In order to cope with this natural hazard, a common practice is the mapping of the areas potentially threatened by means of routing models. Since the topography is the major control over fluxes of water and sediments, the proper representation of the surface morphology through Digital Elevation Models (DEMs) is a precondition for debris flows routing modeling applications. The quality of DEMs depends on the accuracy, density, and spatial distribution of the topographic data (i.e., on the employed survey technique); on the characteristics of the sampled surface; and on the applyed gridding methodology. Therefore, the choice of the survey technique could represent a critical concern for the reliability of debris flows routing modeling outcomes. In this research, we initially investigate and compare the performance of a ground-based (i.e., Global Navigation Satellite System, GNSS) and an airborne-based (i.e., full-waveform Light Detection And Ranging, LiDAR) survey technology in characterizing the complex topography of a debris flow channel located in the Venetian Dolomites. The investigation is carried out through a combination among statistical analysis of DEMs vertical accuracy, spatially distributed DEMs uncertainty modeling, and probabilistic pairwise DEMs comparison. After that, we evaluate if the different topographic characterization of the channel morphology can affect the results of a Geographic Information System (GIS)-based cell model for simulating stony debris flows routing. In detail, we explore the difference in the cell routing model behaviour according to the used topographic surface, by focusing on simulated solid-liquid discharges and channel morphology after the event. The assessment of the survey techniques performance highlights that both of them could be used to generate bias-free and accurate high-resolution DEMs of debris flow channels, also featuring low magnitude uncertainty values in correspondence of the channel bottom. However, the probabilistic pairwise DEMs comparison points out that, although the compared survey techniques provide a comparable topographic characterization of the debris flow channel bathymetry, meaningful discrepancies could be detected in correspondence of morphologically complex channel features. Furthermore, the evaluation of the survey techniques influence on debris flows routing modeling stresses that these discrepancies are able to affect the cell routing model behavior, leading to the conclusion that the choice of the survey technique could represent a critical concern for the reliability of routing modeling outcomes.

[5] The author carried out the analysis on topographic data, the interpolation of DEMs, the comparison among the different survey techniques, the numerical simulations, and the analysis on the obtained results.

3.1 Introduction

According to the original definition proposed by Takahashi (1981), debris flows can be described as massive sediments transport phenomena that occur in mountain streams characterized by steep slopes, where the motion of the granular phase is directly induced by the gravity and the ratio between the liquid and solid transport rates is relatively low.

Among the geomorphic processes occurring in steep mountain basins, debris flows can be regarded as one of the most hazardous phenomena due to their magnitude, routing velocity, and high occurrence rate in a wide spectrum of morphological settings (Hürlimann et al., 2006; Blasone et al., 2014). In order to cope with this natural hazard, a common practice is the mapping of the areas historically or potentially threatened (Ghilardi et al., 2001), by adopting an empirical- (e.g., Scheidl and Rickenmann, 2010; Berti and Simoni, 2014) or a model-based (e.g., Rickenmann et al., 2006; Armanini et al., 2009; Gregoretti et al., 2018) approach. In the latter case, since the motion of gravity-driven flows is extremely sensitive to topographic changes (e.g., slope discontinuities, obstacles or ravine deviations; Rickenmann et al., 2006; Capra et al., 2011), the proper representation of the channel and fan morphology through DEMs is essential for the reliability of debris flows routing models outcomes. As matter of fact, a DEM can be regarded as a digital representation of the bare earth, and from a mathematical point of view it is simply a function $z=f(p)$ mapping a unique height value to each planimetric location $p(x, y)$ (Briese in Vosselman and Maas, 2010; Pfeifer et al., 2005).

DEMs are always generated starting from a given topographic dataset (e.g., points and lines), by means of deterministic or stochastic gridding algorithms (Hengl and Reuter, 2009). The topographic data acquisition method for digital terrain modeling purposes is usually driven by the specific application and its requirements in terms of accuracy and sampled data density (Höhle and Potuckova, 2011). In the past, the analytical aerial photogrammetry along with the classic ground-based topographic surveys were the main measurement techniques for collecting topographic information on areas featuring different extension. In the last two decades, the sensor modernization has promoted the development of new and highly automated remote-sensing techniques, such as the Airborne and Terrestrial Laser Scanning (ALS or LiDAR, and TLS, respectively), the long- and close-range digital photogrammetry, and the Interferometric Synthetic Aperture Radar (InSAR; e.g., Lillesand et al., 2004; Höhle & Potuckova, 2011; Milan et al., 2011; Molina et al., 2014; Adams et al., 2016; Hsieh et al., 2016). All these new survey techniques are able to acquire high-resolution topographic data (i.e., meter and sub-meter data resolution), within a short time, and with a high accuracy level. Nevertheless, classic ground-based surveys by means of GNSS or Total Station (TS) have not been completely set aside, since they ensure a proper trade-off between accuracy and cost for those scenarios involving small areas without the need for a massive topographic data acquisition (Casas et al., 2006; Gomarasca, 2009).

Considered the wide range of ground-, airborne-, and satellite-based survey techniques currently available and their inherent limitations that result in trade-offs between cost, accuracy, resolution, spatial coverage, and sampling frequency, the choice of the appropriate survey method for a given application is not a trivial issue. For this reason, recent research efforts have been undertaken in order to investigate the main benefits and limitations of the available survey techniques under different conditions and environments (e.g., Gallay et al., 2013; Molina et al., 2014; Bangen et al., 2014; Tarolli, 2014; Passalacqua et al., 2015). However, to date little work has been done in order to evaluate the performance of ground- and airborne-based survey techniques in morphologically complex areas, such as those where debris flows occur. Furthermore, notwithstanding a number of researches proved the potential impact of the topographic data source on floods modeling outcomes (e.g., Wilson and Atkinson, 2005; Casas et al., 2006; Cook and Merwade, 2009; Alho et al., 2009; Ali et al., 2015; Bakula et al., 2016; Reil et al., 2017; Bhuyian and Kalyanapu, 2018, Table 3.1S of the supplementary material), no attempt to evaluate the influence of different survey techniques on the debris flows routing models behaviour has been yet carried out.

In order to fill this research gap, in this study we first assess and compare the performance of a ground-based (i.e., GNSS) and an aerial-based (i.e., full-waveform LiDAR) survey technique in characterizing the complex topography of a 1 km length debris flow channel reach located in the Venetian Dolomites. The investigation is performed through a

combination among statistical analysis of DEMs vertical accuracy, spatially distributed DEMs uncertainty modeling, and probabilistic Difference of DEMs (DoD) analysis. After that, we evaluate if the different topographic characterization of the channel morphology can affect the outcomes of a GIS-based cell model for simulating stony debris flows routing, by considering both high- and low-magnitude flow conditions. The assessment is carried out by exploring the difference in the cell routing model behaviour according to the used topographic surface, in terms of simulated solid-liquid discharges and channel morphology after the event. Therefore, this research may be useful for digital elevation data users involved in floods and debris flows hazard modeling and prediction in morphologically complex areas.

The paper is organized as it follows. After a brief statement of the problem (Section 3.1: Introduction), the Section Materials and Methods describes the selected study site (Subsection 3.2.1: Field site), the two employed survey techniques and the related topographic datasets (Subsections 3.2.2 and 3.2.3: Aerial- and Ground-based elevation data, respectively), the DEMs generation methodology (Subsection 3.2.4: Data interpolation) and those followed to assess and to compare the performances of the tested survey methods (Subsections 3.2.5, 3.2.6, and 3.2.7: DEMs vertical accuracy analysis, DEMs vertical uncertainty investigation, and Survey techniques comparison, respectively) and their inhrerent influence on debris flows routing modeling outcomes (Subsection 3.2.8: Evaluation of the survey techniques effects on debris flows routing modeling). After that, the Section Results and Discussion (Section 3.3) summarizes the obtained results for the Subsections 3.2.5-3.2.8. Finally, the Section Conclusions (Section 3.4) completes the paper.

3.2 Materials and Methods

3.2.1 Field site

The present research focused upon a 1 km length reach of the Rovina di Cancia debris flow channel (western slope of Mount Antelao, Venetian Dolomites, North-Eastern Italian Alps, Figure 3.1).

The channel originates in the scree at the base of Salvella fork (2450 m a.s.l.), and ends within a flat circular deposition basin just upstream the village of Borca di Cadore (1000 m a.s.l., Figure 3.1D). Furthermore, at an altitude of about 1340 m a.s.l., just downstream a man-built flat deposition area, there is the intake of the Bus del Diau creek, that mainly provides a liquid contribute to the main channel (Figure 3.1C).

In this basin, debris flows usually initiate at about 1670 m a.s.l. (Figure 3.1A), since the most upper part of the channel is characterized by relatively narrow cross sections delimited by rocky walls, and the channel bottom includes giant and big boulders that prevent the formation of consistent solid-liquid waves.

From a geomorphological point of view, three main sectors can be distinguished within the catchment. In the upper part, massive rock cliffs composed of Upper Triassic to Lower Jurassic dolomites and limestones, underlined by the Raibl Formation, prevail. The medium part is characterized by screes of poorly sorted and highly permeable debris, with boulders that can reach diameters of about 3–4m. Finally, the lower part of the basin is covered by old debris flow deposits, including also post-glacial sediment material.

The study area is prone to stony debris flows owing to the availability of loose and coarse sediments, and the impulsive hydrological regime. In particular, the smaller grain sized material is provided by both the failure and the erosion of the channel banks, whereas gravel, pebbles, and cobbles are provided by rock falls occurring in the upper part of the basin. The pluviometric regime is mainly characterized by short duration and high intensity rainfall events, mostly occurring in July and August (Gregoretti and Dalla Fontana, 2008).

Different stony debris flow events were recorded in the past decades probably due to recent changes in the rainfall pattern. The most significant ones occurred on 2 July 1994, on 7 August 1996, and on 18 July 2009 (Simoni et al., 2018). The first flooded the inhabited fan with about 30000 m^3 of debris. The second mobilized about 45000–60000 m^3 of debris damaging some houses and cars, while the last mobilized about 54500 m^3 of debris and, after the filling of the retaining

basin, it flooded the inhabitated fan causing two casualties. The most recent debris flow events are those occurred on 23 July and on 4 August 2015, which mobilized about 30000 and 25000 m^3 of sediments, respectively.

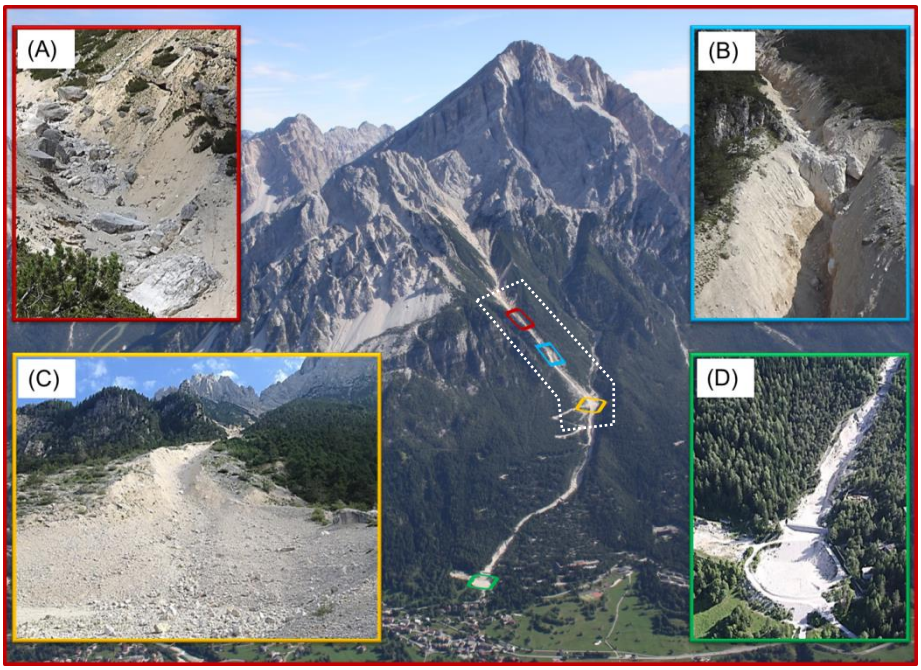

Figure 3.1: Aerial view of the Rovina di Cancia basin. (A) Debris flow triggering area (~1670 m a.s.l.), (B) natural rock step located at the end of the debris flow triggering area (~1500 m a.s.l.), (C) man-built flat deposition area (~1340 m a.s.l.), (D) final flat circular deposition basin (~1000 m a.s.l.). The dotted white line delineates the study reach.

3.2.2 Aerial-based elevation data

Airborne near infrared LiDAR (or ALS) is a well established active remote-sensing technique for precise topographic mapping (e.g., Lillesand et al., 2004; Hengl and Reuter, 2009; Jaboyedoff et al., 2012), having a significant potential for generating accurate and high-resolution DEMs of complex natural environments (Cavalli and Marchi, 2008; Heritage and Large, 2009; Höhle and Potuckova, 2011; Tarolli, 2014). This technology adopts a scanning unit emitting laser light pulses directed towards the earth, and estimates the distance between the scanner and the ground by measuring the return time of the back-scattered pulses. However, these range measurements are not enough to calculate the position of a point on the earth surface. As a matter of fact, accurate position (i.e., x, y, and z) and attitude (i.e., ω, φ, and κ) data need to be simultaneously measured by using a GNSS/IMU combination, and the geometry of the system (i.e., the geometrical relationships among the different reference frames) needs to be known. A complete review of ALS systems can be found e.g., in Wehr and Lohr (1999) and Vosselman and Maas (2010), whereas the state-of-the-art on the full-waveform topographic systems as well as on the related data processing techniques can be found e.g., in Mallet & Bretar (2009) and Wagner et al. (2006).

For the study site of Rovina di Cancia, the LiDAR data were collected on 21 October 2015 by Helica s.r.l.. A full-waveform RIEGL LMS-Q780™ sensor mounted on an I-HBEP helicopter (Eurocopter AS 350B3) flew at about 800 m above the ground level with a scan angle of ± 30° from nadir and a side overlap between adjacent flight strips equal to 50%. An onboard GNSS connected via radio waves to five ground stations located within a maximum distance of 50 km recorded the system carrier position at a frequency of 1 Hz, whereas an IMU rigidly connected to the inner structure of the scanning mechanism sampled the helicopter attitude at a frequency of 200 Hz. Simultaneous aerial photographs were

acquired by means of a calibrated Phaseone iXA 180 medium-format frame digital camera with a forward overlap of 65%.

After the aerial survey, the data provider post-processed the raw topographic measurements by segregating all the recorded returns into ground and over-ground ASCII files consisting of x, y, and z coordinates based on the projected coordinate system WGS84-UTM32. For the selected study area the average points density (i.e., ground and over-ground points density) was 20.79 points m^{-2}, while the average ground points density was 3.33 points m^{-2}. The vertical accuracy of the aerial data was estimated by the vendor by calculating the Root Mean Square Error (RMSE) of elevations for 30 ground control points collected within a nearby area. The stated RMSE value was 0.018 m, with a mean vertical error of -0.007 m.

Since the quality of LiDAR-derived DEMs is strongly affected by classification errors (i.e., commission and omission errors), before gridding the laser data the delivered ASCII files were converted in LAS format and then visually examined. The inspection highlighted many data voids within the ground datasets mainly due to misclassified LiDAR points as over-ground features in correspondence of morphologically complex areas. For this reason, the delivered datasets were re-classified into ground and over-ground points within the software package LAStools™ (Isenburg, 2017), achieving an average ground points density equal to 4.34 points m^{-2} (i.e., 30% more than the density of the delivered ground points datasets). After the reclassification procedure, the ellipsoidal heights were converted in orthometric heights based on the local geoid model ITALGEO2005, with a nominal accuracy conversion equal to ± 0.035 at 1 σ.

3.2.3 Ground-based elevation data

The GNSS is an effective ground-based survey technique allowing the three-dimensional positioning of sampled locations in a geocentric reference frame (e.g., Molina et al., 2014, Gomarasca, 2009), by integrating distance and time measurements referred to constellations of orbiting satellites. The positioning is usually obtained in real-time or post-processing by using two dual frequency ground receivers located at an unknown (i.e., the rover station) and known (i.e., the master station) position, respectively. This GNSS survey protocol allows reducing or eliminating some inherent errors sources (e.g., atmospheric effects, clocks inaccuracies, and satellites orbits errors), gaining the highest accuracy of the method (i.e., millimetric to centimetric). This differential positioning can be carried out as static (e.g., static or fast-static) or kinematic (e.g., stop and go or continuous) relative positioning. In the latter case, the rover station is moving within the survey area enabling the acquisition of a large number of points. The reader is referred to the works of Sickle (2015) and Gomarasca (2009) for a dissertation on GNSS.

The GNSS survey of the Rovina di Cancia channel was carried out in October-November 2015 by using a dual frequency Topcon HiPer V GPS base and rover system, capable of tracking both the United States GPS and the Russian GLONASS satellites constellations. The survey was carried out as real-time, kinematic, stop and go relative positioning based on phase solutions (i.e., rtkGNSS survey), by placing the master station at a known position located within a maximum distance from the survey area of 1 km in order to minimize the measurement errors. Furthermore, during the survey, only fixed solutions were acquired, and the three dimensional position of each sampled point was calculated as the average of the measurements carried out on five epochs. The instrument reported planimetric precision was 0.005 m ± 0.001 m (with a maximum of 0.03 m), whereas the reported vertical one was 0.008 ± 0.002 m (with a maximum of 0.05 m). The average planimetric dilution of precision value was 2.55 ± 0.45 (with a maximum of 3.50). The sampling was carried out according to a cross-sections, morphological guided spatial scheme (e.g., Aguilar et al., 2005; Heritage et al., 2009) in order to describe the channel morphology as accurate as possible. Following this spatial sampling scheme, higher cross-sections and points densities were gathered in correspondence of topographically complex channel areas, with comparable lower densities in areas having homogeneous landforms. Relevant longitudinal and transversal topographic breaklines were also acquired during the field survey. According to the LiDAR data geodetic-cartographic datum (see Subsection 3.2.2: Aerial elevation data), the geographic coordinates of the GNSS measurements were projected in the

coordinate system WGS84-UTM32, and the orthometric heights were computed based on the local geoid model ITALGEO2005.

3.2.4 Data interpolation

Spatially concurrent DEMs were generated within the software package ArcGIS™ (rel. 10.3) by triangulating the GNSS and LiDAR data according to the Delaunay criterion, and then converting the derived Triangular Irregular Networks (TINs) into 1-m resolution raster grids by using the natural neighbor algorithm. Noteworthy, both the DEMs were generated with 1-meter cell size since it was deemed to ensure the best agreement between accurate surface representation and data management efficiency. Furthermore, during the triangulation of the GNSS data also the sampled topographic breaklines were used.

The reason behind the choice of the gridding methodology was threefold. First, the TIN is a vector-based surface model allowing a better characterization of complex topographic features (e.g., slope discontinuities and ridges) via the inclusion of the sampled topographic breaklines as three dimensional polylines. In fact, during the triangulation, they impose a constraint such that no TIN facets cross the corresponding polylines which are set as TIN edges. Secondly, in the planned gridding methodology the TIN represents an intermediary vector-based model enabling the removal of interpolation artefacts and the improving of the shape reliability of the resulting DEM through manual editing operations. Finally, according to Boreggio et al. (2018), the triangulation with linear or natural neighbor interpolation, along with the completely regularized spline and thin-plate spline plus tension basis functions, ensures the best trade-off between interpolation accuracy and shape reliability in this kind of morphological environment. It should be noted that in this research the natural neighbour algorithm was preferred over the simplest linear rasterization since it allows a smoother connection among the triangle edges, thus improving the shape reliability of the resulting DEM mainly in areas featuring a low points density.

3.2.5 DEMs vertical accuracy analysis

Once the DEMs were generated, the performance of each tested survey technique was initially assessed by computing the vertical bias and accuracy of the corresponding gridded surface (i.e., the GNSS- and LiDAR-derived DEMs). Since between the two compared survey methods the GNSS has the highest nominal positioning accuracy, its measurements were used as control points during the DEMs vertical accuracy analysis. As a matter of fact, the nominal positioning accuracy for dual-frequency GNSS receivers operating in real-time kinematic mode and with baseline less than 20 km ranges between 0.02 and 0.05 m, whereas the LiDAR altimetry vertical accuracy is approximately 0.15-0.20 m in open terrain conditions (e.g., Cilloccu et al., 2009; Molina et al., 2014).

In detail, the GNSS points elevation was subtracted from that of the raster grid cells centers containing the GNSS points themselves. Thus, elevation residuals were calculated and used to characterize the DEMs vertical error within the R open-source software package (R Development Core Team, 2008). It must be noted that these elevation residuals were calculated by comparing two points datasets (i.e., the GNSS points and the raster grid cells centers containing the GNSS points themselves) that did not spatially overlap. Furthermore, in the case of LiDAR-derived DEM, the two compared points datasets had also a different support size. As a matter of fact, the LiDAR altimetry provides elevation measurements averaging over the laser beam footprint, whereas the GNSS technique provides elevation measurements at the rod trip scale. On the other hand, in the case of GNSS-derived DEM, the two compared points datasets were not independent since the digital model was interpolated starting from the same points used during the accuracy assessment. As a consequence of the outlined procedure weaknesses, some inherent uncertainties might affect the DEMs vertical accuracy assessment results.

Since the derivation of DEMs accuracy measures has to deal with the presence of outliers and errors distributions that might be not normal (Höhle and Höhle, 2009), the algorithm proposed by Höhle and Potuckova (2011) was followed. It is based on the use of standard (i.e., mean and standard deviation) or robust (i.e., median, Normalized Median of Absolute Deviations (NMAD), and sample quantiles of the absolute errors distribution) accuracy measures depending on whether the vertical errors distribution or the vertical errors distribution without outliers being normal or not. Furthermore, according to Höhle and Höhle (2009), the rule of three times the Root Mean Square Error (RMSE) was used to set the outliers threshold, while the error distributions normality was tested both graphically and statistically by means of the normal Q-Q plot and the D'Agostino K^2 omnibus test, respectively. The null hypothesis of the test was that the error distributions did not deviate from the normal one due to either data skewness or kurtosis, and the test itself was chosen due to its power in the case of large samples having kurtosis slightly higher than the normal distribution.

3.2.6 DEMs vertical uncertainty investigation

As recognized by a number of authors, the vertical error of DEMs is not spatially uniform, but it varies according to some spatial pattern (e.g., Li, 1993; Wood and Fisher, 1993; Wood, 1996; Yang and Hodler, 2000; Weng, 2006; Erdogan, 2009). For instance, we might expect higher DEM errors over areas having low sampled points density and featuring high slope and roughness (e.g., channel banks), respect to areas with high sampled points density and smooth morphology (e.g., alluvial fans). However, the accuracy analysis carried out on the generated DEMs only provided uniform accuracy estimates for the entire digital surfaces, and as a result it did not allow a proper characterization of their inherent vertical error. Furthermore, the analysis was restricted to the grid cells containing surveyed GNSS points, thus not providing comprehensively estimates of the DEMs error. It is also worth pointing out that, as explained in Subsection 3.2.7, the performances of the two investigated survey techniques were compared through DEMs differencing. Since the detectable signal (i.e., the significant discrepancies between the compared survey techniques) was expected to be of small magnitude, a less conservative and more sophisticated model of DEMs error was deemed to be necessary.

To overcome the explained drawbacks, we modelled the DEMs vertical error in a spatially distributed way by using the Fuzzy Inference System (FIS)-based algorithm proposed by Wheaton et al. (2010). It allows readily available proxies for factors contributing to the vertical error of DEMs (e.g., terrain slope and roughness, and points density) to be provided as inputs to a FIS, and by modeling their combined influence on DEMs quality trough a linguistically-based FIS rules system, it is able to predict spatially variable estimates of DEMs elevation uncertainty. For a complete dissertation on the method and on its applicability, the reader is referred to Wheaton (2008).

In the present research, we developed ad-hoc FISs for the GNSS- and LiDAR-derived DEMs described in Subsection 3.2.4. In both the cases, we used three input variables, namely: points density (a proxy for sampling effort), Euclidean distance to the nearest sampled topographic breakline (a proxy for error clustering), and LiDAR-derived DEM slope (a proxy for topography complexity). These spatial indicators of DEMs elevation uncertainty were chosen by previously investigating their relationships with the computed elevation residuals (see Subsection 3.2.5) through univariate correlation analysis. As pointed out by Hensleigh (2014), it represents a preliminary step because the real work in developing a FIS consists in recognizing the variables affecting the DEMs error and in exploring their mutual relationships. For both the FISs, each input variable was classified into three fuzzy sets (i.e., low, medium, and high), whose values ranges were defined by analyzing the variable distribution and the corresponding sample quantiles.

Once the input variables and the corresponding fuzzy sets were defined, the linguistically-based FIS rules systems relating inputs to output (i.e., the DEMs elevation uncertainty) were set up, and then the values ranges of the output variable fuzzy sets were calibrated based on the observed DEMs errors (see Subsection 3.2.5). It is worth noting that three fuzzy sets (i.e., low, medium, and high) were also used for the FISs output variable. Finally, for each possible combination of input variables, the corresponding output fuzzy set was identified.

For both the generated DEMs we developed three separate FISs (i.e., six independent FISs) by changing the fuzzy sets values ranges of both the input and output variables according to Table 3.1 and Table 3.2. Each developed FIS was

then validated by comparing the modeled and observed DEMs error values, and their corresponding distributions. The Geomorphic Change Detection (GCD) ArcGIS plugin (GCD rel. 6.1.14) was used to create the six three input FISs to be used in the present research.

Parameter	**Maximum**	**Range of values for membership function**		
		Low	**Medium**	**High**
FIS 1				
Points density (points m^{-2})	4.00	0.00 – 3.00	0.00 – 4.00	2.00 – 4.00
Euclidean distance to the nearest sampled breakline (m)	25.96	0.00 - 2.00	0.00 - 4.47	3.16 - 25.96
LiDAR-derived DEM slope (degrees)	73.71	0.00 - 38.17	35.00 - 50.42	46.50 - 73.71
DEM elevation uncertainty (m)	0.34	0.00 – 0.23	0.01 – 0.33	0.05 – 0.34
FIS 2				
Points density (points m^{-2})	*4.00*	*0.00 – 3.00*	*0.00 – 4.00*	*2.00 – 4.00*
Euclidean distance to the nearest sampled breakline (m)	*25.96*	*0.00 – 2.00*	*0.00 – 4.00*	*2.82 – 25.96*
LiDAR-derived DEM slope (degrees)	*73.71*	*0.00 – 40.70*	*36.66 – 48.23*	*44.19 – 73.71*
DEM elevation uncertainty (m)	*0.36*	*0.00 – 0.25*	*0.03 – 0.33*	*0.03 – 0.36*
FIS 3				
Points density (points m^{-2})	4.00	0.00 – 3.00	0.00 – 4.00	2.00 – 4.00
Euclidean distance to the nearest sampled breakline (m)	25.96	0.00 – 2.00	0.00 – 4.00	2.82 – 25.96
LiDAR-derived DEM slope (degrees)	73.71	0.00 – 40.70	36.66 – 48.23	44.19 – 73.71
DEM elevation uncertainty (m)	*0.76*	*0.00 – 0.25*	*0.03 – 0.33*	*0.03 – 0.76*

Table 3.1: Parametrizations of the three developed FISs for the GNSS-derived DEM (italics denotes the changes between the developed FISs).

3.2.7 Survey techniques comparison

In this study, spatially variable estimates of the differences between the two tested survey techniques were calculated at the grid cell scale by subtracting the corresponding DEMs elevation values (i.e., GNSS-derived DEM – LiDAR-derived DEM). As a result, a DoD raster grid showing in a spatially distributed way the magnitude of the vertical discrepancies between the two compared survey techniques was obtained.

As stressed out by many authors, in attempting DEMs subtraction exercises it is essential to take into proper account the inherent uncertainties of the differenced gridded surfaces in order to distinguish any detectable signal (e.g., the significant differences between the compared survey techniques) from the noise (e.g., Lane et al., 2003; Wheaton et al., 2010; Milan et al., 2011; Bangen et al., 2014; Passalacqua et al., 2015; Schaffrath et al., 2015). Most DoD analyses are based on the standard DEMs error propagation and on some form of thresholding, thus defining a minimum level of detection ($_{min}$LoD) above which the calculated vertical discrepancies between the differenced surfaces can be assumed to be significant. The three most common used DoD uncertainty approaches are: (1) defining a threshold in the form of a spatially uniform $_{min}$LoD; (2) using a propagated error value estimated by taking the sum in quadrature of the DEMs errors as $_{min}$LoD; (3) probabilistic thresholding of the DoD map at any chosen confidence interval (e.g., 95% confidence interval) by using spatially variable DEMs error estimates (e.g., the FIS-based DEMs elevation uncertainty estimates). In the last case, a unique $_{min}$LoD is calculated on a cell-by-cell basis by multiplying the propagated DEMs error (e.g., the propagated DEMs error defined by using the FIS-based spatially variable uncertainty estimates) by a critical student's *t*-value, by assuming that the individual DEMs cell errors are independent and distributed according to a Gaussian. For instance, a 95% probabilistic confidence interval $_{min}$LoD is obtained by multiplying the propagated DEMs error by a *t*-value of 1.96. All the three outlined approaches are automated within the GCD plugin.

In order to identify the magnitude and spatial distribution of the significant discrepancies between the two compared survey techniques, in the present research we thresholded the generated DoD map at a 95% probabilistic confidence interval by using the spatially variable FIS-based DEMs error estimates. 68.3% and 99% probabilistic confidence intervals were also used to test the influence of the chosen critical student's *t*-value on the DoD analysis results.

Parameter	**Maximum**	**Range of values for membership function**		
		Low	**Medium**	**High**
FIS 1				
Points density (points m^{-2})	38.00	0.00 - 5.00	2.00 - 10.00	7.00 - 38.00
Euclidean distance to the nearest sampled breakline (m)	25.96	0.00 - 2.00	0.00 - 4.47	3.16 - 25.96
LiDAR-derived DEM slope (degrees)	73.71	0.00 - 38.17	35.00 - 50.42	46.50 - 73.71
DEM elevation uncertainty (m)	0.77	0.00 – 0.28	0.03 – 0.41	0.11 – 0.77
FIS 2				
Points density (points m^{-2})	*38.00*	*0.00 – 6.00*	*3.00 - 9.00*	*6.00 – 38.00*
Euclidean distance to the nearest sampled breakline (m)	*25.96*	*0.00 – 2.00*	*0.00 – 4.00*	*2.82 – 25.96*
LiDAR-derived DEM slope (degrees)	*73.71*	*0.00 – 40.70*	*36.66 – 48.23*	*44.19 – 73.71*
DEM elevation uncertainty (m)	*0.36*	*0.00 – 0.31*	*0.03 – 0.43*	*0.12 – 0.77*
FIS 3				
Points density (points m^{-2})	38.00	0.00 – 6.00	3.00 - 9.00	6.00 – 38.00
Euclidean distance to the nearest sampled breakline (m)	25.96	0.00 – 2.00	0.00 – 4.00	2.82 – 25.96
LiDAR-derived DEM slope (degrees)	73.71	0.00 – 40.70	36.66 – 48.23	44.19 – 73.71
DEM elevation uncertainty (m)	*1.13*	*0.00 – 0.31*	*0.03 – 0.43*	*0.12 – 1.13*

Table 3.2: Parametrizations of the three developed FISs for the LiDAR-derived DEM (italics denotes the changes between the developed FISs).

3.2.8 Evaluation of the survey techniques effects on debris flows routing modeling

The routing modeling of the Rovina di Cancia debris flow was carried out by using the GIS-based cell routing model proposed by Gregoretti et al. (2018). It represents the fully bi-phase version of the one proposed by Gregoretti et al. (2016), and it is able to simulate the routing and the entrainment-deposition processes of solid-liquid mixtures with a grain-collision dominated rheology (i.e., stony debris flows; Takahashi, 2007).

In summary, the model discretizes the flow domain through the square cells of a raster grid DEM. In the case of routing along positive slopes, according to the kinematic wave approximation, the flow exchange among neighboring cells is computed through a Chezy-like formula assuming uniform flow conditions. Conversely, in the case of routing along negative slopes, the broad-crested weir equation is used. In both the cases weighted functions allowing multi-flow directions are employed. The rate of change of bed elevation is calculated through the Exner's equation combined with a modified version of the empirical one dimensional law of Egashira and Ashida (1987), assuming the bottom slope and the flow velocity as controlling factors of the erosion/deposition processes. Erosion and deposition are computed only along the steepest downslope flow direction, and the erosion modeling is also limited at the increasing flow depths ($dh/dt>0$) with volumetric sediment concentration of the routing mixture lower than the physic limiting upper value of 0.9 times the dry sediment concentration (Takahashi, 2007). From a numerical point of view, the governing equations of the mathematical model are solved using the finite difference technique with an explicit scheme subject to the Courant-Friedrichs-Lewy stability condition. For a complete dissertation on the employed cell routing model, the reader is referred to Gregoretti et al. (2016) and Gregoretti et al. (2018).

Since an inaccurate model parameterization could mask the effects of the employed survey techniques on debris flows modeling results, all the input parameters of the cell model were previously calibrated by the back-analysis of two debris flow events occurred at Rovina di Cancia on 18 July 2009 and on Ru Secco (San Vito di Cadore, North-Eastern Italian Alps) the 4th of August 2015. Noteworthy, both the back-analyses provided the same optimal model parametrization, thus ensuring a high degree of predictivity (for further details see Gregoretti et al., 2018a,b).

In all the performed model runs, both the calibrated values of the input parameters and the initial conditions (i.e., the upstream solid-liquid hydrograph) were kept unchanged, varying only the initial topographic surface generated according to the two described topographic datasets (see Subsections 3.2.2 and 3.2.3). Therefore, this exercise allowed the investigation of the inherent impact of the survey techniques on routing modeling outcomes.

Two event scenarios (i.e., 50- and 300-year return periods) were defined and used in the different model runs, thus evaluating the influence of survey techniques on routing modeling in two different flow conditions, characteristics of two usual design return periods. A total of 4 simulations were thus carried out (i.e., two topographic surfaces times two event scenarios).

To evaluate the influence of the survey techniques on debris flow routing modeling, the DEMs at the end of the simulation and the simulated solid-liquid discharges in correspondence of five control sections displaced along the 1 km length reach of the Rovina di Cancia channel were compared. It is worth noting that ground reference information for the two modeled event scenarios were not available. Therefore, the investigation carried out must be considered a sensitivity study, rather than an accuracy assessment, answering to the research question “how might we expect the routing model behavior to differ if we use in the different model runs DEMs generated by gridding different topographic datasets”.

3.3 Results and discussion

3.3.1 DEMs vertical accuracy analysis

The vertical accuracy measures computed by comparing the GNSS points elevations to those of both GNSS- and LiDAR-derived DEMs are summarized in Table 3.3. It turns out that in the case of GNSS-derived DEM the standard accuracy measures (i.e., the mean and standard deviation of vertical errors) computed on the errors sample after the outliers thresholding does not significantly differ from the robust ones (i.e., the median and NMAD of vertical errors). Conversely, in the case of LiDAR-derived DEM, the outliers have a great influence on the computed mean and standard deviation of vertical errors values. In fact, after the outliers thresholding their values decrease, remaining in any case greater than the corresponding robust ones.

Figure 3.2 highlights the differences between the employed accuracy statistics. It has been obtained by superimposing to the vertical errors sample distribution of the LiDAR-derived DEM the normal curves calculated by using: (1) the mean and standard deviation values of the vertical errors sample; (2) the mean and standard deviation values of the vertical errors sample after the outliers thresholding; (3) the median and NMAD values of the vertical errors sample. The graph demonstrates that the standard accuracy measures are not able to fit the vertical errors sample distribution, even after the outliers thresholding. Conversely, the robust accuracy measures ensure the best match both at the mean and at the tails of the errors distribution, since they apply a smoother transition between accepting and rejecting an observation from the errors sample. Therefore, the median and NMAD of vertical errors are used to characterize, respectively, the bias and the accuracy of both the generated DEMs. Furthermore, the 95% quantile of the absolute DEM errors distribution is employed as a robust measure of the maximum unsigned vertical error.

The median of vertical errors values can be regarded as negligible for both the gridded surfaces, meaning that the two investigated survey methods are not biased (i.e., they not systematically over- or under-estimate elevation values). The LiDAR-derived DEM median is only slightly biased towards under-estimating elevation values (median of vertical errors equal to -0.030 m). This vertical bias has been eliminated before undertaking the DEMs differencing exercise (see

Subsection 3.2.7) by means of a 2.5D calibration procedure (i.e., a rigid translation in the Z dimension of the LiDAR-derived DEM).

	GNSS-derived DEM	LiDAR-derived DEM
n. outliers (-)	30	50
Mean (m)	-0.001	-0.057
Standard deviation (m)	0.254	0.379
Mean after outliers thresholding (m)	-0.002	-0.050
Standard deviation after outliers thresholding (m)	0.239	0.337
Median (m)	0.000	-0.030
NMAD (m)	0.222	0.297
68.3% quartile (m)	0.230	0.310
95% quartile (m)	0.520	0.790

Table 3.3: Computed standard and robust DEMs accuracy measures.

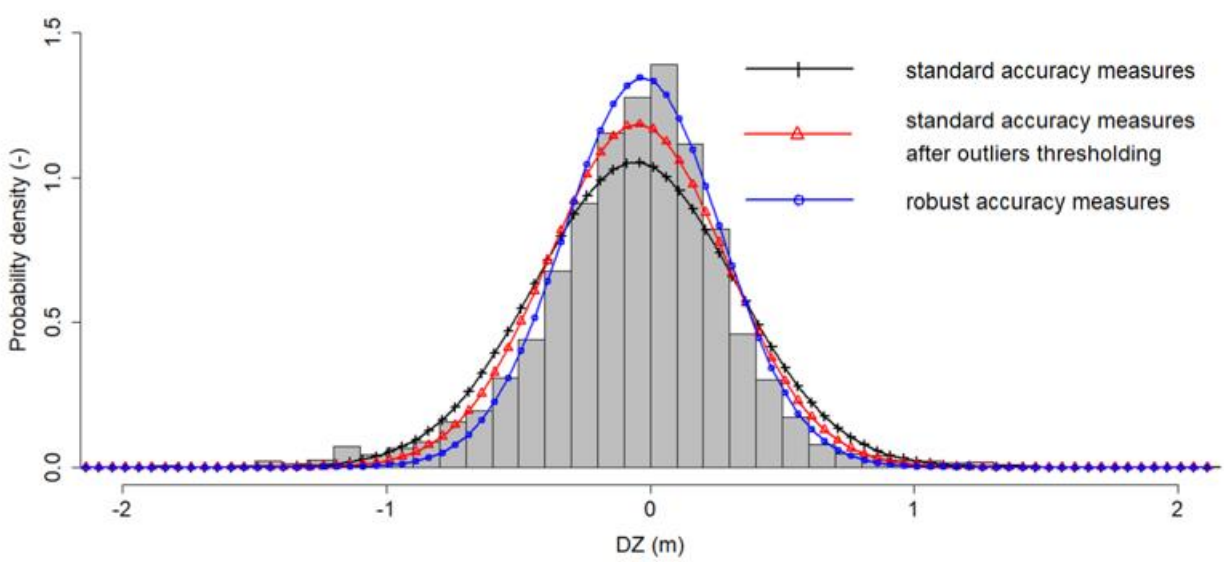

Figure 3.2: Histogram of the LiDAR-derived DEM vertical errors with superimposed the normal distributions having mean and standard deviation values computed though one of the three employed approaches. Note the different degree of fitting at the mean and at the tails of the errors distribution. ΔZ denotes the vertical error.

The DEMs accuracy estimates are better in the case of GNSS-derived DEM (NMAD of vertical errors equal to 0.222 m) than in the case of LiDAR-derived DEM (NMAD of vertical errors equal to 0.297 m). However, it might depend on the use of the GNSS measurements as reference values in the DEMs vertical accuracy assessment (see Subsection 3.2.5). Overall, the accuracy estimates are smaller than 0.300 m, and according to the accuracy-based classification of DEMs proposed by Cilloccu et al. (2009), it means that both the investigated survey techniques can be used to generate

dense and accurate DEMs of morphologically complex areas (e.g., debris flow channels), that are suitable for debris flows routing modeling applications.

3.3.2 DEMs vertical uncertainty investigation

In Figure 3.3, the results of the univariate correlation analysis between the chosen FISs input variables (i.e., points density, Euclidean distance to the nearest sampled topographic breakline, and LiDAR-derived DEM slope; see Subsection 3.2.6) and the observed LiDAR-derived DEM absolute errors are reported as an example.

As expected, the global trends highlight a positive correlation between the slope and the observed DEM absolute errors, and a negative one for both the points density and the Euclidean distance to the nearest sampled topographic breakline. First, it means that overall the DEMs error tends to be higher in correspondence of both high-gradient areas with low sample points density and slope discontinuities, according to what observed by many previous authors (e.g., Scheidl and Rickenmann, 2008; Heritage et al., 2009; Erdogan, 2009; Wheaton et al., 2010; Milan et al., 2011). Secondly, it also means that the chosen indicators of elevation uncertainty are suitable proxies for factor contributing to the DEMs vertical error, that can then be effectively used as input variables in a FIS-based DEM error model. It is also worth highlighting that all the graphs in Figure 3.3 show a megaphone points pattern, meaning that small magnitude DEM elevation uncertainties could be observed in correspondence of both high-gradient areas with low sample points density and slope discontinuities. As a matter of fact, although these conditions increase the potential for higher DEM uncertainties, accurate DEM elevation values are anyhow possible.

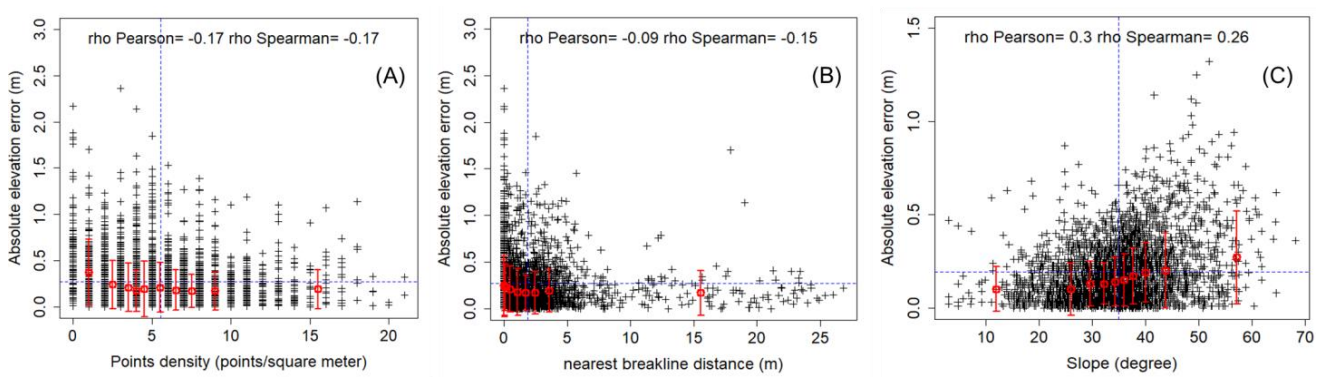

Figure 3.3: Scatterplots of (A) points density, (B) Euclidean distance to the nearest sampled topographic breakline, and (C) LiDAR-derived DEM slope values against the observed LiDAR-derived DEM absolute errors. The dotted blue lines correspond to the marginal mean of the two correlated variables.

For the six implemented FISs, the Q-Q plots of Figure 3.4 and Figure 3.5 summarize the relationships between observed and modeled DEMs errors. For both the generated DEMs, the best agreement is achieved by the FIS 3 (see Table 3.1 and Table 3.2), with a nearly 1:1 relationship between the observed and modeled elevation uncertainty. However, a closer look at the plots reveals that all the FIS-based DEM error models yield a loss of observed error variance, under-estimating the largest observed DEMs error values and over-estimating the smallest ones. As pointed out by Hensleigh (2014), it might be due to the inability of the FIS-based DEM error model to account for situations where the elevation error can be both high and low at the same time, thus not replicating the observed megaphone patterns. Furthermore, the DEM error is a complex function of points quality, sampling points density, morphological complexity, gridding methodology, and raster grid spatial resolution. Therefore, it is unlikely that the developed three input FISs are able to provide a comprehensive characterization of the DEM error itself. However, the FIS-based DEM error model represents a useful mean to address situations where more complex spatially variable DEM error estimates are required.

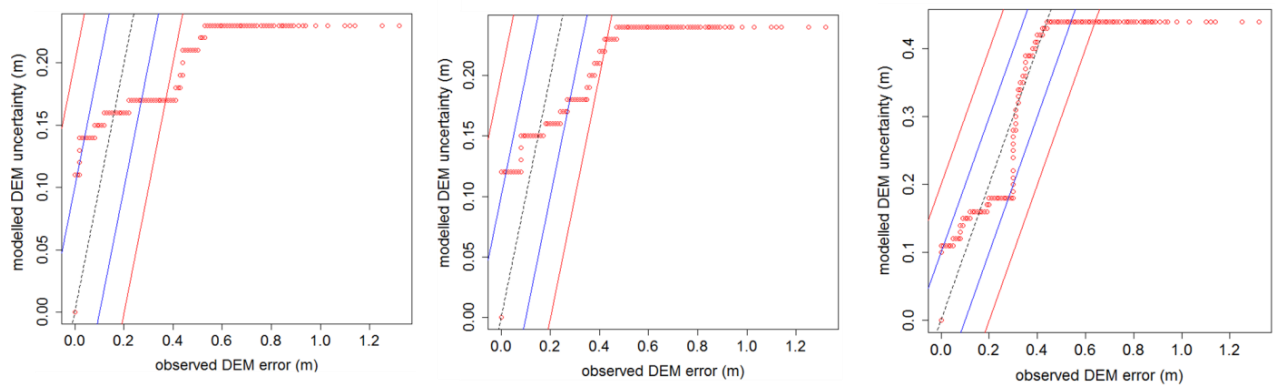

Figure 3.4: Q-Q plots of the observed and modeled elevation uncertainty in the case of GNSS-derived DEM: (A) FIS 1, (B) FIS 2, and (C) FIS 3. The dashed black line depicts the 1:1 relationship, whereas the blue and red continuous lines correspond to a FIS error of ± 0.10 and ± 0.20 m, respectively.

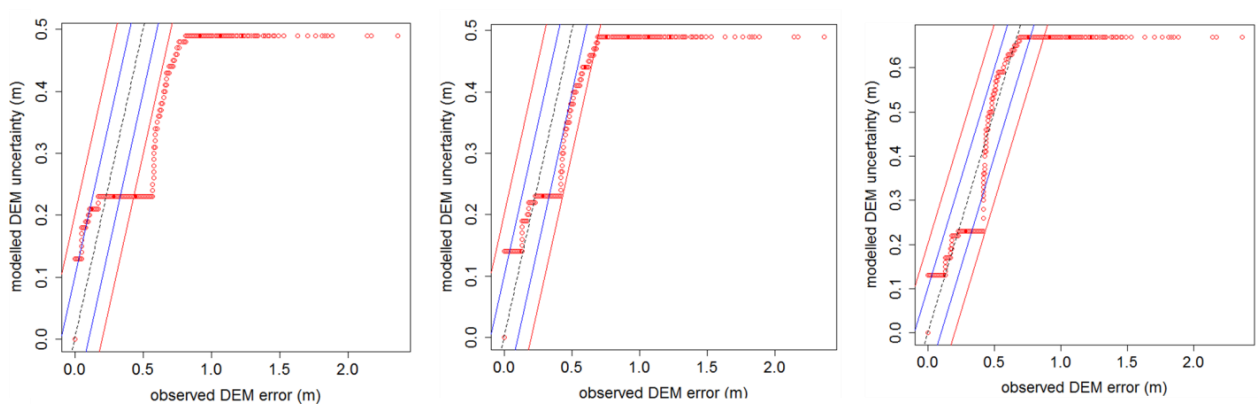

Figure 3.5: Q-Q plots of the observed and modeled elevation uncertainty in the case of LiDAR-derived DEM: (A) FIS 1, (B) FIS 2, and (C) FIS 3. The dashed black line depicts the 1:1 relationship, whereas the blue and red continuous lines correspond to a FIS error of ± 0.10 and ± 0.20 m, respectively.

The FIS 3-based DEMs elevation uncertainty estimates range between 0.100 and 0.440 m, and between 0.123 and 0.673 m in the case of GNSS- and LiDAR-derived DEM, respectively. Furthermore, as shown in Figure 3.6A, the uncertainty estimates are lower (median equal to 0.160 m) and have a smaller variance (standard deviation equal to 0.134 m) in the case of GNSS-derived DEM relative to the LiDAR-derived DEM (median and standard deviation equal to 0.400 and 0.222 m, respectively). However, it must be stressed that the fuzzy sets values ranges of the FISs output variable were calibrated on the elevation residuals computed by using the GNSS measurements as control points (see Subsection 3.2.6).

As shown in Figure 3.6B,C, for both the generated DEMs, the FIS 3-based elevation uncertainty estimates are higher in correspondence of breaks of slope (e.g., at the toe and top of the channel banks, and close to the rock step located about 200 m downstream the debris flows triggering section, Figure 3.1B) and along the channel banks. Conversely, the lowest magnitude uncertainty estimates are observed along the channel bottom. It means that both the investigated survey techniques are able to describe the area mainly affected by channelized debris flow routing with an overall low inherent noise, even if significant uncertainties could be observed in correspondence of morphologically complex transversal (e.g., rock steps and bouldered reaches) and longitudinal (e.g., channel banks) features.

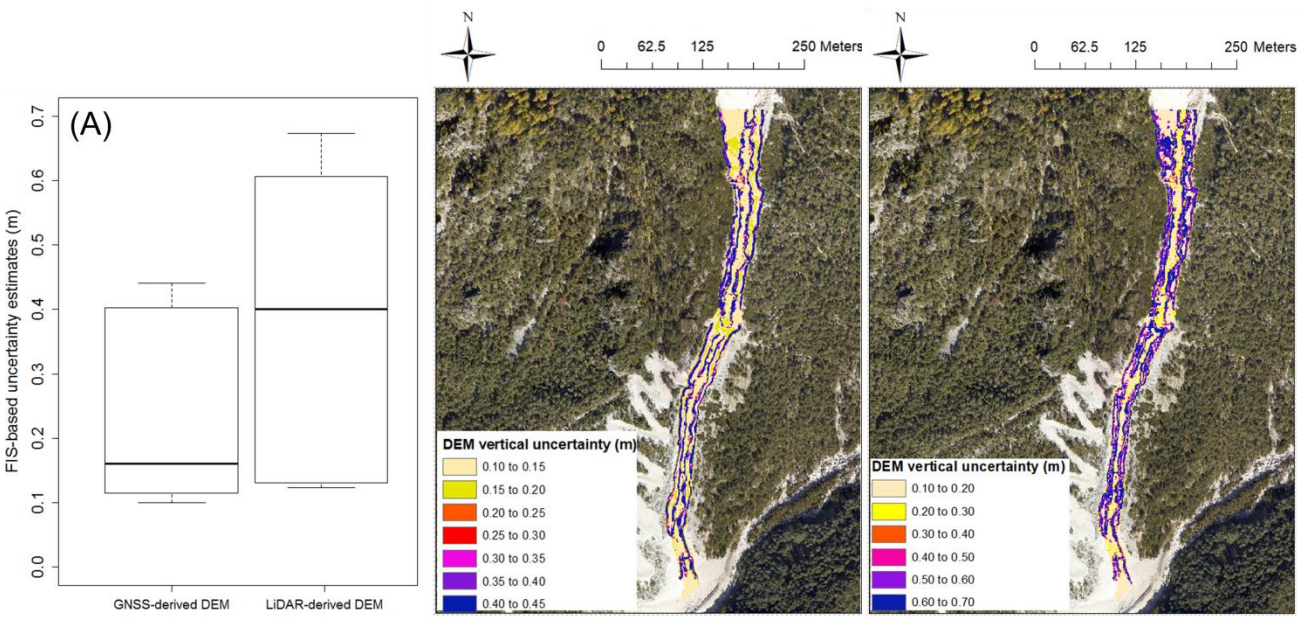

Figure 3.6: FIS 3-based DEMs elevation uncertainty estimates. (A) Box-plots and corresponding raster grids, in the case of (B) GNSS- and (C) LiDAR-derived DEM.

3.3.3 Survey techniques comparison

The unthresholded and probabilistically thresholded at a 95% confidence interval DoD maps, along with the corresponding elevation discrepancy distributions, are respectively shown in Figure 3.7 and Figure 3.8. These distributions represent the volumetric discrepancies between the two compared DEMs, binned according to the magnitude of the observed vertical differences.

The observed discrepancies vary between -4.31 m and 6.39 m, with an average thresholded vertical difference between the compared DEMs equal to -0.07 m. It means that the LiDAR-derived DEM is slightly biased towards over-estimating the GNSS-derived DEM elevations, as also confirmed by the elevation discrepancy distributions of Figure 3.8 (total volume of negative and positive thresholded discrepancies equal to 4253.780 m^3 and 2958.480 m^3, respectively).

The visual assessment of the unthresholded DoD map (Figure 3.7A) reveals that most of the computed elevation discrepancies feature a low magnitude, as also confirmed by the corresponding elevation discrepancy distribution (Figure 3.8A). In fact, it shows that the higher frequencies are centered close to the zero, indicating an overall agreement between the two compared survey techniques. Furthermore, as shown in Figure 3.7B, most of the observed vertical discrepancies are not significant when probabilistically thresholded at a 95% confidence interval (total volumetric unthresholded and thresholded difference between the compared DEMs equal to 11709.820 m^3 and 7212.26 m^3, respectively).

The statistically significant elevation discrepancies are observed along the channel banks and in correspondence of the rock step, where no GNSS measurements were collected owing to site accessibility or safety reasons. Conversely, at the channel bottom no meaningful vertical discrepancies between the two compared survey techniques are observed (Figure 3.7B). It means that a low-altitude, full-waveform LiDAR survey has the capability to provide a topographic characterization of the bathymetry of a debris flow channel comparable (i.e., not significantly different) to that of a morphological guided, ground-based geodetic survey. On the other hand, a GNSS survey could not ensure a reliable characterization of channel bottom form (e.g., rock steps and bouldered reaches) and longitudinal features (e.g., high-gradient channel banks), if they are not properly surveyed. Noteworthy, no remarkable differences in the outlined results are observed by thresholding the DoD map at a 99% and 68.3% probabilistic confidence interval.

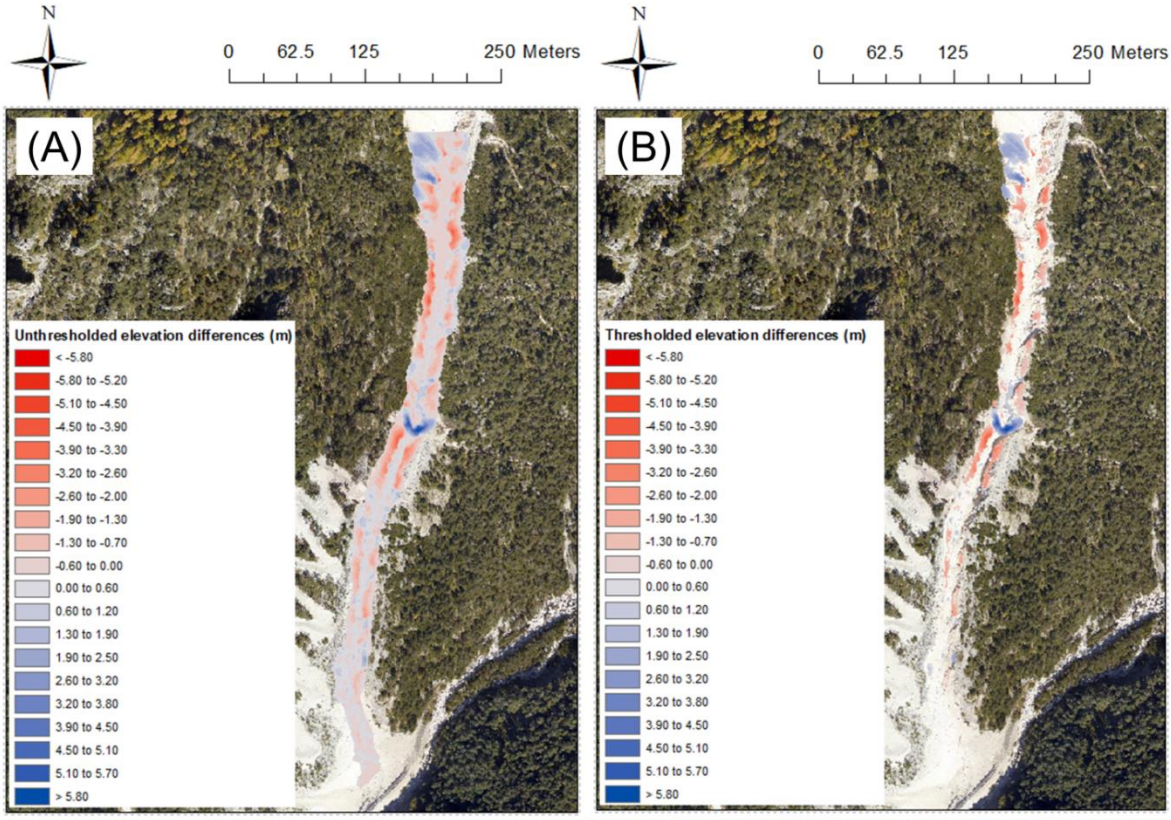

Figure 3.7: (A) Unthresholded DoD map, and (B) corresponding thresholded one (95% probabilistic confidence interval) calculated by using the propagated FIS-based DEMs elevation uncertainty estimates.

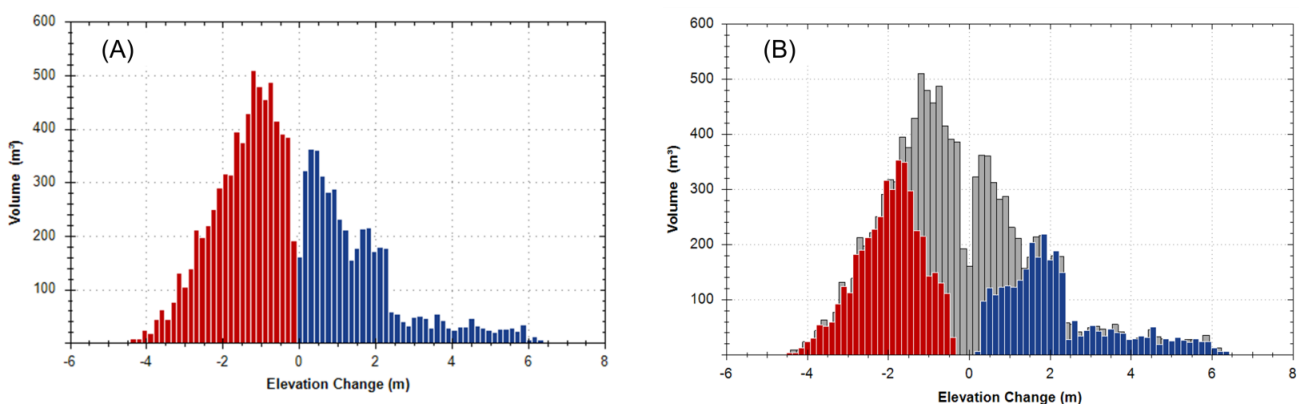

Figure 3.8: Elevation discrepancy distribution of the (A) unthresholded and (B) thresholded at a 95% confidence interval DoD maps. Note that the gray bars correspond to the non-significant elevation discrepancies.

3.3.4 Evaluation of the survey techniques effects on debris flows routing modeling

In Figure 3.9 and Figure 3.10, we report the 300-years return period run results in terms of simulated solid-liquid discharges and changes in the channel morphology in correspondence of the control sections highlighted on the thresholded DoD map.

Figure 3.9 shows that the higher differences between the simulated solid-liquid discharges occur in correspondence of the rock step (e.g., between the control sections 2 and 3), where the thresholded DoD map shows significant elevation discrepancies. Conversely, where no significant elevation discrepancies are observed, no meaningful differences in the modeled solid-liquid discharges are detected (e.g., control sections 1 and 5). A similar behaviour appears when terrain profiles are considered (Figure 3.10): the higher discrepancies between the post-event terrain profiles are detected where the pre-event DEMs show meaningful differences (e.g., control sections 2 and 3).

As shown in Figure 3.11, the observed differences in the model results are due to a significant change in the simulated flow dynamics in correspondence of the rock step, where the two DEMs provide a different topographic characterization of the channel morphology. In detail, just upstream the rock step (Figure 3.11A), the higher erosion depths are modelled by using the LiDAR-derived DEM as input topographic surface, whereas, downstream the rock step, the higher erosion depths are observed in the GNSS-based model run (Figure 3.11B). This evidence is strictly linked to the adopted schematization of the sediments entrainment-deposition processes (see Subsection 2.8). As a matter of fact, the erosion/deposition processes are modeled by assuming the bottom slope and the flow velocity as controlling factors, which in turn depend on the channel morphology. Noteworthy, the recognized change in the cell routing model behaviour also affects the downstream simulated flow dynamics, thus determining relevant discrepancies between the simulated solid-liquid discharges and channel morphology after the event even if no meaningful differences in the input topographic surfaces are observed (e.g., control section 4 of Figure 3.9 and Figure 3.10).

No remarkable differences in the outlined behavior are observed by analyzing the 50-years return period model outcomes, meaning that the influence of the tested survey techniques on the cell routing model is not strongly affected by the magnitude of the modeled event scenario.

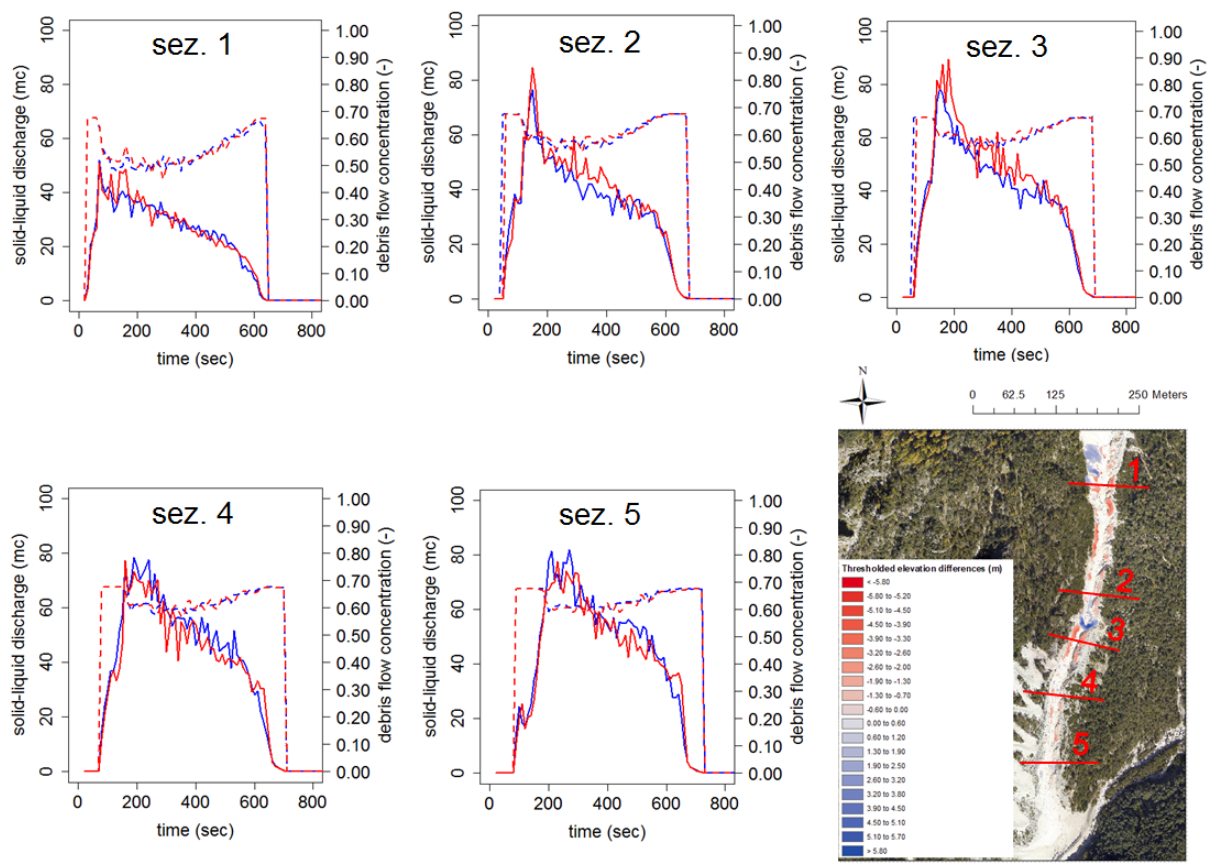

Figure 3.9: Comparison of the simulated 300-years return period debris flow solid-liquid discharges (continuous lines) and corresponding volumetric sediment concentrations (dotted lines), in the case of GNSS- and LiDAR-derived DEMs (blue and red lines, respectively). Insert: thresholded (95% probabilistic confidence interval) DoD map.

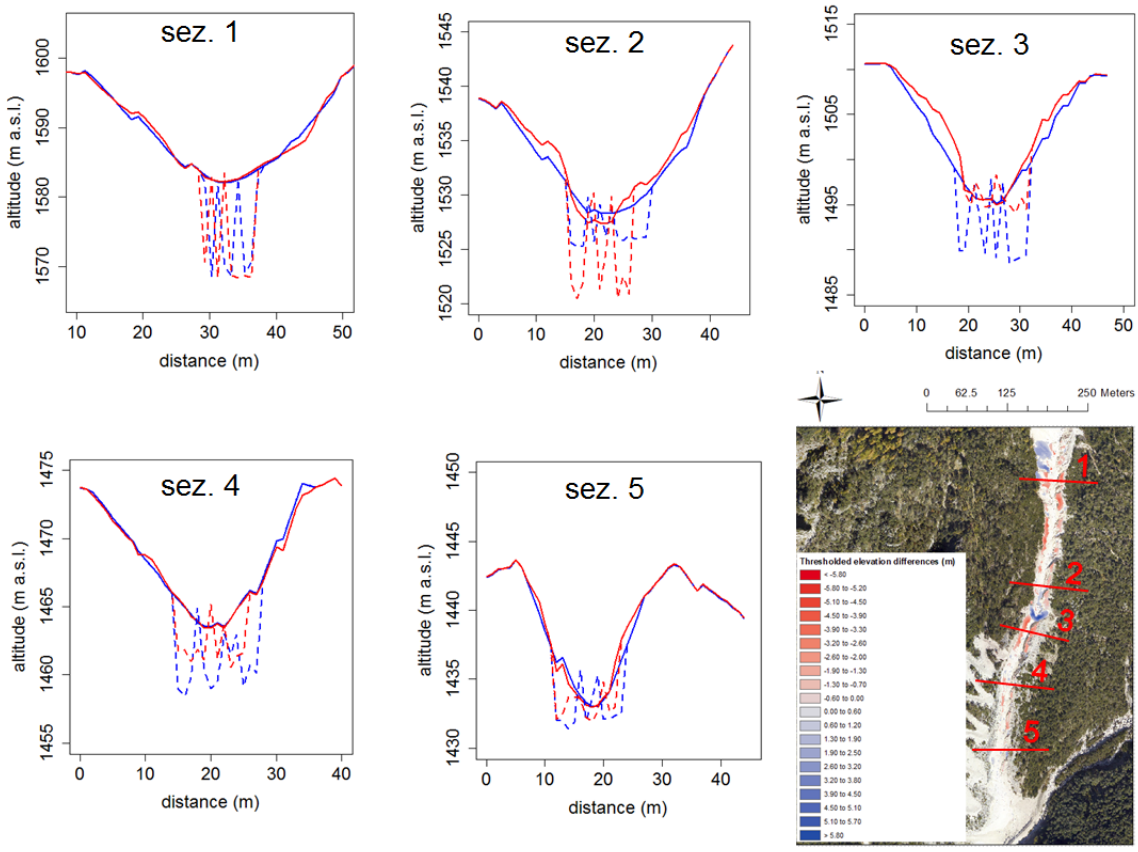

Figure 3.10: Comparison of the terrain profiles before (continuous lines) and after the modeled 300-years return period event scenario (dotted lines), in the case of GNSS- and LiDAR-derived DEMs (blue and red lines, respectively). Insert: thresholded (95% probabilistic confidence interval) DoD map.

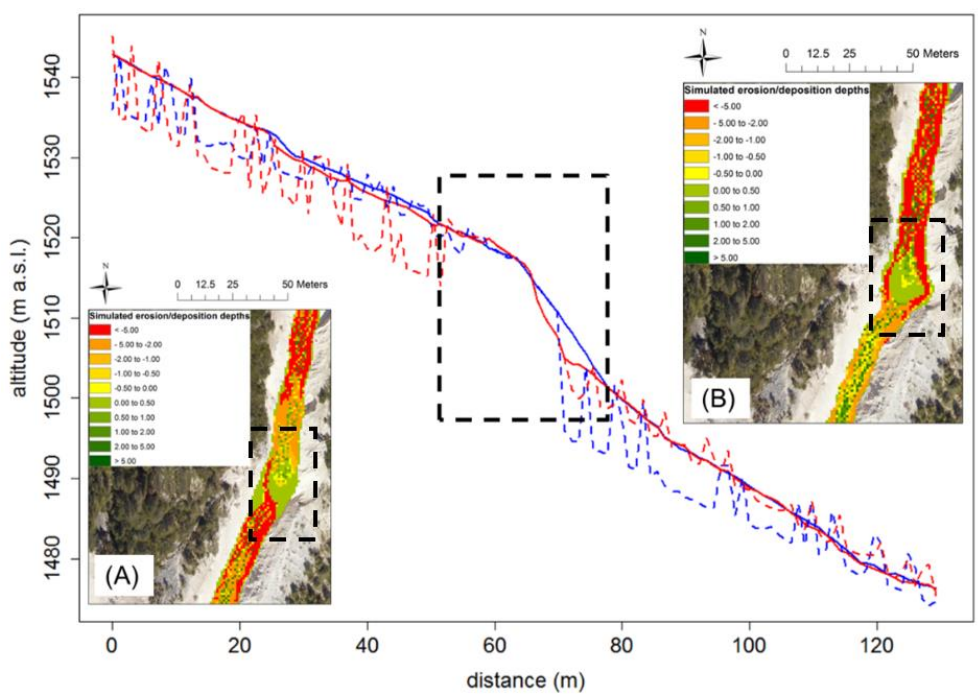

Figure 3.11: Comparison of the terrain profiles before (continuous lines) and after the modeled 300-years return period event scenario (dotted lines), in the case of GNSS- and LiDAR-derived DEMs (blue and red lines, respectively). The inserts correspond to the simulated erosion/deposition depths (m), in the case of (A) GNSS- and (B) LiDAR-derived DEMs. Dotted black line denotes the rock step.

3.4 Conclusions

In the present research, we initially assessed and compared the performances of a ground-based (i.e., GNSS) and an aerial-based (i.e., full-waveform LiDAR) survey technique in characterizing the complex topography of a 1 km length debris flow channel reach located in the Venetian Dolomites. After that, we investigated the influence of the different topographic characterization of the channel morphology on the outcomes of a GIS-based cell model for simulating stony debris flows routing, by considering both high- and low-magnitude flow conditions.

The accuracy and elevation uncertainty analyses carried out on the interpolated DEMs highlighted that both the tested survey techniques could be used to generate bias-free and accurate high-resolution DEMs of debris flow channels, also featuring low magnitude uncertainty values in correspondence of the channel bottom. It might suggest that both the tested survey techniques provide a topographic characterization of a debris flow channel morphology suitable for channelized debris flows routing modeling applications. However, the performed DoD analysis pointed out that, although the two compared survey techniques provide a comparable (i.e., not statistically different) topographic characterization of the channel bathymetry, meaningful discrepancies could be detected in correspondence of morphologically complex channel features (e.g., channel banks and longitudinal/transversal slope discontinuities) mainly due to the inherent limitations of the GNSS technology (e.g., site accessibility).

Furthermore, the research also highlighted that the detected discrepancies have the potential to affect the GIS-based cell routing model behavior, regardless the magnitude of the simulated event scenario. This leads to the conclusion that the choice of the survey technique could represent a determining factor for debris flows routing modeling.

The extrapolation of the research conclusion must be done with care for at least three reasons:

- the investigation was performed by focusing on a channelized debris flow. In the case of non-channelized debris flows, it might be expected a different effect of the survey techniques on the simulated flow dynamics, due to both the lower flow depths and velocities, which could imply processes different from erosion (i.e., deposition or mixed entrainment/deposition processes);
- the investigation was carried out on a debris flow channel reach mainly subject to entrainment processes. Different findings might be obtained by focusing on channelized debris flows mainly featuring sediment deposition or mixed sediment entrainment/deposition processes;
- the use of different rheological models or sediments entrainment-deposition process schematizations might lead to different conclusions.

Therefore, in order to improve the knowledge gained in this work, future researches have to be carried out on the outlined biases.

Supplementary material

Author(s)	Modelling approach (1D, 2D, combined 1D and 2D)	Calibration (validation) exercise	Source of DEMs (spatial resolution, m)	Type of DEMs	Reported DEMs vertical accuracy (m)	Study area	Assessment approach	Main finding(s)
Wilson and Atkinson (2005)	Combined 1D and 2D, unsteady state simulation (return period > 100 years)	No (no)	InSAR (30), Vectorial Cartography 1:10 000 (30), Vectorial Cartography 1:10 000 improved with DGPS measurements (30)	Raster-grid	InSAR = 17.17, Vectorial Cartography 1:10 000 = 1, Vectorial Cartography 1:10 000 improved with DGPS measurements (-)	912 km length reach of Nene River (Northamptonshire, England)	Comparison between observed and simulated flood extents, for a real flood event. Furthermore, also the flow depths at flood peak, flooded areas at flood peak, mean depths over the flooded areas, flood volumes, outflow discharges, times of maximum flood depth, and times of initial flooding simulated by the different model runs were compared	The authors found large differences both in the predicted inundation extents and in the dynamic of the modelled flood event, mainly due to the spatial character of the used topographic data. In detail, the Vectorial Cartography 1:10 000-based model run overestimated the observed inundation extent and predicted greater flooded areas, mean depth over the flooded areas, flood volume, and time of maximum flow depth than the InSAR-based model run, mainly due to surface over-generalisation. The authors highligthed that to make use of contour data for flood inundation modeling they need to be made more representative of the floodplain and channel topography by using additional height measurements
Casas et al. (2006)	1D, steady state simulation (return periods = 2, 5, 25, 50, 100, and 500 years)	No (no)	rtkGPS-EDM including bathymetric data (-), LiDAR (1, 2, 3, 4), Vectorial Cartography 1:5 000 (-), LiDAR improved with bathymetric data (1), LiDAR improved with bathymetric and rtkGPS-EDM data (1), Vectorial Cartography 1:5 000 improved with bathymetric data (-), Vectorial Cartography 1:5 000 improved with bathymetric and rtkGPS-EDM data (-)	TIN	LiDAR (1x1m) = 0.30 (1.60 at low flow zones), LiDAR (2x2m) = 0.41, LiDAR (3x3m) = 0.46, LiDAR (4x4m) = 0.54, Vectorial Cartography 1:5 000 = 2.75 (6.35 at low flow zones)	2 km length reach of the Ter River (Sant Julià de Ramis, Girona, Spain)	Comparison among the flow levels and related rating curves predicted in the different model runs, by assuming the rtkGPS-EDM including bathymetric data-based model run results as reference. Furthermore, also the flooded areas simulated in the different model runs were compared to the ones predicted in the LiDAR improved with bathymetric and rtkGPS-EDM data-based model run, which was assumed as reference. The sensitivity of the hydraulic model results to variations in the roughness coefficient was finally analysed for each employed topographic dataset	Due to the inaccurate representation of the channel and floodplain topography, the authors found that the Vectorial Cartography 1:5 000-based model runs resulted in much higher predicted water surface elevations than those obtained by using the other topographic sources, especially at the lower flood magnitude. For all the model runs, the agreement with the results of the reference one improved by adding the rtkGPS-EDM and bathymetric data. Furthermore, they found both a clear tendency of increasing predicted flooded areas as the accuracy of the used topographic data decreased, and a greater sensitivity of the model run results to roughness coefficient variations for the more detailed and accurate topographic datasets. No meaningful differences in the model performances were observed by changing the spatial resolution.
Cook and Merwade (2009)	1D, 2D, steady state simulation (return period = 100 years)	No (no)	LiDAR (3, 6), USGS (10), USGS (30), LiDAR improved with bathymetric data (3, 6), USGS improved with bathymetric data (10), USGS improved with bathymetric data (30)	Raster-grid	-	Strouds Creek (Orange County, North Carolina), Brazos River (Fort Bend County, Texas)	Comparison between the flood inundation maps predicted in the different models runs and the ones developed by the FEMA through the Map Mod program, which were assumed as reference	The authors found that coarser inaccurate DEMs provided higher flow depths, larger inundation extents, and the worst agreement with the FEMA flood maps. Furthermore, the reserach highligthed both the importance of including bathymetric details in the used topographic dataset, and that the overall uncertainty in flood inundation mapping due to the topography (source and spatial resolution) is reduced when a 2D modeling approach is used

Author(s)	Modelling approach (1D, 2D, combined 1D and 2D)	Calibration (validation) exercise	Source of DEMs (spatial resolution, m)	Type of DEMs	Reported DEMs vertical accuracy (m)	Study area	Assessment approach	Main finding(s)
Alho et al. (2009)	1D, steady state simulation (return period = 100 years)	Yes (no)	LiDAR (1), Vectorial Cartography 1:10 000 (25), Vectorial Cartography improved with stereoscopic measurements of aerial images 1:16 000 (10). All DEMs were integrated with bathymetric data (river cross-sections data derived from ground surveys)	Raster-grid	LiDAR = 0.19, Vectorial Cartography 1:10 000 = 1.79, Vectorial Cartography improved with stereoscopic measurements of aerial images 1:16 000 = 0.81 m	Uskelanjoki River (Salo, Suothern Finland)	Comparison among the flood inundation maps predicted in the different model runs	The authors found that the Vectorial Cartography 1:10 000-based model run results were highly erroneous, mainly due to the poor representation of the channel and floodplain topography. The most reliable flood inundation map was obtained by using the LiDAR-derived DEM as input topographic data, although some inaccuracies were found along the riverbanks. The authors highlighted that the accuracy of flood modelling could be enhanced by integrating the input geometry with additional breaklines on river bank sections and floodplains
Ali et al. (2015)	1D (2D only for comparison), unsteady state simulation (return period -)	Yes (yes)	LiDAR (1, 2, 20, 30, 90), Vectorial Cartography 1:25 000 (20), ASTER (30), SRTM (90). All DEMs were integrated with bathymetric data (river cross-sections data derived from ground surveys)	Raster-grid	LiDAR (1x1m) = 0.58, LiDAR (2x2m) = 0.58, LiDAR (20x20m) = 0.68, LiDAR (30x30m) = 0.79, LiDAR (90x90m) = 1.27, Vectorial Cartography 1:25 000 = 4.66, ASTER = 7.01, SRTM = 6.47	30 km length reach of Johor River (Johor, Malaysia)	Comparison between observed and simulated water levels in correspondence of two internal cross-sections, for two real flood events. Furthermore, also the flow water profiles and inundation areas simulated in the different model runs were compared, by assuming the LiDAR (1x1m)-based model run results as reference	The authors found that the ASTER-based model run results were completely inaccurate. Furthermore, they found relevant differences in the simulated flood profiles and inundation areas, depending on the used topographic surface. The study also showed that the results of flood inundation models are more affected by the accuracy of the DEM than its spatial resolution
Bakula et al. (2015)	Combined 1D and 2D, steady state simulation (return period = 100 years)	Yes (yes)	LiDAR (1), Dense Image Matching supplemented by stereoscopic measurements of aerial images 1:13 000 (3), Analogue Photogrammetry of aerial images 1:13 000 (10), Vectorial Cartography 1:50 000 (60x40), ASTER (30). All DEMS were resampled at a spatial resolution equal to 5m	Raster-grid	LiDAR = 0.17, Dense Image Matching supplemented by stereoscopic measurements of aerial images 1:13 000 = 0.62, Analogue Photogrammetry of aerial images 1:13 000 = 0.95, Vectorial Cartography 1:50 000 = 2.69, ASTER = 5.08	Czarna Staszowska River (Rytwiany municipality, Poland)	Comparison among the flood inundation maps, maximum flow depths, and maximum flow velocities predicted in the different model runs, by assuming the LiDAR-based model run results as reference	The research proved that only the LiDAR and photogrammetric data are reliable elevation data sources for 2D hydraulic modeling. Furthermore, the authors did not recommend the use of small scale Vectorial Cartography- and ASTER-derived DEMs in 2D hydraulic models
Reil et al. (2017)	1D, steady state simulation (return periods = 1, 50, and 100 years)	No (yes)	LiDAR (-), ADCP (-), Total Station (-), LiDAR pre-processed by means of CroSolver*(-)	TIN	-	2.2 km length reach of the Otava River (Bohemia Region, Czeck Republic)	Comparison among the flow levels and flood inundation maps predicted in the different model runs, by assuming the Total Station-based model run results as reference	Regardless of the magnitude of the modelled event scenario, the authors found differences in the simulated flow levels and inundation extents. In detail, the LiDAR-based model run results showed the worst agreement with the reference ones, with the predicted flow depths and inundation extents overestimated mainly due to a coarse representation of the channel bathymetry

Author(s)	Modelling approach (1D, 2D, combined 1D and 2D)	Calibration (validation) exercise	Source of DEMs (spatial resolution, m)	Type of DEMs	Reported DEMs vertical accuracy (m)	Study area	Assessment approach	Main finding(s)
Bhuyian and Kalyanapu (2018)	1D, unsteady state simulation (return period = 10 years)	Yes (no)	LiDAR (3, 10, 27, 81), USGS-NED (3, 9, 28, 83), STRM (28, 83), ASTER (28, 83)	Raster-grid	LiDAR (3x3m) = 2.2, LiDAR (10x10m) = 2.2, LiDAR (27x27m) = 2.4, LiDAR (81x81m) = 3.0, USGS-NED (3x3m) = 2.2, USGS-NED (9x9m) = 2.2, USGS-NED (28x28m) = 2.5, USGS-NED (83x83m) = 3.1, STRM (28x28m) = 4.5, STRM (83x83m) = 4.9, ASTER (28x28m) = 7.4, ASTER (83x83m) = 7.5	35 km length reach of the America River (California)	Comparison among the flow levels and flood inundation maps predicted in the different model runs, by assuming the LiDAR (improved with batimetric data)-based model run results as reference	The authors found that the SRTM- and ASTER-based model runs overstimated both the flow depths and inundated areas, mainly due to a poor representation of the river bathymetry. However, the research highligthed that also the floodplain topography needs to be correct represented in the employed DEM for accurate flood inundation mapping

Table 3.1S: Main findings of researches focused on the influence of topographic data source on floods modeling results.

4 GIS-based cell model for simulating debris flow runout on a fan

This chapter represents an edited version of ***Gregoretti C., Degetto M., Boreggio M.[6] (2016). GIS-based cell model for simulating debris flow runout on a fan. Journal of Hydrology, 534, pp. 326-340.***

Summary

A GIS-based cell model, based on a kinematic approach is proposed to simulate debris flow routing on a fan. The sediment–water mixture is modeled as a monophasic continuum, and the flow pattern is discretized by square cells, 1 m in size, that coincide with the DEM cells. Flow occurs from cells with a higher mixture free surface to those with a lower mixture free surface. A uniform-flow law is used if the elevation of the former cell is higher than that of the latter; otherwise, the flow is simulated using the broad-crested weir law. Erosion and deposition are simulated using an empirical law that is adjusted for a monophasic continuum. The sediment concentration in the routing volume is computed at each time step and controls both erosion and deposition. The cell model is used to simulate a debris flow that occurred on the Rio Lazer (Dolomites, North-Eastern Italian Alps) on November 4th, 1966. Furthermore, the hydrologic and the hydraulic conditions for the initiation of debris flow are simulated, providing the solid–liquid hydrograph of the resulting debris flow. A number of simulations has been carried out with physically reasonable parameters. The results are compared with the extension of the debris-flow deposition area and the map of observed depths of deposited sediments. This comparison shows that the proposed model provides good performance. The analysis of sensitivity carried out by systematically varying the model parameters shows that lower performances are associated with parameter values that are not physically reasonable. The same event is also simulated using a cellular automata model and a finite volume two-dimensional model. The results show that the two models provide a sediment deposition pattern less accurate than that provided by the present cell model.

[6] The author carried out the reconstruction of the historical debris flow event, the field survey, the numerical simulations, and the analysis on the obtained results.

4.1 Introduction

Debris flows are rapid, gravity-induced mass movements consisting of a mixture of water, sediment, wood and anthropogenic debris that propagate along channels incised on mountain slopes and onto debris fans. In the Dolomites of ~~Italy (Ea~~stern Alps), such flows generally occur when sediments accumulated on the beds of channels incising debris fans, are entrained by the runoff descending from the upstream cliffs (Berti and Simoni, 2005; Gregoretti and Dalla Fontana, 2008; Tecca and Genevois, 2009; Degetto et al., 2015). Runoff-generated debris flows also occur in the Western Alps (Theule et al., 2012; Tiranti and Deangeli, 2015), the Pyrenees (Hurlimann et al., 2014), the Japan Alps (Imaizumi et al., 2006), the Rocky Mountains and in Southern California (Cannon et al., 2008; Coe et al., 2008; Kean et al., 2011, 2013; McCoy et al., 2012), the eastern Tibet-Plateau margin (Hu et al., 2016). The initiation and occurrence of debris flows by the sediments entrainment in water runoff has been experimentally demonstrated by Tognacca et al. (2000), Gregoretti (2000a,b) and Stancanelli et al. (2015) and theoretically explained after considering the hydrodynamic forces exerted by stream flows on the surface bed elements (Lamb et al., 2008; Gregoretti, 2008; Recking, 2009; Iverson and Ouyang, 2015). The routing path of debris flows generally coincides with the incised channel in the upper part of the fan, while it can deviate in the medium part (Takahashi, 2007), and spread in the lower part, where the slope of the terrain diminishes (Iverson et al., 1998; Rickenmann, 2005; Berti and Simoni, 2007; Guthrie et al., 2007; DAgostino et al., 2010). These phenomena severely impact the areas that debris flows cross due to the high velocity (up to 10 m/s) and the large volumes of mobilized, transported and deposited sediment. The preparation of hazard maps, therefore, assumes a crucial role for any risk analysis against debris flows (Hurlimann et al., 2006). Hazard mapping consists of identifying the areas that are either historically or potentially threatened by debris flows. Hazard maps, are, thus, generated using data from surveys of areas flooded by debris flows and simulations of potential scenarios. The methods used to simulate a potential scenario are either empirical (Aulitzky, 1973) or model based. Among the large body of models available in literature we here recall the following types: empirical-statistical (Berti and Simoni, 2007; Griswold and Iverson, 2008; Magirl et al., 2010; Scheidl and Rickenman, 2010; Berti and Simoni, 2014), empirical-statistical combined with simple flow equations (Scheidl and Rickenman, 2011), topographic gradient-based (Gruber, 2007), numerically based by integration of shallow water equations (O'Brien et al., 1993; Brufau et al., 2000; Liu and Wang, 2006; Rickenmann et al., 2006; Medina et al., 2008; Armanini et al., 2009; Begueira et al., 2009; Pirulli, 2010; De Blasio et al., 2011; Mergili et al., 2012; Pudasaini, 2012; Rosatti and Begnudelli, 2013; Iverson and George, 2014), SPH or Lagrangian (McDougall and Hungr, 2004; Pastor et al., 2008) and cellular automata (Deangeli and Segre, 1995; DAmbrosio et al., 2003; Deangeli, 2008). In principle, models that guarantee the most reliable results are the shock-capturing models that integrate the depth averaged momentum and continuity flow equations and the sediment balance equation. These models, however, require a considerable computational time and can encounter some difficulties in the case of very sloping and irregular topography that are resolved after some slight terrain elevation adjustment. As a consequence the time occurring for simulating a scenario increases. These aspects prevent their use at the regional scale, in which the number of debris flows to be simulated is very large, and for civil protection when quick investigations of possible inundated areas are requested after a critical rainfall pattern is individuated by now-casting. Currently, regional-scale models used for constructing hazard maps are those based on topographic-gradient and those based on empirical-statistical models. Due to their simplicity, these models require a shorter time both for input data preparation and computation and do not encounter numerical problems in the case of very sloping and irregular topography. However, due to the lack of specific equations modeling the routing phase, simulations often exhibit inaccuracies in reproducing both the inundated areas and the pattern of erosion and deposition depths. A recent attempt to account for debris flow routing has been put forward by Chiang et al. (2012) through a cell model that assumes uniform flow conditions and neglects back water effects as well as erosion and deposition. Therefore, a physically based model that simulates erosion and deposition is still missing for the analysis at regional scale.

With the purpose of overcoming these disadvantages, we propose a GIS-based cell model that suitably solves simplified flow and sediment entrainment/deposition equations. Therefore, this model allows reliable simulations of debris flow routing including the sediments erosion and deposition in a reasonable amount of time, and, without suffering from numerical problems due to the irregularity, complexity and sloping of terrain. Both input data and outputs are binary

raster files, that can be easily managed by any GIS platform. This helps both data preparation and outputs analysis, and allows the construction of simple plugins to run the model in each GIS platform.

A cell model was initially proposed by Zanobetti et al. (1970) for simulating the flood inundation of a large rural area. This model was successively adapted to simulate flood and runoff routing in urban areas (Riccardi, 1997; Bates and De Roo, 2000; Horrit and Bates, 2001; Mascarenhas and Miguez, 2002; Miguez et al., 2009; Chen et al., 2009). The cells are areas of flow field and are linked each other by equations based on the flow characteristics (channel flow, weir flow, and floodplain flow). In particular, Bates and De Roo (2000) denoted this type of model as raster-based model when working in a GIS environment where the cells are the pixels of a raster map. Channel flow equations can either be the uniform flow equation (Zanobetti et al., 1970; Mascarenhas and Miguez, 2002) or the De Saint Venant equation (Miguez et al., 2011). In some cases (Chen et al., 2009) the transfer of water from wet cells to dry cells is simplified and governed by static conditions (level difference) rather than dynamic conditions (flow equations). Cell models based on GIS have been also proposed to simulate rainfall-runoff-soil erosion and sediment outflow from catchments (Beasley et al., 1980; deRoo et al., 1989; Morgan et al., 1998; Ewen et al., 2000; Jain et al., 2005). These models are typically oriented to simulate events at the watershed level for long periods of time (decades or longer). As written above, a cell model was also proposed for debris flow simulation by Chiang et al. (2012). It implements uniform flow and continuity equations after determining the flow path, a priori, along the steepest slope. It, then, requires DEM preprocessing to eliminate holes that can interrupt the flow path and determine an indefinite increase of flow depth. Moreover, it invariably conveys the flow toward the more depressed cell, and does not compute deposition and entrainment. As a consequence, this model does not provide adequate information on the spreading of debris flows in the deposition areas and indications on the distribution of deposition depth needed to quantify building damages in hazard and risk analyses (Fuchs et al., 2007).

The cell model proposed here is based on a kinematic approach that does not require DEM preprocessing for routing simulation. In addition, the empirical erosion–deposition law of Egashira and Ashida (1987) is used to simulate the entrainment-deposition (Brufau et al., 2000, see). The choice of a kinematic routing approach is based on the analysis carried out by Arattano and Savage (1994) who showed that a kinematic model can satisfactorily simulate debris flow routing in a sloping channel. In addition, Di Cristo et al. (2014a,b) recently studied the applicability domain of simplified momentum equations (kinematic, diffusive and quasi-steady wave models) used to model muddy flows. In particular, Di Cristo et al. (2014a) demonstrates that the applicability domain of the kinematic approach for muddy flows is larger than that of turbulent clear water. Therefore, the applicability of the kinematic wave model for the routing of debris flows in the grain-inertial range at high slopes appears to be justified.

The proposed model is tested by comparing the simulation of the debris flow that occurred on Rio Lazer on November 4th, 1966, with the map of observed sediment deposits. The objective is to explore the capability of a simple but robust model to provide reliable estimates of debris flow routing and deposition on a fan.

For this purpose, the same event has been also simulated using a cellular automata model based on a kinematic approach and a finite volume two-dimensional equation model based on the shallow water approximation. Comparison of the results should provide another test of the capability of the proposed model in simulating debris flow.

Gregoretti et al. (2011) conducted simulations of this event using a previous version of the model and a schematic inflow hydrograph derived through an approximated hydrological computation. The main differences in the present work are the input solid–liquid hydrograph, the DEM and the map of observed deposition depths, the algorithm for the sediment deposition and entrainment process, and the sensitivity analysis.

The remainder of this paper is organized as follows. Section 2 presents the model. Section 3 describes the debris flow that occurred on Rio Lazer on November 4th, 1966. Section 4 presents the simulation of the event and its comparison with the estimated deposition depths of the runout area. Section 5 describes the sensitivity analysis and discusses the influence of the model parameters on the simulations. Finally, Section 6 presents some conclusions.

4.2 The model

4.2.1 Overview

The flow cell scheme of Zanobetti et al. (1970) is adapted to simulate the spreading of a debris flow on a fan. Two hydraulic links are used to model the flow exchange of a cell with its neighbors: uniform flow and broad-crested weir equations. The uniform flow equation is used to model debris flow dynamics along positive slopes, whereas the weir equation is considered in the case of adverse slopes. This latter hydraulic link allows the simulation of routing in areas with local depressions and in the presence of obstacles.

The flow pattern is discretized using pixels of the DEM that coincide with the cells. The equation of continuity and the above described discharge relationships between neighboring cells are written for each cell. Eight possible flow directions are assumed (Fig. 4.1a), as in the FLO-2D model (O'Brien, 2007) and in cellular automata models (Deangeli and Segre, 1995). Moreover, sediment entrainment and deposition are simulated by suitably adapting the erosion–deposition law proposed by Egashira and Ashida (1987), as described later on.

The basic generalized assumptions of the model are those given by Mascarenhas and Miguez (2002). They are extended here to the case of debris flows and can be summarized as follows:

1. The solid–liquid mixture is assumed to be a monophasic continuum.
2. The exchange-flow relationships between adjacent cells consist of uniform flow and broad-crested weir equations depending on the slope sign.
3. The flow surface within a cell is assumed to be horizontal.
4. The models considers eight flow directions.
5. The flow sections between cells are considered to be rectangular.
6. The flow volume inside a cell is computed as a function of the flow depth.
7. The exchange flows of a cell with the neighboring ones occur simultaneously.
8. The discharge exchanged between neighboring cells depends on the level of the flow surface and on bottom elevation of the cells.
9. The deposition volume in a time step cannot be larger than the volume of the solid–liquid mixture within a cell after subtraction of the outgoing fluxes.
10. Sediment concentration of the deposited and eroded volumes is the dry solid concentration of the sediment bed.
11. The computational method is explicit, and the time step is computed ensuring the Courant–Friedrichs–Levi, CFL, condition (Courant et al., 1967).

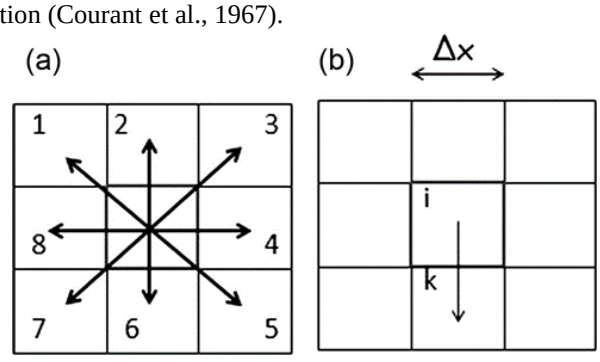

Fig. 4.1. The eight possible flow directions (left) and outflow from central cell (right).

The first assumption fails when sediment concentration is low because velocity lag between the two phases is not negligible (Armanini et al., 2009) and the mixture can no more be treated as monophasic. This occurs when grain size distribution of sediments is narrow so that large voids are among particles and when slope decreases to values

corresponding to the immature debris flows conditions. In essence, this model can be classified as a physically based conceptual model. It can also be viewed as a topographic-gradient model with simplified equations that control routing and sediments entrainment or deposition.

4.2.2 Continuity equation

In differential form, the continuity equation for a cell reads:

$$A\frac{dh_i}{dt} = Ai_{b,i} - \sum_{k=1}^{8} Q_{i,k} \tag{4.1}$$

where the subscripts *i* and *k* refer to the reference cell and the generic surrounding cell, respectively (Fig. 4.1b); *t* is the time; *A* is the area of the cell; h_i is the flow depth of *i*th cell; $i_{b,i}$ is the rate of change of bed elevation of *i*th cell and it is positive when erosion occurs, and negative when deposition occurs); and $Q_{i,k}$ is the discharge exchanged between the *i*th cell and the surrounding *k*th cell (Fig. 4.1b), assumed to be positive if directed toward kth cell and negative otherwise.

4.2.3 Hydraulic links between cells: discharge exchange relationships

As previously described we consider two types of hydraulic links (i.e., relationships providing the exchange discharge) between a cell and those surrounding it with lower mixture surface elevations: the uniform-flow equation proposed by Tsubaki (1972) in the case of positive slopes (Fig. 4.2a) and the modified broad-crested weir-flow equation in the case of adverse slopes (b). The discharge equations read:

$$Q_{i,k} = C\Delta x h_i w_k \sqrt{g h_i sin\theta_{i,k}} \tag{4.2}$$

$$Q_{i,k} = C_q \Delta x s_k \sqrt{2g}(h_i - z_k)^{1.5} \tag{4.3}$$

where *C* is the conductance coefficient (Tsubaki, 1972); Δx is the cell size ($A^{0.5}$); $\theta_{i,k} = \tan^{-1}(z_i - z_k)/\Delta x$ is the angle with respect to the horizontal formed by the line joining the centers of *i*th and *k*th cells; z denotes the bottom elevation and C_q is a discharge coefficient. Two weighting functions w_k and s_k are introduced for flow partitioning along different directions. They read:

$$w_k = \frac{sin\theta_{i,k}}{\sum_{k=1}^{n} sin\theta_{i,k}} \tag{4.4}$$

$$s_k = \frac{h_i - z_k}{\sum_{k=1}^{m}(h_i - z_k)} \tag{4.5}$$

where *n* and *m* are the numbers of surrounding cells for which θ_k and $(h-h_k)$ are positive ($n + m \leq 8$). Eq. (4.2) implies the grain-inertial rheology of the solid–liquid mixture. Indeed it can be straightforwardly derived by integrating along the flow depth the dispersive normal stress given by Bagnold (1954) (Takahashi, 1978, 1991). The discharge coefficient in the absence of experimental observations and as a first approximation, is assumed to be equal to that of water (0.385).

Finally, the weighting functions, w_k and s_k depend on the bed and flow surface drops, respectively, and are used to account for the use of one-dimensional discharge relationships in a two-dimensional flow field.

4.2.4 Erosion and deposition

Erosion and deposition are modeled using the empirical relationship of Egashira and Ashida (1987), also used by Brufau et al. (2000), which is converted for a continuum mono-phase:

$$i_{b,i} = K\left[U_{i,k}\left(sin\alpha_{i,k} - sin\theta_{LIM}\right)\right] \tag{4.6}$$

where K is an empirical constant ranging between 0 and 1; $U_{i,k}$ is the mean velocity corresponding to the discharge $Q_{i,k}$; $\alpha_{i,k} = \theta_{i,k}$ if $\theta_{i,k} > 0$ (uniform flow) and $\alpha_{i,k} = \Theta_{i,k} + \theta_{i,k}$, otherwise (weir flow); with $\Theta_{i,k}$ the angle formed by the line joining the centers of the flow surfaces of the ith and kth cells with the horizontal (Fig. 4.2b); and U_{LIM} and θ_{LIM} are limiting values for U and θ, respectively. The angle $\alpha_{i,k}$ is a reference angle corresponding to the slope that causes the flow of the solid–liquid mixture: the bed slope for uniform flow and the flow surface slope for weir flow. In this last case, the flow surface slope is further decreased of the adverse topographic slope, factor that hinders erosion and promotes deposition. The parameters U_{LIM} and θ_{LIM} assume different values for erosion ($U_{LIM\text{-}E}$ and $\theta_{LIM\text{-}E}$) and deposition ($U_{LIM\text{-}D}$ and $\theta_{LIM\text{-}D}$), so that erosion occurs if $\alpha_{i,k} > \theta_{LIM\text{-}E}$ and $U_{i,k} > U_{LIM\text{-}E}$, and deposition if $\alpha_{i,k} < \theta_{LIM\text{-}D}$ and $U_{i,k} < U_{LIM\text{-}D}$. Moreover, erosion is computed only if $dh/dt > 0$ according to the field observations of (Berger et al., 2011), that it occurs close to the debris flow front and starts before the maximum value for flow depth is reached.

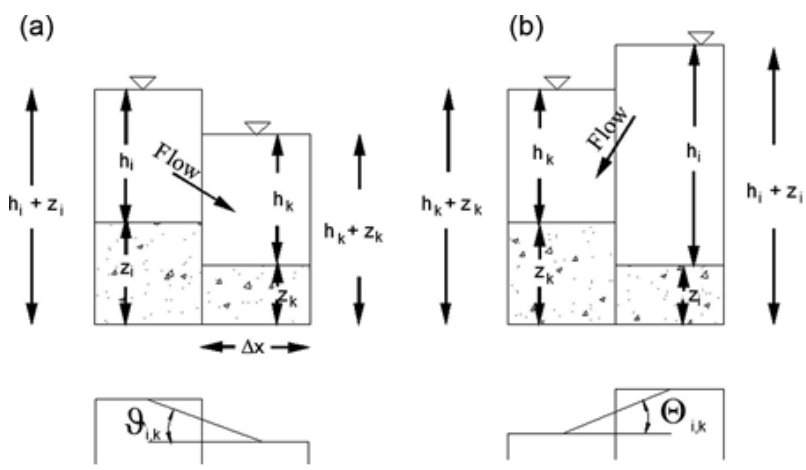

Fig. 4.2. Hydraulic links between two neighboring cells.

Erosion and deposition are computed along the steepest of the flow directions because of the one-dimensional nature of Eq. (4.6). Considering a generic direction transversal to the steepest direction, in fact, could lead to unrealistically large deposition. Moreover, a cell could be subjected to both erosion and deposition at the same time.

According to Rosatti and Begnudelli (2013), entrainment of sediments by the overflowing mixture is possible if its volumetric sediment concentration, c, is smaller than the limiting upper value 0.9 c_* (Takahashi, 2007), where c_* is the solid concentration of dry bed (some authors refer to this concentration as the packing concentration).

Similarly, deposition occurs if c is larger than a limiting lower sediment concentration for debris flow, c_D set equal to 0.05. This limit is introduced to prevent c from becoming negative if a large deposition occurs, even though no substantial differences have been observed by setting $c_D = 0$.

Finally, the sediment concentration of eroded and deposited volumes is set equal to c and erosion and deposition are assumed to occur under saturated conditions. This latter assumption implies that in the case of deposition, the liquid phase remains in the voids between sediments without spilling out and, hence, dewatering of sediment deposits are not accounted as a first approximation.

The reasons for modeling erosion and deposition processes through Eq. (4.6) are explained as follows.

Entrainment occurs if basal shear stress becomes larger than shear strength of sediments bed, whereas deposition occurs when the stresses exerted by the mixture on the flowing sediments, depending on the rheology, are not able to balance the component of gravity force acting on solid particles along the normal to the flow. Unfortunately, general relationships linking these stresses to the erosion or deposition rates are yet missing.

Another approach for computing the erosion and deposition rates is that used by Fraccarollo and Capart (2002), Armanini et al. (2009) and Rosatti and Begnudelli (2013), based on the assumption that sediment concentration immediately adapts to the uniform flow conditions with the local values of flow depth and velocity. The sediment concentration in uniform flow conditions is denoted as transport capacity. Erosion and deposition rates, then, become proportional to the difference between the local sediment concentration and the transport capacity, computed through a rheological or empirical law. In some cases, however, this approach could give uncorrected results, when bed slopes do not correspond to those within the application domain of the equation computing the transport capacity, or during the routing of a formed surge. In this case, the erosion would be mainly computed in the liquid tail where the difference between the local sediment concentration and transport capacity is large, rather than not close the front as it really occurs (Stock and Dietrich, 2003; Reid et al., 2009; Berger et al., 2011), where the local sediment concentration approximates the transport capacity.

In order to avoid all these drawbacks, we decided to compute the erosion and deposition rates by adapting the empirical equation of Egashira and Ashida (1987), i.e. Eq. (4.6).

Bed slope angle (embodied by the reference angle $\alpha_{i,k}$), in fact, results to be a control factor both for deposition and erosion because they occur under (Whipple and Dunne, 1992; Hungr et al., 2005) and over (Stock and Dietrich, 2003; Hungr et al., 2005; Gartner et al., 2015) a limit bed slope angle. Flow velocity also results to be another control factor (Stock and Dietrich, 2003; Jacob, 2005; Gartner et al., 2015). The use of Eq. (4.6) also allows the back simulation of both large deposits, usually observed at the onset of deposition (Rickenmann, 2005; Gregoretti et al., 2011) (when the term sin $\alpha_{i,k}$ - sin $\theta_{LIM\text{-}D}$ is low and the velocity is quite high) and small deposits occurring just downstream the large deposition areas (where the quantity sin $\alpha_{i,k}$ - sin $\theta_{LIM\text{-}D}$ is high and the velocity low). The values of the parameters $U_{LIM\text{-}D}$ and $\theta_{LIM\text{-}D}$ can be determined by field measurements or numerical back analysis of observed events. The present approach, then represents an attempt to relate the erosion and deposition (basically controlled by basal and internal stresses) to well defined kinematic and morphological quantities (flow velocity and bed slope angle).

4.3 Numerical scheme, initial and boundary conditions

The time step Dt is computed according to the CFL condition (Courant et al., 1967) using a Courant number ($a = \Delta t/\Delta x; a = U + \sqrt{gh}$) equal to 0.95. This constraint does not originate from numerical instability problems but is used for the purpose of respecting the physics of routing.

The numerical scheme is explicit, and after integration in time, the Eq. (4.1) for the generic cell ith becomes (see Fig. 4.1b):

$$h_i^{t+\Delta t} = h_i^{t+\Delta t}\left[i_{b,i}^t - \frac{1}{A}\sum_{k=1}^{8} Q_{i,k}^t\right]\Delta t \tag{4.7}$$

where the subscripts *i* and *k* refer to the reference cell and the generic surrounding cell, respectively; apex *t* denotes time; and Δt is the time step.

The computation procedure is as follows: for each cell, the possible flow discharges towards the surrounding cells are computed according to Eqs. (4.2) and (4.3). If the computed outflow volume is larger than the cell volume, the flow discharges are decreased of the same percentage to ensure mass continuity. Afterwards, the rate of change of bed elevation that corresponds to the steepest flow direction is computed according to Eq. (4.6). In the case of deposition, if the computed deposited volume is larger than the difference between the cell and outflow volumes, the rate is decreased to obtain equality between the two volumes.

Oscillations between cells are prevented by decreasing the outflow discharge if the free surface of the receiving cell becomes higher than that of the initial cell to obtain the same level of free surface in both cells. DEM cells are divided into three classes: input cells, outflow boundary cells and routing cells. Input cells are feeded only by means of the input hydrograph and are not subjected to erosion and deposition. Routing cells are those that can exchange flow with all other cells, except inundating input cells. Boundary cells are the cells on the DEM border that can exchange flow with both other routing cells and the exterior. At the first time step, input cells are filled according to the input hydrograph. At the second time step, flow occurs from the input cells, filled during the previous time step, to the surrounding routing cells. At the end of the time step input cells are refilled according to the input hydrograph. At the subsequent time steps, flow occurs from the input cells, and the routing cells that were wetted during the previous time steps toward the surrounding routing cells. At the end of each time step, input cells are again refilled according to the input hydrograph. The flow routing is sequentially computed starting with the input cells followed by the routing cells in order of wetting.

Input data are time series of solid–liquid discharge and sediment concentration. During routing sediment concentration changes if deposition or erosion occur. As written before sediment concentration of eroded and deposited volumes is c_*. Sediment concentration is computed by the following equations:

$$c^{t+\Delta t} = \frac{V_S^{t+\Delta t}}{V_{ROUT}^t + V_{DE}} \tag{4.8}$$

$$V_S^{t+\Delta t} = c^t V_{ROUT}^t + c_* V_{DE} \tag{4.9}$$

where V_S and V_{ROUT} are the solid and solid–liquid routing volumes respectively; V_{DE} is the entrained/deposited volume in the time step Δt (positive if entrained, negative if deposited).

No conditions are applied at the boundary, and the mixture can leave the computational domain as either a uniform flow or as a weir flow (Bates and De Roo, 2000). The flow exchange with the exterior is simulated using Eqs. (4.2) and (4.3), without weighting functions, along the flow directions determined by the local boundary slopes. More specifically, the flow directions and slopes from the boundary cell toward the exterior coincide with those from the neighboring cells to the boundary cell along the same line.

At the end of each time step, the flow surface and bed elevations of all of the cells are simultaneously updated, on the base of the computed outflow/inflow and deposited/entrained volumes.

This parallelization technique is quite similar to that used in the cellular automata models. Therefore, there is a strong similarity between this cell model and cellular automata models.

4.4 Rio Lazer basin and debris flow that occurred on November 4th, 1966

The Rio Lazer basin is located in the Province of Trento (Dolomites, North Eastern Italy), and the maximum altitude is 1608 m a.s.l. Its extension is 1.57 km^2, and its average slope is 30.8%. The Rio Lazer torrent originates at 1200 m a.s.l. and joins the Cismon torrent at 742 m a.s.l., between the built-up areas of Siror and Tonadico (see Fig. 4.3). On November 4th, 1966, a strong meteoric event hit Northern and Central Italy, and several debris flows and floods occurred in mountain areas and plain areas, respectively (the famous town of Florence was subjected to inundation). In the Rio Lazer basin, the debris flow initiated at 1000 m a.s.l. and routed along the main channel. Immediately downstream from the wooded area (Fig. 4.4), the debris flow spilled out of the channel and flooded the entire fan, depositing a volume of sediments of approximately 56,000 m^3. Debris material that laid on the bottom and that originated from bank failures (Fig. 4.4) was mobilized by flowing water, resulting in the occurrence of a debris flow. The map of observed deposition depths provided by the Mountain Basins Agency of the Province of Trento and used by Gregoretti et al. (2011) has been updated and reconstructed after the comparison with the deposits shown in Fig. 4.4. Missing deposition depths were obtained using stereoscopic techniques applied to pairs of photos of deposits taken immediately after the event. The updated map of observed sediment deposits is shown in Fig. 4.5, and it is superimposed over the aerial photograph taken in 1973. The deposition area was divided into four zones corresponding to the deposition depth intervals: 0–0.1; 0.1–0.5; 0.5–1.0 and 1.0–4.0 m. The mean deposition depths are computed as the average of each interval: 0.05, 0.3, 0.75 and 2.5 m. The deposited sediment volume, V_D, (sum of the solid volume with the volume of voids between particles) computed using the mean deposition depths is equal to 55,886 m^3. Analysis of the photos taken after the event shows that the majority of deposits consisted of piles of debris with almost negligible and very small presence of a mud matrix. This result suggests a grain-inertial rheology for the investigated debris flow. The original DEM (Gregoretti et al., 2011) was obtained from a total station survey and shows several inaccuracies that can affect the simulation results. Since the majority of the terrain has remained unchanged, in the present work we have used the LiDAR-based DEM provided by the Province of Trento with a pixel size of 1 m. This DEM was adjusted by reporting only the buildings that were present at the time of 1966 (green houses in Fig. 4.5) and by modifying the altimetry of some small parts that were subjected to changes due to anthropogenic activity since the debris flow event.

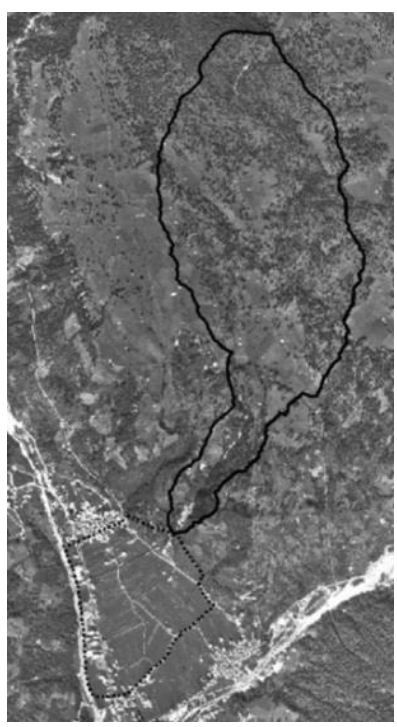

Fig. 4.3. Aerial photo of Rio Lazer flooded area with superimpose d the DEM contours of triggering basin (continuous line) and inundated areas (dotted line).

Fig. 4.4. Photo taken just after the event occurred the 4th of November 1966.

4.5 Simulation of debris flow that occurred on November 4th, 1966

The debris flows occurring in the Dolomites of Italy, as noted in the introduction, are the result of three consecutive physical processes: transformation of rainfall in runoff, entrainment of sediments by runoff and routing of a solid–liquid mixture. The first and second processes can be simulated using a triggering model (Gregoretti and Degetto, 2012), whereas the third process can be simulated using the cell model proposed in this work.

4.5.1 Simulation of debris flow triggering and solid–liquid hydrograph

The triggering model (Gregoretti and Degetto, 2012) is composed of a hydrological model and a model providing the debris flow hydrograph. The hydrological model is that of Gregoretti and Dalla Fontana (2008), which provides the runoff hydrograph for headwater basins. It computes the excess rainfall using the SCS method and routes it to the basin outlet along the steepest path that is divided into slope and channel network paths. The velocity along slope is assigned on the base of the terrain surface (rock, scree, wood…), while the velocity along network corresponds to the peak discharge and is assigned through an iterative method.

The triggering area where debris flow initiated was detected through a careful examination of the photos taken immediately after the event and an accurate field survey recently conducted. It corresponds to the Rio Lazer reach, with deep banks that are subjected to erosion, at approximately 900–1000 m a.s.l (see circle in Fig. 4.4). The slope angle and bottom width of the Rio Lazer are 21.6° (corresponding to 39.6% slope) and 6.0 m, respectively. Fig. 4.6 shows the land use and CN maps of the triggering basin. The values of CN and slope velocity are shown in Table 4.1 for each soil type. The simulated runoff hydrograph (Q_W) is shown in Fig. 4.7, in which the shaded part denotes the amount of runoff that contributed to the debris flow (Q_R). All parts of the hydrograph larger than the critical discharge Q_{CRIT} are taken to contribute to it. Runoff corresponding to the raising limb of the hydrograph and lower than Q_{CRIT}, is antecedent the debris flow initiation and cannot contribute to debris flow. The decreasing part of the hydrograph usually lasts more than observed debris flow hydrographs, and hence, the runoff tail can be disregarded in the computations. As a first approximation here we neglect runoff corresponding to the decreasing part of hydrograph and lower than Q_{CRIT}. Critical discharge value is estimated as the sum of the triggering discharge (i.e. the surface flow discharge that entrain sediments) and the seepage discharge flowing through the debris bed subjected to erosion.

The triggering discharge is computed by multiplying the channel bottom width B by the triggering discharge per unit width, q_{TRIG}, which is given by Gregoretti and Dalla Fontana (2008):

$$q_{TRIG} = 0.78 \frac{d_M^{1.5}}{tan\theta^{1.27}} \tag{4.10}$$

where θ is the bed slope angle in the triggering area (21.6°); d_M is the mean sediment diameter, which was estimated to be 0.35 m through the same technique used to determine the depths of sediment deposits. This estimate takes into account the presence of large boulders and the impossibility of recognizing sediments with diameters smaller than 0.05 m. This leads to an overestimated value of the triggering discharge. The part of the triggering discharge corresponding to the overestimation is assumed to be approximate to the seepage discharge through the saturated debris layer which depends on d_M (Gregoretti and Dalla Fontana, 2008) and cannot be exactly estimated for the same reasons.

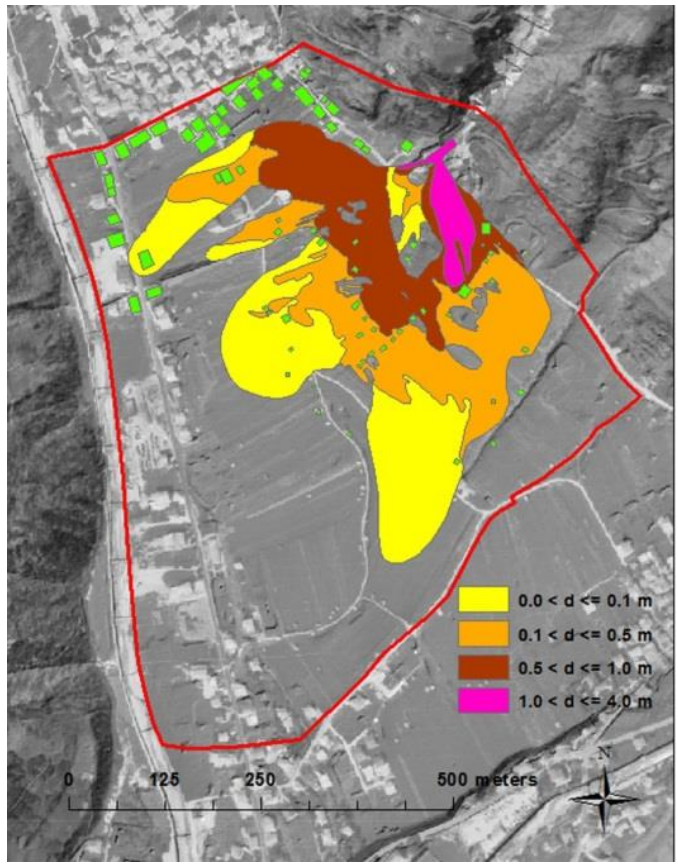

Fig. 4.5. Map of deposition area divided in 4 zones corresponding to 4 classes of deposition depths. The houses in green are those that were present when the event occurred, and the red and blue lines correspond to the DEM contour and the Rio Lazer torrent, respectively.

The solid–liquid flow hydrograph associated with the debris flow at the apex of the fan, just upstream of the deposition area (800 m a.s.l.), is computed observing that the distance between the triggering and deposition areas is relatively short. As a consequence, a front rich with boulders and sediments, implying a triangular peaked is rather unlikely. The debris flow hydrograph, shown in Fig. 4.8, has been assumed to consist of the contributing runoff discharge Q_R (the shaded area in Fig. 4.7) multiplied by the ratio of the input solid–liquid volume, V_T, to the contributing runoff volume, V_R:

$$Q = \frac{V_T}{V_R} Q_R \tag{4.11}$$

The solid–liquid input volume V_T is given by the sum of the entrained sediment volume (assumed to be saturated by the heavy rainfalls precedent the occurred debris flow) and the value of V_R (14,157 m^3). As no erosion phenomena occurred in the area, the entrained sediment volume essentially equates the deposited sediment volume (55,886 m^3). The

input solid–liquid volume, V_T , then turns out to be about 70,000 m^3 with a peak value of the input solid–liquid hydrograph of 40 m^3/s. In present case input sediment volumetric concentration is assumed constant and equal to its average value (ratio between solid and solid–liquid volume). The solid volume of the deposited sediments results to be 34,650 m^3 after assuming c_*=0:62 according to the measurements on loose deposit sediments in the triggering areas of debris flows at the monitored site of Fiames (Cortina d'Ampezzo, North Eastern Italy) carried out by Degetto and Gregoretti (2013). The value of the average sediment concentration is, therefore, 0.495. The interested reader is deferred to Gregoretti and Degetto (2012) for more details and explanations about the method for estimating the solid–liquid input hydrograph.

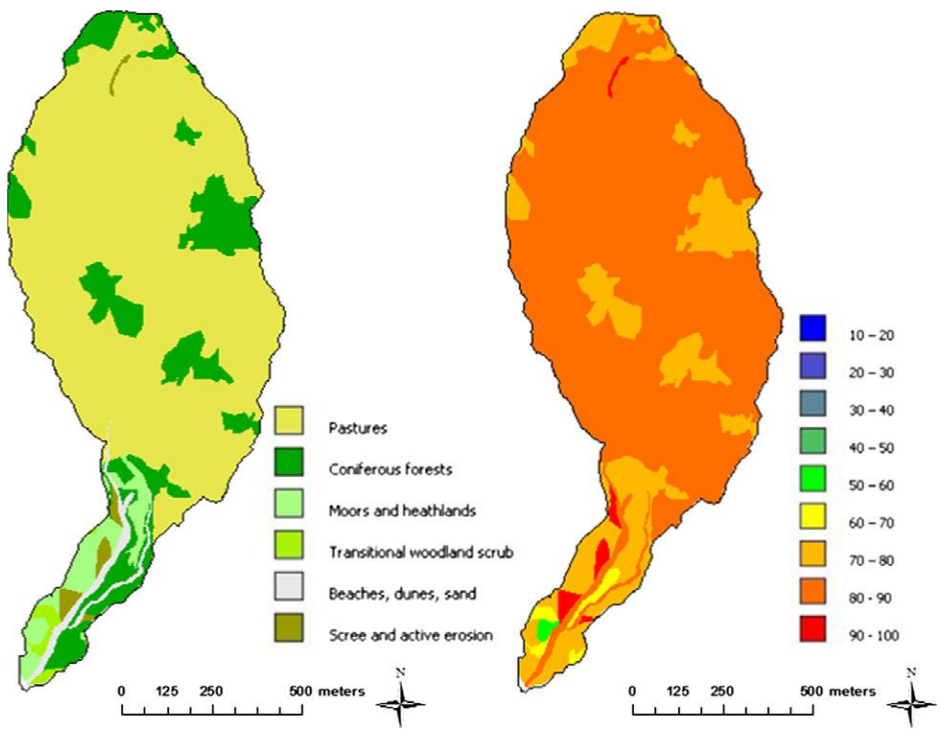

Fig. 4.6. Land use (left) and CN (right) maps of the triggering basin. (For interpretation of the references to color in this figure legend, the reader is referred to the web version of this article).

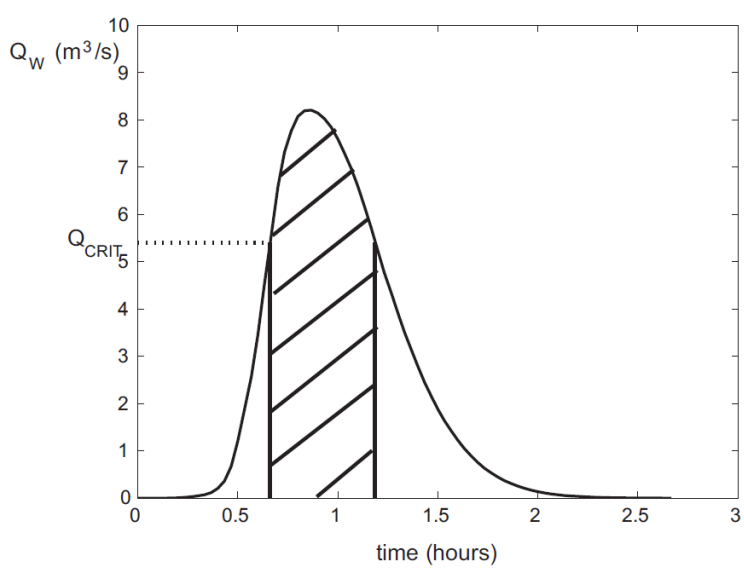

Fig.4. 7. Hydrographs of runoff (Q_W) and runoff contributing to debris flow (shaded part, Q_R).

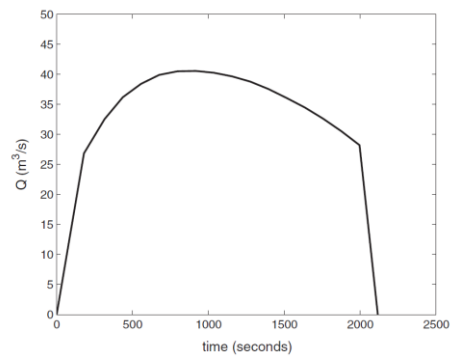

Fig. 4.8. Solid–liquid input hydrograph.

Soil	CN	V_S (m/s)
Pastures	80	0.08
Coniferous forest	65–70	0.05
Moors and heathlands	70–75	0.1
Transitional woodland scrub	65–74	0.1
Torrent bed of gravel and sand	86	0.15
Active erosion	95	0.1

Table 4.1 Values of CN and slope velocity for each soil type of the triggering basin.

4.5.2 Simulation of debris flow spreading along the fan using the cell model

The simulation is conducted using the following values for the main parameters: C=3, K=1, $\theta_{LIM\text{-}D}$=14° and $U_{LIM\text{-}D}$=1 m/s.

The conductance coefficient C has values in the range 2–3 as suggested by Gregoretti (2000c) on the basis of field measurements of flow depth and velocity. The original value of the empirical coefficient K is 1 according to Egashira and Ashida (1987). The upper limit angle for deposition $h_{LIM\ D}$ is assumed to be equal to 14°: according to the flume experiments (Takahashi, 1978; Lanzoni and Tubino, 1993), steady uniform debris flow with grain-inertial behavior likely occurs for bed slope angles equal to or greater than 15°, while for smaller values, sediments are not fully dispersed over the flow depth (immature debris flow). Finally, the limit velocity for deposition has been set to $U_{LIM\text{-}D}$=1 m/s, as a first approximation plausible and physically admissible value.

Fig. 4.9 shows the comparison between the observed and the simulated deposition depths. Through visual inspection, the deposition pattern appears to be well reproduced by the model, for both the extension and deposition depth trends. The extensions of areas occupied by simulated (A_S) and observed deposits (A_D) are almost identical, and the overlapping area, $A_{S\cap D}$, between A_S and A_D is 0.83 A_D. Moreover, Fig. 4.10 shows areas with correctly simulated deposition depths (i.e., those in the range of the measured deposition intervals and denoted in blue), areas with incorrectly simulated deposition depths (red areas), areas with simulated but no observed deposition depths (gray areas) and areas with observed but no simulated deposition depths (green areas). The sum of areas with correctly simulated deposition depths (the blue ones), is A_C=0.34 A_D. This result indicates that approximately half of $A_{S\cap D}$ presents deposition depths that are correctly simulated. Moreover, the zones corresponding to A_C (blue areas) are fully dispersed over the deposition area and are not concentrated in a single part of it. Note also that simulated patterns of deposition depth exhibit larger values at the beginning of the deposition area and smaller values at its border in accordance with the observations. This

is a good result because some numerical models simulating debris flows (Rickenmann et al., 2006; Gregoretti et al., 2011) tend to produce just an inverse deposition pattern with smaller depths at the beginning of deposition area and larger values at the border.

The total deposition volume provided by the simulation (55,940 m^3) is nearly equal to the measured volume (55,886 m^3), and most of volume (98%) deposited in thirty-five minutes, which is consistent with the observed event duration of approximately 30 min according to witnesses. The nearly coincidence of simulated and occurred event durations is an indirect confirmation of the reliability of the simulated flow velocities. Table 4.2 shows the observed and correctly simulated deposition areas for each interval of deposition depths, A_{DD} and A_{CC} , respectively. The values of A_{CC} , ranges from 0.33 to 0.44 A_{DD}. This implies that the percentage of the correctly simulated deposition depth is the same for each interval. In addition, the model performances are analyzed using the fit parameter F, proposed by Bates and De Roo (2000), and the evaluation factor Ω, defined by Scheidl and Rickenman (2010) as follows.

$$F = \frac{X}{X+Y+Z} \tag{4.12}$$

where X is the intersection between the observed and simulated deposition areas (Scheidl and Rickenman, 2010); Y is the deposition area that is simulated but not observed; and Z is the deposition area that is observed but not simulated. Therefore, $A_{S\cap D}=X$, $A_D=X+Z$ and $A_S=X+Y$.

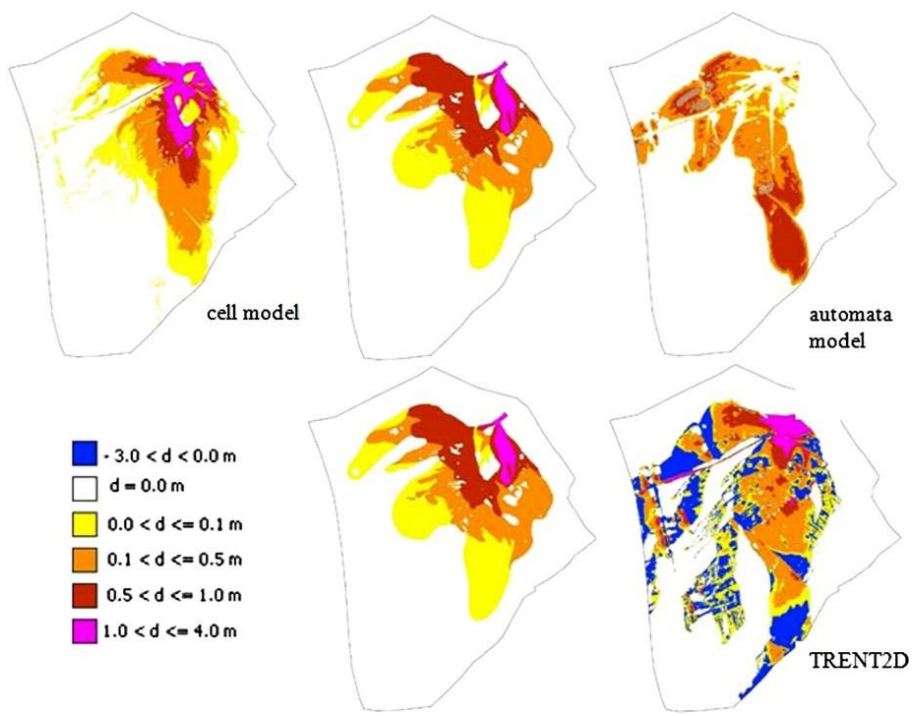

Fig. 4.9. Maps of deposition depths simulated by present model (simulation n. 1, left), observed (middle) and simulated by the automata model (simulation n. 12, top and right) and by the TRENT2D model (simulation n. 20, bottom and right).

The parameter F represents the intersection of the observed and simulated deposition areas as a fraction of the joint simulated and observed deposition areas and ranges between 0 (no fit) and 1 (perfect fit). The evaluation factor Ω reflects the accuracy of the simulation considering both the deposition areas and volumes. This factor is defined as follows:

$$\Omega = \frac{X-Y-Z}{X+Z} + \frac{V_X}{V_D} \tag{4.13}$$

where V_X is the simulated volume of sediments deposit in area X and V_D is the estimated deposited volume (55,886 m^3). The evaluation factor Ω ranges between 2 (no fit) and 2 (perfect fit). The parameter F considers only positive accuracy ($X/(X+Y+Z)$), whereas the parameter Ω considers also the negative accuracy ($Y/(X+Z)$) and the missing accuracy ($Z/(X+Z)$). The expression of Ω proposed by Scheidl and Rickenman (2010), does not account for the correct simulation of deposition depths. As a consequence higher values of Ω could correspond to simulations with V_X close to V_D but incorrectly distributed. Therefore, we propose the substitution of V_X, the overall simulated volume of deposits in area X, with its fraction corresponding to the correctly simulated deposition depths V_{CX} and the expression of the modified factor reads:

$$\Omega_M = \frac{X-Y-Z}{X+Z} + \frac{V_{CX}}{V_D} \tag{4.14}$$

In the case of Ω_M , the range is equal to that of Ω but its value smaller because $V_{CX} \leq V_X$. The values of F, Ω and Ω_M corresponding to the present simulation are 0.694, 1.32 and 0.78, respectively. These values show a high level of fitting between the simulation and observations, that is, a reasonable good performance.

4.6 Sensitivity analysis of parameters and discussion

The numerical results are influenced by the parameters that govern flow resistance and deposition (C, K, $\theta_{LIM\text{-}D}$, $U_{LIM\text{-}D}$). A sensitivity analysis has been performed by varying these parameters in predefined and physically plausible ranges (parameters related to erosion were not considered because it did not occurred).

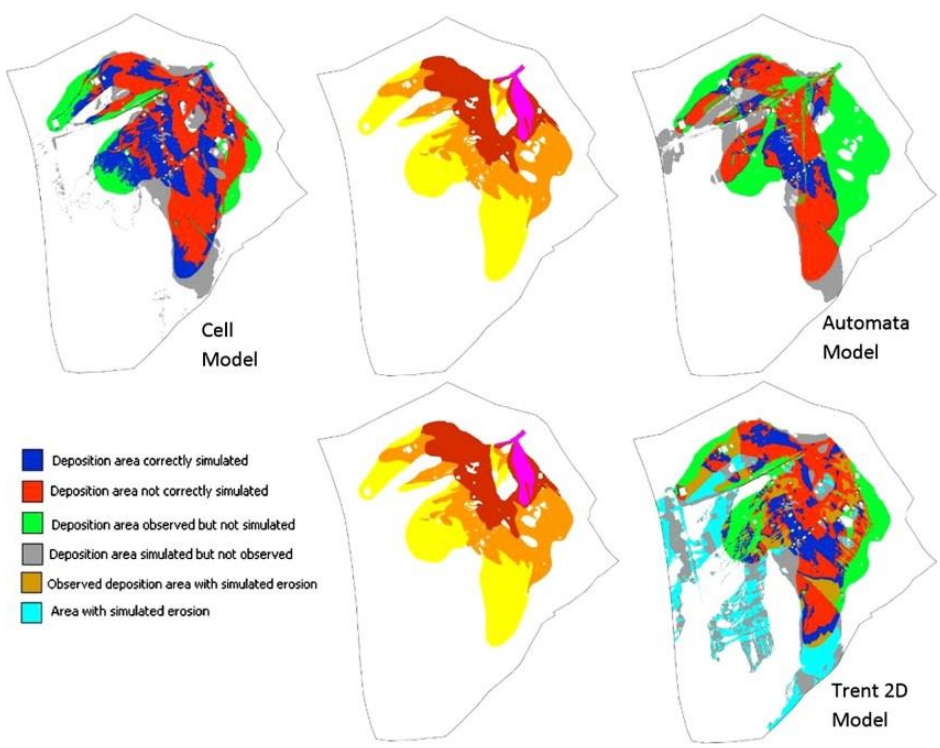

Fig. 4.10. Maps of deposition depths correctly simulated (blue), no-correctly simulated (red), simulated but no observed (gray) and observed but no simulated (green) for the simulations 1 (left), 12 (top and right) and 20 (bottom and right) with that of the observed deposition depths (middle). There also erosion depths simulated but not observed (azure) or corresponding to observed deposition depths (brown).

Class (m)	A_{CC}/A_{DD} (%)	A_{DD}/A_D (%)	A_{CC}/A_D (%)
$0 < d < 0.1$	0.336	0.377	0.127
$0.1 < d < 0.5$	0.373	0.338	0.126
$0.5 < d < 1$	0.328	0.241	0.079
$1 < d < 4$	0.44	0.043	0.019

Table 4.2 Results of simulation 1 for each class of the deposition depth intervals.

Simulations have been performed by varying only one of the parameters used in the simulation presented in the previous section (C=3, K=1, $\theta_{LIM\text{-}D}$=14° and $U_{LIM\text{-}D}$=1 m/s) at any one time. The explored values are: C=2, 4; K=0.5, 1.5; $\theta_{LIM\text{-}D}$=10°,11°,12°; and $U_{LIM\text{-}D}$=0.5, 1.5 m/s. Table 4.3 presents the results of sensitivity analysis in terms of $A_{S\cap D}$, A_C, A_S/A_D, F, Ω and Ω_M.

Considering the ensemble of values shown in Table 4.3, the best simulation (run 1) is that presented in the previous section, i.e. the simulation that ensures a better representation of debris flow routing and deposition.

Runs 3, 4, 5, 8, 9 and 10 provide results that are close to those of run 1, whereas smaller and greater differences are apparent for run 2 (C=2) and runs 6–7 ($\theta_{LIM\text{-}D}$=10-11°), respectively. In the case of C=2 the velocity values are likely to be smaller than those really occurred (simulation deposition time larger than that observed), whereas in the cases of $\theta_{LIM\text{-}D}$=10 and 11°, these values are considerably smaller than those observed experimentally (see previous section). The cell model then seems to provide reliable estimates of debris flow runout. Lower performances of the model are associated with small values of velocity and limiting deposition angle. The parameter $h_{LIM\ D}$ is crucial for simulating deposition and the considered narrow range of valid values 12–14L is just smaller than the limiting value for mature debris flows formation (Takahashi, 1978; Lanzoni and Tubino, 1993). This result further supports the validity of the proposed model and the possibility to use it for simulating routing and deposition of debris flows in the grain-inertial regime.

Previous studies (Whipple and Dunne, 1992; Hungr et al., 2005) have shown that deposition angle mainly depends on the debris flow rheology and for this reason the slopes where deposition begins can differ from case to case (Benda and Cundy, 1990; Hungr et al., 2005; Rickenmann, 2005; Staley et al., 2006; Guthrie et al., 2007; DAgostino et al., 2010). A general criteria to establish the slope where deposition begins is yet missing and strongly needed for practical applications (Hungr et al., 2005). Therefore, the range (12-14°) that provides reasonable estimates of deposition in the grain-inertial regime needs to be modified on the base of available literature data when considering debris flows with other rheological features.

An attempt to determine the effects of the grid size on the predicted results has been conducted by running two simulations (runs 9–10) with the same parameters of run 1 and using DEMs with larger grid sizes: Δx=2 and 4 m, respectively. Due to the lack of original LiDAR points, DEMs with grid sizes of 2 and 4 m are obtained assuming that the original points are the centers of the cells of the DEM with Δx=1 m with the associated elevations.

The corresponding results, shown in Table 4.3, differ from those of run 1 and approach those of runs 6 and 7. This result is essentially due to the differences in elevation between the 1-m cell and the 2.4-m cells in the upper part of the routing zone, close to the input area. This difference is approximately 0.4 m; thus, the flow conveyed on the right side of the basin is much smaller in runs 11 and 12 (2 and 4 m DEMs) than in runs 1–5 and 8–10 (1 m DEM). Similar differences in model results were observed by Bates and De Roo (2000) when employing their raster-based model for flood inundation on grids of different sizes. Additionally, Rickenmann et al. (2006) reported that only an accurate representation of topography will allow a good simulation of the observed deposition pattern. Nevertheless, the values of Ω of runs 10 and 11 are closer to those of runs 3 and 4 rather than those of runs 6 and 7. This is due to the values of V_X corresponding to

runs 10 and 11 that are larger than those corresponding to runs 6 and 7. This supports our proposal of substituting Ω with Ω_M .

Run	Values of parameter				Δx (m)	$A_{S\cap D}/A_D$ (%A_D)	A_C (%A_D)	A_S/A_D	F	Ω	Ω_M
	C	K	$\theta_{LIM\text{-}D}$ (°)	$U_{LIM\text{-}D}$ (m/s)							
1	3	1	14	1	1	82.5	33.5	1.03	0.69	1.32	0.78
2	**2**	1	14	1	1	66.3	26.5	0.76	0.6	1.07	0.56
3	**4**	1	14	1	1	83	29.8	1.21	0.6	1.17	0.54
4	3	**0.5**	14	1	1	85.4	36.1	1.13	0.67	1.31	0.78
5	3	**1.5**	14	1	1	81.2	32.2	1.01	0.68	1.31	0.78
6	3	1	**10**	1	1	62.9	16.2	0.87	0.51	0.89	0.19
7	3	1	**11**	1	1	59.8	16.2	0.83	0.49	0.84	0.16
8	3	1	**12**	1	1	79.3	28.3	1.04	0.633	1.22	0.61
9	3	1	14	**0.5**	1	83.2	31.3	1.06	0.68	1.34	0.76
10	3	1	14	**1.5**	1	81.6	33.5	1.06	0.66	1.27	0.71
11	3	1	14	1	**2**	67.7	20.4	0.96	0.53	0.97	0.12
12	3	1	14	1	**4**	69.7	18	0.95	0.56	1.07	0.15

Table 4.3 Simulation results with present model: percentages of the simulated deposition areas respect to that measured and values of evaluation factors/parameters. In bold the value of the parameter that is varied respect to run 1.

Simulations of the debris flow that occurred on Rio Lazer have been also performed using two other models: the cellular automata model of Deangeli (2008), modified by Gregoretti and Degetto (2012) after introducing the input hydrograph and substituting the uniform flow equation proposed by Takahashi (1991) with that of Tsubaki (1972), i.e. Eq. (4.2), and the TRENT2D model (Transport in Rapidly Evolutive Natural Torrent) of Armanini et al. (2009).

The modified model of Deangeli (2008) is based on the uniform flow equation of Tsubaki (1972) and on the continuity equation. The parameters of this model are the conductance coefficient C and the static friction angle φ. Deposition occurs when the terrain slope is less than, tan φ $(\rho_s/\rho+(1-c))$, with ρ_s and ρ the sediment and water density respectively. Simulations have been conducted assuming C=3 and by varying φ in the range 10–20°. The results of runs 13–15 (see Table 4.4) are very similar, and the best result corresponds to φ=15° (run 14). Additional tests conducted with values of φ out of the 10–20° range, exhibited very low performance. Figs. 4.9 and 10 also show the comparison between the simulated sediment deposition depths of run 14 and those observed. The simulated deposition exhibits smaller depths values in the upper part of the deposition area and larger values in the downstream zone, which is the inverse of that observed.

The model of (Armanini et al., 2009) consists of the depth-averaged mass and momentum balance equations in a two-dimensional domain, obtained through the shallow water approximation and solved through a finite volumes numerical scheme. Deposition and erosion are computed by assuming the immediate adaptation of sediment concentration to the transport capacity. The closure laws for the basal shear stress and transport capacity are specified by assuming a grain-inertial rheology and a semi-empirical approach. The parameters of the model are the dynamic friction angle φ_D and relative submergence $Yd = h/d_g\sqrt{b}$ (where d_g is the grain size of mixture and b is a constant of dynamic origin). These parameters have been varied in the physically plausible range: 15≤Yd≤25 and 30°≤φ_D≤40° by considering different pairs of parameters (see Table 4.4). The results of the different simulations (see Table 4.4, runs 16–22) are very similar; the best simulation (run 22) corresponds to Yd=25 and φ_D≤40°. Comparisons among computed (run 22) and observed

deposition depths are shown in Figs. 4.9 and 4.10. The extension of the simulated deposition area is smaller than that observed. Most of the computed deposits occur in the upstream part of the inundated areas, with deposition depths much larger than observed depths. Moreover, the model suggests that large areas are subjected to erosion in the downstream part of the basin (Fig. 4.10). This unrealistic result could depend on low values attained by sediment concentration downstream of the area where most of the sediments deposit. These values of c result smaller than transport capacity and, hence, thus leading to erosion. This behavior has been also observed by Stancanelli and Foti (2015).

On the whole, deposition depths simulated using both a simpler model (Deangeli, 2008) and a more sophisticated model (Armanini et al., 2009) are consistent. Nevertheless, the correspondence with the observed deposition pattern is less satisfactory than that resulting from the present model. The main reason for this result depends on the schematization of the deposition process. On one hand, the condition for the sediment deposition adopted in the cellular automata model (Deangeli, 2008), being based on a single parameter, is too simple and cannot account for all the possible situations characterizing a complex terrain. On the other hand, the Armanini et al. (2009) model uses a more sophisticated equation for simulating deposition, which however, provides unreliable results when the transport capacity estimates are no more valid owing to a significant reduction of slope. We also note that the schematization of deposition adopted here depends on three parameters (K, $\theta_{LIM\text{-}D}$ and $U_{LIM\text{-}D}$), possibly ensuring a better performance of the present model. In conclusion, simulations of debris flow runout appear to be more influenced by the schematization of deposition process rather than the modeling of mixture dynamics.

	Run	**Values of parameter**				Δx **(m)**	$A_{S\cap D}/A_D$ **(%A_D)**	A_C **(%A_D)**	A_S/A_D	F	Ω	Ω_M
		C	φ (°)	φ_D (°)	Yd							
13	(Deangeli, 2008)	3	10	–	–	1	56.1	15.2	0.87	0.43	0.34	-0.081
14	(Deangeli, 2008)	3	15	–	–	1	55.7	14.8	0.75	0.466	0.41	0.022
15	(Deangeli, 2008)	3	20	–	–	1	53.7	14.4	0.75	0.441	0.35	-0.036
16	(Armanini et al., 2009)	–	–	38	20	1	56.9	22.8	0.86	0.57	0.59	0.23
17	(Armanini et al., 2009)	–	–	38	15	1	56.2	22.4	0.83	0.56	0.61	0.26
18	(Armanini et al., 2009)	–	–	38	25	1	57.1	22.5	0.87	0.57	0.6	0.24
19	(Armanini et al., 2009)	–	–	30	20	1	57.8	23.1	0.87	0.58	0.61	0.26
20	(Armanini et al., 2009)	–	–	40	20	1	57.8	22.7	0.87	0.58	0.62	0.26
21	(Armanini et al., 2009)	–	–	30	15	1	56.2	22.7	0.84	0.56	0.6	0.25
22	(Armanini et al., 2009)	–	–	30	25	1	58.4	23	0.89	0.58	0.62	0.26

Table 4.4 Simulation results with the models of Deangeli (2008) and Armanini et al. (2009): percentages of the simulated deposition areas respect to that measured and values of evaluation factors/parameters.

4.7 Conclusions

We have proposed a GIS-based cell model for simulating debris flow routing and deposition on a fan. Flow routing is governed by two simple relationships (i.e. a uniform-flow equation and a broad-crested weir-flow relation) that correspond to a kinematic approach. Deposition and erosion are governed by the empirical law given by Egashira and Ashida (1987). The model has been tested by simulating the debris flow that occurred on Rio Lazer on November 4th, 1966. An input debris flow hydrograph has been constructed using a triggering model and the estimated rainfalls. The comparison between simulated and observed deposition depths suggests a good performance of the model. In particular, approximately 80% of the extension of the observed deposition area is simulated, and in about half of this area, simulated and observed deposition depths seasonably agree. The values attained by the overall evaluation parameters proposed by Bates and De Roo (2000) and Scheidl and Rickenman (2010) are quite good as well. Remarkably, the values of the model parameters used in the simulation ensuring a more robust prediction, are those that are more physically plausible.

Sensitivity analysis of the parameters relative to flow resistance and deposition rate shows that only physically-not plausible-values (small values of the limiting angle for deposition, $\theta_{LIM\text{-}D}$, and of the conductance coefficient, C), could introduce significant differences in the simulations. Simulations performed using larger grid sizes (2 and 4 m) exhibit lower performances due to smoothing of the terrain in the upper part of the basin, where a splitting of the flow occurs.

The robustness of the present model has been also assessed by simulating the same debris flow event by using a cellular automata model (Deangeli, 2008) and a two-dimensional finite volume model (Armanini et al., 2009). Compared to the model presented in this work, the former is much simpler and the latter is more sophisticated. The performances of both the models are lower than those of the present cell model. The main reason for this result is likely related to the different schematization of sediment deposition process.

Based on the simulations carried out with various models, the main conclusions of this work can be summarized as follows.

The present model seems to provide reliable simulations of debris flow. Its simplicity and robustness makes it a suitable tool for simulations of hazard scenarios at basin and/or regional scales, as well as for predicting imminent scenarios after an alert given by now-casting. The model can also be easily interfaced with any GIS platform without any pre- or post-processing steps because of its raster-based nature.

Our analysis shows that simulation of sediment deposition is considerably influenced by the adopted schematization. A simple scheme based on a single reference angle (Deangeli, 2008) appears too simple, since it cannot account for the variable topography of a complex terrain. The assumption of an immediate adaption of sediment concentration to the transport capacity (Armanini et al., 2009), widely used in fluvial hydraulics, exhibits low performances if the closure laws do not correctly interpret the rheology of the solid–liquid mixture to be simulated. A schematization of deposition process based on flow velocity and bed slope angle, as considered in the present model, appears to provide more reliable and robust results.

A correct simulation of the deposition depths distribution appears to be more important than predicting accurately the overall deposition volume. A precise estimate of the deposition volume, in fact, is useless for vulnerability analysis if the deposition depths are not well reproduced.

The validity of the proposed model should be further tested considering other field data of debris flows events leading to significant erosion and occurred in other geological contexts, such as on screes (where the increase in roughness should imply smaller values of C and larger values of $\theta_{LIM\text{-}D}$). The use of a more accurate description of flow routing, i.e. implementing a more refined momentum equation (Di Cristo et al., 2014a,b), is a further improvement of the model that should be considered in the near future.

5 The Debris Flow Occurred at Ru Secco Creek, Venetian Dolomites, on 4 August 2015: Analysis of the Phenomenon, Its Characteristics and Reproduction by Models

This chapter represents an edited version of: ***Gregoretti C., Degetto M., Bernard M., Boreggio M.[7] (2018). The debris flow occurred at Ru Secco Creek, Venetian Dolomites, on 4 August 2015: analysis of the phenomenon, its characteristics and reproduction by models.*** *Frontier in Earth Sciences, doi: 10.3389/feart.2018.00080.*

Summary

On 4 August 2015, a very high intensity storm, 31.5 mm in 20 min (94.5 mm/h), hit the massif of Mount Antelao on the Venetian Dolomites triggering three stony debris flows characterized by high magnitude. Two of them occurred in the historical sites of Rovina di Cancia and Rudan Creek and were stopped by the retaining works upstream the inhabited areas, while the third routed along the Ru Secco Creek and progressively reached the resort area and the village of San Vito di Cadore, causing fatalities and damages. The main triggering factor of the Ru Secco debris flow was a large rock collapse on the northern cliffs of Mount Antelao occurred the previous autumn. The fallen debris material deposited on the Vallon d'Antrimoia inclined plateau at the base of the collapsed cliffs and part reached the Ru Salvela Creek, covering it from the head to the confluence with the Ru Secco Creek. The abundant runoff, caused by the high intensity rainfall on 4 August 2015, entrained about 52,500 m^3 of the debris material laying on the Vallon d'Antrimoia forming a debris flow surge that hit and eroded the debris deposit covering the downstream Ru Salvela Creek, increasing its volume, about 110,000 m^3 of mobilized sediments. This debris flow routed downstream the confluence, flooding the parking of a resort area where three people died, and reached the village downstream damaging some buildings. A geomorphological analysis was initially carried out after surveying the whole basin. All liquid and solid-liquid contributions to the phenomenon were recognized together with the areas subjected to erosion and deposition. The elaboration of pre and post-event topographical surveys provided the map of deposition-erosion depths. Using the rainfall estimated by weather radar and corrected by the nearest rain gauge, about 0.8 km far, we estimated runoff by using a rainfall-runoff model designed for the headwater rocky basins of Dolomites. A triggering model provided the debris flow hydrographs in the initiation areas, after using the simulated runoff. The initial solid-liquid surge hydrographs were, then, routed downstream by means of a cell model. The comparison between the simulated and estimated deposition-erosion pattern resulted satisfactory. The results of the simulation captured, in fact, the main features of the occurred phenomenon.

[7] The author contributed to the preparation of the routing model input files, and to the analysis of the modeling outcomes.

5.1 Introduction

The Boite Valley in Venetian Dolomites (Northestern Italian Alps) was affected by several runoff generated debris flows during the summer of 2015 (Baglioni and De Marco, 2015). The evening of 4 August a high intensity storm hit the top area of the Monte Antelao massif and caused three stony debris flows of high magnitudo on the sites, South to North of Rio Rudan Creek, Rovina di Cancia channel and Ru Secco Creek (Fig. 5.1). The first two sites are periodically affected by debris flows (Gregoretti and Dalla Fontana, 2008) and are defended by a check dam and some retaining basins respectively that reduced and stopped the solid part of the solid-liquid waves. Ru Secco Creek just experienced its first debris flow since 1950s and was without any defense. Consequently, the debris flow flooded from it causing three deaths in the parking of a resort area and partially damaging some buildings of the village of San Vito di Cadore downstream. The runoff generated debris flows are very common in the Boite Valley (Berti and Simoni, 2005; Gregoretti and Dalla Fontana, 2008) as elsewhere on Alps (Theule et al., 2012; Navratil et al., 2013; Tiranti and Deangeli, 2015; Destro et al., 2018) and worldwide (Imaizumi et al., 2006; Cannon et al., 2008; Coe et al., 2008; Okano et al., 2012; Kean et al., 2013; Hurlimann et al., 2014; Hu et al., 2016). The aim of the present research is the study of this debris flow event by means of pre and post-event topographical data, post-event direct surveys and its reproduction by modeling the physical processes associated to its occurrence. Multi-temporal topographical data and direct post- event surveys are important for identifying the phenomenon models is also important, because it shows the evolution of the event. In addition, it is a reliability test of the models. Models, in fact, can play a crucial role in hazard assessment and in risk analysis, and, only the use of models satisfactorily tested against field data can provide reliable results. Consequently, we propose both a methodology for simulating the cascade of the physical processes that origin a debris flow phenomenon and a fully bi-phase GIS-based model, update of a previous quasi bi- phase version. This update version allows a better simulation of the entrainment processes that have a crucial role in the estimation of the sediment volume transported by a debris flow as also pointed out by Reid et al. (2016). After the debris flow occurrence, all the areas surrounding the Ru Secco Creek were carefully surveyed with the scope of identifying the development of the phenomenon and its characteristics. This field survey gave the general view of all the single phenomena that contributed to the formation and routing of the solid-liquid surge along the Ru Secco Creek. All the areas that provided solid-liquid or liquid flows were identified with the corresponding watersheds.These results were used for identifying the watersheds where modeling runoff and solid-liquid hydrographs as well the debris flow routing. After building the DEMs of all the contributing watersheds, needed for the hydrological simulations, pre and post-event topographical data were used for building the pre and post-event DEMs of the area affected by the occurred debris flow. The difference between the pre and post-event DEMs provided the map of the deposition-erosion depths and the total sediment volume mobilized during the event. The result of field surveys and analysis of this map showed the main features of the occurred phenomenon. Rainfalls on the contributing watershed were obtained through radar estimates corrected by rainfall depths measurements given by a rain gauge placed at the base of the southern rock walls of Mount Antelao, in the contiguous basin of Rovina di Cancia at an altitude of about 2,150 m a.s.l. (Fig. 5.1). Runoff hydrographs were, then, modeled by the rainfall-runoff model proposed by Gregoretti et al. (2016a) for headwater rocky basins while the solid-liquid hydrographs were modeled extending the method proposed by Gregoretti et al. (2016b). Finally, we used an updated version of the GIS-based cell model of Gregoretti et al. (2016b) that ensures a fully bi-phase routing for modeling the debris flow propagation downstream the initiation areas. The comparison between the simulation results with the deposition-erosion depth map accounts for the reliability of the phenomenon reconstruction, that is the capturing of its main features.

The remainder of this paper is organized as follows. Section 5.2 describes the materials and methods, divided in four sub-sections concerning: the study site of Ru Secco Creek with the big rock fall occurred on November 2014, the topographical data and the set up of pre and post-event DEMs, the correction of the radar rainfalls estimates and the models used for the simulations. The field surveys and the geomorphical analysis of the occurred phenomena are presented in section 5.3, while section 5.4 shows the reconstruction of the phenomenon by models. Section 5.5 discusses the results and, finally, section 5.6 reports the conclusions.

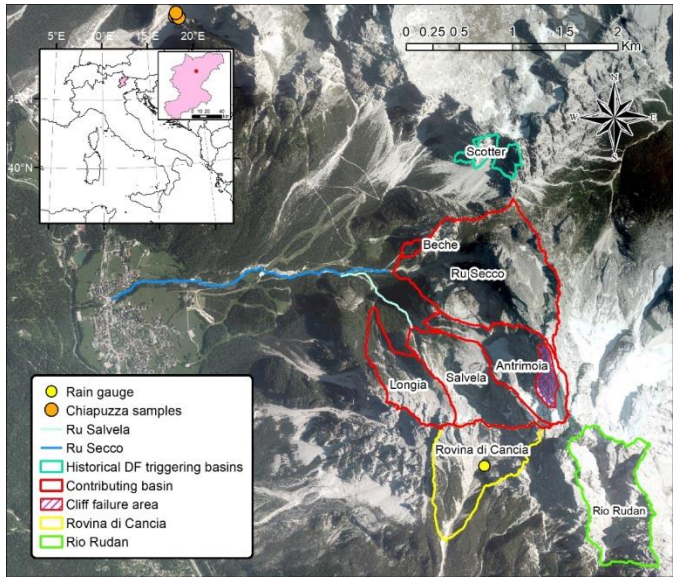

Fig. 5.1. Aerial view of whole area with the contributing hydrological basins and the basins of Rovina di Cancia and Rudan.

5.2 Materials and Methods

5.2.1 The Study Site and the Rock Fall Occurred on 14 November 2014

The storm event of the 4 August 2015 hit all the areas contributing to Ru Secco Creek. Fig. 5.1 shows the plan view of the sub-basins that provided runoff and the routing paths. Fig. 5.2 shows a frontal view of the upper part of the study area, where the arrows point the path of the liquid and solid-liquid contributions to the whole phenomenon. Ru Secco Creek origins downstream Forcella Piccola Fork and following a quasi straight route reaches the bottom of the Boite Valley where it crosses the village of San Vito di Cadore and flows into the Boite river. It initially flows between two rocky walls and after a drop, it runs on the bottom of the valley between the northern rocky slopes of Mount Antelao, where Ru Salvela Creek origins (Fig. 5.1), and the slopes starting at the feet of the rocky massif between Bel Pra and Scotter tops along Northwest-Southeast direction. Along its route, downstream the drop, Ru Beche and Ru Salvela Creeks join it on the right and left side (Fig. 5.3a) respectively. About 800 m downstream the second confluences, the Ru Secco Creek is culverted to allow the joining of a slope ski on the right side with a chairlift located on the left side of the creek (Fig. 5.3b). In the reach from a location about 300 m upstream the culvert to the inhabitated of San Vito di Cadore, the bed of the Ru Secco creek is protected by a series of check dams. At the entrance of the inhabitated of San Vito di Cadore the Ru Secco is again culverted, and after the exit, it flows into the Boite river. This area, located in the Venetian Dolomites, is dominated by carbonatic Platform formations. The rocky massifs are formed of a thick succession of the calcareous "'Dolomia Principale" Formation with overlaying limestones of the "Calcari Grigi" Formation. The night of 12 November 2014 a cliff failure on the northern side of Mount Antelao (Fig. 5.1, Fig. 5.4) caused a large rock fall that part deposited on the rocky sloping surface of Vallon d'Antrimoia at the base of the collapsed cliffs and part traveled downstream along the Ru Salvela Creek. It reached the confluence with the Ru Secco Creek and stopped just a hundred meters downstream. All the Ru Salvela Creek, and the Ru Secco Creek from the confluence to a hundred meters downstream, were covered by a thick layer of debris material. In Fig. 5.3a, Fig. 5.4 the debris thick layer covering the Ru Salvela and Ru Secco Creeks (about 175,000 m^3 according to the computations of section 5.3). Starting from the Ru Secco Creek, debris material began to be removed: Fig. 5.3a shows the situation about 1 month before the occurrence of the debris flow event with the works for reducing the large debris deposits on the Ru Salvela Creek.

Fig. 5.2. Frontal view of the upper basins that contributed to the phenomenon. The blue arrows show the runoff routing, the red arrows the debris flow starting locations and its routing, and the black arrows the path of the debris flow on the right slope, that did not contribute significatively to solid-liquid wave routing along Ru Secco (flight of 5 August 2015).

About the characteristics of sediments forming the debris deposits that were eroded by runoff and debris flows, we can refer to the grain size analysis carried out through the frequency-by-weight method, on five samples taken on the channelized initiation area of Chiapuzza debris flow (about 1 km north) located on the scree of Cadino dei Ross formed by the rocks collapsed from the overhanging rocky walls of Punta Ross Top. Both the debris deposits on the sites of Vallon d'Antrimoia-Ru Salvela Creek and Cadin dei Ross formed for the collapse of the overhanging rocky cliffs with the same geological Formations. For these reasons, the properties and the characteristics of the debris material are assumed to be quite the same. The five samples of material have a composition ranging in the following intervals for each type of soil: 4% silt ($0.002 \leq d < 0.063$ mm), 33–50% sand ($0.063 \leq d < 2$ mm), 48–58% gravel ($2 \leq d < 63$ mm), and 1–3% cobbles ($63 \leq d < 200$ mm), with a mean density of 2.62 kg/m^3 and a solid volumetric concentration of 0.73. The static friction angle, 39°, was also estimated through triaxial tests.

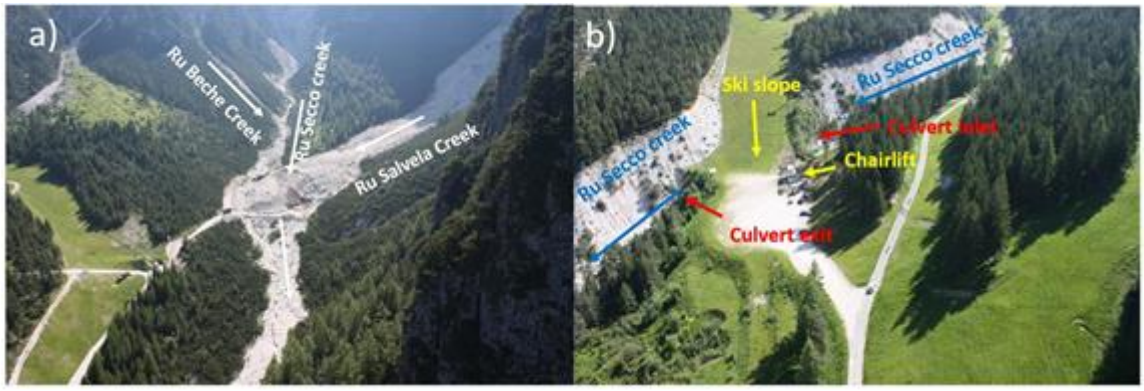

Fig. 5.3. Pre-event images: view of the large debris deposits covering the Ru Salvela and Ru Secco creeks during their removal (flight of 1 July 2015) (a) and the culverting of the Ru Secco in correspondence with the ski resort area (b).

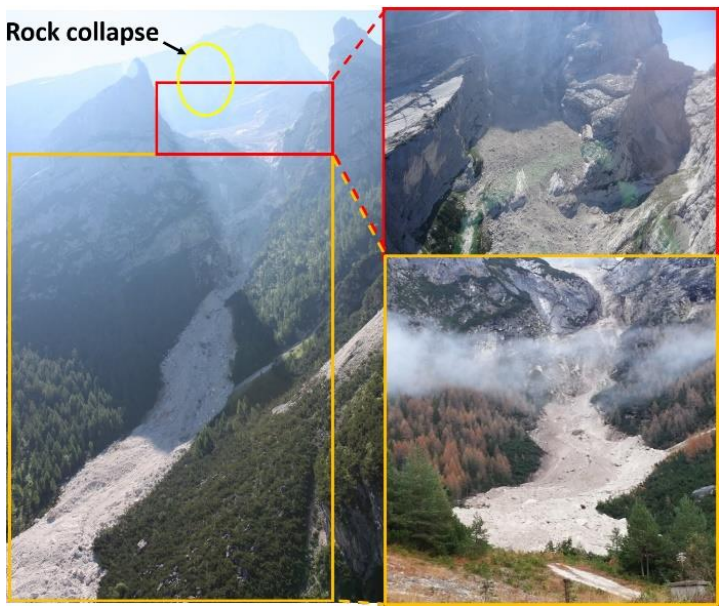

Fig. 5.4. View of the collapsed cliff on the northwestern side of the Mount Antelao (flight of 1 July 2015) and the deposits of debris material from the base of the collapsed cliff to just upstream the confluence with Ru Secco creek. Top right insert shows the debris material covering the Vallon d'Antermoia rocky surface at the base of the collapsed cliff (flight of 1 July 2015). Bottom right insert shows the Ru Salvela creek covered by debris material tilling the confluence with Ru Secco creek that was obstructed (picture taken on November 2014).

5.2.2 Topographical Data

Topographical data are given by two LiDARs flights held on November 2011 and 2015, the photogrammetric restitution of photos of the large debris deposit taken 1 month before the event, a drone photogrammetric flight held 2 days after the event and direct GPS survey held about 2 months after the event.

Fig. 5.5 gives a schematic view of the cover provided by the different topographical data. The pre-event Digital Elevation Model (DEM) is built by using the LiDAR 2011 for all the areas but the debris deposit covering the Ru Salvela Creek till the confluence with Ru Secco Creek where photogrammetric points provided by photos elaboration, are used. The post-event DEM is built using the GPS points, the drone photogrammetric points and for the areas uncovered by this flight the LiDAR 2015. GPS points corresponding to the check dams are also used for the pre-event DEM because they

remained substantially unchanged. The DEMs for the hydrological simulations of the basins depicted in Fig. 5.1 were built by using the LiDAR 2015. LiDAR 2011, in fact, does not cover the upper part of the basins that in part changed after the cliff failure of November 2014, and, the DEMs derived by points along the contour lines of the Regional Techinical Map are characterized by a poor accuracy that could cause a noticeable underestimation of the simulated peak discharge (Degetto et al., 2015). Therefore, as only a part of the surface of the Vallon d'Antrimoia changed after the event due to the erosion, with no significative influence on the hydrological simulation, we used the LiDAR 2015. Density points of the LiDAR 2011 survey is about 1.2 pts/m^2 while that of LiDAR 2015 is about 1.5 pts/m^2. Points provided by the drone flight have a larger density, about 30 pts/m^2. The photogrammetric restitution through the photos relative to the Ru Salvela Creek after the rockfall of November 2014 and before the debris flow event (one is that shown in Fig. 5.3a), was carried out by using the software 3DF Zephyr (Lo Brutto and Meli, 2013).

Usually, the accuracy assessment of DEMs is carried out through independent topographic survey points called checkpoints, which should be at least three times more accurate than the DEM elevations being evaluated (Höhle and Höhle, 2009). Unfortunately, an unchanged and significant area, where independent ground control points could be taken, was not available because of the restoration works. This hampered the possibility to perform an extensive vertical accuracy assessment of each employed topographic dataset in a common area. About LiDAR2015 an extensive vertical accuracy assessment was performed using independent Real Time Kinematic GPS measurements, acquired according to a cross-sections morphological-guided spatial sampling scheme along the upper part of the Rovina di Cancia channel on November 2015 (Boreggio et al., 2018). The median of the errors was equal to 0.020 m, and it represents the systematic vertical shift between LiDAR point cloud and the GPS validation data. Conversely, the robust standard deviation of the errors (i.e., the Normalized Median of Absolute Errors) was equal to 0.237 m, which corresponds to the random error component of the LiDAR dataset. More details are in Boreggio et al. (2018). About "photogrammetric points" and "drone points" on some small areas of the Ru Salvela Creek that remained unchanged during the debris flow event we compared the two points data sets. It resulted a nearly good agreement with average differences of about 0.1 m and the largest of 0.4 m.

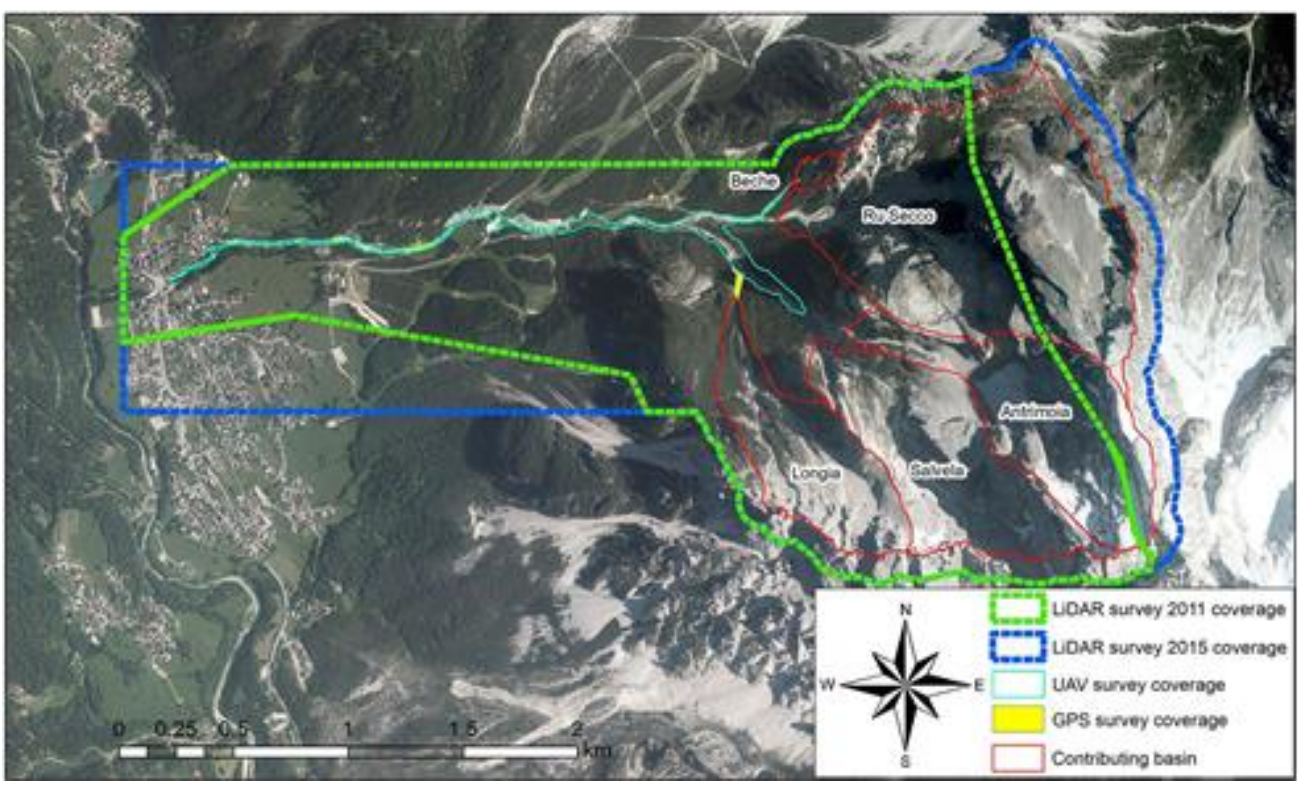

Fig. 5.5. Schematic view of the cover of the topographical data.

5.2.3 The Precipitation

The rainfall on the five basins depicted in Fig. 5.1 that mainly contributed to the event was obtained after the correction of weather radar estimates with the data of the rain gauge of the monitoring and alarm system installed on the Rovina di Cancia channel by the Province of Belluno. This rain gauge is located at the base of the southeastern cliffs of the Monte Antelao group, at an altitude of 2,150 m a.s.l. and is about 0.8 km far from the centroids of the Salvela and Antrimoia hydrological basins (Fig. 5.1).

Fig. 5.6 shows the rainfall depths sampled at 5 min by the rain gauge with those of the corrected radar estimates for each of the five considered hydrological basins. On average the observed rainfall depths are just a slightly smaller than those given by the radar corrected estimates. The core of the precipitation that caused the larger quantity of runoff lasted 20 min and ranged in a 31.5–36.2 mm interval for all the five basins. The corresponding mean intensity values ranged between 94.5 and 108.6 mm/h, while the largest intensity values corresponding to the depth in 5 min, between 118.8 and 159.6 mm/h. This very high intensity and short duration rainfall is a typical precipitation causing the runoff generated debris flows that occur along the Boite valley (Bacchini and Zannoni, 2003; Berti and Simoni, 2005; Gregoretti and Dalla Fontana, 2007).

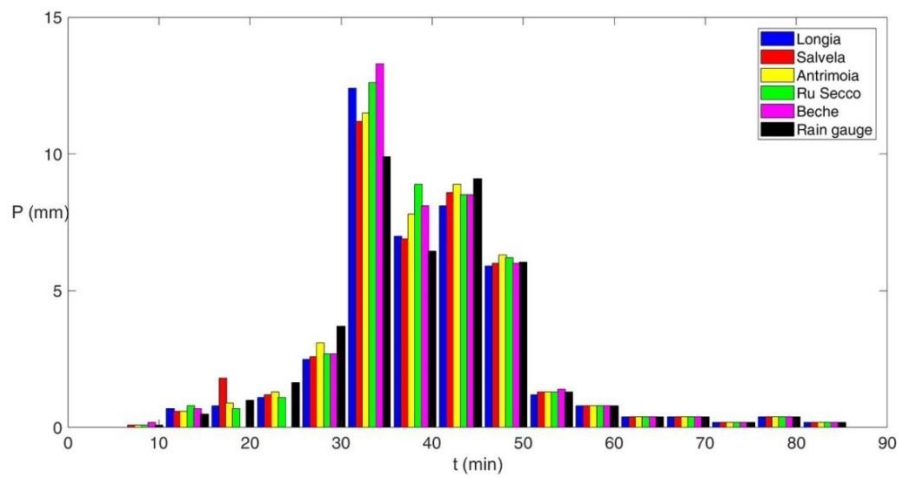

Fig. 5.6. Hyetograph of the rainfall depths from the rain gauge and the corrected radar estimates.

5.2.4 The Models

In this section, the models used for modeling rainfall-runoff and debris flow routing are presented.

5.2.4.1 Hydrological Modeling

The hydrological model used in the present study was proposed for headwater rocky catchments by Gregoretti et al. (2016a), after directly testing it by runoff discharge measurements at the outlet of a rocky channel incised on the cliffs of the Dimai Peak (14 km far from Ru Secco Creek), and also indirectly by the debris flow/runoff transit in the initiation area of two other dolomitic catchments, the Acquabona and Rovina di Cancia basins according to Rengers et al. (2016). The centroids of these basins are 8 and 1 km far from the Antrimoia hydrological basin centroid respectively. All these catchments belong to the same geological context and have very similar morphological features.

The excess rainfall P_e contributing to the runoff discharge is computed by coupling the SCS-CN method with a simplified Horton equation that assumes a constant infiltration rate f_c. At each time step t, P_e is given by:

$$P_e(t) = \begin{cases} 0 & \text{if } t \leq t_{Ia} \\ \frac{(P(t)-Ia)^2}{P(t)-Ia+S} & \text{if } t > t_{Ia} \text{ and } I < f_c \\ P_e(t-\Delta t) + [P(t) - P(t-\Delta t)] - f_c \Delta t & \text{if } t > t_{Ia} \text{ and } I > f_c \end{cases} \tag{5.1}$$

where I_a is the initial abstraction, t_{Ia} is the time within I_a occurs, $I_a = 0.2S$, S is the potential maximum retention ($S = 1000/CN - 10$), I is the mean rainfall intensity during the time step t, and P_{eSCS} is the excess rainfall of the total precipitation determined through the SCN-CN method. The empirical parameter CN depends on the type, use, and antecedent moisture condition (*AMC*) of the terrain. Three *AMCs* are assumed: I, dry condition *AMC* II, standard condition; *AMC* III, wet condition. Following Gregoretti et al. (2016a) for mountain watersheds I_a=0.1S while Bernard (2018), after examining a larger number of runoff events, diminishes to 2 days the previous rainfall depth for determining the antecedent moisture conditions (*AMC*). Excess rainfall is conveyed to the channel network along the steepest direction, with a constant value of runoff velocity U, that varies with the terrain typology. The contributes to the channel network are routed to the outlet of the basin using the matched diffusivity kinematic-wave model proposed by Orlandini and Rosso (1996), providing the liquid hydrograph.

5.2.4.2 The GIS-Based Cell Model

The routing model here introduced is the bi-phase version of the GIS-based cell model proposed by Gregoretti et al. (2016b) that provides a better simulation of the entrainment process (Gregoretti et al., 2018). The governing flow equations are those of mass and momentum conservation coupled with the Exner equation and a modified version of the empirical law of Egashira and Ashida (1987) to express the rate of change of the bed elevations. The mass conservation is stated by means of the continuity equations of the mixture and of the solid phase, while the momentum conservation by means of simplified motion equations of the mixture because equal velocities are assumed for both the solid and liquid phases according to Rosatti and Begnudelli (2013). The flow pattern is discretized by the square cells of the DEM. At the cell scale, the continuity equations read

$$A\frac{d(h+z)}{dt} + \sum_{k=1}^{8} Q_k = 0 \tag{5.2}$$

$$A\frac{d(ch+c_* z)}{dt} + \sum_{k=1}^{8} Q_k = 0 \tag{5.3}$$

where A is the area of the cell, t is time, z is the bottom elevation, h is the flow depth, c is the sediment volumetric concentration of the mixture, c_* is the solid volumetric concentration of the dry bed, and Q_k is the discharge exchanged with the surrounding cells along the kth direction (Fig. 5.7a), assumed to be positive if outflowing and negative otherwise. Following the kinematic wave approach, a uniform flow equation is locally applied if the flow occurs along positive slopes while a broad-crested weir equation is considered if the flow occurs along adverse slopes (Fig. 5.7b). The discharges are expressed by the following relationships:

$$Q_{i,k} = C\Delta x h w_k \sqrt{g h sin\theta_k},\ w_k = \frac{sin\theta_k}{\sum_{k=1}^{n} sin\theta_k},\ \theta_k = tan^{-1}\frac{z-z_k}{\Delta x} \tag{5.4}$$

$$Q_{i,k} = C_q \Delta x s_k \sqrt{2g}(h-z_k)^{1.5},\ s_k = \frac{h-z_k}{\sum_{k=1}^{m}(h-z_k)},\ \Theta_k = tan^{-1}\frac{h+z-h_k-z_k}{\Delta x} \tag{5.5}$$

where x is the cell size ($=A^{0.5}$), θ_k is the angle formed with the horizontal by the line joining the center of the considered cell with that of the kth adjacent cell, C is the conductance coefficient (Tsubaki, 1972), and C_q is a discharge coefficient, assumed equal to that of the water (0.385) because of the missing of experimental observations. The two weighting functions w_k and s_k are introduced for partitioning the flow along the eight ($n+m \leq 8$) different directions issuing from a given cell to the adjacent cells, provided that the corresponding bed (θ_k) and flow surface ($h-z_k$) drops are positive.

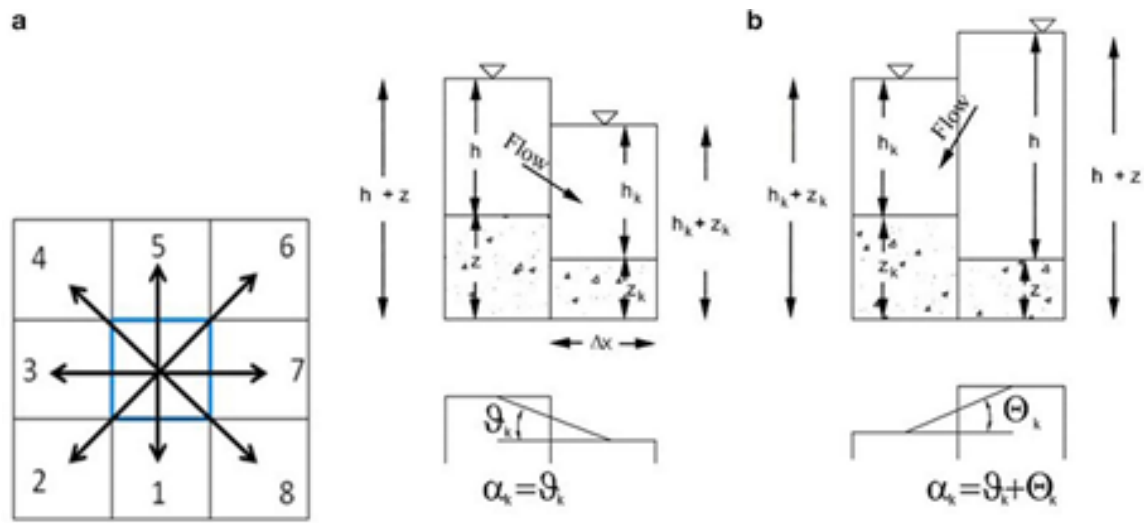

Fig. 5.7. The eight possible flow directions (a) and the two possible flow conditions of the routing model (b); partial redrawing of the Figures 1 and 2 of Gregoretti et al. (2016b).

The choice of the kinematic approach is justified by the analysis of Arattano and Savage (1994), and Di Cristo et al. (2014) for which a kinematic model can provide reliable simulations of debis flow propagation along sloping channels. The uniform flow Equation (5.4) can be straightforwardly derived by integrating along the flow depth the dispersive normal stress given by Bagnold (1954), typical of a grain-collision dominated rheology that rules the stony debris flows dynamics (Takahashi, 2007). The use of such a law (i.e., the assumption of grain-inertial rheology) is here justified by the absence of clay and the poor percentages of silt in the material sampled in the initiation areas of neighboring area of Chiapuzza having nearly the same characteristics of that eroded on Vallon d'Antrimoia and Ru Salvela Creek (see section 5.2.1). Takahashi (2007) provided also an expression for the conductance coefficient C, depending on an empirical constant that can vary on a large interval, and consequently C up to ten times (Gregoretti, 2000; Takahashi, 2007; Armanini et al., 2009). Therefore, it should be calibrated against field measurements. The Exner equation:

$$\frac{dz}{dt} = D - E \tag{5.6}$$

between the deposition (D) and erosion (E) rates. This difference is modeled modifying the empirical relationship of Egashira and Ashida (1987) (see also Brufau et al., 2000; Egashira et al., 2001):

$$E - D = K[(sin\alpha_k - sin\theta_{LIM})V_{max}] \tag{5.7}$$

where K is an empirical constant, ranging between 0 and 1, $\alpha_k = \theta_k$ in the case of the uniform flow described by Equation (5.4), and $\alpha_k = \Theta_k + \theta_k$ in the case of the weir flow associated with Equation (5.5), with Θ_k the angle that the horizontal forms with the line joining the center of the flow surface of the considered cells along which the flow is directed (Fig. 5.7b). Erosion and deposition are computed along the steepest direction, where the maximum value V_{max} of the mean velocities contributing to the discharges Q_k is attained. In particular, deposition occurs if $V_{max}<V_{LIM}$ and $\alpha_k<\theta_{LIM}$, while

erosion requires that $V_{max}>V_{LIM}$ and $\alpha_k>\theta_{LIM}$. The limiting values V_{LIM} and θ_{LIM} are different for deposition (V_{LIM-D}, θ_{LIM-D}) and erosion (V_{LIM-E}, θ_{LIM-E}). Note that, considering a generic direction transversal to the steepest direction could lead to unrealistically large depositions. Furthermore, a cell could be subjected to both erosion and deposition at the same time.

In addition three more conditions descending from the debris flow physics are imposed. Erosion is computed only if $dh/dt>0$ because according to the field observations of Berger et al. (2011) erosion generally occurs during the passage of the debris flow front, and starts before the maximum value of the flow depth is reached. Moreover, erosion cannot indefinitely occur (i.e., sediment concentration tending to unity) and is allowed within a given cell if $c<0.9c_*$, maximum transport concentration value according to Takahashi (2007). Likewise deposition can take place if $c>c_D$.

The limiting concentration for deposition, $c_D=0.05$, is introduced to prevent c from becoming negative if large deposition rates occur, even though no substantial quantitative differences have been observed by setting $c_D=0$.

The original law of Egashira and Ashida (1987) was adapted after eliminating the reasons for the equilibrium angle because it can lead to uncorrect results. In Gregoretti et al. (2016b) more details about it with its physical justification. Please note that also Hussin et al. (2012) use, even if more simplified, a similar approach to estimate the bed deposition/entrainment rate.

An explicit scheme is used to solve numerically the model equations with the time step computed according to the Courant-Friedrichs-Lewy stability condition. Flow discharges and the rate of change bed elevation are computed for each cell by Equations (5.4–5.7) and used in Equation (5.2) to provide the flow depth. Finally Equation (5.3) provides the sediment concentration. The reader is referred to Gregoretti et al. (2016b) for more details and explanations about the numerical integration.

5.3 The debris flow event: Geomorphological Analysis

The geomorphological analysis is essential for understanding whichever gravitative mass movement on earth, and allowing its reliable reproduction by models. It also provides information about its occurrence and behavior to be used in future studies as recommendations for countermeasures. All the basin was carefully surveyed to identify all the contributions, liquid or solid-liquid, to the debris flow that routed along Ru Secco. The entrained and deposited sediment volumes were estimated through the deposition-erosion depths map (Fig. 5.8a, Fig. 5.9) that was obtained differencing the pre and post-event DEMs. The deposition and erosion depths are grouped into classes of 2 m size, about twenty and five times larger the average and maximum error (that of photogrammetric points) respectively. The map of Fig. 5.9 allows the computation of the sediment volumes deposited and entrained: 108,700 and 57,165 m^3, respectively. Their difference 51,535 m^3 is the sediment volume that runoff entrained on the Vallon d'Antrimoia sloping plateau, upstream the Ru Salvela head. This volume is increased to 52,535 m^3 to consider the sediment volume that reached the Boite River, so that the total mobilized sediment volume raises up to about 110,000 m^3. Therefore, the debris flow event was triggered upstream the Ru Salvela Creek. Abundant runoff descending the northern cliffs of Mount Antelao corresponding to the basins of Antrimoia and Salvela in Fig. 5.1, hit the debris deposits laying on the Vallon d'Antrimoia inclined plateau (upper blue arrows in Fig. 5.2) and entrained enough sediment to generate a solid-liquid surge. This surge descended along the rock chutes linking the Vallon d'Antrimoia with the Ru Salvela head (upper red arrows in Fig. 5.2) and propagated over the debris deposit covering the Ru Salvela Creek. This deposit (Fig. 5.3a, Fig. 5.4) has a volume of 175,000 m^3 obtained differencing the pre-event DEM with that before the rock collapse on November 2014, obtained through the LiDAR 2011 points. During the propagation over the rock fall deposits on Ru Salvela Creek, it entrained the debris material and meanwhile received the liquid contribution from Ru Longia (blue arrow on the right in Fig. 5.2), that increased its erosive power. At the confluence with Ru Secco Creek, the well formed debris flow was supplied with the stream flow descending along Ru Secco Creek and the solid-liquid contribution from the debris flow triggered along the Ru Beche. These contributions increased its solid-liquid volume. The large runoff amount and the entrained sediments

deriving from cliffs collapse in absence of clay and low percentage of silt, point out to a debris flow of stony type (Takahashi, 2007).

The deposition-erosion map of Fig. 5.8a clearly shows the erosion occurred along the middle part, in longitudinal sense, of the debris deposit covering the Ru Salvela Creek where the solid-liquid surge, descending from the Vallon d'Antrimoia inclined plateau, excavated a channel (bottom middle insert of Fig. 5.8a). Both the sides of this channel are characterized by small debris deposits, i.e., the typical lateral levee that debris flow creates during its routing. These deposits usually occur on debris flow sides when the relative flow depth is small and terrain roughness is able to stop the flowing material.

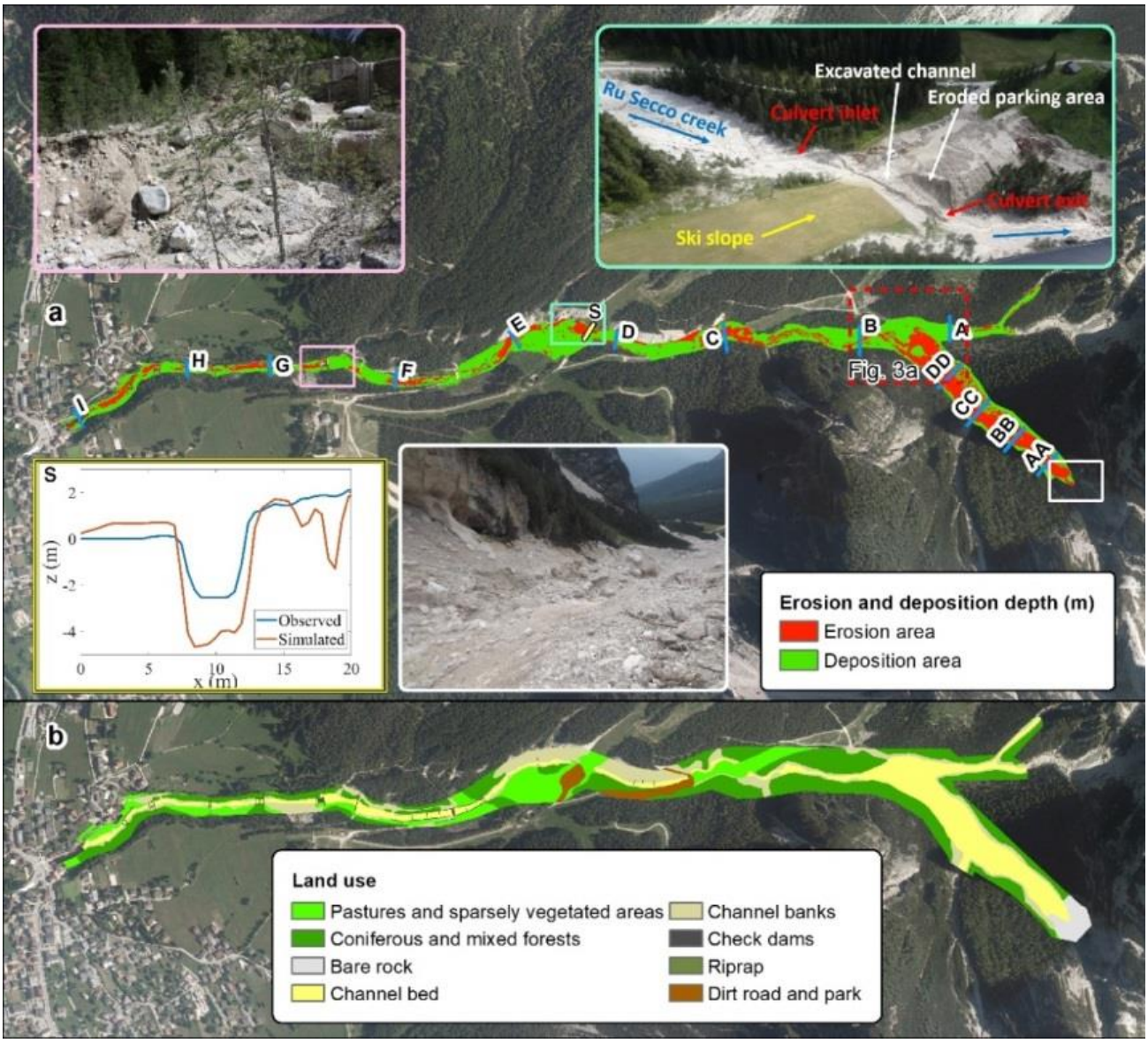

Fig. 5.8. View of the area subjected to deposition or erosion and land use. The upper image (a) is the general view of the areas routed by debris flows and subjected to deposition or erosion. The top right insert is the post-event view of the area depicted in Fig. 5.3b while the other three inserts show the downstream view of debris flow route incising the debris material covering the Ru Salvela creek (bottom middle), the observed and simulated cross-section of the channel excavated by debris flow above the culvert (bottom left) and a particular of a bank erosion after the upper culvert (top left). The position of the cross-sections that are shown in the supplemental materials is also indicated. The lower image (b) is the landuse of terrain for the routing simulation.

Upstream the confluence, debris flow began also to deposit significative quantities of sediments anticipating that occurred in larger size on the right side of Ru Secco Creek just before and in correspondence of the confluence. Fig. S5.1 shows the bottom longitudinal profile of the channel excavated by debris flow on the debris deposit covering Ru Salvela Creek with some cross-sections. It can be observed that in the upstream part, debris flow entrained most of the debris material of deposit from the rock collapse while in the downstream part it did not. Debris flow, then, channelized along Ru Secco mainly depositing sediments on the sides and eroding the bed in the middle. About 380 m upstream the first culvert inlet, debris flow began to deposits. This reach is in fact protected by check dams and the bed slope diminishes. The debris flow front reached the inlet culvert where it stopped. Photos taken during the sediment removal operations and located in the supplemental material (Fig. S5.2) show some big rocks obstructing inlet, i.e., the debris flow front that stopped, while the culvert is not clogged of sediments. In the same Fig. S5.2, the exit of the culvert just after the event appears mainly free. The stoppage of the front imposed the deposition of the solid part of the current flowing behind it, that extended both in depth and upstream (up to 380 m), interesting all the creek cross-section and only the liquid part flowed downstream. Fig. S5.3 shows the pre and post-event bottom longitudinal profiles along Ru Secco Creek from the confluence to the village with nine cross-sections (A–I). Upstream the culvert, the bottom is in general raised up respect to the pre-event situation. Nevertheless, the rear part of the solid-liquid current, flowing over this large deposit, reached the culvert and flooded all the area surrounding it. This overflow caused sediments deposition on the main part of the parking and flow returned to the Ru Secco Creek after eroding all the border area of the parking on the creek side (top right insert of Fig. 5.8a). The overflow on the terrain above the culvert eroded it creating an erosion channel. Top right and bottom left inserts of Fig. 5.8a shows the downstream view of this channel and its cross section respectively. The re-channalized flow routed downstream causing erosion on some bends and mainly downstream the check dams (top left insert of Fig. 5.8a) because of the large drop (see also sections E and F of Fig. S5.3). The distribution of the volumes of deposited and eroded sediments is analyzed after dividing the flow pattern in five significant areas. Fig. 5.9 shows the areas with a table listing the corresponding entrained and deposited sediment volumes: most of erosion downstream the Vallon d'Antrimoia inclined plateau, occurred on the debris deposit covering the Ru Salvela Creek (35,400 m^3, about 63% of the total), while most of deposition occurred along Ru Secco between the confluence with the Ru Salvela Creek and the culvert inlet (62,700 m^3, about 55% of the total). The values of the volumes of the deposited and eroded sediments downstream the culvert, about 29,581 and 12,721 m^3 respectively, show that debris flow transformed in an hyperconcentrated flow. This occurred for two main reasons: (1) the large deposition occurred upstream the culvert that stopped the anterior part of debris flow that is usually richer of sediments; (2) the bed slope, that in this reach decreases from 11 and 2°, is not able to guarantee the transport of large quantities of sediments. The view of the cross-sections E–I, downstream the culvert with the pre and post-event bottom longitudinal profiles of the Ru Secco Creek (Fig. S5.3) shows that some reaches were subjected to deposition (the larger part), while other subjected to erosion. In Fig. 5.2 it can be also observed a small debris flow channel joining the Ru Secco on its right side. Direct field survey showed that its contribution was negligible and for this reason it was not considered in the routing simulations. Until late '50s the slopes on the right side were routed by debris flow providing the main solid-liquid contributions to Ru Secco (Fig. S5.4, Fig. S5.5). The works for transforming this area in a touristic resort area stopped them. About 200 m downstream the base of the overhanging rocky cliffs, the slope was reshaped, and, where needed, some protection works (walls and pottings) were built. The small debris flow routed a new path on the reshaped slope, avoiding, the protection works.

5.4 The phenomenon reproduction by models

This section concerns the reproduction of the entire phenomenon by models. It is divided in three subsections relative to the hydrological modeling, the solid-liquid hydrographs determination and the debris flow routing. The hydrological modeling provides runoff hydrographs that directly contributed to the phenomenon or entrained the debris material forming the solid-liquid hydrographs of the initial surges. Both runoff and solid liquid hydrographs are the input for the routing modeling.

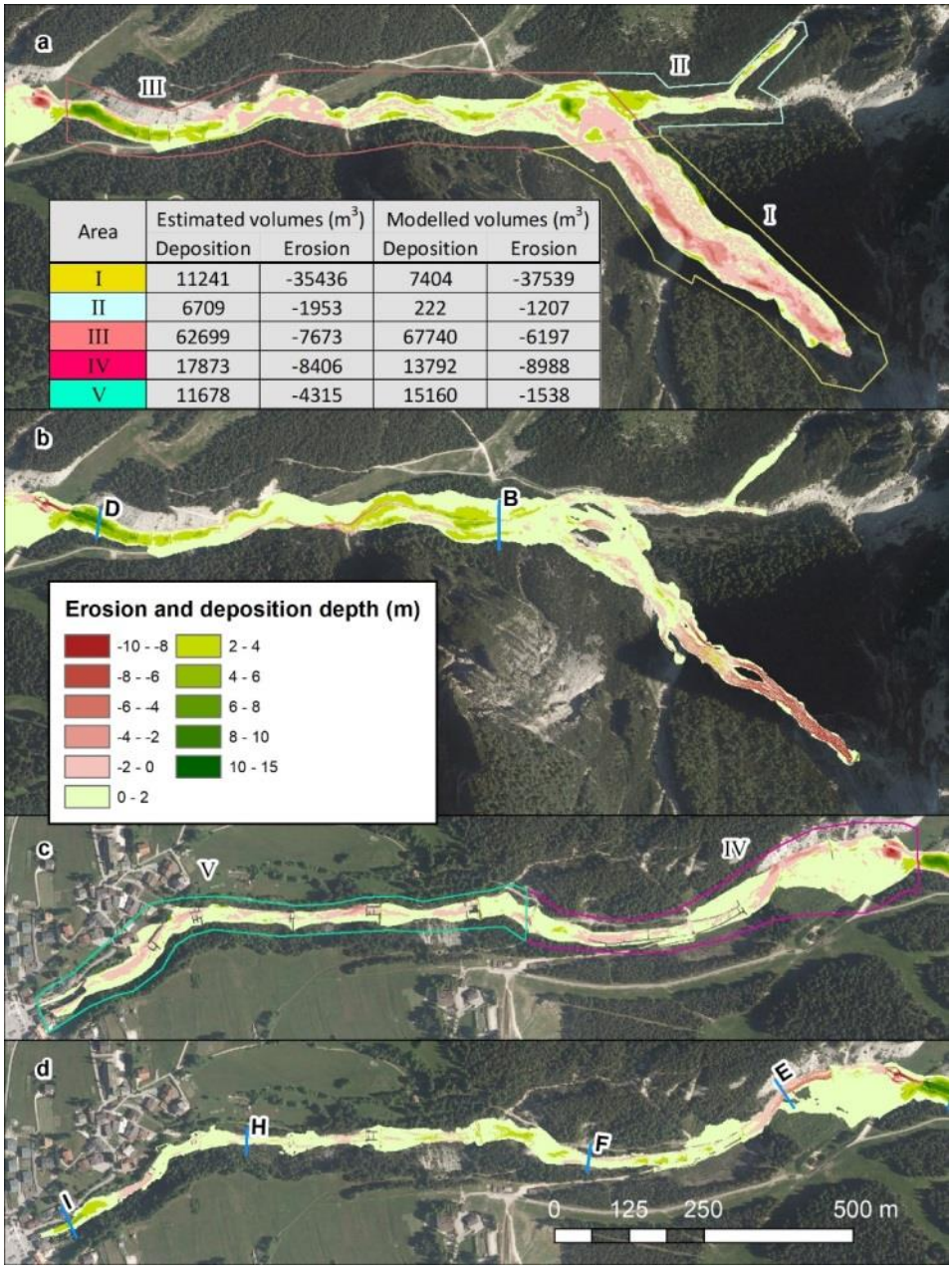

Area	Estimated volumes (m^3)		Modelled volumes (m^3)	
	Deposition	Erosion	Deposition	Erosion
I	11241	-35436	7404	-37539
II	6709	-1953	222	-1207
III	62699	-7673	67740	-6197
IV	17873	-8406	13792	-8988
V	11678	-4315	15160	-1538

Fig. 5.9. Deposition and erosion depths map for the two groups of reaches. Upper image (a) is the map of estimated deposition and erosion for the reaches I-III, while the image below (b) is that simulated. Images (c,d) are the corresponding of (a,b) for the reaches IV-V respectively. The position of the six sections (B, D, E, F, H, and I) is also shown.

5.4.1 Hydrological Simulations

The rainfall-runoff modeling for the five basins depicted in Fig. 5.1 was carried out by the model of Gregoretti et al. (2016a). The model computes the excess rainfall for each cell of the basin and routes it through the steepest path to the channel network. The routing to the channel network occurs with constant velocity while that along the channel network to the outlet is ruled by means of a matched-diffusivity kinematic wave model. Parameters for the excess rainfall computation and slope routing are *CN*, the infiltration rate f_C and slope velocity *U* which assume different values for each soil typology covering the basin. The values of these parameters are shown in Table 5.1 with those of *CN* and f_C for rocky soil updated by Bernard (2018). Parameters for channel network routing are the roughness coefficient k_S=9m$^{1/3}$/s, the

channel width at the outlet, b_0, and a morphological exponent, b_1=0.26. The values of b_0 were measured in the case of the basins of Ru Longia, Ru Secco and Ru Beche, while for the Salvela and Antrimoia basins, they were obtained by LiDAR 2015 data. These values are shown in Table 5.2. The event occurred in *AMC* I conditions, because it did not rain in the previous 2 days (Bernard, 2018). The flow path from each cell of the basin to the channel network is obtained through the DEM (see Gregoretti et al., 2016a for details). The channel network cannot be provided by cells with a drainage area larger than 0.005 km^2 as proposed by McGlynn and Seibert (2003) and McGuire et al. (2005). This threshold value was successfully tested by Gregoretti et al. (2016a) in the head water rocky basin of Dimai that has the same morphological features of those investigated here and about 10 km far but, unfortunately, it cannot be applied to the Ru Beche basin. Its area is too small (about 0.022 km^2) and that threshold does not work because too large. For this reason, we investigated the transition from slope to channel routing by using two different methodologies: (1) the convergence of the upslope drainage area values after using different techniques (Wilson and Gallant, 2000); (2) the slope scaling method (Ijjasz-Vasquez and Bras, 1995). The first method examines the convergence of values of the upslope drainage area computed following the *D8* and $D\infty$ methods (Tarboton, 1997). The value where the values of drainage areas converge, is the area threshold value for determining the channel network. The second method explores the behavior of the drainage area vs. its mean slope. The drainage area values, where there is a discontinuity, correspond to the transition from slope routing to channel routing. The two methods provide the same results supporting the reliability of the obtained threshold value for the determining the channel network. Fig. S5.6 shows the results of the two methods. These values together those of the morphometric characteristics of the basins are shown in Table 5.2. Simulations were carried out using both the radar estimates and the observed rainfall depths. Results are shown in Fig. 5.10. Simulations corresponding to the corrected radar estimates provide runoff hydrographs slightly larger except that of the Ru Secco basin whose peak value is about 25% larger.

Coefficient	**Rocky surface**	**Mountain pine slopes**	**Scree slopes**
CN	91.4	61.0	65–70
U (m/s)	0.70	0.05	0.10
f_C (cm/h)	3.5	5.5	10.8

Table 5.1. Parameters adopted in the hydrological model. Symbols are defined as follows: CN, Curve Number for computing the excess rainfall; U, runoff velocity; fc infiltration rate.

	Ru Longia	**Salvela**	**Antrimoia**	**Ru Secco**	**Ru Beche**
A_B (km^2)	0.4	0.57	0.57	1.25	0.022
A_T (km^2)	0.0096	0.0095	0.0098	0.0096	0.00071
z_O (m a.s.l.)	1,537	1,698	1,873	1,477	1,578
z_M (m a.s.l.)	2,112	2,303	2,584	2,143	1,727
z_{MAX} (m a.s.l.)	2,557	3,142	3,218	2,900	1,889
SL_{MEAN} (%)	113	145	2,584	119	175
SL_{MAX} (%)	2,759	6,044	3,218	5,362	1,684
b_0 (m)	2.5	3	3	3	1.5

Table 5.2. Morphometric characteristics of the basins: AB, basin area; AT, threshold area for channel network; zO, basin outlet altitude; zM, mean basin altitude; zMAX , maximum basin altitude; SLMEAN, mean slope; SLMAX, maximum slope; b0, outlet width.

5.4.2 The solid-liquid hydrographs

The sites on the Vallon Antrimoia sloping plateau where the solid-liquid surges formed after the impact of runoff with the debris deposits could not be surveyed because of their inacessibility. Therefore, we determineted the solid-liquid hydrographs at the middle of the rock chute. Following Gregoretti et al. (2012), and Han et al. (2017), we adopted a triangular shape of the solid-liquid hydrograph with an abrupt raise to peak and a less rapid decreasing because downstream the triggering area, the debris flow surge tends to assume such a shape. Following Gregoretti et al. (2016b) the solid-liquid volume is given by the sum of the solid volume with the volumes of runoff contributing to debris flow and of the interstitial water of the entrained sediments. Because of the high intensity precipitation and the quite high permeabilty of the debris, deposits are assumed to be nearly in saturated conditions. The solid volume can be obtained by the volume of sediments entrained on the Vallon d'Antrimoia that is provided by the difference between the computed deposited and eroded sediment volumes downstream it: 108,700−57,165 = 51,535 m^3. This volume is increased to 52,535 m^3 to consider the sediment volume that reached the Boite River (see the previous section). The solid volume is the entrained sediments volume multiplied by c_*. The runoff contributing to debris flow is the part of runoff hydrograph where the runoff discharge is larger than the triggering discharge. In the present case, the inaccessibility of the triggering site prevented direct measurements, and the unit width triggering discharge was estimated as 0.05 m^2/s through the relationship proposed by Gregoretti and Dalla Fontana (2008) after assuming reasonable values of sediments mean size (0.1 m) and bed slope angle (30°). The interstitial water volume is given by the difference between the entrained sediments volume and the just computed solid volume. The solid-liquid hydrograph is the triangle with the height equal to the peak discharge value and the base equal to the ratio between the double of the solid-liquid volume and the peak value. The peak solid-liquid discharge, Q_P, is computed following the relationship provided by Lanzoni et al. (2017):

$$\frac{Q_P}{Q_0} = 0.75\frac{c_*}{c_* - c_F} \tag{5.11}$$

where c_F is the solid volumetric concentration of the debris flow front, and, Q_0 is the runoff peak discharge. The value for c_* is assumed equal to 0.62 (value proposed by Gregoretti et al., 2016b for unchannelized debris deposits that are not subjected to compaction) and that for c_F equal to $0.9c_*$ (0.558) according to Takahashi (2007). The two solid-liquid hydrographs are computed by using the runoff hydrograph of the two basins of Antrimoia and Salvela after partioning the sediments volume (52,535 m^3) in 38,035 and 14,500 m^3, respectively. The Antrimoia basin, in fact, occupies the larger part of the Vallon Antrimoia sloping plateau where debris deposits lie. The resulting solid-liquid hydrographs are shown in Fig. S5.7.

5.4.3 Routing Simulations

Parameters of debris flow routing simulation depend on the terrain (channel, scree, grass, wood) and slope because flow resistance and deposition-entrainment processes vary with them. Fig. 5.8b shows the land use of the terrain interested by the phenomenon. The values of parameters used for the routing simulation are shown in Table 5.3. Until the culvert, these values are those proposed by Gregoretti et al. (2016b), except the conductance coefficient, *C*, that was increased from 3 to 5 where the flow is channelized. Gregoretti et al. (2016b) in fact simulated the dispersion in several directions on a fan of an occurred debris flow of high magnitude while in present case the flow is channelized. In the case of channelized flow, estimates of *C*, from field data of stony debris flows with a magnitude much lower than that here studied (Gregoretti, 2000; Hurlimann et al., 2003; Okano et al., 2012), mostly range in the interval 1–3. Flume experiments of Tognacca (1999) and Lanzoni et al. (2017) on stony debris flows show that the velocity increases with the triggering discharge much more than the flow depth, and consequently also the conductance coefficient C increases with it. Fig. 5.8 shows, in fact, the growth of the experimental values of *C* with the triggering discharge. This means that the debris flow

discharge, and thus the magnitude of the debris flow, increases with the amount of the runoff generating the event, while the flow resistance decreases. Therefore, the value of the conductance coefficient used in the simulation of the present channelized debris flow was raised to 5 because this event, characterized by a magnitude higher than that of the observed and above referenced debris flows, was triggered by a larger runoff amount. Downstream the culvert, debris flow transforms to hyperconcentrated flow because most of solid material deposited upstream and bed slope decreases from 11° to 2° along the flow direction. This means an increase of the conductance coefficient and a decrease of the limit values of angle and velocity both for deposition and entrainment because the transported solid concentration decreases (Armanini, 2015). For all the channelized flows, different values of parameters were adopted for the banks where, due to the low submergence, flow resistance is larger and for the wooded and grass areas. The value of θ_{LIM-E} was assumed equal to 16°, inferior angle associated to the occurrence of mature channalized stony debris flows according to the experiments of Lanzoni et al. (2017). This value was also confirmed by the field observations of Jordan (1994). For the value of V_{LIM-E}, we chose the reasonable value of 1.8 m/s that provided the better results (it is a calibrated value). We also adopted values of K equal to 0.1 and 0.5 for deposition and entrainment respectively. The values of parameters downstream the culvert were assigned after calibration.

The simulated deposition and erosion depths are shown together those estimated in Fig. 5.9. The flow pattern, for a better comparison between simulation and estimate of the deposited and eroded sediments volume, has been divided in five reaches: the Ru Salvela Creek (I), the Ru Beche (II), the Ru Secco Creek upstream the culvert (III), the Ru Secco Creek downstream the culvert with a mean bed slope of 8° (IV) and the ending reach with a mean bed slope of 4.5° (V). In particular both the simulated and estimated deposition and erosion depths are shown in two groups of reaches, I–III and IV–V respectively, allowing a more detailed analysis together with a table the values of the simulated and estimated sediment volumes, that were eroded and deposited for each reach. The comparison of simulation results with the observations (Fig. 5.9) shows that the main features of the deposition-erosion pattern are captured by the simulation except at the confluence of Ru Salvela with Ru Secco Creek and in the downstream part of the ending reach where the bed sloping angle decreases to a value of about 2°. The simulated volumes of deposited and eroded sediments are 104,318 and 55,469 m^3, respectively. Both of them underestimate those observed of 4 and 3% respectively. The examination of the results reach by reach allows a better understanding of the model capability to simulate the occurred phenomenon. In reach I (that of Ru Salvela creek), the simulated eroded sediment volume quasi coincides with that estimated but it is more concentrated in the upstream part of Ru Salvela. This could be due to an imperfect reproduction of the pre-event DEM at the head of the Ru Salvela. This zone is just under the cliffs and some three dimensional shapes of debris deposits could be not detectable by the photos by which the pre-event DEM has been built. For this reason, in the upstream part, the simulated debris flow front mainly concentrated in a narrow path that was highly eroded. Resulting debris surge was too concentrated and, therefore, eroded a smaller amount of sediments in the downstream part. About deposition, the large deposits at the confluence were not satisfactory reproduced due to missed local bed reproduction of the terrain in the pre-event DEM. The deposits on this area were subjected to excavation during the restoration works in the month between the photo time and the event. Therefore, some path and the flat area built by the excavators, that we could not to reproduce, could have significatively conditioned the flow routing. Sediment volume that did not deposited there during simulation, in fact, deposited just downstream the confluence (beginning of reach III). In fact simulated deposition depths, there, are on average larger than those estimated. Routing along Ru Beche (reach II) was satisfactory simulated but not that along the Ru Secco Creek between the two confluences with Ru Beche and Ru Salvela Creeks. This could be a result of the missed deposition of flow arriving from the Ru Salvela Creek, explained above. There is a quite good agreement between simulation results and observations along reach III: nearly coincidence of areas subjected to the main deposition and erosion phenomena combined with the nearly coincidence of the simulated and estimated sediments volumes that were depositated and entrained (the percentage of simulated deposited sediments volume is 8% higher than that observed due to the missing of simulated deposits at the confluence). The flooding of the park and the erosion of it, together the excavation of a channel in the terrain overlaying the culvert, is also nearly satisfactory simulated. The bottom left insert of Fig. 5.8a shows the comparison between the surveyed and simulated cross section of the excavated channel. The simulation of the excavation appears fairly satisfactorily, even if larger. For the reach IV visual inspection of Fig. 5.9c,d shows that erosion and deposition pattern is well reproduced and the simulated eroded sediments volume nearly coincides

with that estimated. Only the deposition volume is underestimated. For the reach V, the agreement is not so satisfactory both for the volumes and the areas. In fact the erosion on its downstream part is not captured, while conversely deposition is overestimated. Fig. 5.11 shows the simulated solid-liquid and solid discharge, Q (left) and Q_S (right) respectively, for the six sections shown in Fig. 5.9. The solid-liquid discharge reaches its maximum after the confluence and then it begins to decrease. The solid discharge is consistent until section F (Fig. 5.9) due to the large erosion occurred upstream. After that, it decreases to negligible values, characteristics of bed-load sediment transport.

5.5 Discussion of results

The direct post-event field survey and the analysis of the pre-event morphology during time allowed the geomorphological analysis of the event. It consisted in the recognition of the phenomenon occurrence and of its main features. The analysis of the pre-event morphology between ’50s and nowadays also showed that slopes on the right side of Ru Secco Creek were routed by debris flows before their transformation in a ski resorting area while the left side was not subjected to debris flow phenomena (Fig. S5.4, Fig. S5.5). In the present case study, the environmental changes due to man works can stop or reduce debris flow activity in areas prone to debris flow susceptibility, while those due to natural causes, as the formation of debris deposits caused by local terrain instabilities, if connected to the channel network (Cavalli et al., 2013; Tiranti et al., 2016, 2018), allow the conditions for debris flow occurrence, where it never did. Both the historical basins where debris flows formed until ’50s and the new one of Ru Salvela are debris flow dominated according to the geomorphic indexes: the ruggedness number of Melton close or larger than 1 [0.75 is the inferior threshold value according to DeScally and Owens (2004) and local slope larger than 0.6 m/m in the schematic diagram between local slope and drainage area proposed by Montgomery and Foufoula-Georgiou (1993) for the hillslope to valley transition also used by Tarolli and Dalla Fontana (2009). Therefore, even if the basins are prone to debris flow activity according to the geomorphic indexes above, debris flow occurrence is determined by sediment availability as the concentration of abundant runoff on it. Finally, the geomorphological analysis, providing a reliable description of the occurred phenomenon, is at the base of simulation of the phenomenon by models.

The reproduction of the occurred phenomenon was the results of two phases: a careful survey of all the sub-basins supplying solid-liquid and liquid flows both the debris deposits covering Ru Salvela Creek and the Ru Secco Creek, allowed the identification of all the significative solid-liquid and liquid contributions (1); simulation by models of the formation and routing of these contributions and their impact on debris deposits (2). Reliable models results were allowed by trustworthy rainfall estimates that provided the input to the hydrological model and by topographical data that provided the base for running and testing them. The pre-event topographical data provided the DEM for running the routing simulations.

The post-event topographical data were used for determining the post-event DEM of the area routed by debris flow that, subtracted to the pre-event DEM, provided the deposition-erosion depths map, essential for understanding the phenomenon and testing the modeling. For this reason, the availability of pre and post-event data becomes fundamental for a reliable understanding of the phenomenon, as for its reproduction by models. Unfortunately, the simultaneous availability of pre and post-event data is not frequent but rare because in many cases the pre event terrain topography is usually unknown: previous occurred debris flow phenomena, also of small magnitude, and local instability phenomena (rock falls from upstream cliff and/or channel bank failures) can significatively change the flow path morphology, and consequently, debris flow routing could not be captured by simulations.

The reproduction of the occurred phenomenon, shown in the previous section, appears, in general, satisfactory. The deposition and erosion pattern, in fact, is quite well reproduced both in terms of areas and volumes apart some parts of the Ru Salvela Creek and of the ending reach. The simulation in the upstream reaches of Ru Salvela and Ru Secco Creeks is conditioned by pre-event local topographical data that are partially inaccurate and missing respectively. In the first case, the exact shape of pre-event debris deposit at the head of the Salvela Creek was not captured, while in the second case, due to the restoration work, the topography of some areas close to the confluence of Ru Salvela Creek with

Ru Secco Creek changed. The presence of excavator tracks and flat areas due to the debris deposits reworking could have significatively conditioned the local routing simulation. As a consequence the deposition at the confluence was understimated. The simulation downstream these reaches provides quite good results: the areas subjected to large phenomena of deposition and erosion are captured. Only the deposition depths upstream the culvert slightly overstimate those observed because of the missed deposition at the confluence of Ru Salvela Creek with Ru Secco Creek, and some areas subjected to erosion in the ending reach are missed. Moreover, the shape of the channel excavated by the debris flow after the culvert occlusion is nearly approximated (bottom left insert of Fig. 5.8a).

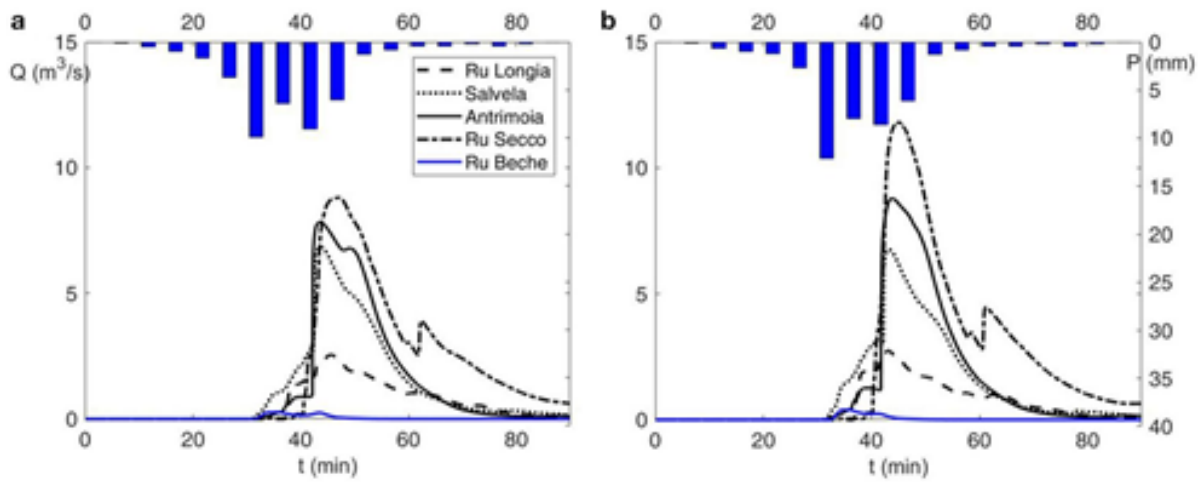

Fig. 5.10. Modeled runoff hydrographs for the five basins corresponding to the measures (a) and corrected radar estimates (b) of rainfall depth.

Terrain	C	θ_{LIM-D} (°)	V_{LIM-D} (m/s)	θ_{LIM-E} (°)	V_{LIM-E} (m/s)
Debris flow channel	5	14	1	16	1.8
Debris flow channel banks	3	8	0.5	9	0.9
Channel downstream culvert - upper reach	6	5	0.8	9	1.3
Banks downstream culvert - upper reach	4	4	0.5	7	0.8
Channel downstream culvert - lower reach	6	2.5	0.8	5	1.3
Banks downstream culvert - lower reach	4	2	0.5	4	0.8
Wood	1	12	0.8	20	3
Grass	3	14	1	20	2
Parking	5	8	0.8	12	1

Table 5.3. Values of the parameters used in the routing simulations for the different terrains.

The analysis of the solid-liquid and solid discharges (Fig. 5.11) allows a better understanding of the occurred phenomenon. After the confluence of Ru Salvela with Ru Secco the debris flow discharge peak has the maximum value and that of solid discharge is nearly the half (cross-section B). Just upstream the culvert (cross-section D) the solid-liquid discharge peak is reduced to less than 50% while that of solid one to about 30% due to the large deposition phenomena mostly due to the culvert occlusion. In the reach upstream the culvert solid-liquid and liquid discharge are in phase while in the downstream reach, it does not occur. In the cross-section E, downstream the culvert, the discharge in the first ten minutes is mostly liquid because the occlusion at the culvert inlet causes the deposition of most of solid phase. Solid

discharge, in fact after an initial but moderate increase, decreases to a neglegible value and then increases again to a value nearly the half of the total discharge. This behavior is the consequence of the initial erosion on the bend downstream the culvert followed by that of the parking on the Ru Secco side and on the terrain overlaying the culvert. Fig. 5.12 shows the time evolution of the simulated deposition and erosion pattern with the flow depth in correspondence of the culvert: at the beginning there is only a mainly liquid flow over the terrain downstream the culvert inlet that reaches the Ru Secco and causes the erosion on its right side as shown by Fig. 5.12a–c. This is coherent with the initial moderate solid discharge peak in cross-section E (Fig. 5.11). In the following 20 min the deposition and erosion on parking become consistent with the excavation of the channel just over the culvert (Fig. 5.12d–f) that is responsible of the second solid discharge peak in cross–section E (Fig. 5.11b). In cross-section F the behavior is analogous but for the absence of the initial moderate peak of solid discharge, reasonably due to an upstream deposition. Along cross-sections H and I solid-liquid peak discharge remains unchanged while flow volumes diminish because of the deposition. The solid discharge, in fact, decreases to negligible values, typical of bed load sediment transport. This could be the main reason for the not satisfactory simulation of the end part of the last reach V. In fact the hyperconcentrated flow transforms to a flow with low concentration values that on bed sloping angles of about 4.5° the cell model could be not able to simulate with efficacy.

The in general satisfactory and reliable reproduction of the occurred phenomenon provides a confirm of the methodology here followed for simulating a runoff generated debris flow when information on the triggering site are scarce: simulation of runoff, determination of the solid-liquid hydrograph in the initiation area and simulation of its downstream routing. Concerning the debris flow initiation, McGuire et al. (2017) proposed a more general and refined mathematical modeling, here not usable due to lack of information on the triggering area that resulted inaccessible. However, the simple and direct determination of the solid-liquid hydrograph, here proposed, proved to be reasonable and reliable. For debris flow routing, only models that consider deposition and entrainment should (Chen et al., 2006; Medina et al., 2008; Armanini et al., 2009; Hussin et al., 2012; Frank et al., 2015; Cuomo et al., 2016) should be used, provided their capability to simulate these processes. Finally, present work of back analysis of the phenomenon is also important, because it provides the framework and data needed for testing other models.

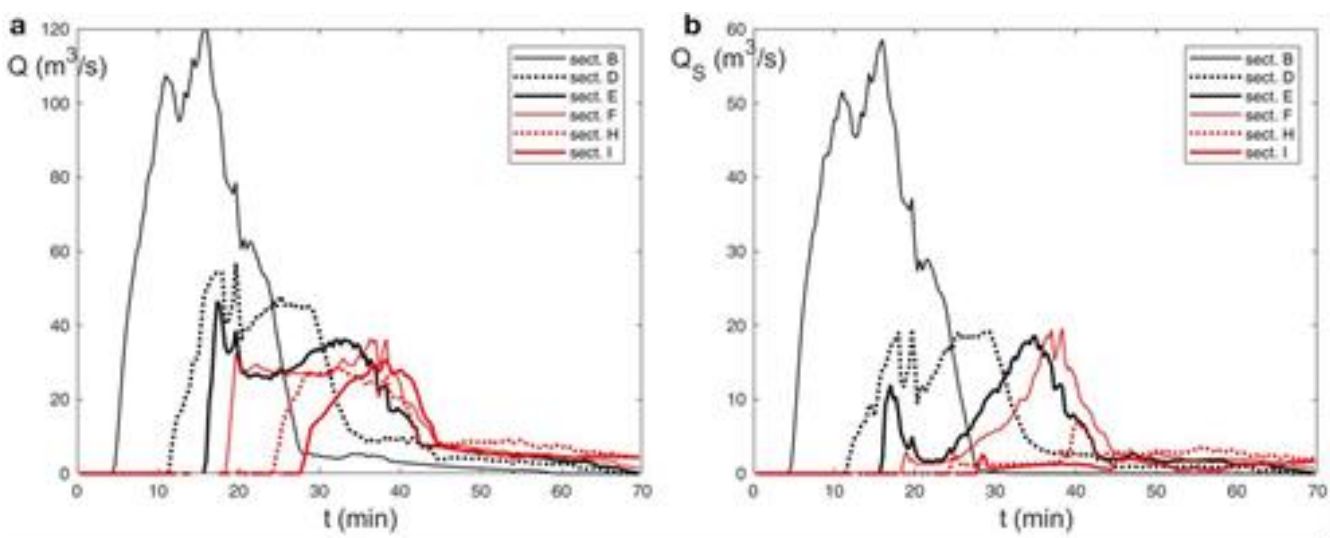

Fig. 5.11. Simulated hydrographs of solid-liquid (a) and solid discharge (b), Q and QS respectively, corresponding to the traces of the six sections of Fig. 5.9.

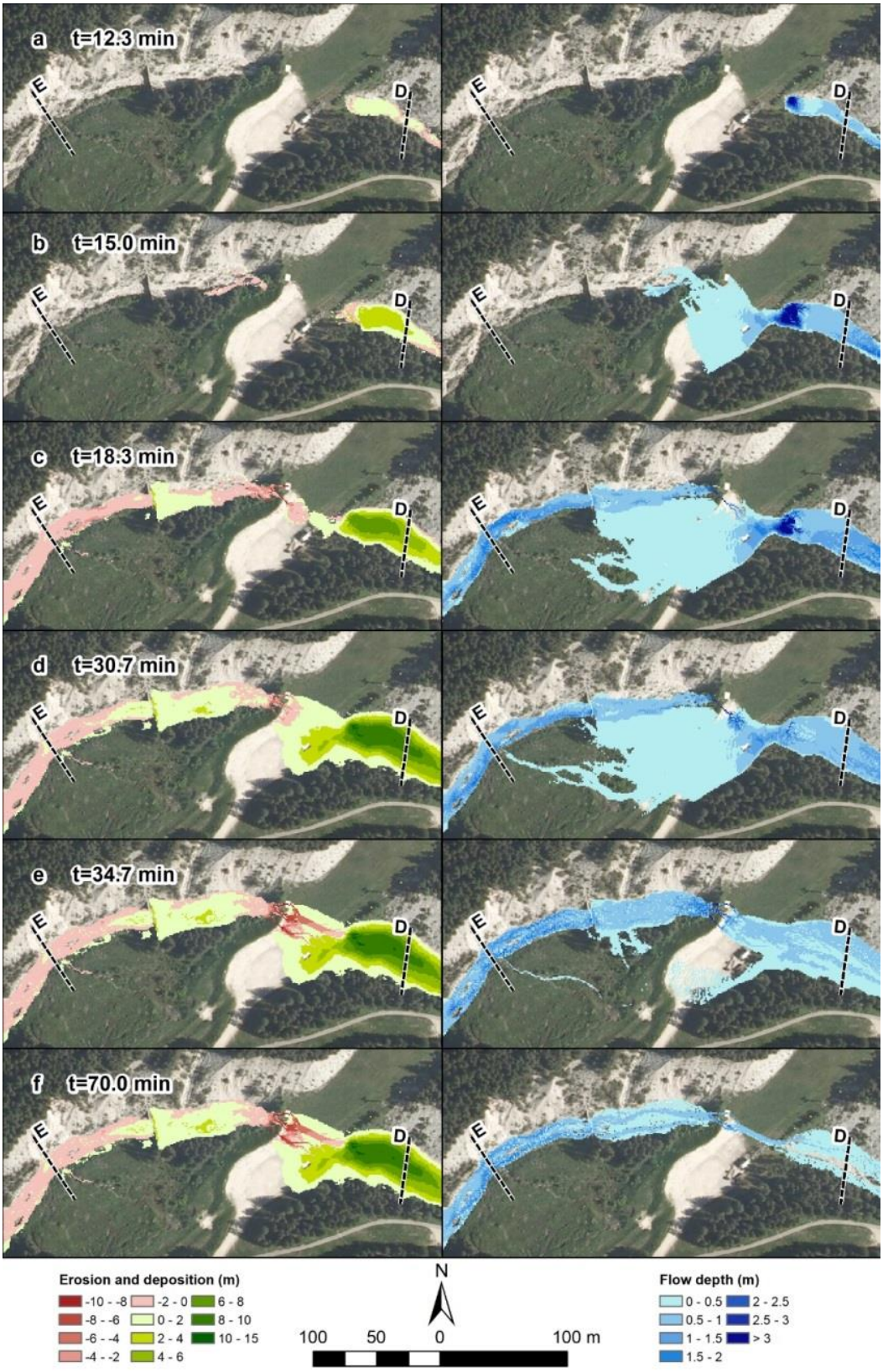

Fig. 5.12. The deposition and erosion depths (Left) and flow depths (Right) maps at different times [(a) t = 12.3 min, (b) t = 15.0 min, (c) 18.3 min, (d) t = 30.7 min, (e) t = 34.7 min, (f) t = 70.0 min] from the beginning of the simulation of the area close to the culvert and parking.

5.6 Conclusions

The 4th of August 2015, a high intensity storm concentrated on a square of about two kilometres and triggered some in-channel debris flows on Venetian Dolomites. The debris flow occurred on Ru Secco Creek was of large magnitude with about 100,000 m^3 entrained sediments. Ru Secco Creek was not routed by debris flows since late '50s after works for transforming its right side generally affected by debris flows, into a ski resort area. The debris flow of August 2015 started, in fact, on the opposite side because of the presence of very large debris deposits at the base of northeastern cliffs of Mount Antelao after a rock collapse occurred on November 2014. Direct field surveys and the analysis of pre and post-event topography allowed the recognition of liquid and solid-liquid contributions to the occurred phenomenon and its main features, as well as the map of deposition and erosion depths. Finally the phenomenon was modeled from rainfall-runoff transformation to deposition-erosion processes with satisfactory results: most of entrainment and deposition processes were captured except where initial topography data were partially inaccurate or missing or when solid discharge decreased to values typical of bed load. For the part strictly concerning the routing, these results were mainly due to the update of the cell model of Gregoretti et al. (2016b) that allows a better simulation of the entrainment process. Based on these analysis and modeling results, the main conclusions of this work can be summarized as follows. One of the main triggering factor for runoff generated debris flows is the sediment availability. The presence of debris deposits, due to local terrain instability phenomena, lead to the occurrence of a debris flow where it never occurred before. Furthermore, the satisfactorily results obtained in the reproduction of the phenomenon suggest that a reliable reproduction of an occurred debris flow should be based on four factors:

1. an accurate geomorphic analysis showing the main processes that caused it and occurred during its evolution. This analysis provides a guide for the implementation of the models simulating the physical processes concurrent to its development as well as the initial conditions;
2. a sufficiently accurate topographic base for the generation of DEMs on which models should run. Inaccuracy of topographical data or their missing can lead to unexpected and unreliable results;
3. a models cascade simulating all the physical processes associated to the debris flow occurrence;
4. the capability of the used models of capturing the main features of the phenomena associated to debris flow occurrence as the impulsive response of runoff to rainfall at the base of rocky cliffs and the entrainment and deposition processes occurring during the debris flow routing.

The in general satisfactory reproduction of the phenomenon by models proved the reliability of both the used methodology and single models. It should be stressed that the values of parameters used for running the models are mostly those resulting from the comparison between observations and simulations of other events. This is a good outcome because it shows the predictability characteristics of the models here used. Reliability of models is very important because a trustworthy prediction of debris flow routing (discharge hydrograph, deposition and erosion depths as the inundated area) is essential in any analysis of hazard assessment and countermeasures planning. At this purpose, the capability of the routing model to adequately simulate the entrainment process has a crucial role because the solid-liquid discharge peak and the transported sediments volume mainly depend on it. At least the updated cell model used here for the routing simulation proved to give reliable results also for hyperconcentrated flow and bed slopes larger than 8°.

Supplementary material

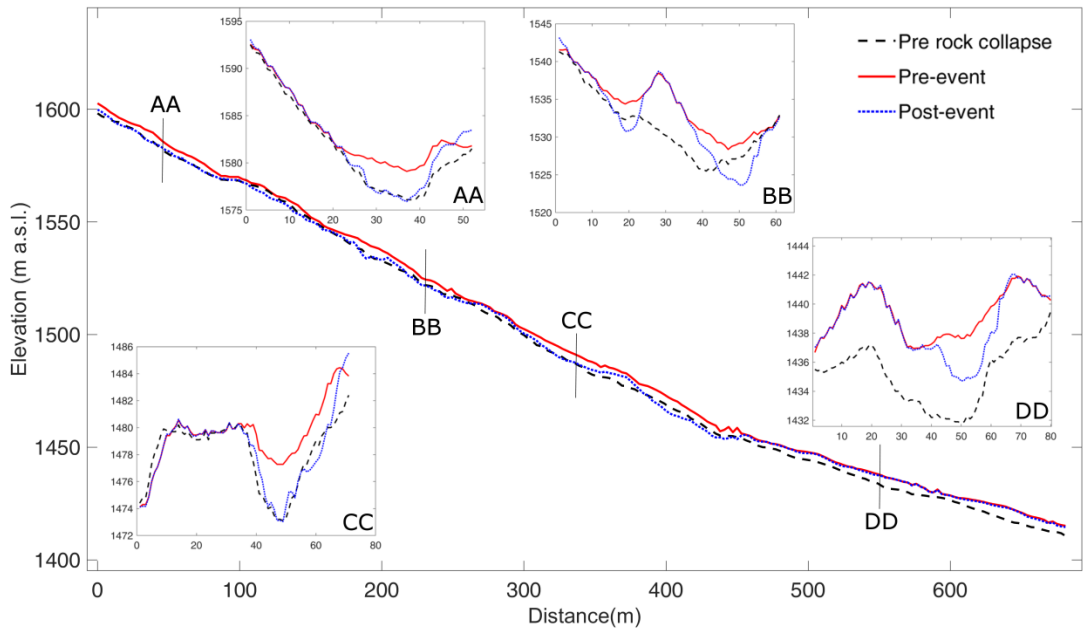

Fig. S5.1. Longitudinal bottom profile of the channel excavated by the debris flow on the debris deposit of Ru Salvela Creek with the cross-sections AA-DD of Fig. 5.8a.

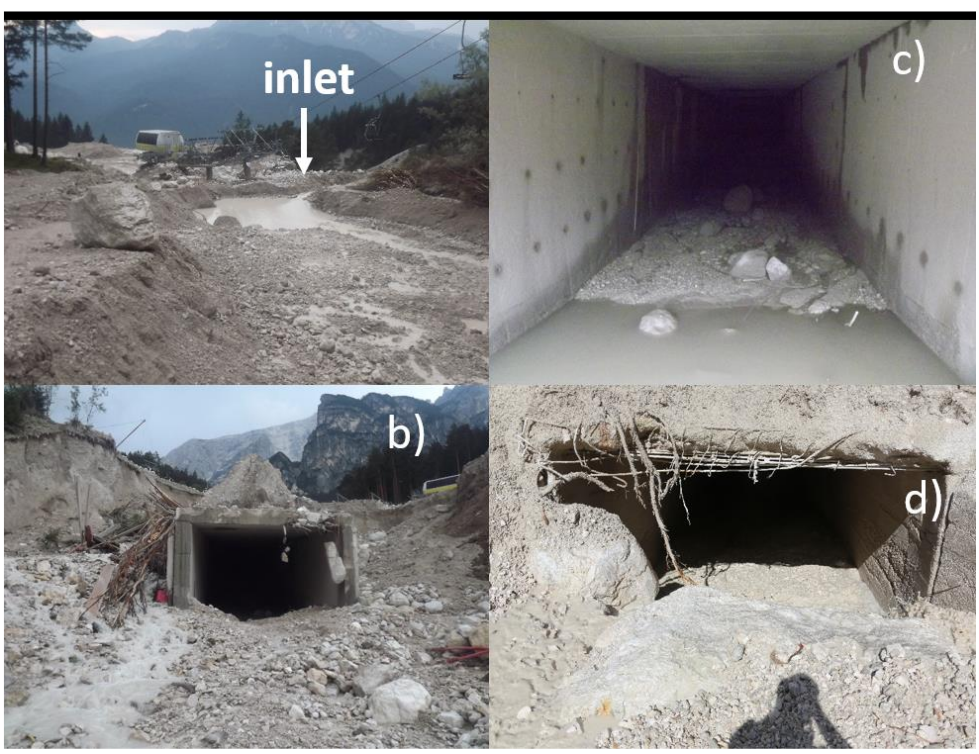

Fig. S5.2. Images of the culvert. Images of the inlet and exit of the culvert. Image a) the Ru Secco creek with the inlet submerged by deposits just after the event; b) inside the culvert close to the exit just after the event; c) the exit just after the event; d) the inlet during the sediment removal operations.

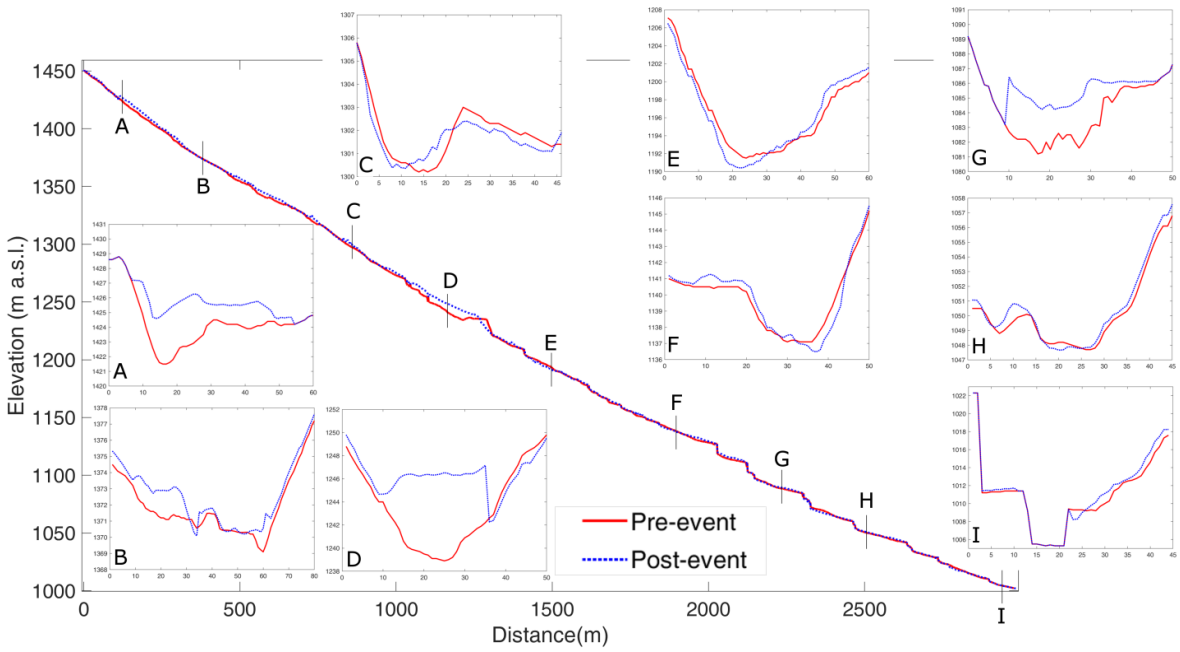

Fig. S5.3. Longitudinal bottom profile of the Ru Secco Creek from the confluence with Ru Salvela to the village with the cross-sections A-I of Fig. 5.8a.

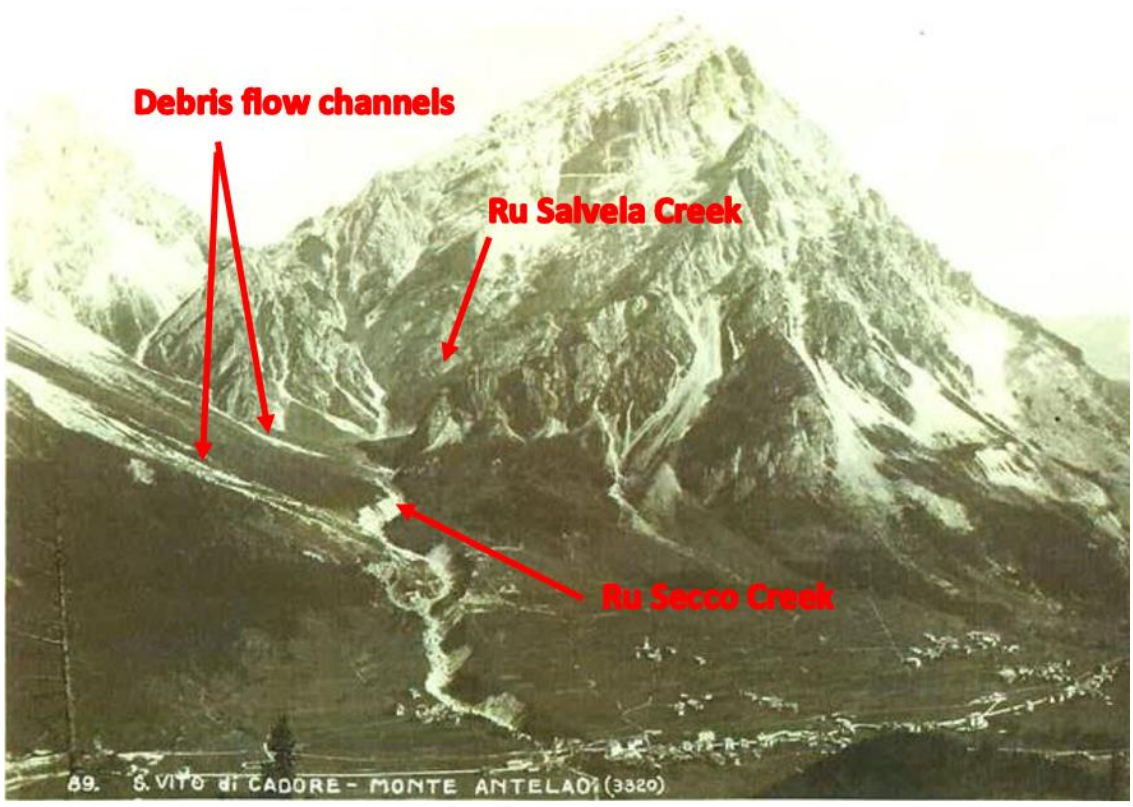

Fig. S5.4. Image of the Ru Secco creek of 20-30s. In this period, debris flows occurred on the right side.

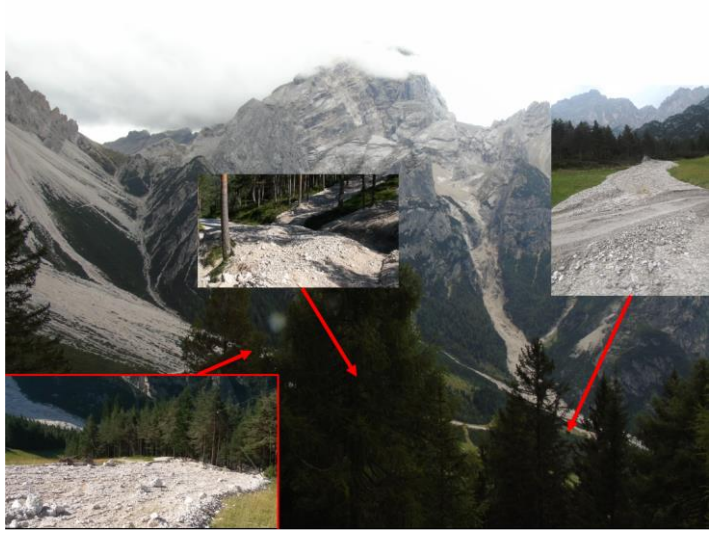

Fig. S5.5. Enlarged view of Fig. 5.2 with some images of the debris flow that reached the Ru Secco Creek on the right side.

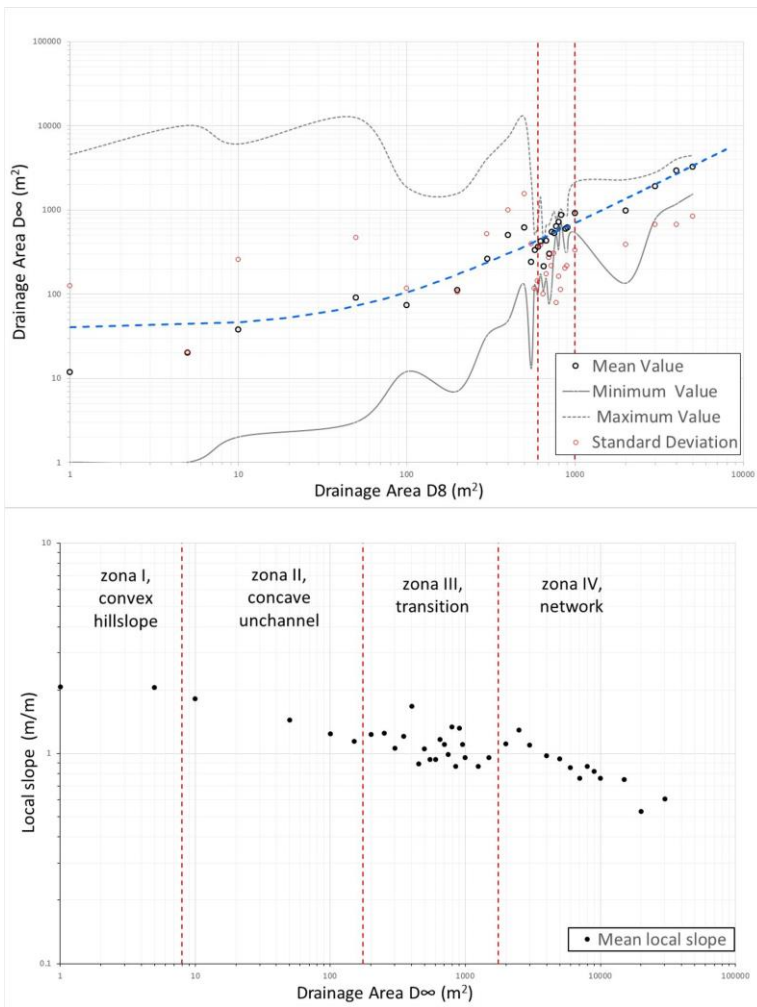

Fig. S5.6. The upper image shows the maximum, minimum and mean values of the drainage area computed for all the cells of the Ru Beche basin after using the D∞ and D8. The lower image shows the mean values of the local slope of cells of the Ru Beche basin with the same drainage area value.

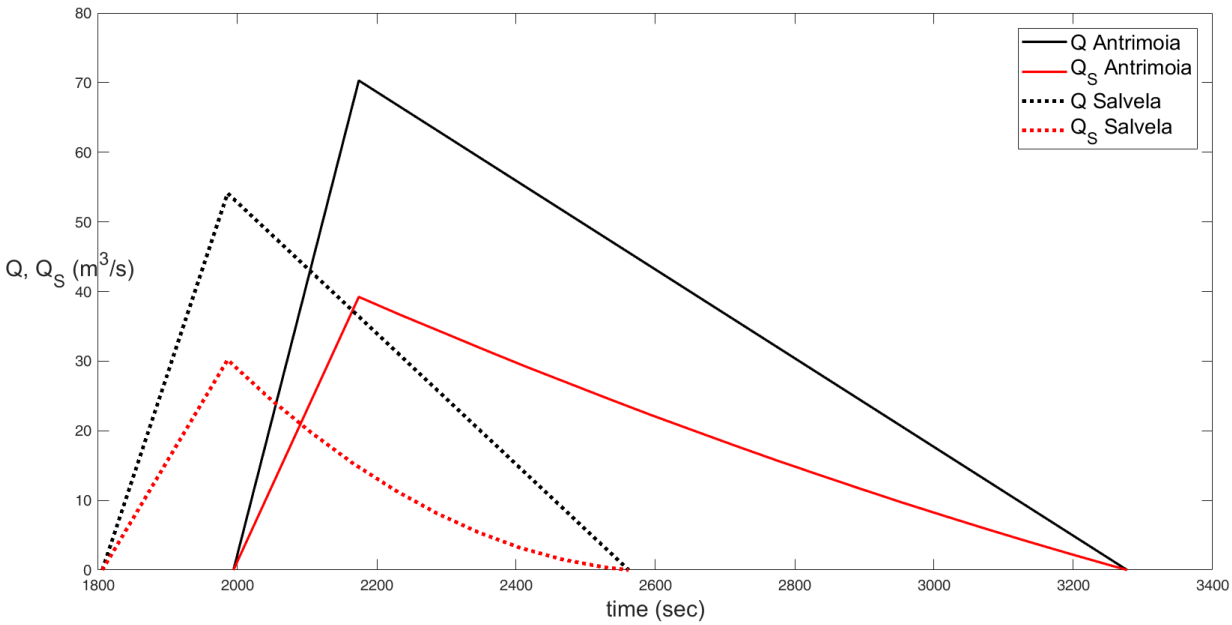

Fig. S5.7. The computed solid-liquid discharge Q (continuous lines) with the solid ones Q_S (dotted lines) of debris flows generated along Antrimoia and Salvela basins.

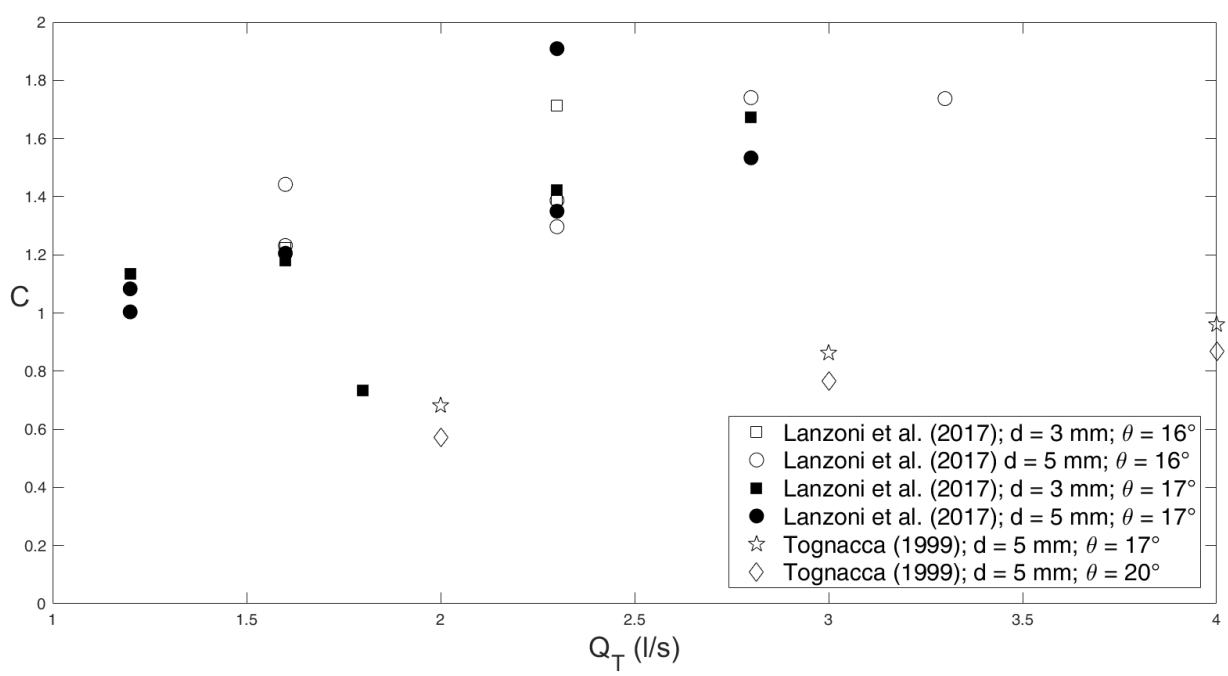

Fig. S5.8. Experimental values of the conductance coefficient C versus the triggering discharge Q_T.

6 Conclusion

In order to gain insight about the influence of geomatic techniques on the numerical modeling of debris flows routing the research initially assessed and compared the performances of different gridding and survey techniques commonly used in digital terrain modeling, by focusing on a morphologically complex area such as that of a debris flow channel. After that, the research investigated their inherent impact on the behaviour of a GIS-based cell model for simulating stony debris flows routing (introduced in Chapter 4).

In detail, in Chapter 2, we first investigated the performances of twelve digital terrain modelling algorithms (i.e., linear triangulation, natural neighbor, nearest neighbor, inverse distance to a power, ANUDEM, completely regularize spline function, thin-plate spline function, thin-plate spline plus tension function, multi-quadratic function, inverse multi-quadratic function, point ordinary kriging, and block ordinary kriging) in building DEMs with the complex topography of a debris flow channel, by using a combination among statistical analysis of vertical accuracy, algorithm robustness, and spatial clustering of vertical errors, and multi-criteria shape reliability assessment. After that, by integrating visual (e.g., cross-profiling) and statistical techniques (e.g., moving-windows spatial correlation analysis), we analysed their inherent influence on the outcomes of the cell routing model, previously calibrated and validated against two real debris flow events (the back-analysis of the event occurred on the Ru Secco creek the 4th of August 2015 is reported as an example in Chapter 5). Once identified the gridding routines ensuring a proper trade-off between elevation accuracy and shape reliability for the study area, in Chapter 3 we assessed and compared the capability of a ground-based (i.e., GNSS) and an airborne-based (i.e., full-waveform LiDAR) survey technique in characterizing the topography of the selected debris flow channel, by integrating statistical analysis of vertical accuracy, spatially distributed DEMs uncertainty modeling, and probabilistic pairwise DEMs comparison. Finally, we analyzed their inherent impact on the cell routing model behavior in terms of simulated solid-liquid discharges and channel morphology after the event, by considering both high- and low-magnitude flow conditions (300- and 50-years return period, respectively).

On one hand, in Chapter 2, the research has showed that the ordinary kriging[8] is inadequate in reproducing the complex topography of a debris flow channel. As a matter of fact, it has demonstrated an overall unsatisfactory statistical performance, a low robustness, and a poor shape reliability. Furthermore, also the ANUDEM algorithm has exhibited a poor performance from both the quantitative and qualitative point of view, despite it represents an interpolation method specifically intended for digital terrain modeling. Conversely, the thin-plate spline function has proved to be the most accurate and stable interpolation algorithm, along with the multi-quadratic radial basis function. However, these gridding routines have also showed a low ability in faithfully representing the shape of the channel, mainly due to function under- and over-shooting in correspondence of slope discontinuities. Therefore, it can be stated that for applications where the absolute accuracy of DEM elevation values is the most important precondition (e.g., imagery orthorectification), these algorithms could represent the best choice also in natural landscapes featuring a high morphological complexity (e.g., mountain basins). Conversely, for applications relying on the proper representation of the surface shape (e.g., hydraulic and hydrological modeling), the linear triangulation, the natural neighbor algorithm, and the thin-plate spline plus tension and completely regularized spline basis functions could represent a better choice since they have ensured a suitable trade-off between elevation accuracy and shape reliability. However, with regard to debris flows routing modeling applications, the research has showed that the choice of the interpolation methodology does not represent a determining factor. In fact, the statistical analysis carried out on the model outcomes has detected only a weak correlation between the uncertainty in the cell elevations due to the different tested interpolation methods and the uncertainty in the corresponding simulated erosion/deposition depths. Furthermore, also the comparison of the different model runs results in terms of simulated areas, erosion and deposition volumes, solid-liquid discharges, and channel morphology after the event has highlighted differences that can be regarded as negligible when the cell routing model is used at forecasting purposes or to identify the areas mainly subjected to large erosion and deposition phenomena.

[8] Applied by using a theoretical variogram model fitted on the directional empirical one computed perpendicularly to the linear trend direction.

On the other hand, in Chapter 3, the research has highlighted a high degree of interoperability between the GNSS and the full-waveform LiDAR technology in characterizing the topography of morphologically complex areas. As a matter of fact, the vertical accuracy and elevation uncertainty analyses carried out on the corresponding DEMs have showed that both the survey techniques have the potential to generate bias-free and accurate high-resolution digital models of debris flow channels, also featuring low magnitude elevation uncertainty values in correspondence of the channel bottom. However, the probabilistic pairwise comparison of the GNSS- and LiDAR-derived DEMs has revealed that, although the two tested survey techniques provide a comparable (i.e., not statistically different) topographic characterization of the debris flow channel bathymetry, meaningful discrepancies could be detected in correspondence of morphologically complex channel features (e.g., channel banks and longitudinal/transversal slope discontinuities) mainly due to the inherent limits of the GNSS technology (e.g., site accessibility). Therefore, it can be inferred that a low-altitude, full-waveform LiDAR survey has the capability to provide a topographic characterization of the bathymetry of a debris flow channel comparable to that of a morphological-guided, ground-based geodetic survey. Conversely, a ground-based GNSS survey could not ensure a reliable characterization of channel bottom form (e.g., rock steps, and bouldered reaches) and longitudinal features (e.g., high-gradient channel banks), if they are not properly surveyed. Furthermore, it must be noted that the research has also pointed out a potential impact of the detected discrepancies on the GIS-based cell routing model behaviour, which is linked to the adopted schematization of the sediments entrainment-deposition process. In fact, the visual assessment of the model outcomes has revealed significant differences in the simulated solid-liquid discharges and terrain profiles after the event in correspondence of the control cross-sections showing meaningful discrepancies between the two interpolated DEMs, regardless the magnitude of the modelled event scenario. Therefore, for debris flows routing modeling applications the choice of the survey technique has the potential to affect the models outcomes, and could then represent a more critical concern than the choice of the interpolation methodology. On the other hand, no statements can be drawn about which is the better survey technique and related data processing approach for this kind of morphological environments. In fact, the investigation carried out has to be regarded as a sensitivity study rather than an accuracy assessment, due to the lack of ground reference information for the two modeled event scenarios. Furthermore, other ground- and aerial-based survey techniques (e.g., TLS, UAV-based LiDAR and close-range photogrammetry, and TS) have to be considered in order to gain a clearer framework.

It is worth pointing out that the extrapolation of the research conclusion must be done with care, mainly because the research has focused on a channelized-debris flow. In the case of non-channelized debris flows, low-magnitude elevation errors resulting from the interpolation procedure might have a greater impact on the dynamics of the simulated flow, and thus on the resulting erosional/depositional pattern. Similarly, also the detected effect of the survey technique on the routing modeling outcomes might be different in the case of non-channelized debris flows, due to both the lower flow depths and velocities, which could imply processes different from erosion (i.e., deposition or mixed entrainment/deposition processes). Furthermore, the research has considered a 1 km length reach of the Rovina di Cancia debris flow channel mainly subject to entrainment processes in order to elucidate the influence of the survey techniques on routing modeling outcomes. As a consequence, different findings might result focusing on debris flow channel reaches where mainly sediments deposition or mixed sediments entrainment/deposition processes occur. Finally, also the use of different rheological models or sediments entrainment-deposition process schematizations could lead to different conclusions. Therefore, in order to improve the knowledge gained by the present research, future work has to be carried out focusing on its outlined biases.

Bibliography

Adams M. S., Fromm R., Lechner V. (2016). High-resolution debris flow volume mapping with unmanned aerial systems (UAS) and photogrammetric techniques. Int. Arch. Photogramm. Remote Sens. Spatial Inf. Sci., XLI-B1, 749-755.

Aguilar F. J., Agüera F., Aguilar M. A., Carvajal A. F. (2005). Effects of Terrain Morphology, Sampling Density, and Interpolation Methods on Grid DEM Accuracy. Photogrammetric Engineering & Remote Sensing, 71(7), 805-816.

Alho P., Hyyppä H., Hyyppä J. (2009). Consequence of DTM Precision for Flood Hazard Mapping: A Case Study in SW Finland. Nordic Journal of Surveying and Real Estate Research, 6(1).

Ali M. D. A., Solomatine D. P., Di Baldassarre G. (2015). Assessing the impact of different sources of topographic data on 1-D hydraulic modelling of floods, Hydrol. Earth Syst. Sci., 19, 631-643.

Arattano, M., and Savage, W. (1994). Modelling debris flows as kinematic waves. *Bull. Int. Assoc. Eng. Geol.* 49, 3–13.

Arattano M., Franzi L. (2003). On the evaluation of debris flows dynamics by means of mathematical models. Natural Hazards and Earth System Science, 3(6), 539–544.

Arattano M., Franzi L. (2010). On the application of kinematic models to simulate the diffusive processes of debris flows. Natural Hazards and Earth System Science, 10(8), 1689–1695.

Armanini, A., Fraccarollo, L., and Rosatti, G. (2009). Two-dimensional simulation of debris flows in erodible channels. Comput. Geosci. 35, 993–1006.

Armanini, A. (2015). Closure relations for mobile bed debris flows in a wide range of slopes and concentrations. Adv. Water Resour. 81, 75–83.

Aulitzky, H., (1973). Bercksichtigung der Wildbach-und Lawinengefahrengebiete als Grundlage der Raumordnung von Gebirgslndern. 100 Jahre Hochschule fr Bodenkultur, Band IV, Teil 2, 81–117 (in German).

Axelsson P. (2000). DEM generation from laser scanner data using adaptive TIN models. International Archives of the Photogrammetry and Remote Sensing, XXXIII Part B4/1, 110-117.

Bacchini, M., and Zannoni, A. (2003). Relation between rainfall and triggering of debris flow: case stydu of cancia (dolomites, northeastern italy). Nat. Hazards Earth Syst. Sci. 3, 71–79.

Baglioni, A., and De Marco, P. (2015). Fenomeni di colata detritica ed inondazione verificatosi nel bacino del Ru Secco (San Vito di Cadore) il 4/8/2015. Osservazioni geologiche preliminari. Technical Report - Regional Civil Work Agency of Veneto Region.

Bagnold, R. A. (1954). Experiments on a gravity-free dispersion of large solid spheres in a Newtonian fluid under shear. Proc. R. Soc. Lond. Ser. A 225, 45–63.

Bakuła K., StĘpnik M., Kurczyński Z. Acta Geophys. (2016) 64: 1176.

Bangen S. G., Wheaton J. M., Bouwes N., Bouwes B., Jordan C. (2014). A methodological intercomparison of topographic survey techniques for characterizing wadeable streams and rivers. Geomorphology 206 (2014) 343–361.

Bater C. W., Coops N. C. (2009). Evaluating error associated with lidar-derived DEM interpolation. Computers and Geosciences 35: 289–300.

Bates, P.D., De Roo, A.P.J., (2000). A simple raster-based model for flood inundation simulation. J. Hydrol. 236, 54–77.

Beasley, D.B., Huggins, L.F., Monke, E.J., (1980). ANSWERS: a model for watershed planning. Trans. ASAE 23, 938–944.

Begueira, S., Van Asch, Th.W.J., Malet, J.P., Grondahl, S., (2009). A GIS-based numerical model for simulating the kinematics of mud and debris flows over complex terrain. Nat. Hazard Earth Syst. Sci. 9, 1897–1909.

Benda, L.E., Cundy, L.W., (1990). Prediction depositions of debris flow in mountain channels. Can. Geotech. J. 27, 409–417.

Berger C., McArdell B. W., Schlunegger F. (2011). Direct measurement of channel erosion by debris flows, Illgraben, Switzerland. Journal of Geophysical Research. 116, F01002.

Bernard, M. (2018). Analysis of Rainfalls Triggering Debris Flows and Modelling of Corresponding Runoff. PhD. Thesis - Università degli Studi di Padova.

Berti M., Genevois R., Simoni A., Tecca R. P. (1999). Field observations of a debris flow event in the Dolomites. Geomorphology 29 1999 265–274.

Berti M., Simoni A. (2005). Experimental evidences and numerical modeling of debris flow initiated by channel runoff. Landslides, 2(3), 171–182.

Berti, M., Simoni, A., (2007). Prediction of debris flow inundation areas using empirical mobility relationships. Geomorphology 90, 144–161.

Berti M., Simoni A. (2014). DFLOWZ: A free program to evaluate the area potentially inundated by a debris flow. Computers & Geosciences 67 (2014) 14–23.

Bhuyian M. N., Kalyanapu A. (2018). Accounting digital elevation uncertainty for flood consequence assessment. J Flood Risk Management, 11: S1051-S1062.

Blasone G., Cavalli M., Marchi L., Cazorzi F. (2014). Monitoring sediment source areas in a debris flow catchment using terrestrial laser scanning. Catena 123 (2014) 23–36.

Blöschl G., Grayson R. (2000). Spatial Observations and Interpolation. Spatial Patterns in Catchment Hydrology: Observations and Modeling, 113(10), 13–16.

Boreggio M., Bernard M., Gregoretti C. (2018). Evaluating the Differences of Gridding Techniques for Digital Elevation Models Generation and Their Influence on the Modeling of Stony Debris Flows Routing: A Case Study From Rovina di Cancia Basin (North-Eastern Italian Alps). Front. Earth Sci. 6:89.

Bossi G., Cavalli M., Crema S., Frigerio S., Luna B. Q., Mantovani M. (2014). Multi temporal LiDAR-DTMs as a tool for modeling a complex landslide: a case study in the Rotolon catchment (Eastern Italian Alps). Natural Hazards and Earth System Sciences Discussions, 2(10), 6453–6474.

Brufau, P., Garcia-Navarro, P., Ghilardi, P., Natale, L., and Savi, F. (2000). 1-d mathematical modelling of debris flow. J. Hydraul. Res. 38, 435–446.

Cannon, S., Gartner, J. E., Wilson, R. C., Bowers, J. C., and Laber, J. L. (2008). Storm rainfall conditions for floods and debris flows from recently burned areas in southwestern Colorado and southern california. Geomorphology 96, 250–269.

Capra L., Manea V. C., Manea M., Norini G. (2011). The importance of digital elevation model resolution on granular flow simulations: A test case for Colima volcano using TITAN2D computational routine. Natural Hazards, 59(2), 665–680.

Caroti G., Piemonte A. (2010). Analisi dei dati altimetrici disponibili per il territorio comunale di Pisa, Geomatica le radici del futuro, pp.157-161, Edizioni SIFET, ISBN 88-901939-6-4.

Carrara A., Bitelli G., and Carla R. (1997). Comparison of techniques for generating digital terrain models from contour lines. International Journal of Geographical Information Science 11: 451–472.

Casas A., Benito G., Thorndycraft V. R., Rico M. (2006). The topographic data source of digital terrain models as a key element in the accuracy of hydraulic flood modelling. Earth Surface Processes and Landforms, 31(4), 444–456.

Cavalli, M., Marchi, L. (2008). The effectiveness of airborne LiDAR's data in the recognition of channel-bed morphology. Catena 75, pp. 249-260.

Cavalli, M., Trevisano, M., Comiti, F., Bowers, J. C., and Marchi, L. (2013). Geomorphometric assessment of spatial sediment connectivity in small alpine catchments. Geomorphology 188, 31–41.

Chaplot V., Darboux F., Bourennane H., Leguedois S., Silvera N., Phachomphon K. (2006). Accuracy of interpolation techniques for the derivation of digital elevation models in relation to landform types and data density. Geomorphology, 77 (1-2), 126-141. ISSN 0169-555X.

Chen, H., Crosta, G., and Lee, C. (2006). Erosional effect on run-out of fast landslide, debris flows and avalanches: a numerical investigation. Geotechnique 56, 305–322.

Chen, J., Arleen, A.H., Urbano, L.D., (2009). A GIS-based model for urban flood inundation. J. Hydrol. 373, 184–192.

Chiang, S.H., Chang, K.T., Mondini, A.C., Tsai, B.W., Chen, C.Y., (2012). Simulation of event-based landslides and debris flows at watershed level. Geomorphology 138, 306–318.

Chiles J. P. (1984): in G. Verly et al. (Eds.), Geostatistics for Natural Resources Characterization: NATO-ASI serie C, v. 122, Reidel, p. 1–20.

Cilloccu F., Dequal S., Brovelli M., Crespi M., Lingua A. (2009). Ortoimmagini 1:10.000 e modelli altimetrici. Linee Guida. C.I.S.I.S. - Centro Interregionale per i Sistemi informatici, geografici e statistici. Roma.

Coe, J. A., Kinner, D. A., and Godt, J. W. (2008). Initiation conditions for debris flows generated by runoff at Chalk Cliffs, Central Colorado. Geomorphology 96, 270–297.

Cook A., Merwade V. (2009). Effect of topographic data, geometric configuration and modeling approach on flood inundation mapping. J Hydrol, 377: 131-142.

Courant, R., Friedrichs, K., Lewy, H., (1967). On the partial difference equations of mathematical physics. IBM J., 215–234

Cuomo, S., Pastor, M., Capobianco, V., and Cascini, L. (2016). Modelling the space- time bed entrainment for flow-like landslide). Eng. Geol. 212, 10–20.

d'Agostino, V., Cesca, M., Marchi, L., (2010). Field and laboratory investigations of runout distances of debris flows in the Dolomites (Eastern Italian Alps). Geomorphology 115, 294–304.

d'Ambrosio, D., Di Gregorio, S., Iovine, G., Lupiano, V., Rongo, R., Spataro, W., (2003). First simulations of the Sarno debris flows through Cellular Automata modelling. Geomorphology 54, 91–117.

De Blasio, F.V., Breien, H., Elverhoi, A., (2011). Modelling a cohesive-frictional debris flow: an experimental, theoretical, and field-based study. Earth Surf. Process. Land. 36, 753–766.

Deangeli, C., Segre, E., (1995). Cellular automaton for realistic modelling of landslide. Nonlinear Process. Geophys. 2, 1–15.

Deangeli C. (2008). Laboratory granular flows generated by slope failures. Rock Mech. Rock Eng. 41 (1), 199–217.

Declercq F. A. N. (1996). Interpolation methods for scattered sample data: accuracy, spatial patterns, processing time. Cartography and Geographical Information Systems 23(3): 128–44.

Degetto, M., Gregoretti, C., (2013). Debris Flow Modeling Tool: User Manual.

Degetto M., Gregoretti C., Bernard M. (2015). Comparative analysis of the differences between using LiDAR and contour-based DEMs for hydrological modeling of runoff generating debris flows in the Dolomites. Front. Earth Sci. 3:21.

deRoo, A.P.J., Hazelhoff, L., Burrough, P.A., (1989). Soil erosion modeling using ANSWERS and geographical information system. Earth Surf. Process. Land. 14, 517–532.

DeScally, F., and Owens, I. (2004). Morphometric controls and geomorphic responses on fans in the Southern Alps, New Zealand. Earth Surf. Process. Landforms 29, 311–322.

Desmet P. J. J. (1997). Effects of Interpolation Errors on the Analysis of DEMs. Earth Surf. Process. Landforms, 22: 563–580.

Destro, E., Amponsah, W., Nikolopoulos, E., Marchi, L., Marra, F., Zoccatelli, D., et al. (2018). Coupled prediction of flash flood response and debris flow occurrence: application on an alpine extreme flood event. J. Hydrol. 558, 225–237.

Di Cristo, C., Iervolino, M., Vacca, A., (2014a). Simplified wave models applicability to shallow mud flows modeled as power-law fluids. J. Mt. Sci. 11 (6), 1454–1465.

Di Cristo, C., Iervolino, M., Vacca, A., (2014b). Applicability of kinematic, diffusion and quasi-steady dynamic wave models to shallow mudflows. J. Hydrol. Eng. 19 (5), 956–965.

Easterling D. R., Evans J. L., Groisman P. Y., Karl T. R., Kunkel K. E., Ambenje P. (2000). Observed Variability and Trends in Extreme Climate Events: A Brief Review. Bull. Am. Meteorol. Soc. 81, 417–425.

Egashira S., Ashida K. (1987). “Sediment transport in steep slope flumes”. Proc. of Roc Japan Joint Seminar on Water Resources.

Egashira, S., Honda, N., and Itoh, T. (2001). Experimental study on the entrainment of bed material into debris? ow. Phys. Chem. Earth (C) 26, 645–650.

El-Sheimy N., Valeo, C., Habib A (2005). Digital Terrain Modeling Acquisition, Manipulation, and Applications; Artech House: Boston, MA, USA.

Erdogan S. (2009). A comparison of interpolation methods for producing digital elevation models at the field scale, Earth Surf. Proc. Land., 34, 366–376.

Ewen, G., Parkin, G., O’Connel, P.E., (2000). Shetran: distributed river basin flow and transport modeling system. J. Hydrol. Eng. ASCE 5 (3), 250–258.

Floris M., D’Alpaos A., Squarzoni C., Genevois R., Marani M. (2010). Recent changes in rainfall characteristics and their influence on thresholds for debris flow triggering in the Dolomitic area of Cortina d’Ampezzo, north-eastern Italian Alps. Nat. Hazards Earth Syst. Sci. 10, 571–580.

Fonstad M. A., Dietrich J. T., Courville B. C., Jensen J. L., Carbonneau, P. E. (2013). Topographic structure from motion: A new development in photogrammetric measurement. Earth Surface Processes and Landforms, 38(4), 421–430.

Fraccarollo L., Papa M. (2000). Numerical simulation of real debris-flow events. Physics and Chemistry of the Earth, Part B 25 (9), 757–763.

Fraccarollo, L., Capart, H., (2002). Rieman wave description of erosional dam-break flow. J. Fluid Mech. 461, 183–228.

Frank, F., McArdell, B., Huggel, C., and Vieli, A. (2015). The importance of entrainment and bulking on debris flows runout modeling: examples from the swiss Alps. Nat. Hazards Earth Syst. Sci. 15, 2569–2583.

French J. R. (2003). Airborne LiDAR in support of geomorphological and hydraulic modeling. Earth Surface Processes and Landforms, 28(3), 321–335.

Fuchs, S., Heiss, K., Huebl, J., (2007). Towards an empirical vulnerability function for use in debris flow risk assessment. Nat. Hazards Earth Syst. Sci. 7, 495–506.

Gallay M., Lloyd C. D., McKinley J., Barry L. (2013). Assessing modern ground survey methods and airborne laser scanning for digital terrain modeling: A case study from the Lake District, England. Computers & Geosciences, 51, 216-227.

Garnero G., Godone D. (2011). Accuratezza nell'interpolazione dei DTM: analisi dei fattori determinanti. 1121–1127.

Gartner, J.E., Santi, P.M., Cannon, S.H., (2015). Predicting location of post-fire debris flows erosion in the San Gabriel Mountains of southern California. Nat. Hazards.

Ghilardi P., Natale L., Savi F. (2001). Modeling debris-flow propagation and deposition. Physics and Chemistry of the Earth, Part C 26 (9), 651–656.

Gomarasca M. A. (2009). Basics of Geomatics. Eds. Springer Netherlands.

Gregoretti, C. (2000). "Estimation of the maximum velocity of a surge of debris flow propagating along an open channel," in International Symposium Interpraevent 2000 Villach 26-30, June, 99–108.

Gregoretti, C., (2000a). Experimental evidence from the triggering of debris flow along a granular slope. J. Phys. Chem. Earth B 25 (4).

Gregoretti, C., (2000b). The initiation of debris flow at high slopes: experimental results. J. Hydraul. Res. 38 (2), 83–88.

Gregoretti, C., (2000c). Estimation of the maximum velocity of a surge of debris flow propagating along an open channel. In: Interpraevent2000 Villach 26–30 June, pp. 99–108.

Gregoretti, C., and Dalla Fontana, G. (2007). "Rainfall threshold for the initiation of debris flows by channel bed failure of the dolomites," in Proceedings of the Fourth International Conference on Debris Flow Hazards Mitigation, eds C. L. Chen and J. J. Major (Chengdu: Balkema), 11–21.

Gregoretti, C., (2008). Inception sediment transport relationships at high slopes. J. Hydraul. Eng. 134 (11), 1620–1629.

Gregoretti C., Dalla Fontana G. (2008). The triggering of debris flow due to channel-bed failure in some alpine headwater basins of the Dolomites: analyses of critical runoff. Hydrological Processes, 22(13), 2248–2263.

Gregoretti, C., Furlan, M., Degetto, M., (2011). Gis-based cell model for simulating debris flow routing and deposition phases on a fan. In: Prestininzi, Hamilton, Genevois (eds.), Proceedings of the Fifth International Conference on Debris Flow Hazards Mitigation Padova, June, 425434.

Gregoretti, C., Degetto, M., (2012). Debris Flow Modeling Tool: Reference Manual.

Gregoretti, C., Adams, M., Hagen, K., Laigle, D., Liebault, F., Degetto, M., et al. (2012). "Forecast system guidelines debris flows. Guidelines for the implementation of forecast system against debris flow hazard (wp6)," in Project PARAmount imProved Accessibility: Reliability and Security of Alpine Transport Infrastructure Related to Mountainous Hazards in a Changing Climate, Alpine Space, European Regional Development Fund (ERDF) (Brussels).

Gregoretti C., Degetto M., Boreggio M. (2016a). GIS-based cell model for simulating debris flow runout on a fan. Journal of Hydrology, 534, pp. 326-340.

Gregoretti C., Degetto M., Bernard M., Crucil G., Pimazzoni A., De Vido G., Berti M., Simoni A., Lanzoni S. (2016b). Runoff of small rocky headwater catchments: Field observations and hydrological modeling. Water Resources Research 52, 8138–8158.

Gregoretti C., Degetto M., Bernard M., Boreggio M. (2018a). The debris flow occurred at Ru Secco Creek, Venetian Dolomites, on 4 August 2015: analysis of the phenomenon, its characteristics and reproduction by models. Frontier in Earth Sciences.

Gregoretti, C., Stancanelli, L. M., Bernard, M., Boreggio, M., Degetto, M., and Lanzoni, S. (2018b). Relevance of erosion processes when modelling in-channel gravel debris flows for efficient hazard assessment. Journal of Hydrology, Volume 568, January 2019, Pages 575-591.

Griswold, J.P., Iverson, R.M., (2008). Mobility statistics and automated hazard mapping for debris-flows and rock avalanches. US Geological Survey Scientific Investigation Report 5276, US Geological Survey: Reston, VA 59.

Gruber, S., (2007). A mass-conserving fast algorithm to parameterize gravitational transport and deposition using digital elevation models. Water Resour. Res. 43.

Guthrie, R.H., Hockin, A., Colquhoun, L., Nagy, T., Evans, S.G., Aylesber, C., (2007). An examination of controls on debris flow mobility: evidence from coastal British Columbia. Geomorphology 114, 601–613.

Han, X., Chen, J., Xu, P., and Zhan, J. (2017). A well-balanced numerical scheme for debris flows run-out predictions in the xiaojia gully considering different hydrologic designs. Landslide 14, 2105–2114.

Hancock G. R. (2006). The impact of different gridding methods on catchment geomorphology and soil erosion over long timescales using a landscape evolution model. Earth Surf. Process. Landforms, 31: 1035–1050.

Hengl T. (2006). Finding the right pixel size. Computers and Geosciences, 32(9), 1283–1298.

Hengl T., Reuter H. I. (Eds.) (2009). Geomorphometry: Concepts, Software, Applications. Developments in Soil Science, vol. 33, Elsevier, 772 pp.

Hensleigh J. (2014). Geomorphic Change Detection Using Multi-Beam Sonar. All Graduate Plan B and other Reports. 376.

Heritage G. L., Large A. R. G. (2009). Laser scanning for the environmental sciences. Wiley-Blackwell, London.

Heritage G. L., Milan D. J., Large A. R. G., Fuller I. (2009). Influence of survey strategy and interpolation model upon DEM quality. Geomorphology 112, 334–344.

Hodgson M. E., Bresnahan P. (2004). Accuracy of Airborne Lidar-Derived Elevation. Photogrammetric Engineering & Remote Sensing, 70(3), 331–339.

Höhle, J., and Höhle, M. (2009). Accuracy assessment of digital elevation models by means of robust statistical methods. ISPRS J. Photogrammet. Remote Sens. 64, 398–406.

Höhle J., Potuckova M. (2011). Assessment of the Quality of Digital Terrain Models. European Spatial Data Research, Official Publication n. 60.

Horrit, M.S., Bates, P.D., (2001). Effects of spatial resolution on a raster based model of flood flow. J. Hydrol. 253, 239–249.

Hsieh, Y.-C., Chan, Y.-C., & Hu, J.-C. (2016). Digital Elevation Model Differencing and Error Estimation from Multiple Sources: A Case Study from the Meiyuan Shan Landslide in Taiwan. Remote Sensing, 8(3), 199.

Hu, W., Dong, X. J., Wang, G. H., van Asch, T. W. J., and Hicher, P. Y. (2016). Initiation processes for run-off generated debris flows in the wenchuan earthquake area of china. Geomorphology 253, 468–477.

Hungr, O., McDougall, S., Bovis, M., (2005). Entrainment of material by debris flows. In Jacob, M., Hungr, O. (eds.), Debris-flows Hazards and Related Phenomena, Praxis, Chichester, pp. 135–158.

Hurlimann, M., Rickenmann, D., and Graf C. (2003) Field and monitoring data debris-flow events in the Swiss Alps. Can. Geotech. J. 40, 161–175.

Hurlimann, M., Copons, R., Altimir, J., (2006). Detailed debris flow hazard assessment in Andorra: a multidisciplinary approach. Geomorphology 78, 359–372.

Hurlimann, M., Abanco, C., Moya, J., and Villalosana, I. (2014). Results and experiences gathered at the rebaixader debris-flow monitoring site, central Pyrenees, Spain. Landslide 2, 161–175.

Hussin H. Y., Quan Luna B., van Westen C. J., Christen M., Malet J. P., van Asch Th. W. J. (2012). Parameterization of a numerical 2-D debris flow model with entrainment: a case study of the Faucon catchment, Southern French Alps, Nat. Hazards Earth Syst. Sci., 12, 3075–3090.

Hutchinson M. F. (1996). A locally adaptive approach to the interpolation of digital elevation models. In Proceedings, Third International Conference/Workshop on Integrating GIS and Environmental Modeling, Santa Fe, NM, January 21-26, 1996. Santa Barbara, CA: National Center for Geographic Information and Analysis.

Ijjasz-Vasquez, E., and Bras, L. (1995). Scaling regimes of local slope versus contributing area in digital elevation models. Geomorphology 12, 299–311.

Imaizumi, F., Sidle, R. C., Tsuchiya, S., and Ohsaka, O. (2006). Hydrogeomorphic processes in a steep debris flows initiation zone. Geophys. Res. Lett. 33, 157–171.

Isaaks E. H., Srivastava R.M. (1989). An Introduction to Applied Geostatistics. Oxford University Press, Oxford.

Isenburg, M. (2017). LAStools - efficient LiDAR processing software (version 170608, unlicensed).

Iverson, R.M., Schilling, S.P., Vallance, J.W., (1998). Objective delineation of lahar-inundation hazard zones. GSA Bull. 110 (8), 972–984.

Iverson R. M. (2005). Debris-flow mechanics, in Debris-Flow Hazards and Related Phenomena. pp. 105–131, Springer, Berlin.

Iverson, R.M., George, D.L., (2014). A depth-averaged debris-flow model that includes the effects of evolving dilatancy. I. Physical basis. Proc. R. Soc. London A 470 (2170).

Iverson, R.M., Ouyang, C., (2015). Entrainment of bed material by Earth-surface mass flows: review and reformulation of depth-integrated theory. Rev. Geophys. 53.

Jaboyedoff M., Oppikofer T., Abellán A., Derron M. H., Loye A., Metzger R., Pedrazzini A. (2012). Use of LIDAR in landslide investigations: A review. Natural Hazards, 61(1), 5–28.

Jacob, M., (2005). Debris flows hazard analysis. In: Jacob, M., Hungr, O. (eds.), Debris-flows Hazards and Related Phenomena, Praxis, Chichester, pp. 411–443.

Jain, M.K., Kothyari, U.C., Ranga Raju, K.G., (2005). GIS based distributed model for soil erosion and rate of sediment outflow from catchments. J. Hydraul. Eng. ASCE 131 (9), 755–769.

Johnston K., Ver Hoef J., Krivoruchko K., Neil L. (2001). Using ArcGIS™ Geostatistical Analyst, ESRI™, USA.

Jordan M. (1994). Debris Flows in the Southern Coast Mountains, British Columbia: Dynamic Behaviour and Physical Properties. PhD. thesis, University of British Coulumbia, Vancouver, BC.

Kean, J.W., Staley, D.M., Cannon, S.E., (2011). In situ measurements of post-fire debris flows in Southern California: comparison of the timing and magnitude of 24 debris flows events with rainfall and soil moisture conditions. J. Geophys. Res. 116, F04019.

Kean, J., McCoy, S. W., Tucker, G. E., Staley, D. M., and Coe, J. A. (2013). Runoff-generated debris flows: observations and modeling of surge initiation, magnitude and frequency. J. Geophys. Res. 118, 2190–2207.

Krause P., Boyle D. P., Bäse F. (2005). Comparison of different efficiency criteria for hydrological model assessment. Advances in Geosciences, 5, 89-97.

Lamb, M.P., Dietrich, W.E., Venditti, J.G., (2008). Is the critical Shields shear stress for incipient sediment motion dependent on channel-bed slope? J. Geophys. Res. 113, F02008.

Lane S. N., Westaway R. M., Hicks D. M. (2003). Estimation of erosion and deposition volumes in a large, gravel-bed, braided river using synoptic remote sensing. Earth Surface Processes and Landforms 28(3): 249–271.

Lanzoni, S., Tubino, M., (1993). Rheology of debris flows: experimental observations and modelling problems. Exceptra 7, 201–236.

Lanzoni, S., Gregoretti, C., and Stancanelli, M. (2017). Coarse-grained debris flow dynamics on erodible beds. J. Geophys. Res. 122, 592–614.

Li Z. (1993). Theoretical models of the accuracy of digital terrain models: an evaluation and some observations. The Photogrammetric Record 14(82), 651–660.

Lillesand, T.M., Kiefer, R.W. and Chipman, J.W. (2004) Remote Sensing and Image Interpretation. 5th Edition, John Wiley, New York.

Liu, K.F., Wang, M.C., (2006). Numerical modelling of debris-flow with application on hazard area mapping. Comput. Geosci. 10, 221–240.

Lo Brutto, M. C., and Meli, P. (2013). “Performance evaluation of 3d web-services and open-source software for digital modeling of archeological finds,” in Proceedings of Archeofoss, eds F. Stanco and G. Gallo, 11–21.

Magirl, C.S., Griffiths, P.G., Webb, R.H., (2010). Analyzing debris flows with the statistically calibrated empirical model LAHARZ in southeastern Arizona, USA. Geomorphology 119, 111–120.

Mallet C. & Bretar F. (2009). Full-waveform topographic LiDAR: State-of-the-art. ISPRS Journal of Photogrammetry and Remote Sensing, 64(1), 1–16.

Mascarenhas, F.C.B., Miguez, M.G., (2002). Urban flood control through a mathematical cell model. Water Int. IWRA 27 (2), 208–218.

McCoy, S.W., Kean, J.W., Coe, J.A., Tucker, G.E., Staley, D.M., Wasklewicz, W.A., (2012). Sediment entrainment by debris flows: In situ measurements from the headwaters of a steep catchment. J. Geophys. Res. 117, F03016.

McDonnell R. A., Lloyd C.D. (2015). Principles of geographical information systems. Oxford University Press.

McDougall, S., Hungr, O., (2004). A model for the analysis of rapid landslide motion across three-dimensional terrain. Can. Geotech. J. 41 (6), 1084–1097.

McGlynn, B, L., and Seibert, J. (2003). Distributed assessment of contributing area and riparian buffering along stream networks. Water Resour. Res. 39:1082.

McGuire, K. J., McDonnell, J. J., Weiler, M., Kendall, C., McGlynn, B. L., Welker, J. M., et al. (2005). The role of topography on catchment-scale water residence time. Water Resour. Res. 41:W05002.

McGuire, L., Rengers, J., Kean, J., and Staley, D. (2017). Debris flow initiation by runoff in a recently burned basin: is grain-by-grain. Geophys. Res. Lett. 44, 7310–7319.

Medina, V., Hurlimann, M., Bateman, A. (2008). Application of FLATModel, a 2D finite volume code, to debris flows in the Northeastern part of Iberian Peninsula Experimental evidences and numerical modeling of debris flow initiated by channel runoff. Landslide 5, 127–142.

Mergili, M., Schratz, K., Ostermann, L., Fellin, W., (2012). Physically-based modelling of granular flows with Open Source GISNat. Nat. Hazards Earth Syst. Sci. 12, 187–200.

Miguez, M.G., Canedo de Magalhaes, L.P., Vellozo DAlterio, C.F., (2009). Planning and design of urban flood control measures: assessing effect combination. J. Urban Plann. Dev. ASCE 135 (3), 100–109.

Miguez, M.G., Mascarenhas, F.C.B., Verol, A.P., (2011). A mathematical model for urbanflood simulation and flood control design. In: Acqua e citt 2011 – 4 Convegno Nazionale di Idraulica Urbana Venezia, 21–24 Giugno.

Milan D. J., Heritage G. L., Large A. R. G., Fuller I. C. (2011). Filtering spatial error from DEMs: implications for morphological change estimation. Geomorphology 125, 160–171.

Mitas L. & Mitasova H. (1999). Spatial interpolation. Tutorial, 481–492.

Molina J. L., Gonzalves P. R., Molina C., Aguilera D. G., Espejo F. (2014). Geomatic methods at the service of water resources modelling. Journal of Hydrology 509 (2014) 150–162.

Montgomery, D., and Foufoula-Georgiou, E. (1993). Channel network source representation using digital elevation models. Water Resour. Res. 29, 3925– 3934.

Moore I. D., Grayson R. B. (1991). Terrain-based catchment partitioning and runoff prediction using vector elevation data. Water Resources Research 27: 1177–91.

Morgan, R.P.C., Quinton, J.N., Smith, R.E., Govers, G., Poesen, G.A.W., Auerswald, K., Ghisci, G., Torri, D., Styczen, R.E., (1998). The European Soil Erosion Model (EUROSEM): a dynamic approach for predicting sediment transport from field and small catchments. Earth Surf. Process. Land. 23, 527–544.

Navratil, O., Liebault, F., Bellot, H., Travaglini, E., Theule, J., Chambon, G., et al. (2013). High frequency monitoring of debris flows propagation along the real torrent, southern french alps. Geomorphology 201, 157–171.

O'Brien, J.S., Julien, P.J., Fullerton, F.T., (1993). Two-dimensional water flood and mudflow simulation. J. Hydraul. Eng. ASCE 119 (2), 244–261.

O'Brien, J.S., (2007). FLO-2D Reference Manual.

Okano, K., Suwa, H., and Kanno, T. (2012). Characterization of debris flows by rainstorm condition at a torrent on the mount yakedake volcano, Japan. Geomorphology 136, 88–94.

Oliver M. A., Webster R. (2014). Catena: A tutorial guide to geostatistics: Computing and modeling variograms and kriging. Catena, 113, 56–69.

Orlandini, S., and Rosso, R. (1996). Diffusion wave modeling of distributed catchment dynamics. J. Hydrol. Eng. 1, 103–113.

Passalacqua P., Belmont P., Staley D., Simleym J., Arrowsmith J. R. (2015). Analyzing high resolution topography for advancing the understanding of mass and energy transfer through landscapes: A review. Earth-Science Reviews, Elsevier, 148, pp.174-193.

Pastor, M., Haddad, B., Sorbino, G., Cuomo, S., Demptric, V.A., (2008). A depth integrated-coupled SPH model for flow like landslides and related phenomena. Int. J. Numer. Anal. Meth. Geomech.

Pfeifer N. (2005). A subdivision algorithm for smooth 3D terrain models. ISPRS Journal of Photogrammetry and Remote Sensing Volume 59, Issue 3, May 2005, Pages 115–127.

Pirulli, M., (2010). On the use of the calibration-based approach for debris-flow forward-analyses. Nat. Hazard Earth Sci. 10, 1009–1019.

Podobnikar T. (2009). Methods for visual quality assessment of Digital Terrain Model. Journal of SAPIENS (Surveys and Perspectives Integrating Environment and Society), Vol. 2/n°2 Special issue.

Pourali S., Arrowsmith C., Chrisman N. (2014). Vertical accuracy assessment of LiDAR ground points using minimum distance approach. In: S. Winter and C. Rizos (Eds.).

Pudasaini, S.P., (2012). A general two-phase debris flow model. J. Geophys. Res. 117, F03010.

R Development Core Team (2008). R: A language and environment for statistical computing. R Foundation for Statistical Computing, Vienna, Austria. ISBN 3-900051-07-0, URL http://www.R-project.org.

Raber G., Jensen J. R., Hodgson M. E., Tullis J. A., Davis B. A., Berglund J. (2007). Impact of Lidar Nominal Post-spacing on DEM Accuracy and Flood Zone Delineation. Photogrammetric Engineering & Remote Sensing.

Recking, A., (2009). Theoretical development on the effect of changing flow hydraulics on incipient bed load motion. Water Resour. Res. 45, W04401.

Reid, M.E., Iverson, R.M., Lahusen, R.G., Logan, M., Godt, J.W., Griswold, J., Swinford, K.J., Denlinger, R.P., (2009). Entrainment of bed sediments by debris flow: large scale experiments. In: Paper presented at 2009 Geological Society of America annual meeting, Geol. Soc. AM., Portland, Oregon, 18–21 October.

Reid, M. E., Coe, J. A., and Dianne, L. B. (2016). Forecasting inundation from debris flows that grows volumetrically during travel, with application to the Oregon Coast Range, USA. Geomorphology 273, 396–411.

Reil A., Skoulikaris C., Alexandridis T. K., Roub R. (2017). Evaluation of riverbed representation methods for 1D flood hydraulics model. Journal of Flood Risk Management

Rengers, F. K., McGuire, L. A., Kean J. W., and Hobley, D. E. (2016). Model simulations of flood and debris flow timing in steep catchments after wildfire. Water Resour. Res. 52:6041.

Reutebuch S. E., McGaughey R. J., Andersen H. E., Carson W. W. (2003). Accuracy of a high-resolution lidar terrain model under a conifer forest canopy. Canadian Journal of Remote Sensing, 29(5), 527–535.

Riccardi, G.A., (1997). The mathematical modelling of flood propagation for the delineation of flood risk zones. Sustainability of water resources under increasing uncertainty. Procedings of the Rabat Symposium. IAHS Publ., p. 240.

Rickenmann, D., (2005). Runout prediction methods. In Jacob, M., Hungr, O. (eds.), Debris-flows Hazards and Related Phenomena, Praxis, Chichester, pp. 305–321.

Rickenmann D., Laigle B., McArdell B.W., Hubl J. (2006). Comparison of 2D debris-flow simulation models with field events. Computational Geosciences 10:241–264.

Rosatti, G., and Begnudelli, L. (2013). Two-dimensional simulations of debris flows over mobile beds: enhancing the trent2d model by using a well-balanced generalized roe-type solver. Comput. Fluids 71, 179–185.

Saksena S., Merwade V. (2015). Incorporating the effect of DEM resolution and accuracy for improved flood inundation mapping. Journal of Hydrology 530 (2015) 180–194.

Schaffrath K. R., Belmont P., Wheaton J. M. (2015). Landscape-scale geomorphic change detection: Quantifying spatially variable uncertainty and circumventing legacy data issues. Geomorphology 250, 334-348.

Scheidl C., Rickenmann D., Chiari M. (2008). The use of airborne LiDAR data for the analysis of debris flow events in Switzerland. Nat. Hazards Earth Syst. Sci. 8, 1113–1127.

Scheidl C., Rickenman D., (2010). TopFlowDF-A simple GIS based model to simulate debris-flow runout on the fan. In Proceedings of the Fifth International Conference on Debris Flow Hazards Mitigation Padova, June, Prestininzi, Hamilton, Genevois (eds): 253-262.

Scheidl, C., Rickenman, D., (2010). Empirical prediction of debris-flow mobility and deposition fans. Earth Surf. Process. Land. 35, 157–173.

Scheidl, C., Rickenman, D., (2011). TopFlowDF-A simple gis based model to simulate debris-flow runout on the fan. In: Prestininzi, Hamilton, Genevois (eds.), Proceedings of the Fifth International Conference on Debris Flow Hazards Mitigation Padova, June, pp. 253–262.

Schwendel A. C., Fuller I. C., Death, R. G. (2012). Assessing DEM Interpolation Methods for Effective Representation of Upland Stream Morphology for Rapid Appraisal of Bed. River Research and Applications.

Setiawan M. A., Rutzinger M., Wichmann V., Stoetter J., Sartohadi J. (2013): Evaluation of Methods for Digital Elevation Model Interpolation of Tillage Systems. Journal of Natural Resource Development, 3:1 28–1 39.

Sickle V. J. (2001). GPS for Land Surveyors. 4th ed. CRC Press.

Simoni A., Bernard M., Berti M., Boreggio M., Lanzoni S., Stancanelli L. M., Gregoretti C. (2018). Observation of initiation conditions and role of sediment availability in run-off generated debris flows at Cancia (North Eastern Italian Alps). Geographical Research Abstract. Vol. 20, EGU2018-9091, 2018. EGU General Assembly 2018.

Smith S., Holland D., Longley P. (2005). The importance of understanding error in LiDAR digital elevation models. 20 th ISPRS Conference. Istanbul, Turkey, 12–34.

Sodnik J., Podobnikar T., Mikoš M. (2012). Using LiDAR Data for Debris Flow Modeling, 12th Congress INTERPRAEVENT 2012, Grenoble/France. pp. 573–583.

Staley, D.M., Wasklewicz, T.A., Blaszczynski, J.S., (2006). Surficial patterns of debris flow deposition on alluvial fans in Death Valley, CA, using airborne laser swath mapping data. Geomorphology 74, 152–163.

Stancanelli, L., Lanzoni, S., Foti, E., (2015). Propagation and deposition of stony debris flows at channel confluences. Water Resour. Res. 51, 5100–5116.

Stancanelli, L.M., Foti, E., (2015). A comparative assessment of two different debris flows propagation approaches – blind simulation on a real debris flow event. Nat. Hazard Earth Syst. Sci. 15, 375–746.

Stock, J.D., Dietrich, W.E., (2003). Erosion of steepland valleys by debris flows: evidence of topographic signature. Water Resour. Res.

Stock, J.D., Dietrich, W.E., (2003). Valley incision by debris flows: evidence of topographic signature. Geol. Soc. Am. Bull. 118, 1125–1148.

Takahashi T. (1978). Mechanical characteristics of debris flow. Journal of Hydraulic Division. ASCE 104: 1153–1169.

Takahash Takahashi, T. (1981) Debris Flow. Annual Review of Fluid Mechanics, 13, 57-77.

Takahashi, T., (1991). Debris Flows: Mechanics, Prediction and Countermeasures. Balkema, Rotterdam.

Takahashi (2007). Debris Flow, Mechanics, Prediction and Countermeasures. Leiden: Taylor and Francis/Balkema.

Tarboton, D. (1997). A new method for the determination of flow directions and upslope areas in grid digital elevation models. Water Resour. Res. 33, 309–319.

Tarolli P., and Dalla Fontana G. (2009). Hillslope-to-valley transition morphology: new opportunities from high resolution DTMs. Geomorphology 113, 47–56.

Tarolli P. (2014). High-resolution topography for understanding Earth surface processes: opportunities and challenges, Geomorphology, 216, 295–312.

Tecca, P.R., Genevois, R., (2009). Field observations of the June 30, 2001 debris flow at Acquabona (Dolomites, Italy). Landslides.

Theule, J., Liebault, F., Loye, A., Laigle, D., and Jaboyedoff, M. (2012). Sediment budget monitoring of debris flow and bedload transport in the manival torrent, se france. Nat. Hazard Earth Sci. 12, 731–749.

Tiranti D., Deangeli C. (2015). Modeling of debris flow depositional patterns according to the catchment and sediment source area characteristics. Frontier in Earth Science, v. 3.

Tiranti, D., Cavalli, M., Crema, S., Comiti, F., Zerbato, M., Graziadei, M., et al. (2016). Semi-quantitative method for the assessment of debris supply from slopes to river in ungauged catchments. Sci. Total Environ. 554–555, 337–448.

Tiranti, D., Cavalli, M., Crema, S., and Deangeli, C. (2018). An integrated study to evaluate debris flow hazard in alpine environment. Front. Earth Sci. 6:60.

Tognacca, C. (1999). Beitrag zur Untersuchung der Entstehungsmechanismen von Murgängen. Doctoral Thesis, ETH Zurich.

Tognacca, C., Bezzola, G.R., Minor, HE., (2000). Threshold criterion fo debrisflow initiation due to channel bed failure. In: Wiezczorek, Naeser (eds.), Proceedings of the Second International Conference on Debris Flow Hazards Mitigation Taipei, August, pp. 89–97.

Tsubaki (1972). “Keikoku taiseki dosha no ryndo,” in XXVII Japanese National Congress on Civil Engineering.

Vosselman G. V., Maas H. G. (Eds.) (2010). Airborne and terrestrial laser scanning. Whittles.

Wagner W., Ullrich A., Ducic V., Melzer T., Studnicka N. (2006). Gaussian decomposition and calibration of a novel small-footprint full-waveform digitising airborne laser scanner, 60, 100–112.

Webster T. L., Dias G. (2006). An automated GIS procedure for comparing GPS and proximal LIDAR elevations. Computers & Geosciences, 32(6), 713–726.

Wehr A., Lohr U. (1999). Airborne Laser Scanning: An Introduction and Overview. ISPRS Journal of Photogrammetry and Remote Sensing, Vol. 54, No. 2-3, pp. 68-82.

Weng Q. (2006). An evaluation of spatial interpolation accuracy of elevation data. In Progress in Spatial Data Handling, Riedl A, Kainz W, Elmes GA (eds). Springer-Verlag: Berlin; 805–824.

Wheaton JM. (2008). Uncertainty in morphological sediment budgeting of rivers. Unpublished PhD, University of Southampton, Southampton, 412 pp.

Wheaton J. M., Brasington J., Darby S. E., Sear D. A. (2010). Accounting for uncertainty in DEMs from repeat topographic surveys: improved sediment budgets. Earth Surface Processes and Landforms 35(2): 136–156.

Whipple, K.X., Dunne, T., (1992). The influence of debris flow rheology on fan morphology, Owens Valley, California. Geol. Soc. Am. Bull. 104, 887–900.

Wilson J. P., Gallant J. C. (2000). Digital terrain analysis. In: Wilson JP and Gallant JC (eds) Terrain Analysis: Principles and Applications. New York: Wiley, 1–28.

Wilson M. D., Atkinson P. M. (2005). The use of elevation data in flood inundation modelling: a comparison of ERS interferometric SAR and combined contour and differential GPS data, Intl. J. River Basin Management, 3, 3–20.

Wise S. M. (2000). Assessing the quality for hydrological applications of digital elevation models derived from contours. Hydrological Processes 14:1909.1929.

Wise S. M. (2007). Effect of differing DEM creation methods on the results from a hydrological model. Computers and Geosciences 33: 1351–1365.

Wood J. D., Fisher P. F. (1993). Assessing Interpolation Accuracy in Elevation Models. IEEE Computer Graphics and Applications, 13, 48-56.

Wood J. D. (1996). The geomorphological characterisation of digital elevation models. Unpublished doctoral thesis, University of Leicester.

Yang X., Hodler T. (2000). Visual and statistical comparisons of surface modeling techniques for point-based environmental data, Cartography and Geographic Information Science, 27(2):165–175.

Zanobetti, D., Lorgere, H., Preissman, A., Cunge, J.A., (1970). Mekong Delta mathematical program construction. J. Waterways Harbour Div. ASCE 96 (2), 181–199.